No. 292
January 1985

HYDRODYNAMICS OF HIGH-SPEED SMALL CRAFT

by

Lawrence J. Doctors
Visiting Associate Professor

Department of Naval Architecture
and Marine Engineering
College of Engineering
The University of Michigan
Ann Arbor, Michigan 48109

PREFACE

These notes cover the hydrodynamic aspects of air-cushion vehicles, hydrofoil boats, planing craft, and water propellers. In each case, the emphasis has been placed on a physical description of the problem, together with a theoretical development of the results. Comparison of the available theories with experiments has been supplied where possible.

In almost all of the problems discussed, the theory uses knowledge that an engineer will have acquired in basic courses on fluid mechanics and engineering dynamics. However, in a small number of sections, it has been necessary to simply quote results, without being sidetracked by a lengthy mathematical development.

Enough information is supplied so that the student will be able to estimate the powering requirements of these high-performance craft. An extensive bibliography is provided to enable further reading on detailed aspects of these vehicles.

The chapters are written so that they can be read independently of each other. For this reason, a small amount of repetition was necessary -- mainly in the definition of symbols. The notation was chosen to be as uniform and consistent as possible throughout the text. The principle exception to notational uniformity is with regard to the use of the symbol L which can mean either the length or lift according to the context. The formulas are all presented in consistent units. A minor exception to this rule occurs in Chapter 5, where it was decided to remain faithful to the planing-boat tradition of measuring angles in degrees rather than radians.

I would like to extend my appreciation to Mrs. Paula Bousley for the excellent assistance she gave me. Her help was in the area of typing the text, laying out of the diagrams, and editorial advice. It would have been

impossible to prepare these extensive notes, with such a high standard of presentation, without being able to rely on her many skills.

CONTENTS

LIST OF FIGURES

LIST OF TABLES

1. INTRODUCTION

1.1. Definition of High-Performance

Small high-performance craft are characterized as having a relatively high speed for their size. That is to say, the Froude number is large. The Froude number is defined by

$$F = V/\sqrt{gL} \quad , \tag{1.1}$$

where V is the velocity, g is the acceleration due to gravity, and L is the craft length. The "length" to use in (1.1) is often poorly defined in the case of high-speed craft, since the effective, or hydrodynamic, length can change considerably with respect to the speed.

Thus, for a planing boat, the effective wetted length becomes less as the speed increases, and therefore, a beam Froude number is often used instead. This is defined as

$$F_B = V/\sqrt{gB} \quad , \tag{1.2}$$

in which B is the craft wetted beam. Savitsky (1964), for example, used the beam to define the lift and drag coefficients, as well as the Froude number (referred to by him as the speed coefficient).

Generally speaking, the higher performance, or speed, requires a considerably increased installed power. This is because the drag is a strongly increasing function of the speed. Thus, if we took the drag to depend on the square of the speed, then the required propulsive power would be

$$P = DV \tag{1.3}$$

$$= k V^3 \quad . \tag{1.4}$$

Thus, doubling the installed power, for example, results in an increase in speed of only 26%.

A second difficulty with attempting to increase the speed is the resulting poor ride in rough water.

Both of these problems -- too large a required installed power, and unacceptable accelerations in rough water -- need novel approaches to the design.

1.2. Typical Design Problems

The air-cushion vehicle (ACV) experiences less drag by being supported on its cushion above the water. Problem areas of interest are:

1) How to minimize the lift power,
2) How to minimize the response to waves -- yet maintain adequate stability. (These are conflicting requirements.),
3) How to achieve adequate control,
4) How to reduce the noise level which is characteristic of ACVs, and
5) How to reduce the high cost of construction and maintenance.

The hydrofoil is also based on the principle of lifting the craft out of the water to reduce drag and motions in waves. Problems which are of concern to designers are:

1) The choice of optimum foils to give maximum lift-to-drag ratio,
2) Avoid cavitation which results in a loss of lift and erosion of the foils,
3) In the case of a high-speed hydrofoil, cavitation can not be avoided. In this case special supercavitating sections are used to minimize the effects referred to above,
4) Stability has to be adequate,

5) The response to waves must be minimized. This conflicts with the previous requirement. This is done either naturally or artificially in the case of fully-submerged foils,

6) The achievement of adequate control, and

7) The transmission of the power to the water.

Finally, in the case of planing boats, we are usually confronted with the following questions:

1) Maintaining a reasonably low resistance,

2) Minimizing the effect of waves -- usually in the form of slamming,

3) Avoidance of porpoising, and

4) The transmission of the power to the water.

1.3. Transport Efficiency for Different Craft

As noted previously in Sec. 1.1, one pays a penalty for high speed, in terms of the installed power. The transport efficiency is defined as

$$\eta_{TRANS} = WV/P \quad , \tag{1.5}$$

where W is the craft weight and P is the power. In the case of ACVs we should use the total installed power. The weight is taken as the total weight. However, a case could be made in this definition for using the useful payload instead.

It is clear that the effective lift-to-drag ratio of a vehicle is given by the relationship:

$$(L/D)_{EFF.} = (WV/P)/\eta$$

$$= \eta_{TRANS}/\eta \quad , \tag{1.6}$$

where η is the propulsive efficiency. Thus η_{TRANS} represents the

efficiency of the entire vehicle, while $(L/D)_{EFF.}$ is the efficiency of the craft alone.

For the air-cushion vehicle, we should write the following:

$$\eta P = \eta_P P_P + \eta_L P_L \quad , \tag{1.7}$$

where P_P and P_L are the propulsion and lift powers, and η_P and η_L are the propulsion and lift efficiencies. The effective lift-to-drag ratio can then be found from (1.6).

Fig. 1.1, taken from Mantle (1975), shows how the efficiency drops off with speed for most craft. It also shows the relatively lower efficiency obtained by the more exotic craft. The effects are very pronounced when we consider the logarithmic scales that are being used.

The achievement level -- indicated by the von Karman-Gabrielli line of 1950 -- represents the best that had been obtained at that time. With technological improvements, this line has been pushed upward.

1.4. Dimensional Analysis

Dimensional analysis is a useful tool in the design of high-performance vehicles. It is used particularly when setting up model tests, to ensure that the full-size craft is being properly represented by the model.

The following variables are of particular importance:

TABLE 1.1. Principal Dimensional Variables

Symbol	Name	Symbol	Name
L	craft length	W	craft weight
ρ_w	water density	S	planform area
ρ	air density	h	hover height
μ_w	water viscosity	P	power
μ	air viscosity	m	craft mass
g	acceleration due to gravity	λ_w	wave length
p_c	cushion pressure	τ	surface tension of the water
Q	air flow	N	angular speed of propeller
h_w	wave height		
p_a	atmospheric pressure	D	propeller diameter
D	drag	p_v	vapor pressure of the water

The above list is not exhaustive. In addition, not all the variables are applicable in some cases. For example, cushion pressure p_c, and hover height h, have no relevance for hydrofoil boats and for planing craft.

For a model to simulate a full-size craft correctly, all the applicable dimensionless parameters have to be preserved. The most common ones are shown below:

From Mantle (1975, p. 3-19)

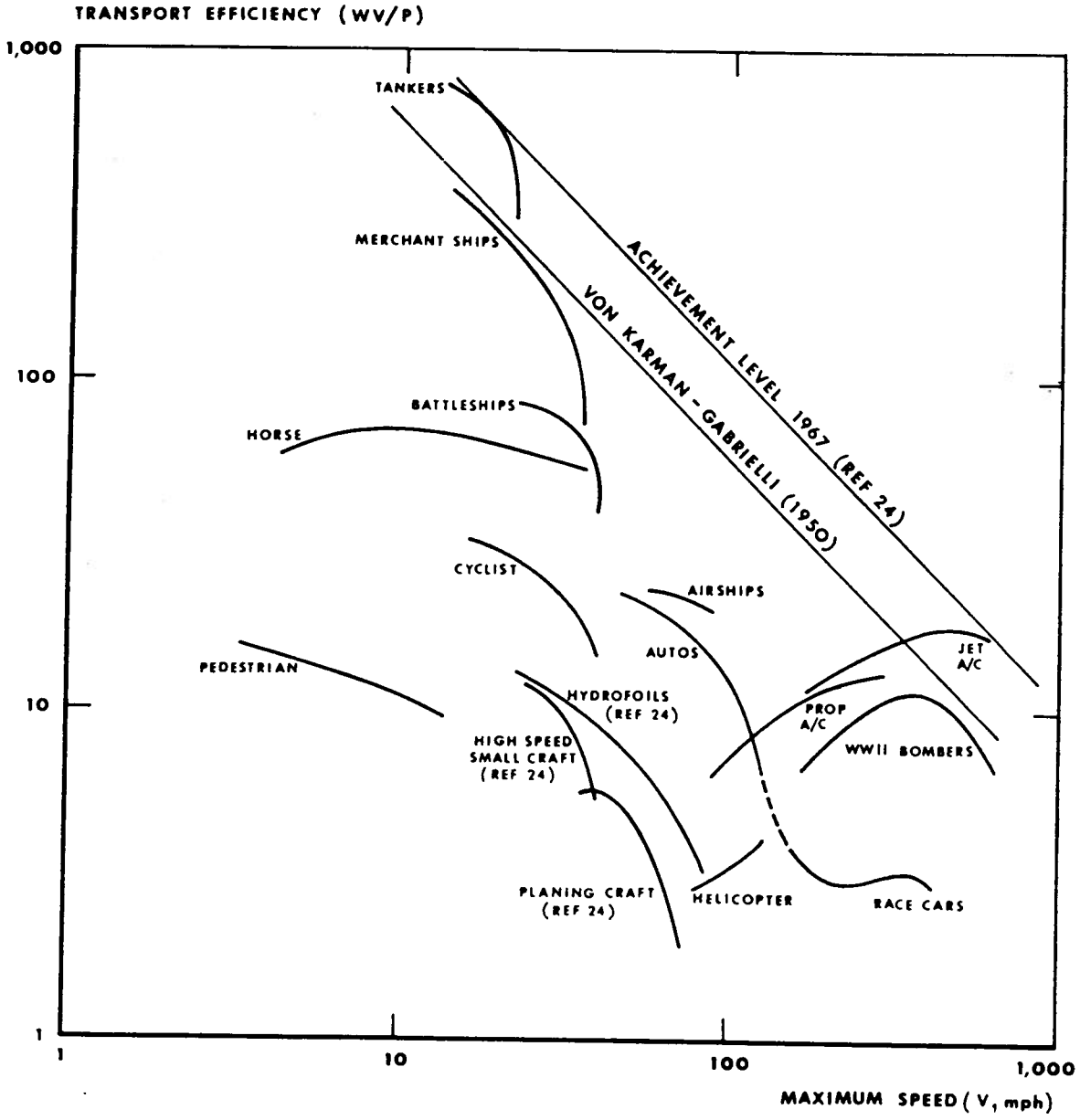

Figure 1.1: Transport Efficiency of Several Craft

TABLE 1.2. Dimensionless Quantities

Symbol	Definition	Name
R	$\rho VL/\mu$	Reynolds number for the air
R_w	$\rho_w VL/\mu_w$	Reynolds number for the water
F	$V/\sqrt{gL}$	Froude number
σ_N	$(p_a-p_v)/\frac{1}{2}\rho V^2$	cavitation number
W_e	$V\sqrt{gL/\tau}$	Weber number
k_w	h_w/L	sea roughness number
J	V/ND	advance ratio
N^*	$N/\sqrt{L/g}$	dimensionless frequency
C_p	$p_c/\rho_w gL$	cushion density number
C_a	$p_a/\rho_w gL$	compressibility number
k	$\frac{1}{2}\rho V^2/p_c$	pressure number
C_Q	Q/VL^2	flow coefficient

The last four coefficients are relevant only to air-cushion vehicles. It is common practice to use Froude scaling in model testing. That is, we ensure that F is the same for model and prototype. This means that $V \propto L^{1/2}$. At the same time, the air and water densities are generally the same for the model and prototype cases. In addition, one must preserve ratios of lengths. These include h/L, h_w/L, L^2/S, and λ_w/L.

An examination of Table 1.2 will show that it is possible to ensure that almost all these dimensionless parameters can be kept the same for the model by using Froude scaling. The notable exceptions are: the two Reynolds numbers, the cavitation number, the compressibility number, and the Weber Numbers.

Unfortunately, there is no way that the Reynolds numbers can be preserved for the model, since we cannot substantially reduce the two viscosities on the model scale. This means that any phenomenon related to frictional losses, such as the drag, are pronounced on the model. Corrections are often made for this discrepancy.

In a similar way, the surface tension of the water is beyond any reasonable control, and so the Weber number is wrong on the model. The Weber number basically affects spray generation, of which there will be much less on the model. The implication is that skirt-wetting drag on a model hovercraft will be too small. The Weber number is not important for other vehicles, though.

Regarding the cavitation number and compressibility number, these will both be too large on the model, unless the air in the model basin can be evacuated. This expensive procedure is sometimes carried out -- notably at the Netherlands Ship Model Basin. The method is to scale the atmospheric pressure so that $(p_a - p_v) \propto L$. Non-scaling of the atmospheric pressure results in too little (or delayed) cavitation at the model scale. This would be unimportant if there were also no cavitation at the full scale.

Non-scaling of the atmosphere also affects the motions of air cushion vehicles, because of compressibility of the air. Consequently, models generally exhibit smaller motions than they should.

1.5. System of Units

All equations in these notes are dimensionally consistent. This means that any consistent set of units can be used. Examples of units are given in Table 1.3.

TABLE 1.3. Some Common Units

Quantity	S.I. Symbol	English Symbol
mass	kg	slug
length	m	ft
time	s	sec
velocity	m/s	ft/sec
acceleration	m/s^2	ft/sec^2
area	m^2	ft^2
force	$kg \cdot m/s^2 = N$	$slug \cdot ft/sec^2 = lbf$
torque	Nm	lbf•ft
pressure	$N/m^2 = Pa$	lbf/ft^2
discharge	m^3/s	ft^3/sec
mass flow	kg/s	slug/sec
density	kg/m^3	$slug/ft^3$
dynamic viscosity	kg/sm	slug/sec•ft
kinematic viscosity	m^2/s	ft^2/sec
surface tension	kg/s^2	$slug/sec^2$
angular speed	s^{-1}	sec^{-1}
work	Nm=J	lbf•ft
power	J/s=W	lbf•ft/sec

2. AIR-CUSHION VEHICLES

2.1. Types of Air-Cushion Vehicles

The simplest type of ACV is the so-called plenum-chamber craft, in which air is just pumped into the cushion and allowed to escape around the edge of the craft. Obviously, to gain extra clearance, one needs to expend more lift power and hence a flexible skirt can be used to great advantage to reduce the necessary clearance for traveling in rough water.

In the early days, the plenum-chamber design was superceded by the peripheral-jet type due to the greater efficiency of the latter. That is, a greater lift could be achieved for the same power. With the advent of more advanced skirts, however, the plenum-chamber has become more popular. These vehicles are shown in Fig. 2.1.

For completeness we show the elements of the sidewall or sidehull ACV (also know as a surface-effect ship, or SES) in Fig. 2.2. The SES has been the subject of much study by the U.S. Navy. The ram-wing design is shown in Fig. 2.3, but few models have been built and tested at full scale.

2.2. Lift Performance

2.2.1. Plenum-Chamber

The cushion pressure of a plenum-chamber craft, shown in Fig. 2.4, is given by

$$p_c = W/S \quad , \tag{2.1}$$

where S is the base area, measured at the skirt hem. The flow through the system can be obtained by applying the Bernoulli equation between a point in the cushion and a point in the jet of air escaping from the craft. That is

From Mantle (1975, p. 2-4)

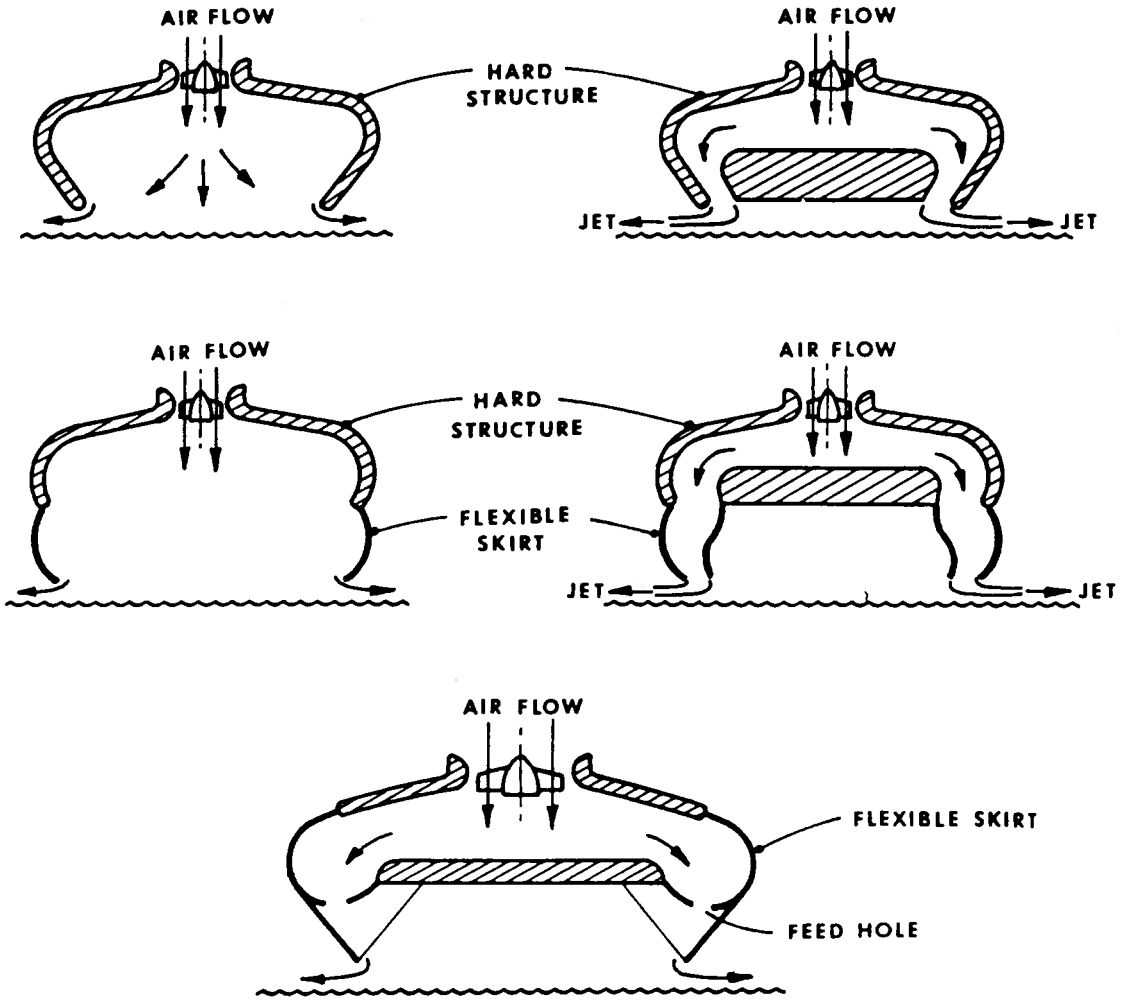

Figure 2.1: Plenum and Peripheral-Jet Craft

From Mantle (1975, p. 2-7)

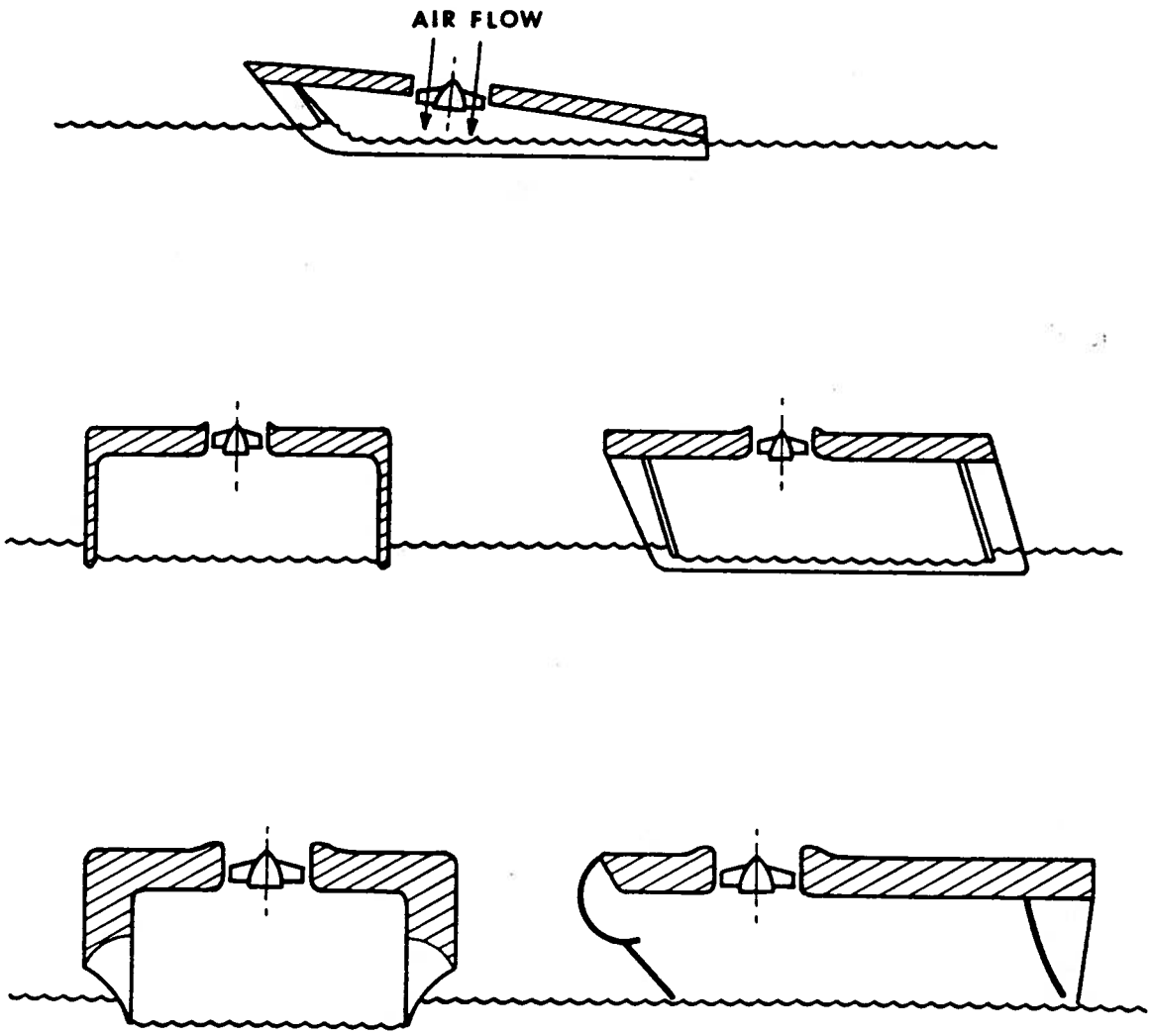

Figure 2.2: Sidewall Craft and Surface-Effect Ships

From Mantle (1975, p. 2-9)

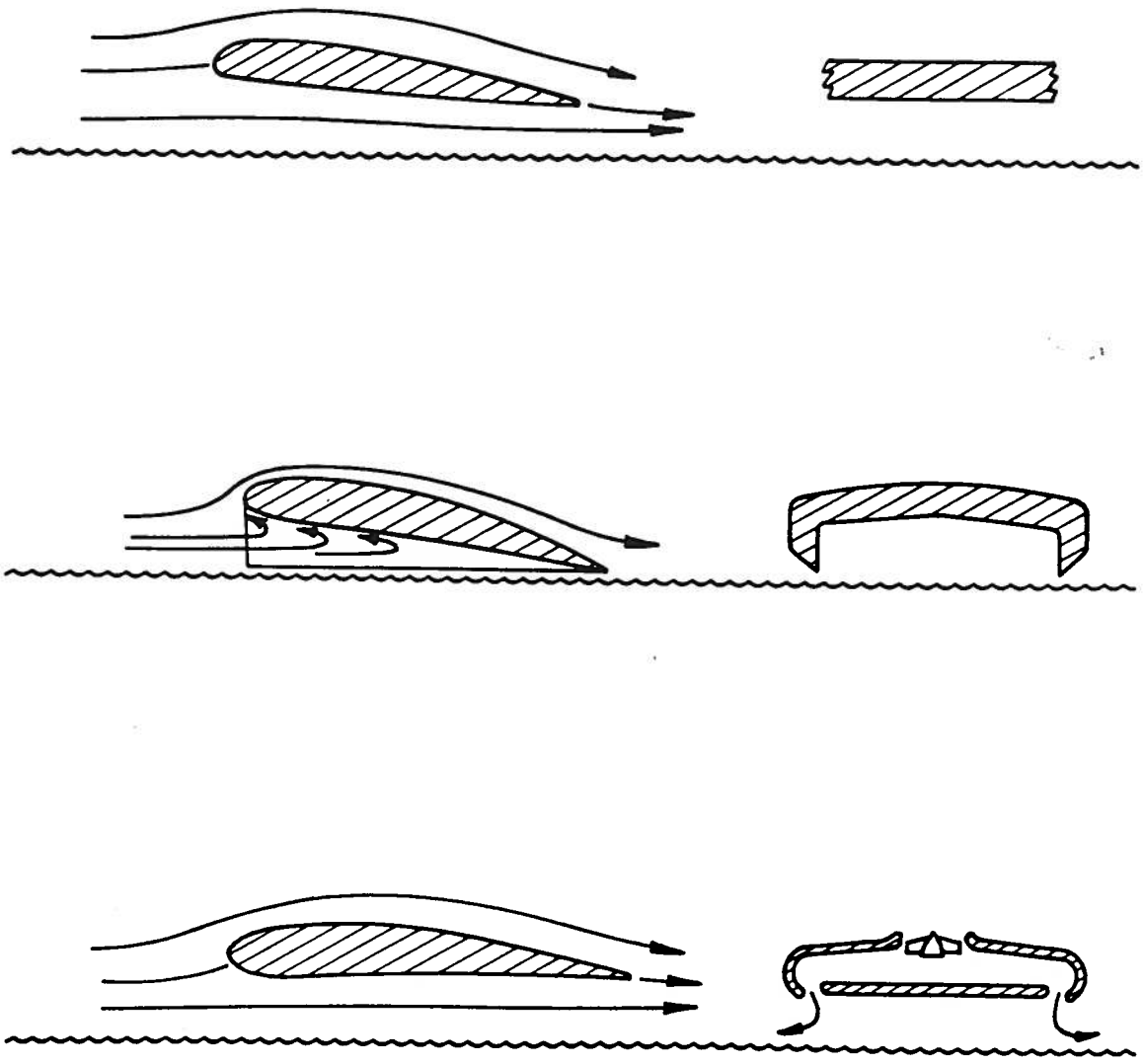

Figure 2.3: Dynamic-Lift and Ram-Wing Craft

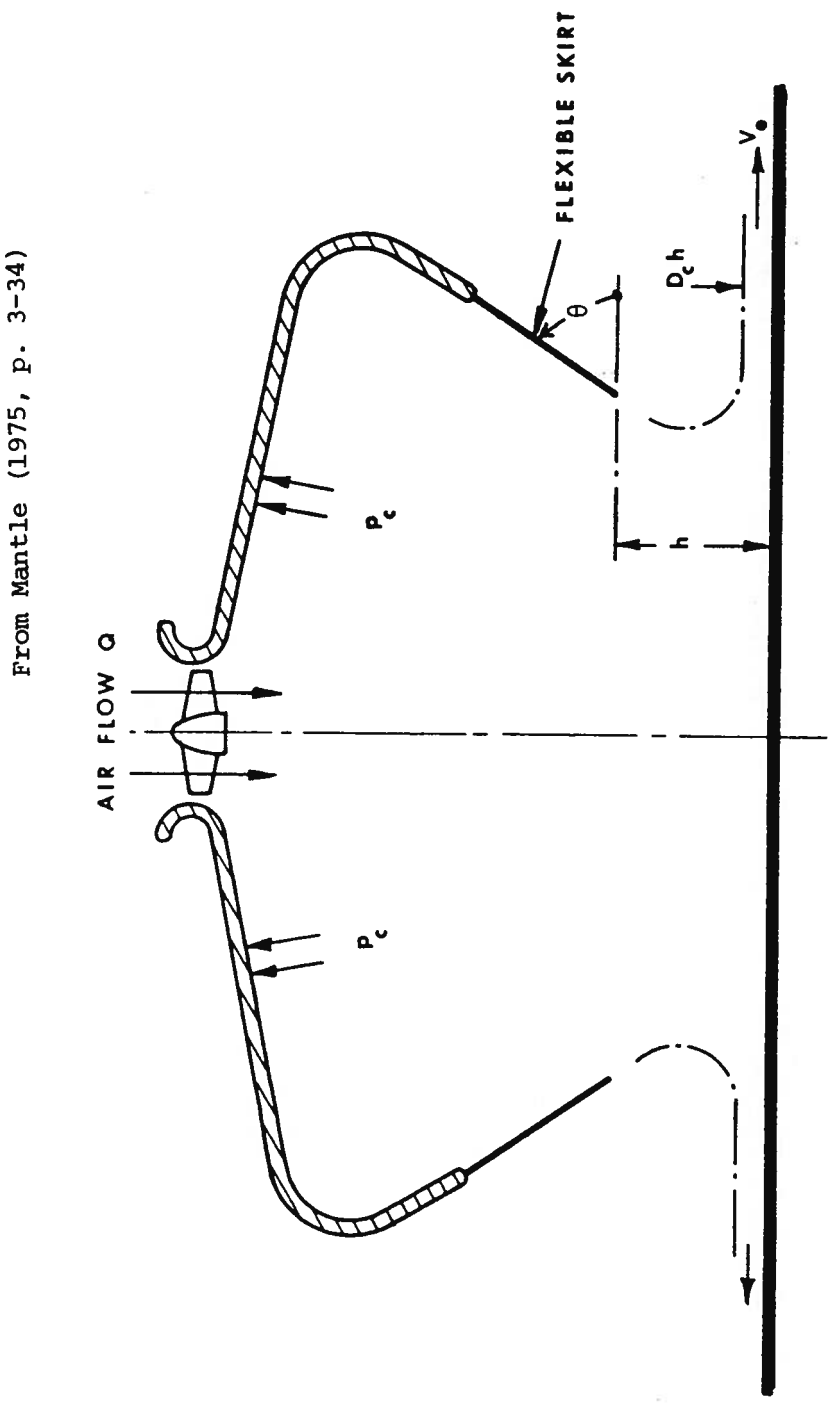

Figure 2.4: Nomenclature for Plenum-Chamber Craft

$$p + \frac{1}{2}\rho v^2 + \rho g z = \text{const.} = p_T \quad , \tag{2.2}$$

where ρ is the air density, v is the local velocity, and z is the height above some datum. The constant p_T is the total pressure. The third term (the hydrostatic one) is very small, and can be ignored. Thus:

$$p_c + \frac{1}{2}\rho v_c^2 = \frac{1}{2}\rho v_e^2 \quad ,$$

where v_c is the velocity of the air in the cushion and v_e is the velocity in the jet (assumed constant across its thickness). Obviously, v_c varies within the chamber. However, since the hoverheight is usually quite small, typically 1/20 of the chamber height, we see that v_c/v_e is about 1/20. Hence, $\frac{1}{2}\rho v_c^2 \sim \frac{1}{2}\rho v_e^2/400$ and can be neglected. Thus we have

$$p_c = \frac{1}{2}\rho v_e^2 \quad . \tag{2.3}$$

The volume flow is given by

$$Q = Ch\, D_c\, v_e \quad , \tag{2.4}$$

where D_c is the discharge coefficient, which takes into account flow contraction and viscous effects, and C is the craft perimeter. Combining these results, we have

$$Q = ChD_c\sqrt{2p_c/\rho} \quad . \tag{2.5}$$

The power required to provide this flow is given by

$$P_L = Qp_c \quad , \tag{2.6}$$

or

$$P_L = ChD_c p_c \sqrt{2p_c/\rho} \quad . \tag{2.7}$$

This analysis has ignored the efficiency of the fan and any ducting losses, as well as any alleviation in lift due to the effect of forward speed. The inlet ram recovery has also not yet been considered here.

The discharge coefficient (more precisely, the contraction coefficient) can be found by an ideal-flow analysis in the neighborhood of the lip of the plenum. Useful results can be obtained from two-dimensional theory, which yields values shown in Table 2.1.

TABLE 2.1. The Discharge Coefficient

θ	0°	45°	90°	135°	180°
D_C	0.500 1/2	0.537	0.611 $\pi/(\pi+2)$	0.746	1.000 1

A typical value of θ is 45°, which gives a discharge coefficient only 7% more than the minimum.

2.2.2. Peripheral jet

We consider the simple thin-jet theory first. The arrangement of a peripheral-jet craft is shown in Fig. 2.5, while the details of the thin-jet approximation are shown in Fig. 2.6a.

By geometry we have

$$h = r(1 + \cos\theta) \quad , \tag{2.8}$$

where r is the radius of curvature of the air jet.

Now, the concept of centrifugal force gives the normal acceleration in the jet as

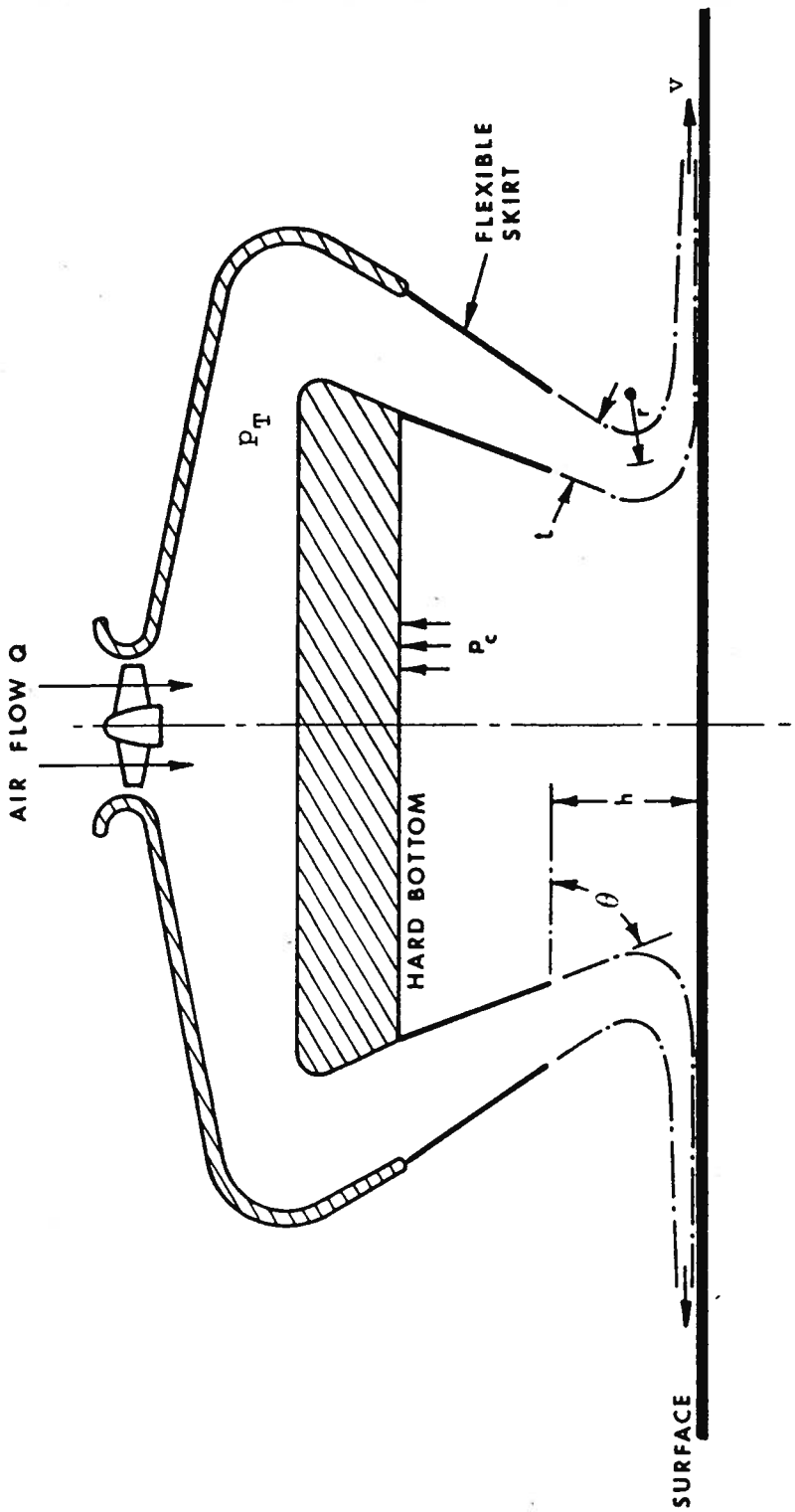

From Mantle (1975, p. 3-27)

Figure 2.5: Nomenclature for Peripheral-Jet Craft

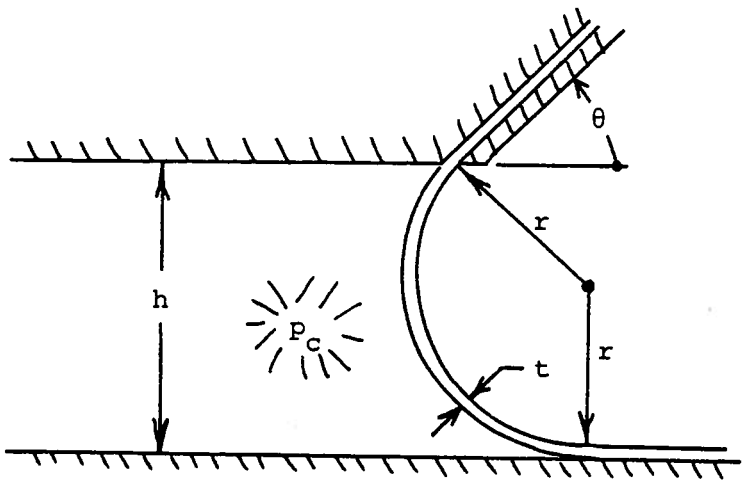

(a) Thin-Jet Theory

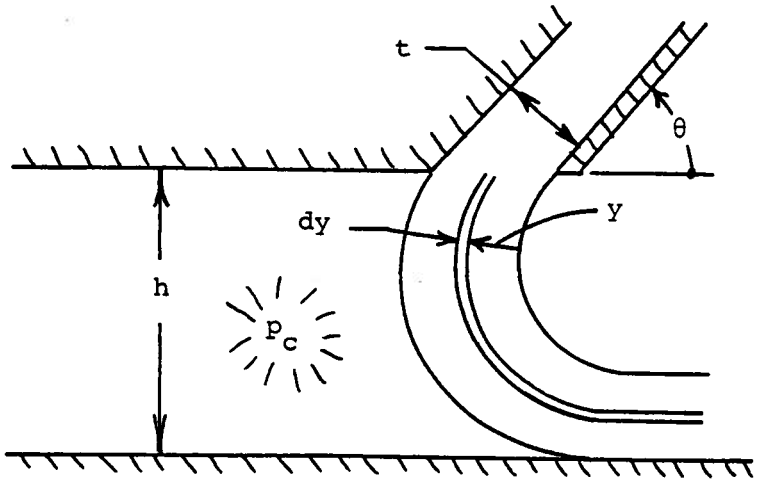

(b) Thick-Jet Theory

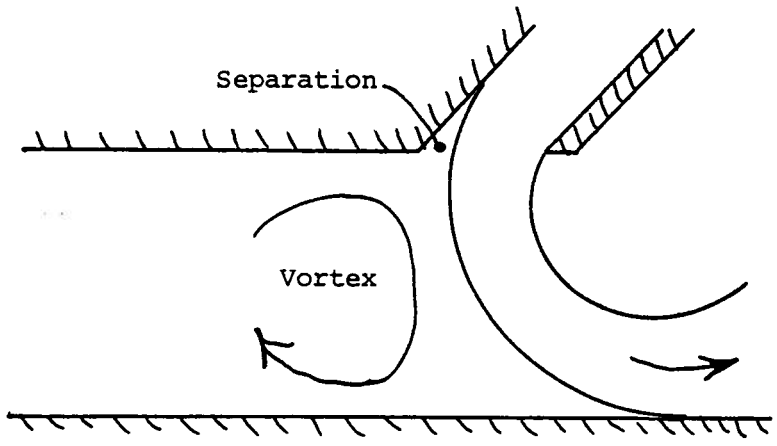

(c) Separation and Vortex in a Real Fluid

Figure 2.6: Details of Thin-Jet and Thick-Jet Theory

$$a = v^2/r = \frac{2}{\rho}(p_T - p)/r = F/m \quad ,$$

where the Bernoulli equation (2.2) has also been used. We utilize the simple mean pressure across the jet, so that $p = p_C/2$, and thus

$$a = \frac{\frac{2}{\rho}(p_T - \frac{1}{2}p_C)}{h/(1 + \cos\theta)} = p_C dA/\rho t dA \quad ,$$

or

$$2p_T - p_C = p_C \frac{h}{t(1 + \cos\theta)} \quad .$$

This may be rearranged to give

$$\frac{p_C}{p_T} = \frac{2x}{1 + x} \quad , \tag{2.9}$$

$$\text{where} \quad x = \frac{t}{h}(1 + \cos\theta) \quad . \tag{2.10}$$

The thick-jet theory, shown in Fig. 2.6b, considers the details of the pressure variation across the thickness of the jet.

We repeat the analysis, but for a stream tube of the jet as shown:

$$a = \frac{v^2}{r} = \frac{\frac{2}{\rho}(p_T - p)}{r} = \frac{F}{m} = \frac{dp\ dA}{\rho dA dy} \quad .$$

Hence

$$\frac{dp}{p_T - p} = \frac{2}{r} dy \quad ,$$

or $$\int_{p=0}^{p} \frac{dp}{p_T - p} = \frac{2}{r} \int_{0}^{y} dy \quad .$$

Thus $$\left[-\ln(p_T - p)\right]_{p=0}^{p} = \frac{2y}{r} \quad ,$$

and $$-\left[\ln(p_T - p) - \ln(p_T)\right] = \frac{2y(1 + \cos\theta)}{h} \quad ,$$

and $$\ln \frac{p_T - p}{p_T} = - \frac{2y(1 + \cos\theta)}{h} \quad . \tag{2.11}$$

Hence, $$1 - \frac{p}{p_T} = e^{-2x} \quad .$$

Finally, we substitute p_C for p, and t for y, to obtain:

$$\frac{p_C}{p_T} = 1 - e^{-2x} \quad . \tag{2.12}$$

Notes:

1) Thick-jet theory ignores the fact that r varies with y.

2) It also ignores the separation that occurs in the case of a real fluid when the hoverheight becomes small. An example of this separation is shown in Fig. 2.6c.

3) It can be shown mathematically that the thin- and thick-jet formulas (2.9) and (2.12) approach each other as x becomes small.

4) This is also seen in Fig. 2.7, which compares the theories with experimental results.

The volume flow can be calculated as follows:

$$Q = C \int_{y=0}^{t} v \, dy$$

From Mantle (1975, p. 3-31)

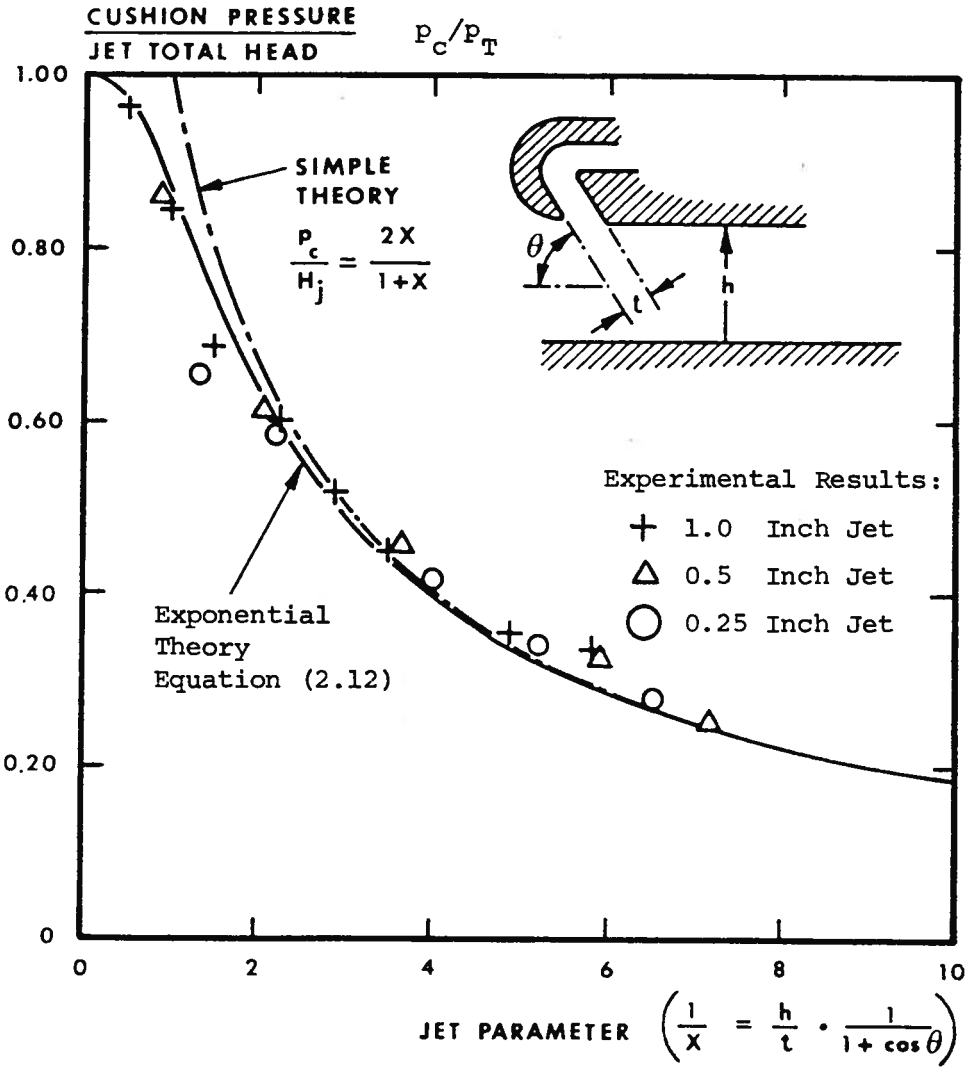

Figure 2.7: Thin- and Thick-Jet Theories Compared with Experimental Results

$$= C \int_0^t \left[\frac{2}{\rho}(p_T - p) \right]^{1/2} dy \quad .$$

Now, from (2.11),

$$Q = \left(\frac{2}{\rho}\right)^{1/2} C \int_0^t \sqrt{p_T}\, e^{-y(1 + \cos\theta)/h}\, dy$$

$$= \left(\frac{2}{\rho}\right)^{1/2} C \sqrt{p_T}\, \frac{-h}{1 + \cos\theta} \left[e^{-y(1 + \cos\theta)/h} \right]_0^t$$

$$= \left(\frac{2p_T}{\rho}\right)^{1/2} C \frac{h}{1 + \cos\theta} \left[1 - e^{-t(1 + \cos\theta)/h} \right] \quad ,$$

and we obtain,

$$Q = \frac{Ch}{1 + \cos\theta} \left(\frac{2p_T}{\rho}\right)^{1/2} (1 - e^{-x}) \quad , \tag{2.13}$$

and $$P_L = Q p_T \quad . \tag{2.14}$$

2.3. Skirts

2.3.1. The basic purpose

Skirts are used to increase the obstacle-clearing capability of an ACV, thus permitting operations in a reasonable sea state.

Specific design styles include:

1) Jet extension or trunk,

2) Jetted bag,

3) Bag and finger,

4) Loop and finger (or segment),

5) Peripheral skirt and jupes,

6) Pericell,

7) Planing surfaces, and

8) Flexible bags.

The term "seal" is usually applied to (7) and (8) when used on surface-effect ships, or sidehull hovercraft. These components are then used at the bow and stern between the sidehulls.

Fig. 2.8 shows the development and use of trunks and jetted bags, and finally bags and fingers by the British Hovercraft Corporation. It is interesting to note the peculiar "inside-only" half trunk, that was originally used.

In Fig. 2.9 are shown illustrations of (a) a bag and fingers, (b) loop and segments, and (c) jupes.

In Fig. 2.10, examples of (a) the pericell, and (b) seals that are used for sidewall ACVs, or SESs, are given.

2.3.2. Stability

To achieve stability, some type of compartmentation is required in order to prevent cross flow, so that the pressure in the cushion will be higher under the "down side" of the craft.

This is shown in Fig. 2.11, which illustrates a variety of ways of dividing the cusion by means of jets, bags, and fingers.

More specific information for the British Hovercraft Corporation SR.N4 is shown in Fig. 2.12. It is seen that the cushion is divided into three volumes. The cross-wise bags are split into two to increase the freedom of passage of obstacles (such as waves) under the craft.

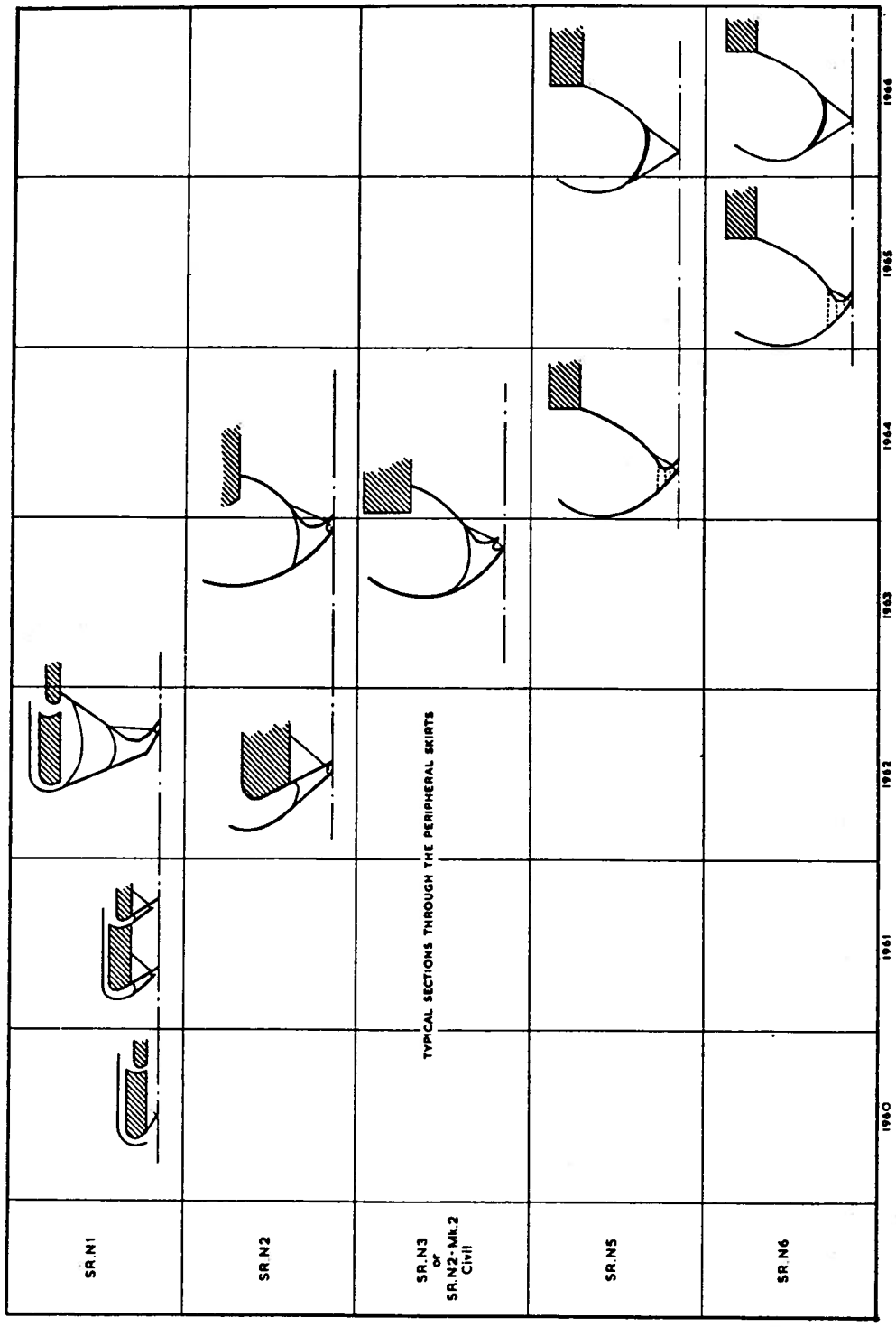

From Mantle (1975, p. 5-5)

Figure 2-8: Development of Bag-and-Finger Skirt

From Mantle (1975, p. 5-2)

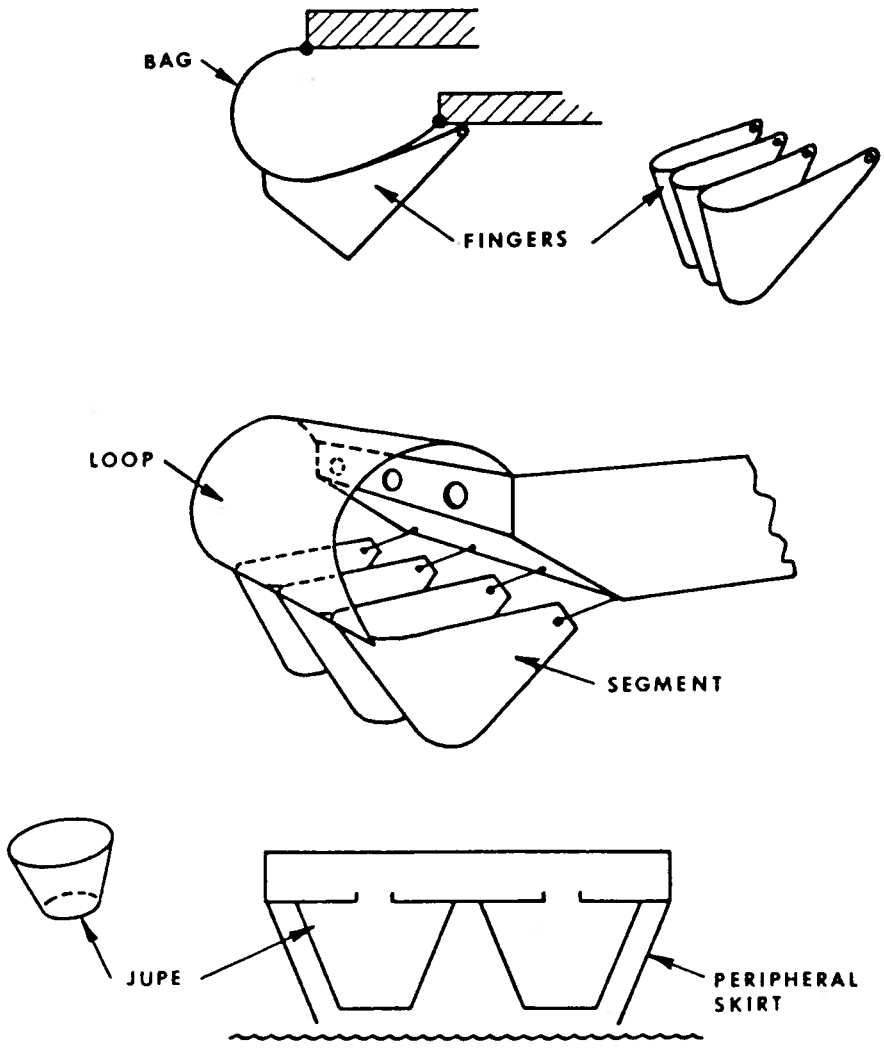

Figure 2.9: Basic Skirt Systems

From Mantle (1975, p. 5-3)

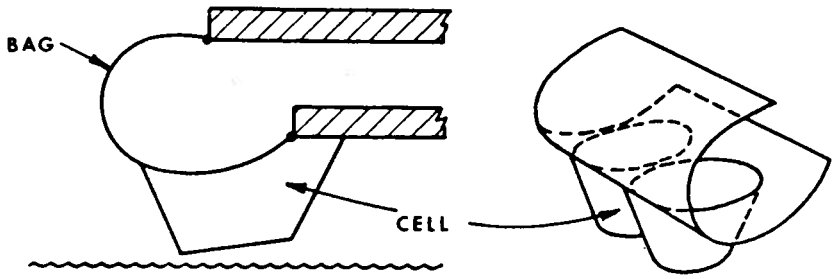

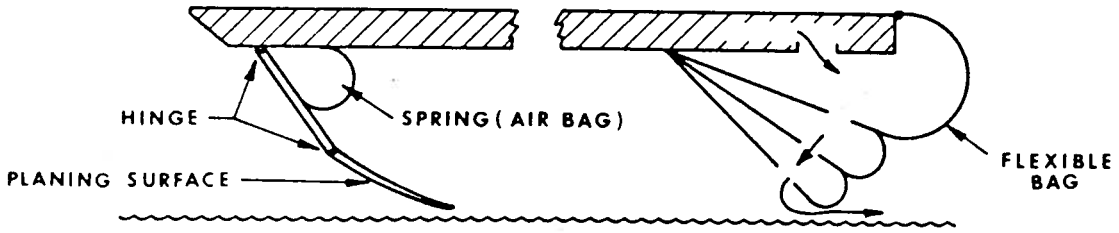

Figure 2.10: Basic Skirt Systems (continued)

From Mantle (1975, p. 5-14)

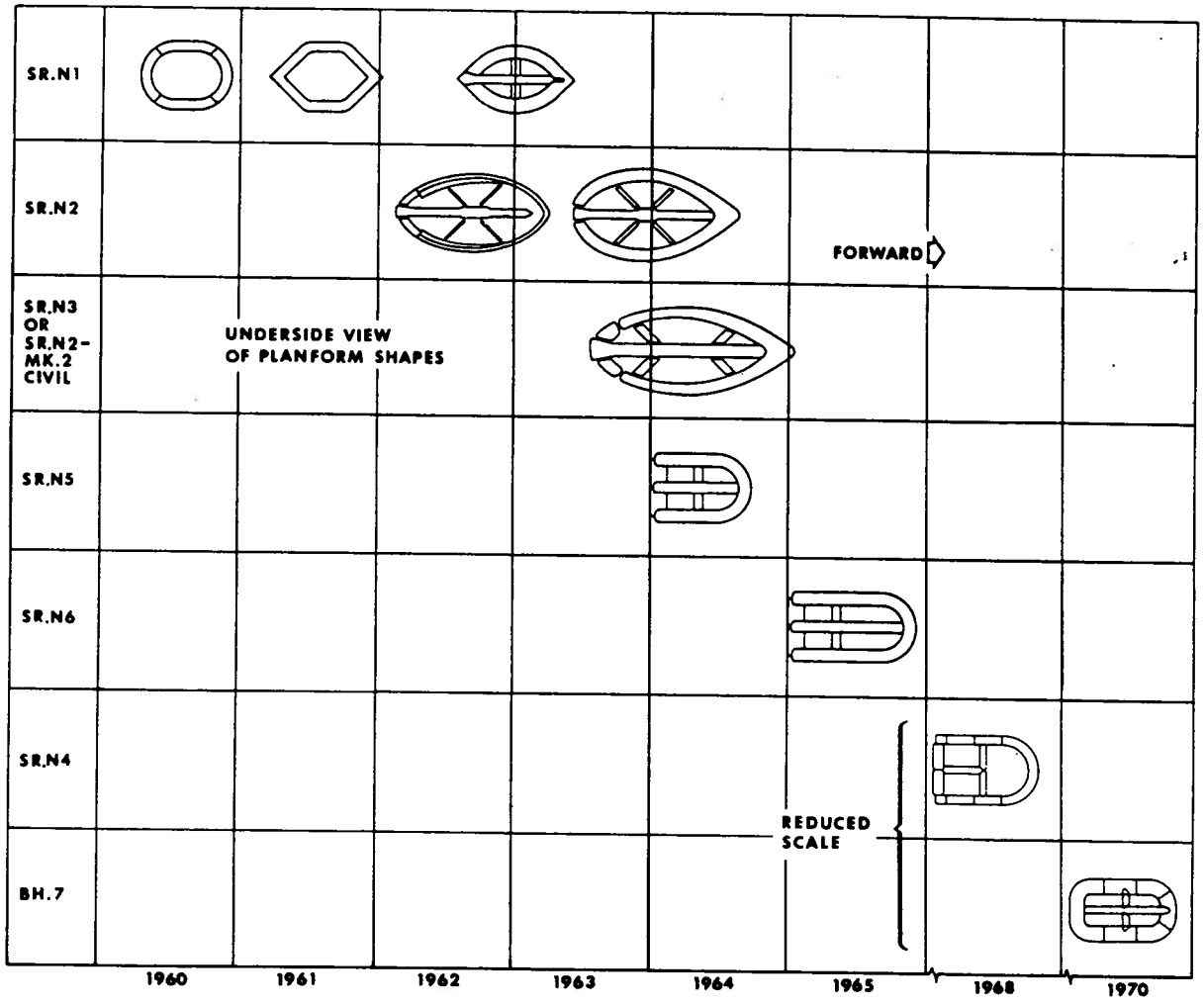

Figure 2.11: Development of Compartmentation

From Mantle (1975, p. 5-9)

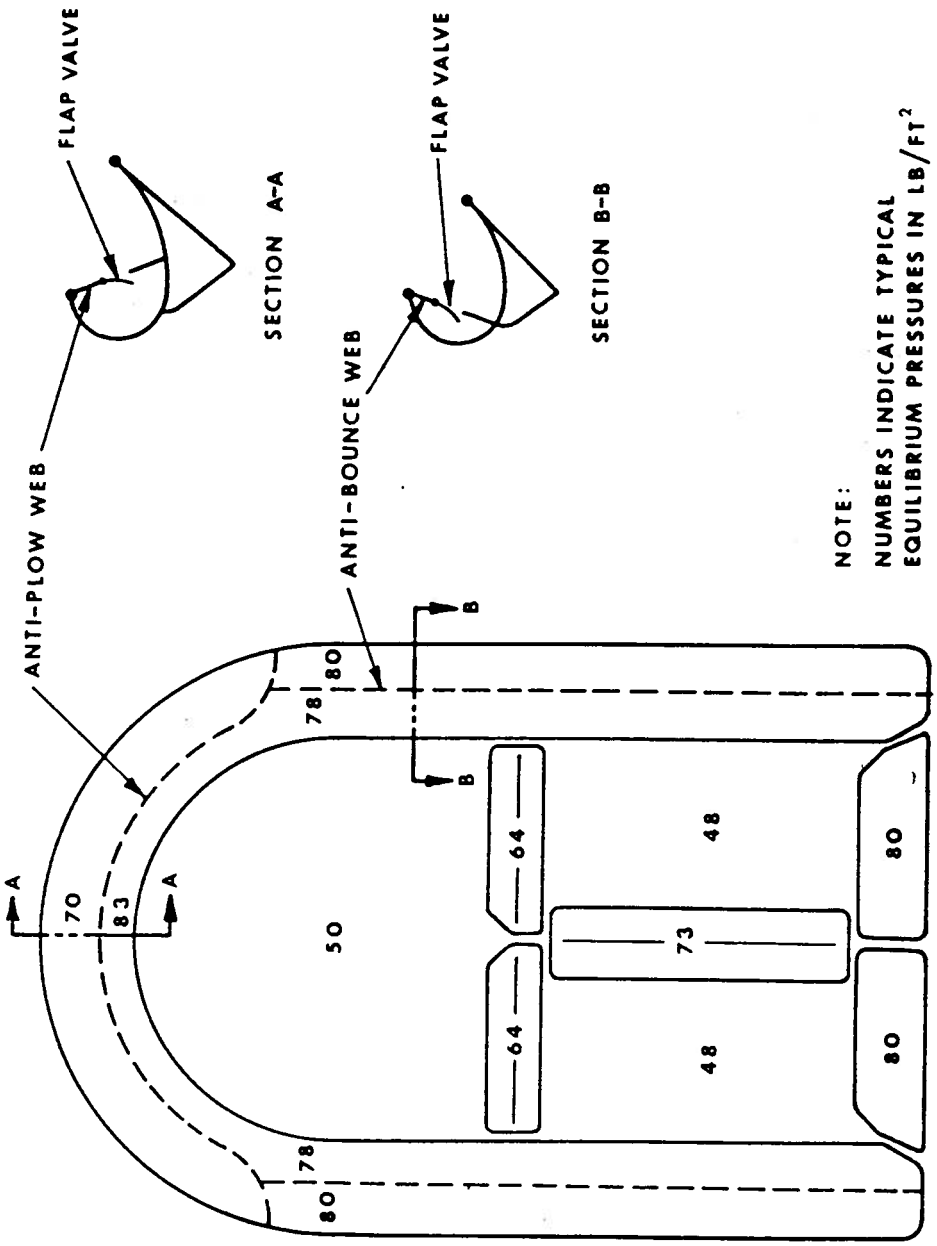

Figure 2.12: Anti-plow and Anti-bounce Webs for the SR.N4 Hovercraft

The pressures used in the bags are also noted. Two additional features of the bags are (a) the anti-plow web in the forward section, and (b) the anti-bounce web in the side sections. The former is to prevent the bow skirt from being dragged back too far in an extreme situation resulting in an aft movement of the center of pressure, which would aggravate the bow-down trim of the craft. The anti-bounce web acts to damp an inherent up-and-down motion instability in the side bags, under smooth conditions of the sea.

Further details of the longitudinal keel are shown in Fig. 2.13.

Cones or closed fingers are used at the stern to prevent scooping of the water.

The sizing of the holes, shown in Fig. 2.14, can be made to generate the desired pressure in the bag, so that it will achieve the appropriate shape when inflated.

2.3.3. Materials

The most commonly used materials are a woven nylon fabric cloth coated with neoprene and natural rubbers such as styrene butadiene rubber, which have been found to give the best results with respect to endurance.

The strength of the materials results mainly from the fabric cloth, while the sealing and resistance to delamination is handled by the coating.

Special flagellators, devices which blow air and water over a specimen of the skirt, simulate the flapping action of the skirt as it passes over waves. This action causes the delamination, which is the main source of wear of skirt fingers, whose life is typically 200 to 600 hours of operation.

Bags tend to last longer, perhaps up to 2000 hours of operation --

From Mantle (1975, p. 5-15)

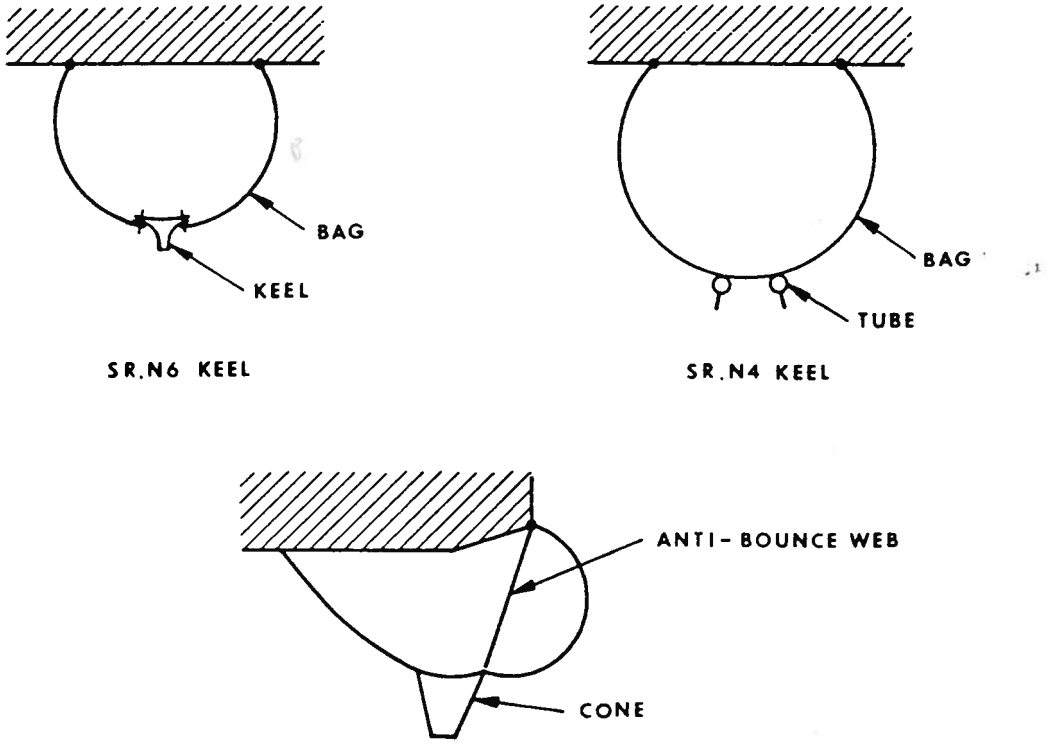

Figure 2.13: Keel and Rear-Skirt Sections

From Mantle (1975, p. 5-17)

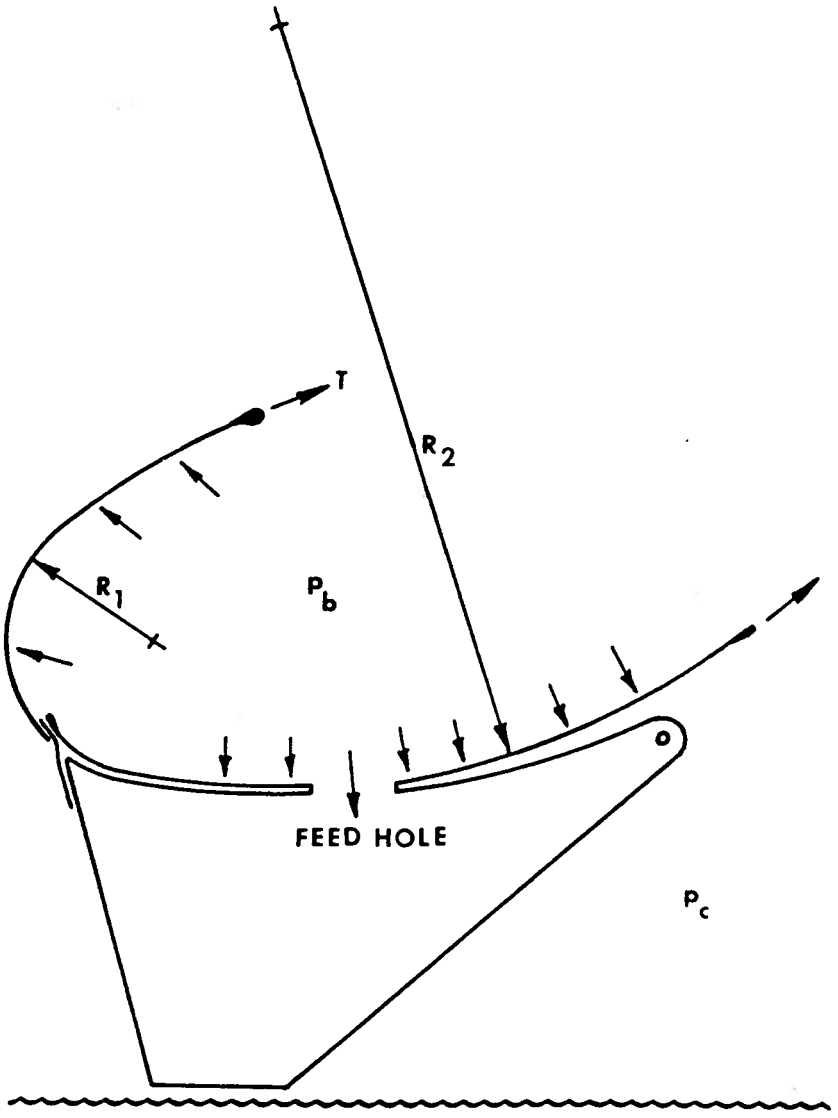

Figure 2.14: Two-Dimensional Section of a Bag-and-Finger Skirt

representing around 100,000 miles of travel.

Interestingly, abrasion of the skirt on hard ground is not a major factor in skirt wear, as was originally thought.

2.4. Stability and Motions in Waves

2.4.1. Static stability of a plenum chamber in heave

We need to consider the fan and duct characteristics. This is done by plotting the dimensionless pressure

$$\psi = p_f/\rho\omega^2 D^2 \tag{2.15}$$

against the dimensionless flow rate

$$\phi = Q/\omega D^3 \quad , \tag{2.16}$$

where p_f is the fan pressure rise, ω is the rotational speed in radians per unit time, D is the fan diameter, and Q is the flow. The fan efficiency is defined as

$$\eta_L = p_f Q/P_L \quad , \tag{2.17}$$

where P_L is the power absorbed by the fan.

Typical fan curves are shown in Fig. 2.15. The fans are categorized according to the specific speed and specific diameter defined below:

$$N_S = \phi^{1/2}/\psi^{3/4} = \omega Q^{1/2}/(p_f/\rho)^{3/4} \quad ,$$

and (2.18)

$$D_S = \psi^{1/4}/\phi^{1/2} = D(p_f/\rho)^{1/4}/Q^{1/2} \quad .$$

If we assume that the ducting losses are proportional to the square of the velocity (which will vary along the ducting), it will also be proportional to the square of the volume flow. This neglects any minor effect of the Reynolds number. Hence, we have

From Mantle (1975, p. 7-12)

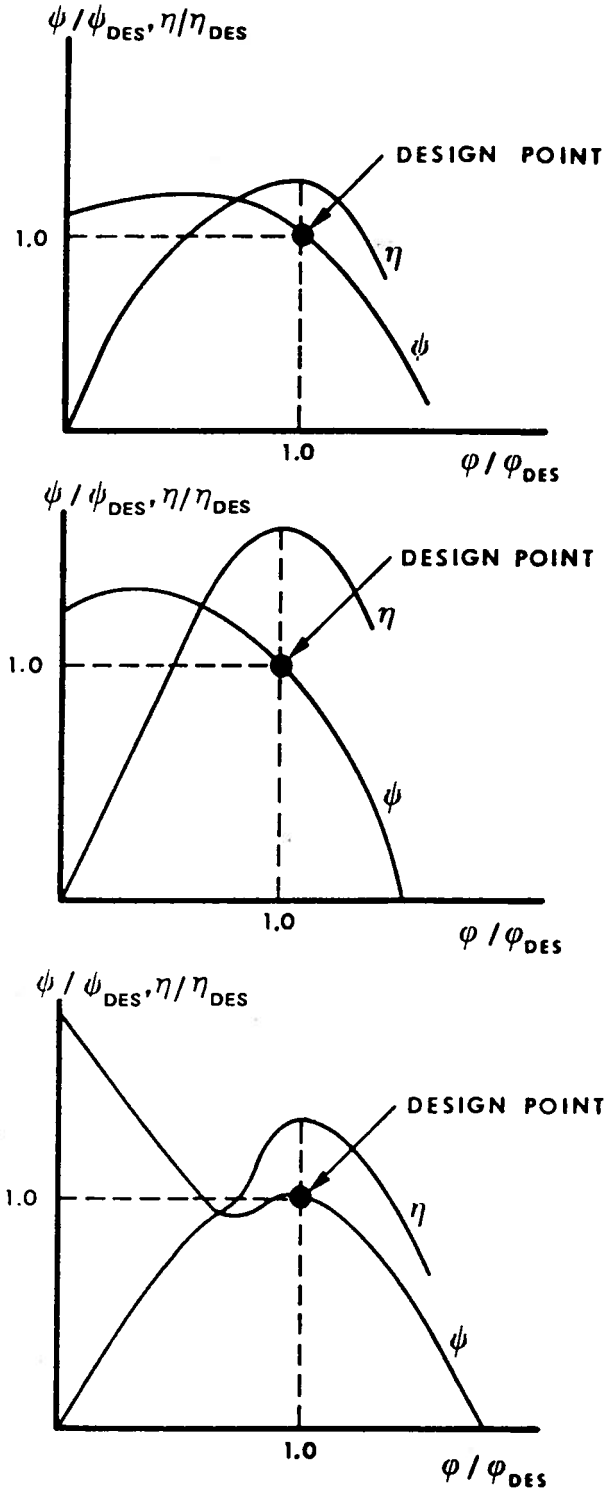

CENTRIFUGAL FAN

(BACKWARD CURVED)

$N_s < 3$

MIXED FLOW FAN

$2 < N_s < 4$

AXIAL FAN

$N_s > 3$

Figure 2.15: Typical Pressure-Flow and Efficiency Curves

$$p_c = p_f - k_D Q^2 \quad , \tag{2.19}$$

whereas the fan curve (at constant speed, say) is defined by

$$p_f = p_f(Q) \quad . \tag{2.20}$$

We can now combine (2.1) and (2.19) to determine the equilibrium fan flow:

$$\frac{W}{s} = p_f(Q) - k_D Q^2 \tag{2.21}$$

Notes:

1) Eq. (2.21) is nonlinear, but can be solved numerically, if $p_f(Q)$ is known.

2) A graphical method can be employed, by plotting the curve $p_{required} = \frac{W}{s} + k_D Q^2$ on the fan curve. The intersection point gives the solution.

3) The analysis assumed a constant engine speed. It could be extended to include engine-fan coupling effects.

If we now displace the ACV from the equilibrium condition, we obtain the perturbation to the lift. (Eq. (2.1) does not apply in the non-equilibrium condition.) Thus, we have

$$p_c = p_f(Q) - k_D Q^2 \quad \text{with} \quad Q = C_h D_c \sqrt{2p_c/\rho} \quad .$$

Carrying out the calculation of the small changes:

$$dp_c = \frac{dp_c}{dQ}\, dQ$$

$$= \left(\frac{\partial p_f}{\partial Q} - 2k_D Q\right)\left(\frac{\partial Q}{\partial h}\, dh + \frac{\partial Q}{\partial p_c}\, dp_c\right)$$

$$= \left(\frac{\partial p_f}{\partial Q} - 2k_D Q\right)\left(C\, D_c\sqrt{2p_c/\rho}\; dh + ChD_c \times \frac{1}{2}\sqrt{2/p_c\rho}\; dp_c\right)$$

$$= \left(\frac{\partial p_f}{\partial Q} - 2k_D Q\right)\left(\frac{Q}{h}\, dh + \frac{Q}{2p_c}\, dp_c\right) \quad ,$$

or $$\left[\, 1 - \frac{Q}{2p_c}\left(\frac{\partial p_f}{\partial Q} - 2k_D Q\right) \,\right] dp_c = \frac{Q}{h}\left(\frac{\partial p_f}{\partial Q} - 2k_D Q\right) dh$$

Thus
$$\frac{\partial p_c}{\partial h} = \left.\frac{\frac{Q}{h}\left(\frac{\partial p_f}{\partial Q} - 2k_D Q\right)}{1 - \frac{Q}{2p_c}\left(\frac{\partial p_f}{\partial Q} - 2k_D Q\right)}\right|_{\substack{p_c, Q, h \\ \text{at eqm.}}} \quad . \qquad (2.22)$$

Notes:

1) We first solve the equilibrium problem, to obtain the values of Q and h. The value of p_c at equilibrium is known directly from (2.1).

2) The cushion stiffness is then computed from (2.22).

3) The heave natural frequency is given by Newton's law:

$$m\ddot{z} = F$$

$$= \left.\frac{\partial p_c}{\partial h}\right|_{\text{eqm.}} \times Sz \quad ,$$

where z is the vertical displacement, and m is the mass of the craft given by

$$m = W/g \quad . \qquad (2.23)$$

The equation of heave motion is then

$$\ddot{mz} - s\frac{\partial p_c}{\partial h} z = 0 \quad .$$

Thus

$$\ddot{mz} + kz = 0 \quad , \tag{2.24}$$

$$k = -s\ \partial p_c/\partial h \quad , \tag{2.25}$$

$$\omega_n = \sqrt{k/m} \quad . \tag{2.26}$$

4) This theory ignores compressibility effects which can be important on a full-size craft, although not for a model of typical dimensions.

2.4.2 Static stability of a plenum chamber in pitch or roll

A plenum (and a peripheral jet) craft is unstable in these modes unless operated at a very low clearance. This instability is a result of the cross flow under the cushion, which is seen in Fig. 2.16.

As the air flows from left to right in the diagram, it slows down, and hence there is a pressure rise due to the effect of the Bernoulli equation. The pressure distribution is such as to destabilize the craft. Three common methods are used to prevent this cross flow.

1) Compartmentation has the effect of converting the craft into a number of separate (or roughly so) chambers, each of which is stable in heave.

2) Center-of-Pressure Shift is created by the effective increase in area caused by the buckling of the skirt on the "down side" of the craft.

3) Pressure Rise or Pericell concept which yields a higher pressure in the individual cells as they are blocked off on the "down side" of

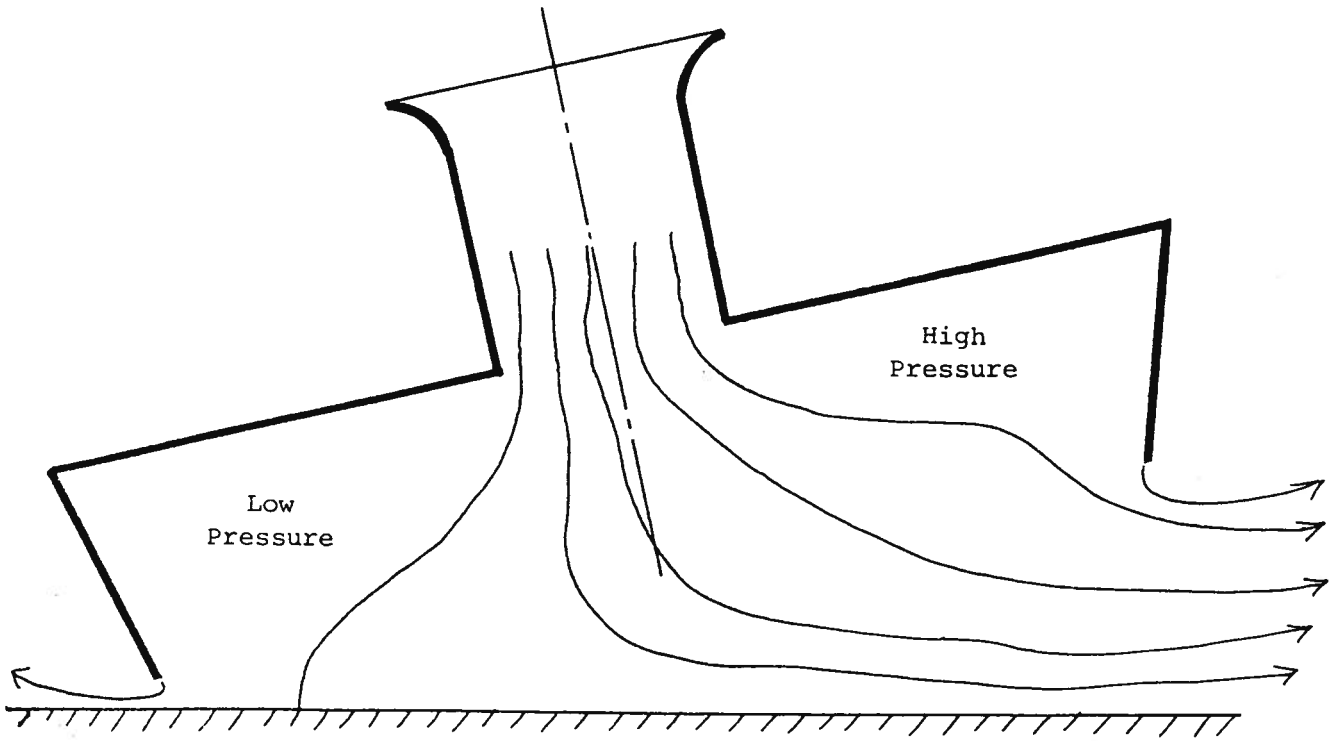

Figure 2.16: Destabilizing Cross Flow under a Plenum-Chamber Craft

the craft.

These ideas are displayed in Fig. 2.17.

2.4.3. Motions in waves

The problem of computing the motions of ACVs in waves is a very complicated one, which has not been solved in a completely satisfactory way. There are many features of the dynamic system which should be modeled. These include the unsteady internal aerodynamics of the craft, and the influence of compressibility of the air. The water surface is compliant and therefore the hydrodynamics need to be considered too. The engine and fan, which are coupled together, fluctuate in speed during the cyclic motion of the vehicle. In principle, all these aspects should be considered together when computing the craft motion.

An idea of the response to waves can be judged from some data given by Stanton-Jones (1968), shown in Fig. 2.18, which depicts heave and pitch motion results taken from a model of the SR.N2 hovercraft in regular harmonic waves. One can see that the overall response is approximately the same as that for a simple linear mass-spring-damper system. In this case, the dimensionless damping is around 0.25 for pitching, and about 0.5 for heaving. For both modes of motion, it would be desirable to increase the damping, if possible.

The data displays considerable scatter -- illustrating how difficult it is to get repeatable results in such tests. It is surprising that shorter skirts seem to give better results (that is, less motion) for the pitching mode. The longer skirts do, however, give better results for the heaving case. Unfortunately, these graphs do not show the effect of different wave heights, so it is not clear how linear the system is.

From Mantle (1975, p. 4-18)

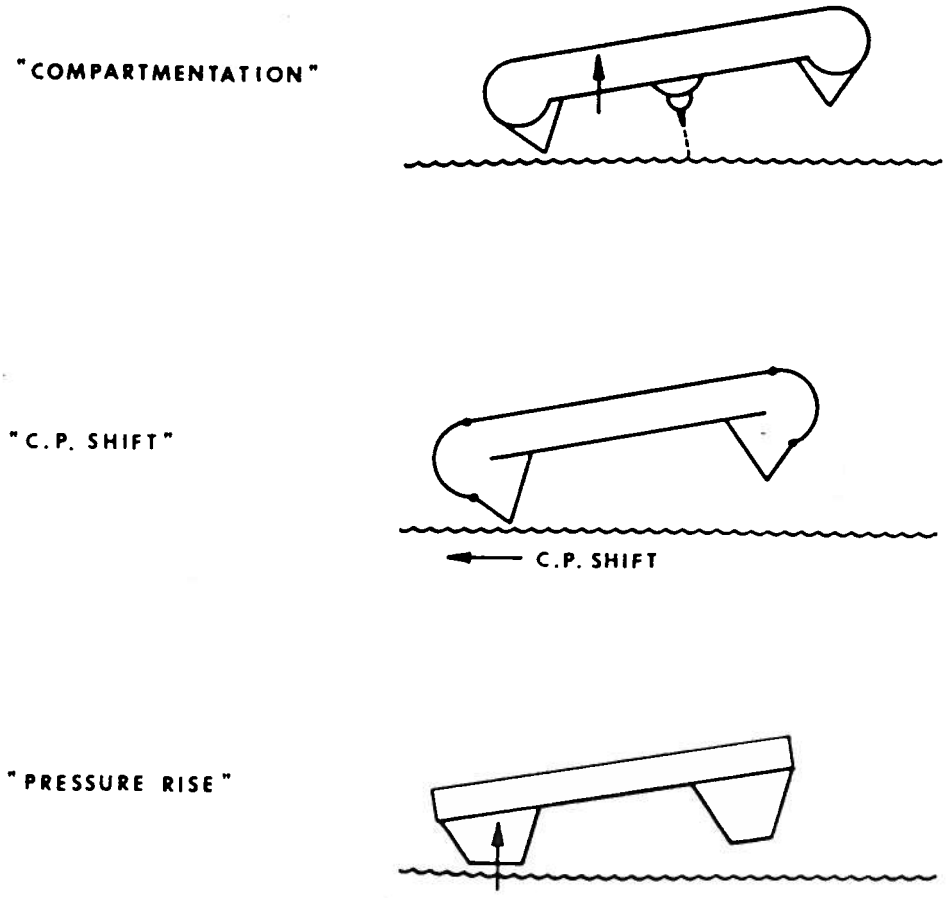

Figure 2.17: Methods of Achieving Cushion Stability

From Stanton-Jones (1968, p. 512)

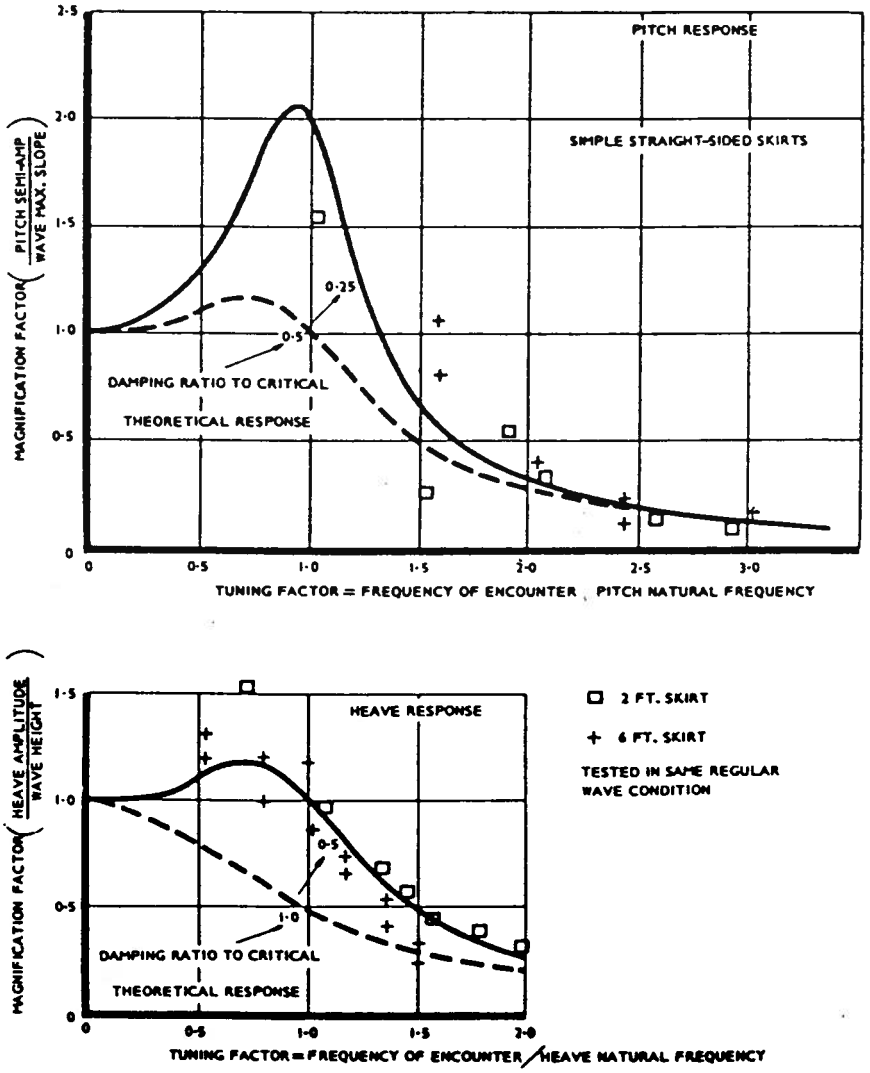

Figure 2.18: Pitch and Heave Response of a Model Hovercraft

The results in Fig. 2.18 were for a jetted skirt. A comparison of this type of skirt with a bag-and-finger skirt is shown in Fig. 2.19. Again, the scatter in the data is large, but the important point is that the use of the finger skirt results in a much reduced pitch motion. This is one reason why this type of skirt has become more popular.

The outcome of some theoretical calculations by Doctors (1976) is shown in Fig. 2.20. In this work, the steady equations of flow were used to describe the air flow in the craft. The fans were assumed to be running at a constant speed. Thus the operating point was considered to move up and down a known fan curve, such as that shown in Fig. 2.15.

Three basic methods of calculation were considered. In the first one, the so-called "over land" case, the water surface was taken to be rigid. Air compressibility was ignored. In the "over water" case, the unsteady depression of the water was included in the calculation. In the third case, the effect of air compressibility was included. The compressibility was included to the extent that it would affect the mass of air within the cushion. As the air speeds are relatively low compared to the speed of sound, the incompressible Bernoulli equation was used for computing pressure-velocity relationships.

It is encouraging to note the generally correct form of the resulting response curves, when compared to the experimental results already discussed. These curves also show the nonlinearity that exists, for the curves with different h_w/L do not collapse together, as they would in a linear system. Relatively strong effects of air compressibility and water compliance are also indicated. The air compressibility is measured by the parameter

$$C_a = p_a/\rho_w g L \quad ,$$

From Stanton-Jones (1968, p. 513): SR.N5 Model

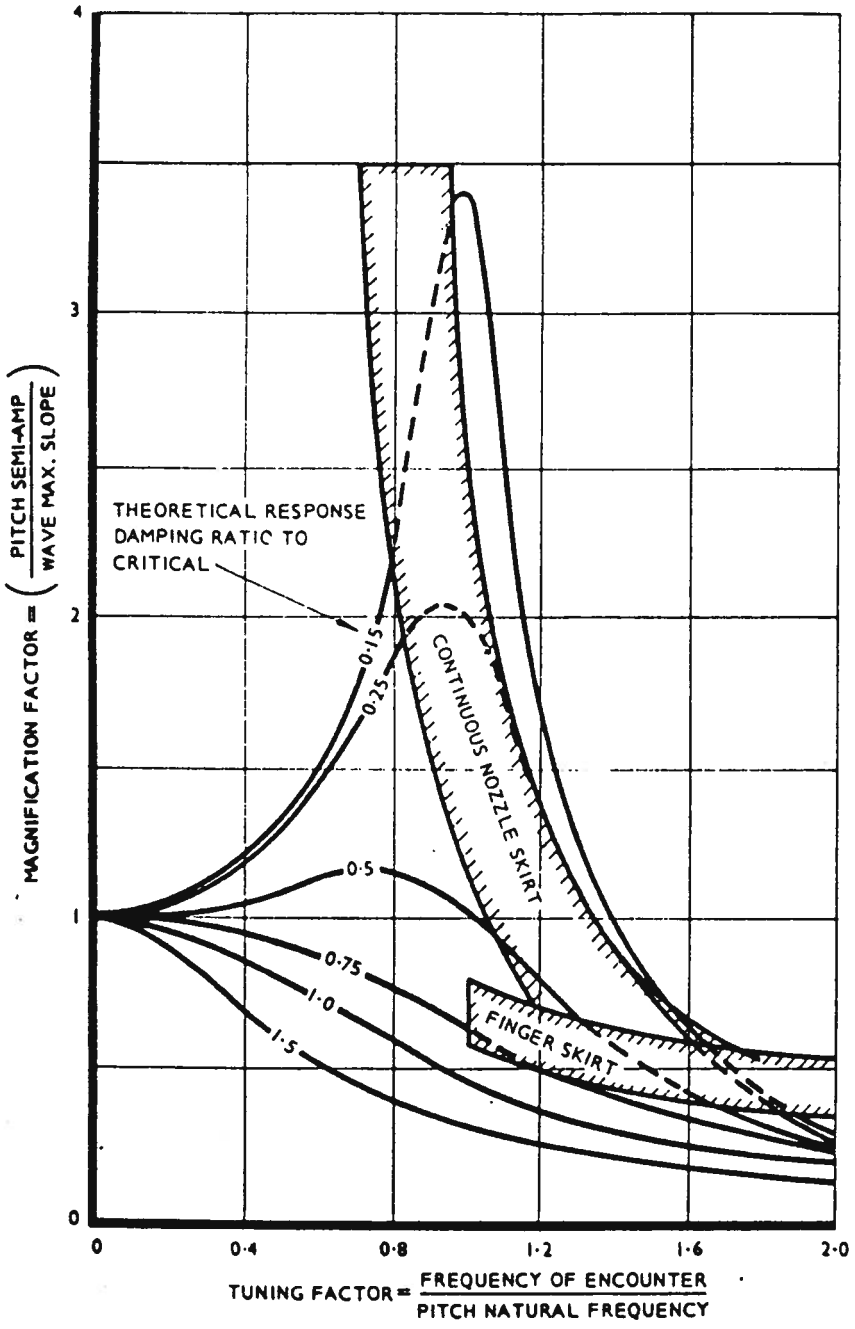

Figure 2.19: Comparison of Nozzle Skirt with a Bag—and—Finger Skirt

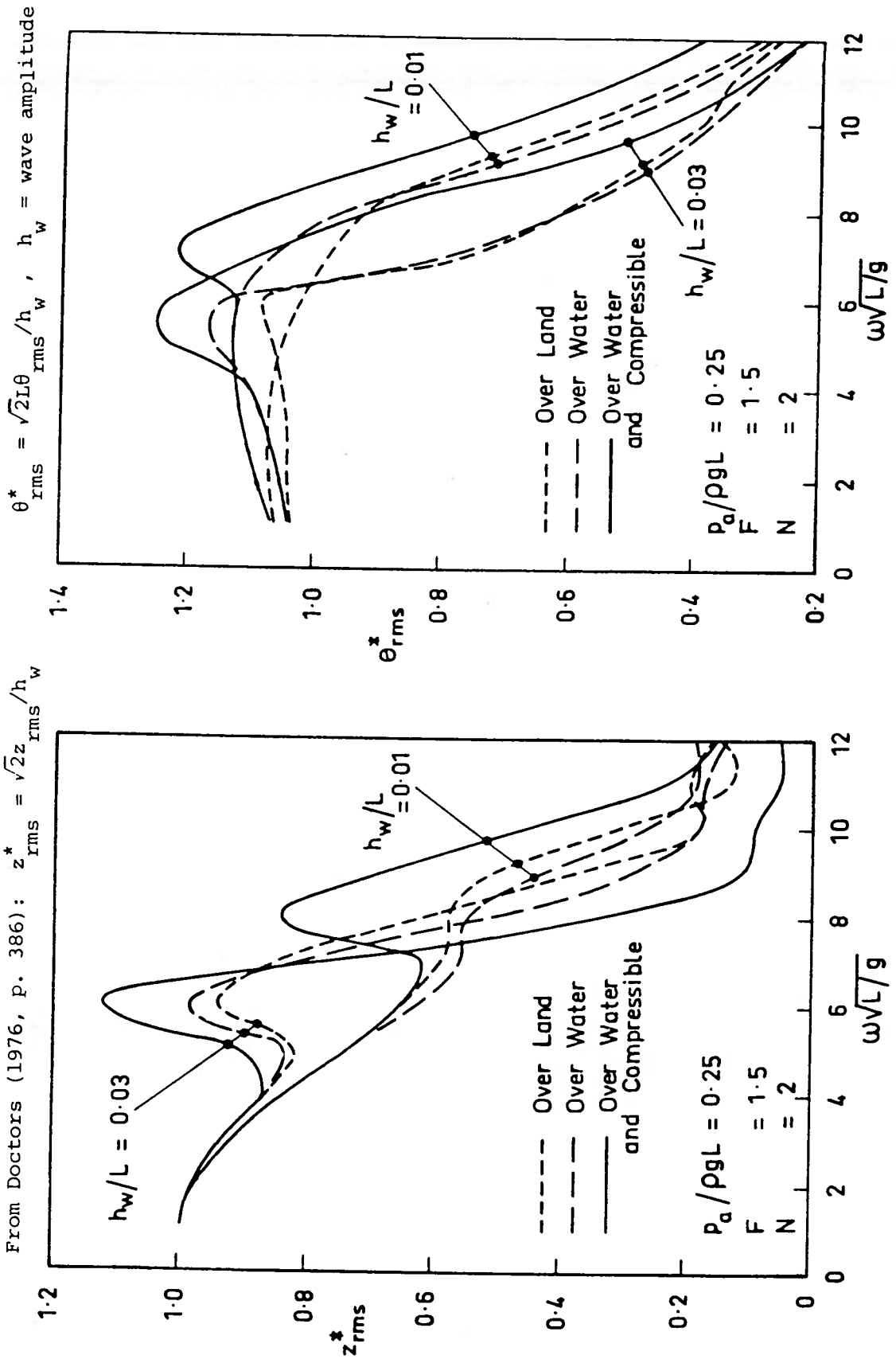

Figure 2.20: Theoretical Calculation of Heave and Pitch

where p_a is the atmospheric pressure. This parameter is seen to be important. Therefore, when conducting model tests, the atmosphere should be evacuated to maintain its value. Otherwise, the model tests tend to be conservative. This point was also made by Mantle (1975, p. 4-13).

2.5. Resistance Calculations

2.5.1. Introduction

The resistance of an ACV is composed of a number of forces, which in reality interact with each other in a very complicated way. However, most authors consider each component of drag separately, and then simply add them together, as follows: aerodynamic drag, momentum drag, cushion wave resistance, skirt drag (wetting, wavemaking, and rough-water). We can therefore write

$$D = D_a + D_m + D_w + D_{sk_w} + D_{sk_{wm}} + D_r \quad . \tag{2.27}$$

A typical breakdown of the components is shown in Fig. 2.21.

2.5.2 Aerodynamic drag

This drag component represents the force required to drive the vehicle along just above the ground (that is, there is no wave generation). The effect of the lifting air flow is ignored. In the usual terminology, we have

$$D_a = \frac{1}{2}\rho V^2 S_F C_D \quad , \tag{2.28}$$

where S_F is the frontal area of the craft, and C_D is the drag coefficient based on S_F .

Notes:

1) The drag coefficient is in reality a function of the Reynolds number. This effect is usually ignored. That is, model and full-size

From Mantle (1975, p. 3-57)

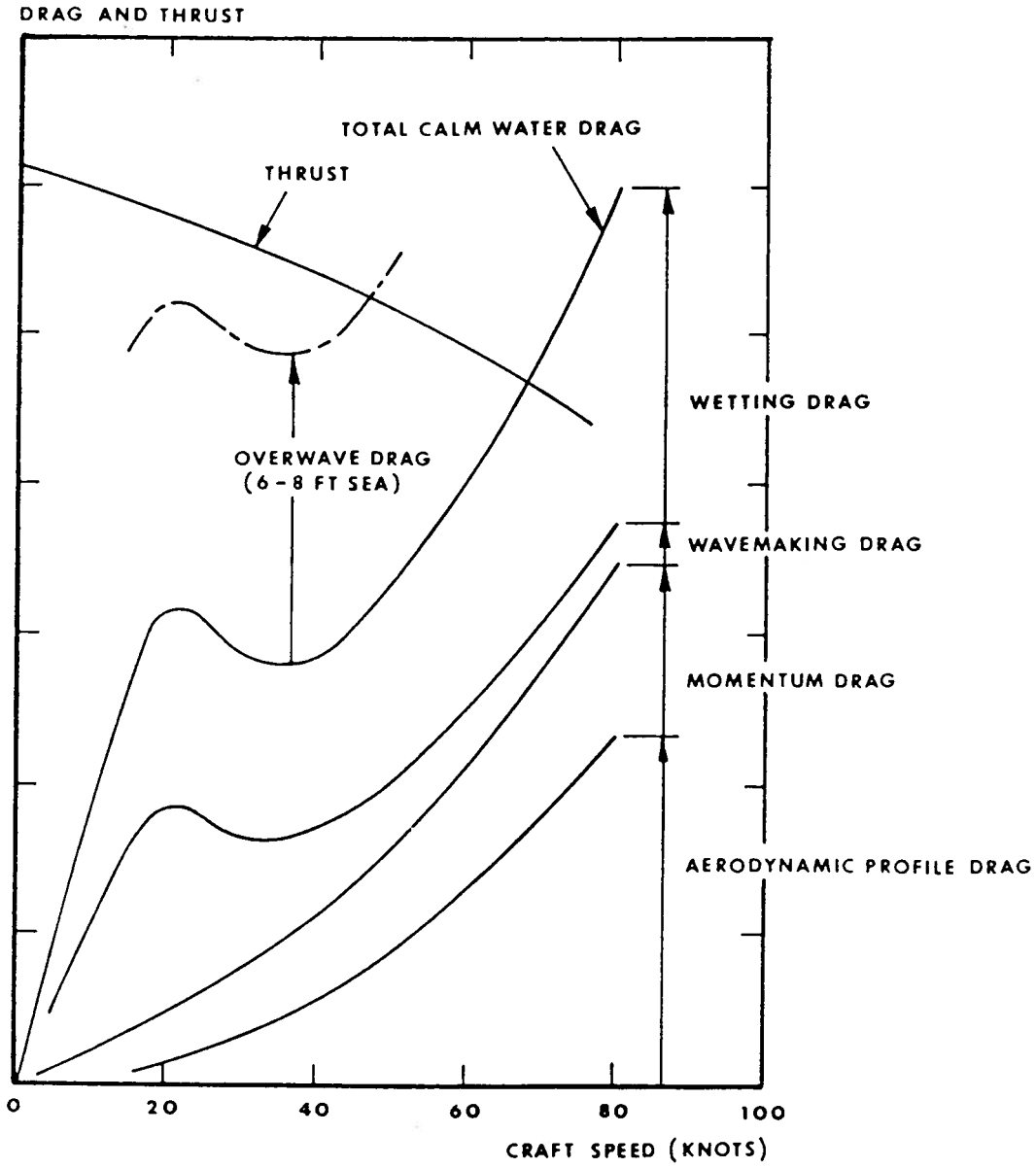

Figure 2.21: Drag Breakdown of Typical Large Air-Cushion Craft

values are assumed to possess the same drag coefficient.

2) Typical values of C_D range from 0.25 for a well designed craft to 0.38 for an average shape to perhaps 0.50 for a badly designed body.

2.5.3. Momentum drag

This drag component results from the need to accelerate the stationary air around the ACV, that is sucked into the fan intakes, up to the speed of the vehicle. Newton's law states that this force is equal to the time-rate change of momentum of the air. That is

$$D_m = \rho Q V \quad . \tag{2.29}$$

Notes:

1) On early craft, D_m was a major part of the drag, because of the large daylight clearances requiring a large value of Q .

2) By the use of skirts, Q is greatly reduced, resulting in a lowering of both lift-air requirements and propulsion power.

2.5.4. Cushion wave resistance

Introduction. The term "cushion wave resistance" refers to the drag experienced by the ACV due to the production of waves by the pressure acting down on the water.

The theory behind the calculation makes the following assumptions:

1) The water is inviscid. That is, the effect of viscosity is ignored. The theory is therefore referred to as an ideal-fluid theory.

2) The relative level of the cushion pressure is small. This is defined by the dimensionless pressure, or cushion-density parameter

$$C_p = p_c/\rho_w g L \quad , \tag{2.30}$$

where ρ_w is the water density, and L is the craft length.

Since the static depression under the ACV is given by

$$\delta = p_c/\rho g \quad , \tag{2.31}$$

We see that the cushion density is just

$$C_p = \delta/L \quad . \tag{2.32}$$

Therefore, C_p represents the ratio of the static cushion depression to the cushion length.

Typical values of the cushion density lie in the range 0.01 (a "low-density" craft) to 0.02 (a "high-density" craft).

3) Surface tension is ignored.

4) The theory also assumes that the water is initially at rest and extends to infinity everywhere.

Two-Dimensional Theory. A simple approach to the solution is to consider the superposition of two semi-infinite pressure distributions, as shown in Fig. 2.22.

The downstream wave profile is sinusoidal in form, and was given by Lamb (1932), as

$$\zeta_1 = \frac{2p_c}{\rho_w g} \cos\left[(x - L/2)g/V^2\right] \quad , \tag{2.33a}$$

for the first (positive) pressure, while the downstream wave profile for the second (negative) pressure is

$$\zeta_2 = -\frac{2p_c}{\rho_w g} \cos\left[(x + L/2)g/V^2\right] \quad . \tag{2.33b}$$

These expressions show that the effective origin of each wave system is where the pressure jump occurs. The length of the wave is seen to be given by

$$\lambda = 2\pi/k_0 \quad , \tag{2.34}$$

where $k_0 = g/V^2$. (2.35)

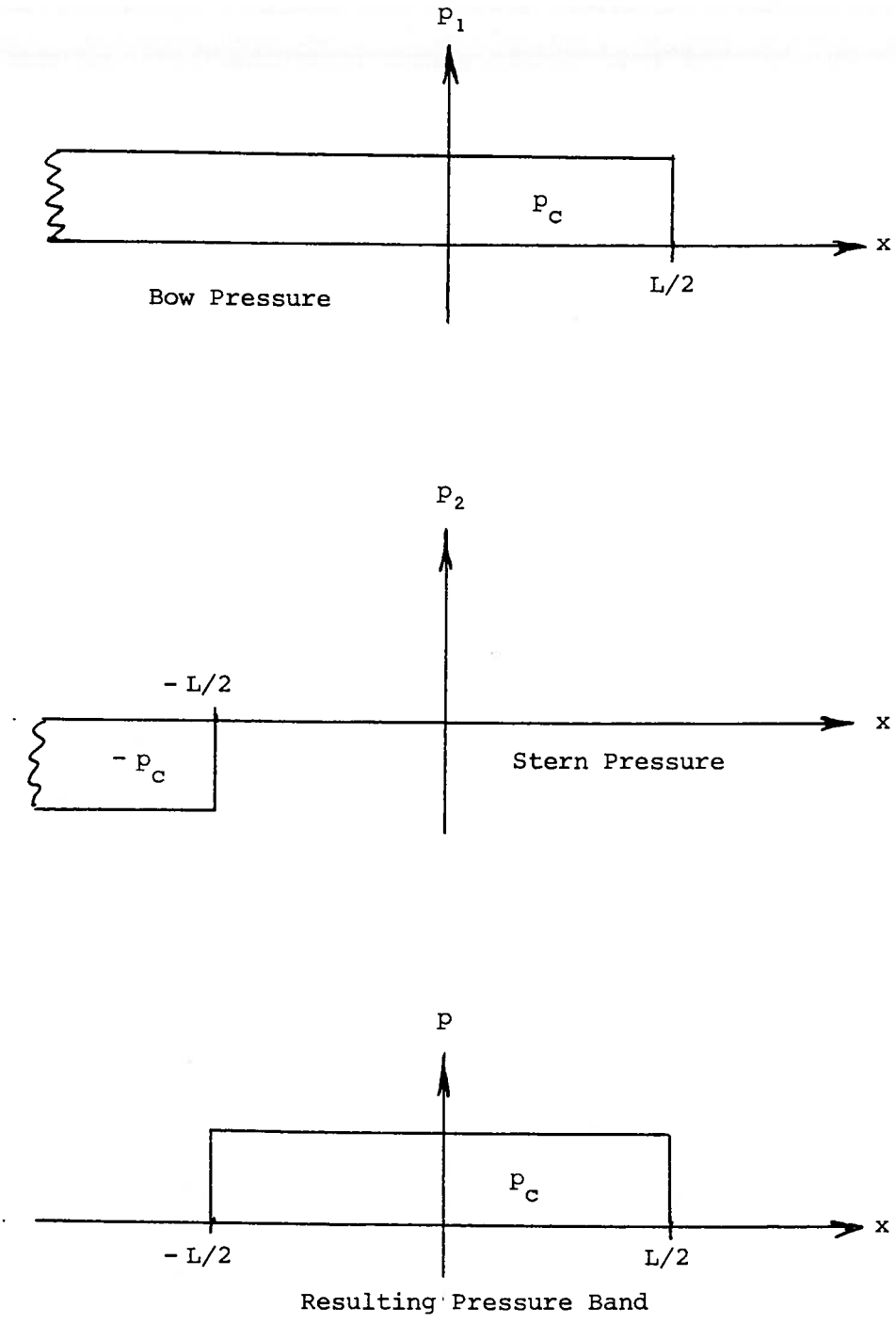

Figure 2.22: Superposition of Elementary Pressure Bands in Two Dimensions

Eq. (2.33) indicates that the wave elevation is proportional to the pressure. This is a consquence of assuming that p_c is small in (2.30).

We can now combine the bow and stern wave systems to get the resulting wave elevation:

$$\zeta = \zeta_1 + \zeta_2$$

$$= \frac{4p_c}{\rho g} \sin(gL/2V^2) \sin(gx/V^2) \quad . \tag{2.36}$$

This result shows that the amplitude of the waves is given by

$$A = \frac{4p_c}{\rho g} \sin(gL/2V^2) \quad , \tag{2.37}$$

and that we expect a maximum downstream wave at certain speeds. These speeds occur when

$$1/2F^2 = \left(n - \frac{1}{2}\right)\pi \quad , \quad \text{for} \quad n = 1,2,3,\ldots \; . \tag{2.38}$$

Physically, this situation reflects the fact that the bow and stern waves can combine with each other at appropriate Froude numbers. The outcome is that the wave-resistance curve has maxima, or "humps" in it. The following table illustrates this point:

TABLE 2.2. Location of Resistance Humps

n	Name of Hump	Froude Number
1	Main Hump	0.564
2	Secondary Hump	0.326
3	Tertiary Hump	0.252

On the other hand, we find that at

$$1/2F^2 = n\pi \qquad \text{for} \quad n = 1,2,3,\ldots, \tag{2.39}$$

no downstream wave is generated. This corresponds to the minima, or "hollows" in the wave-resistance curve, when plotted against the speed. The first few hollows are given in the table below:

TABLE 2.3. Location of Resistance Hollows

n	Name of Hollow	Froude Number
1	Main Hollow	0.399
2	Secondary Hollow	0.282
3	Tertiary Hollow	0.230

We are mainly interested in the wave resistance. It can be shown (see Newman (1980, pp. 266-270)) that this is given by

$$D_w = \frac{1}{4} \rho_w g \, A^2 \quad . \tag{2.40}$$

It is interesting to note that as the wave amplitude A is proportional to the cushion pressure p_c, so the wave resistance is proportional to the square of the pressure. This has an important consequence for the wave resistance of an ACV: any increase in overall weight results in a much bigger increase in wave drag.

Substitution of (2.37) into (2.40) yields

$$D_w = \frac{4p_c^2}{\rho_w g} \sin^2(1/2F^2) \quad . \tag{2.41}$$

This formula is plotted in Fig. 2.23, where the resistance coefficient is

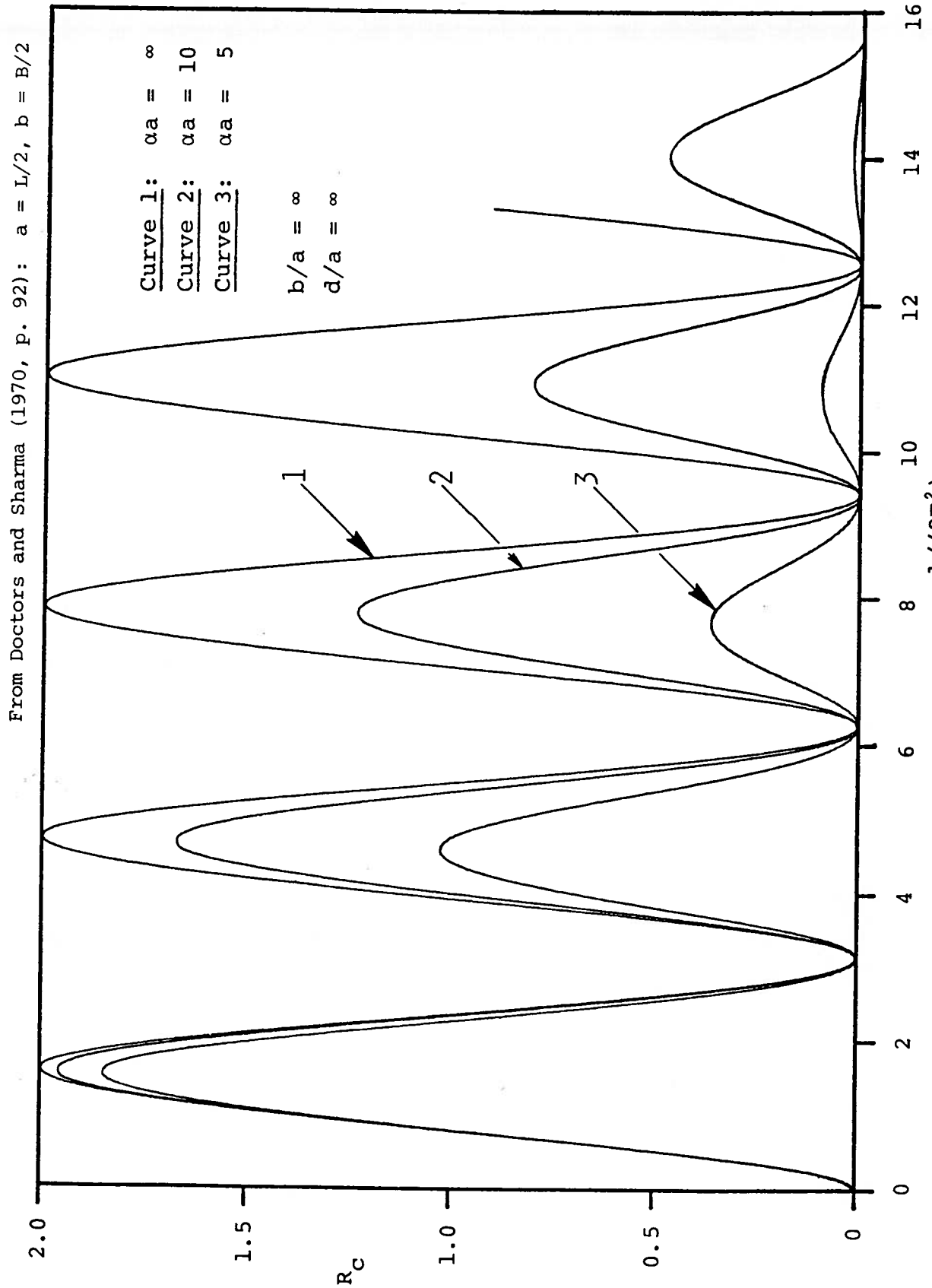

Figure 2.23: Two-Dimensional Wave Resistance Showing Effect of Smoothing

defined as

$$R_C = \frac{D_w}{W} \cdot \frac{\rho_w g L}{2p_c} \quad . \tag{2.42}$$

The diagram shows three curves. The curve corresponding to $\alpha L = \infty$ represents the sharp-edged pressure band, which was the subject of the discussion that led to (2.41). The strong interferences in the wave system are evident. The curves corresponding to $\alpha L = 20$ and $\alpha L = 10$ involve smoothing of the edges of the pressure distribution. The smoothing has the effect of reducing the magnitude of the low-speed humps -- more in keeping with experimental results.

Three-Dimensional Theory. The three-dimensional theory is more complicated than the two-dimensional one in that there is wave motion transversely as well as longitudinally. The details of the theory can be found in Barratt (1965) and Doctors and Sharma (1970). The final result is

$$D_w = \frac{1}{\pi \rho_w g} \int_0^{\pi/2} k^3 \cos\theta \, (P_e^2 + P_o^2 + Q_e^2 + Q_o^2) \, d\theta \quad , \tag{2.43}$$

where

$$\begin{matrix} P_e \\ P_o \\ \\ Q_e \\ Q_o \end{matrix} = \iint_S p(x,y) \begin{matrix} \cos \\ \sin \\ \\ \sin \\ \cos \end{matrix} (wx) \begin{matrix} \cos \\ \sin \\ \\ \cos \\ \sin \end{matrix} (uy) \, dxdy \quad , \tag{2.44}$$

and

$$k = k_0 \sec^2\theta$$

$$w = k \cos\theta$$

$$u = k \sin\theta \quad . \tag{2.45}$$

In order to use these formulas, one first chooses a pressure distribution, from which the four wave functions in (2.44) can be found as a function

of the wave angle θ . For example, a rectangular ACV can be represented by a constant pressure p_c over an area of dimensions L by B . In this case, (2.44) yields

$$P_e = 4p_c \frac{\sin(wL/2)}{w} \frac{\sin(uB/2)}{u} \tag{2.46}$$

and $P_o = Q_e = Q_o = 0$.

In this example, three out of the four wave functions in (2.46) are zero because the chosen pressure distribution has two axes of symmetry. The result (2.46) must now be substituted into (2.43) using (2.45). The integration has to be performed numerically.

A typical set of results is shown in Fig. 2.24, which are seen to resemble those of the previous figure for the two-dimensional case. The case of $\beta L = \infty$ indicates a sharp pressure fall-off at the side edges (the case that led to (2.46)). In addition, pressure distributions with side smoothing ($\beta L = 10$) are shown.

It is noteworthy that the simple two-dimensional results are an excellent guide to the three-dimensional ones -- particularly in regard to the location of the humps and hollows -- although the magnitude of these is different. For smaller beam-to-length ratios (Fig. 2.25), there is a greater discrepancy between two- and three-dimensional results for the wave resistance. The main effect is a reduction in the magnitude of the humps.

Finally, Figs. 2.26 through 2.29 show the effect of considering water of finite depth d . (In this case, (2.43) and (2.45a) have to be modified.) The result is a greatly increased resistance when the critical depth Froude number given by

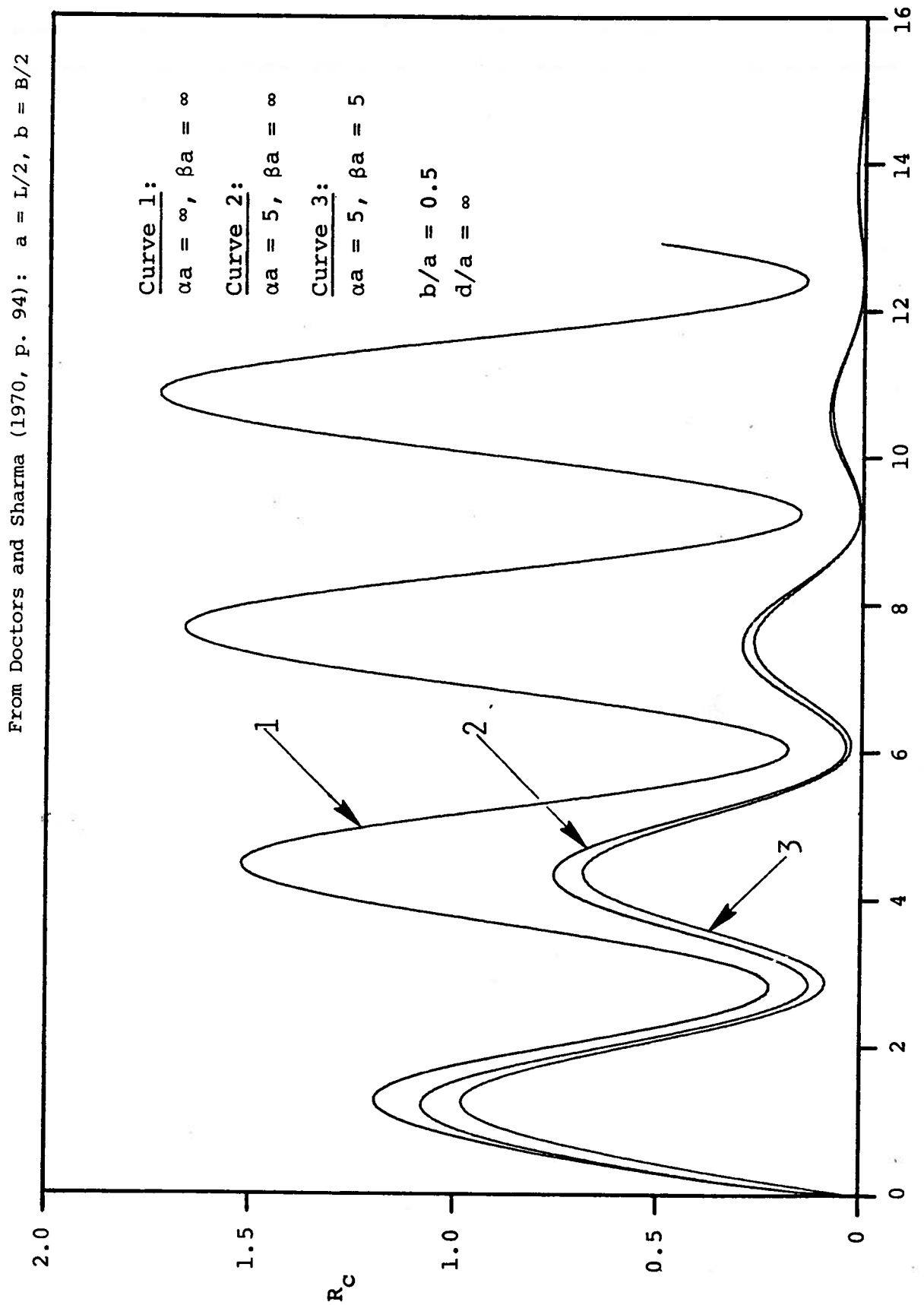

Figure 2.24: Wave Resistance Showing the Effect of Smoothing

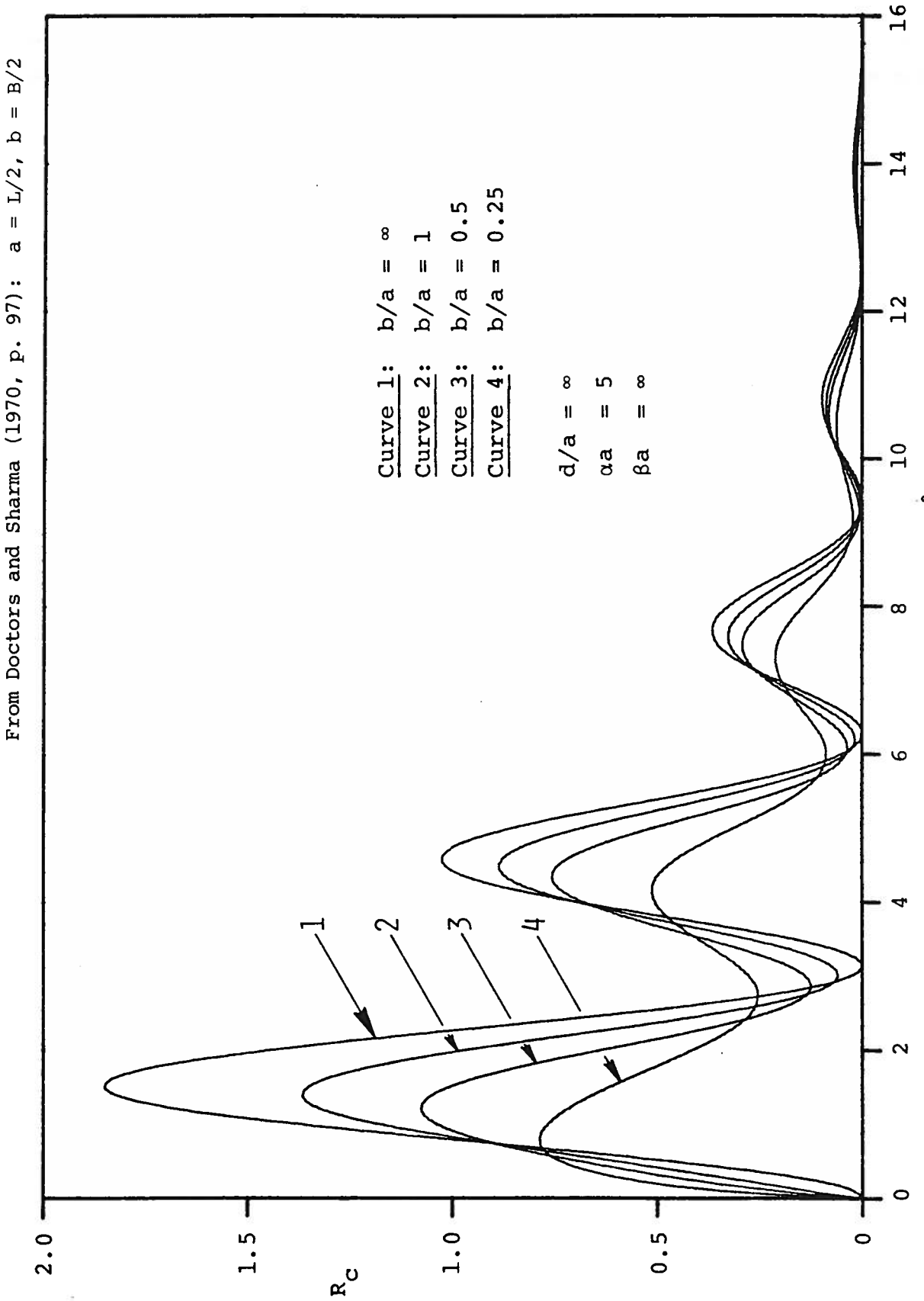

Figure 2.25: Wave Resistance Showing the Effect of Beam-to-Length Ratio

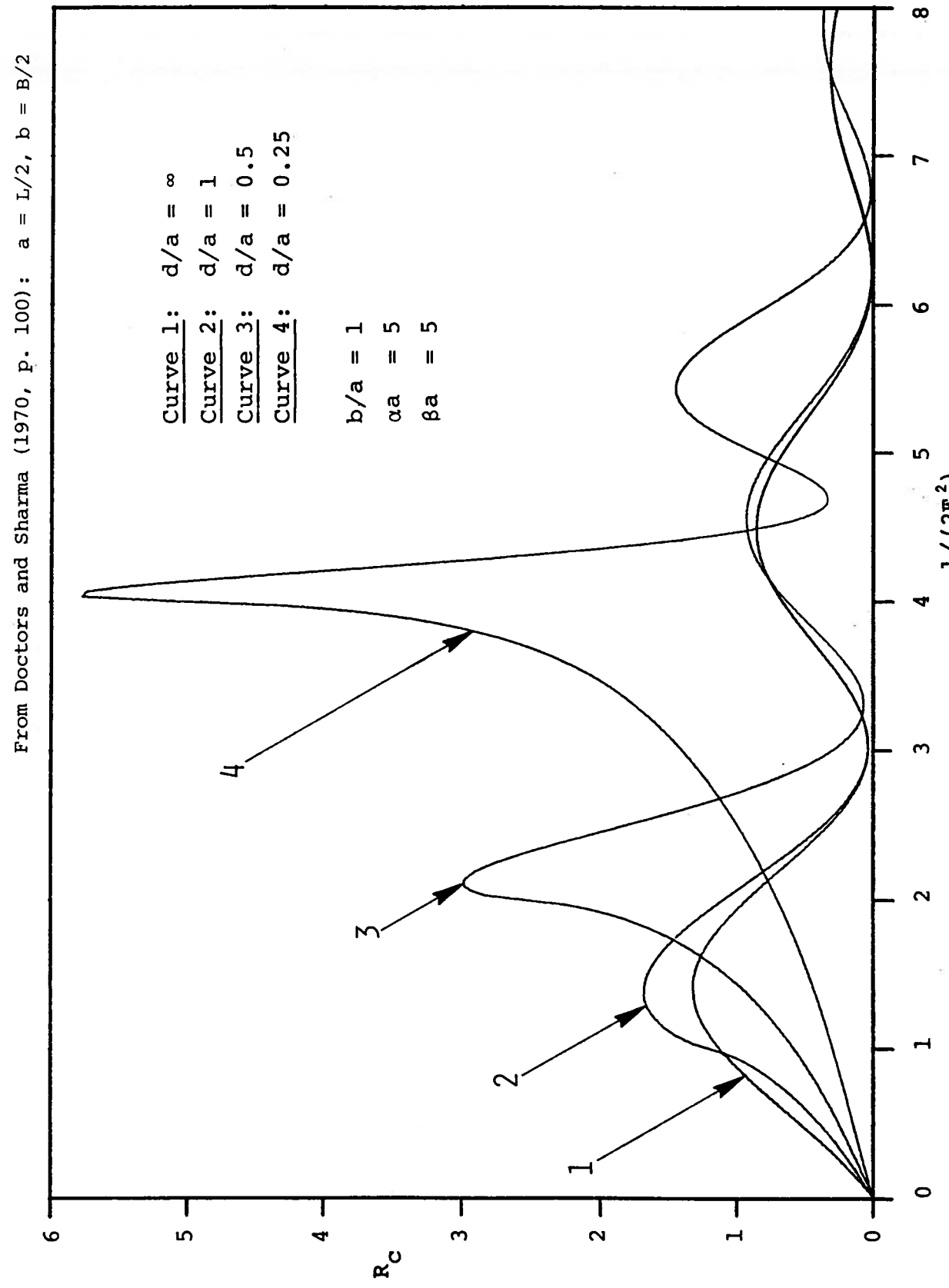

Figure 2.26: Wave Resistance Showing the Effect of Water Depth (B/L = 1)

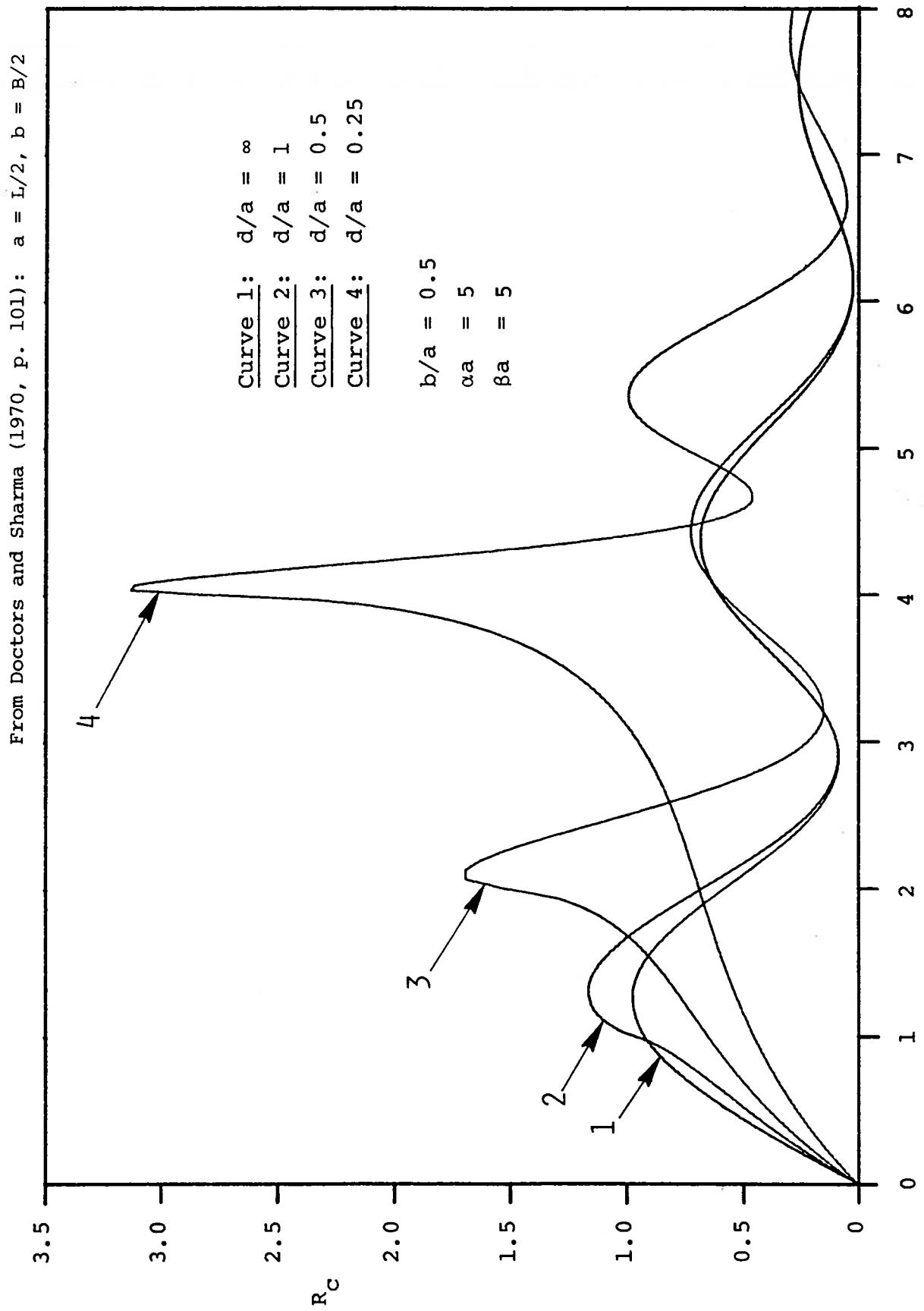

Figure 2.27: Wave Resistance Showing the Effect of Water Depth (B/L = 0.5)

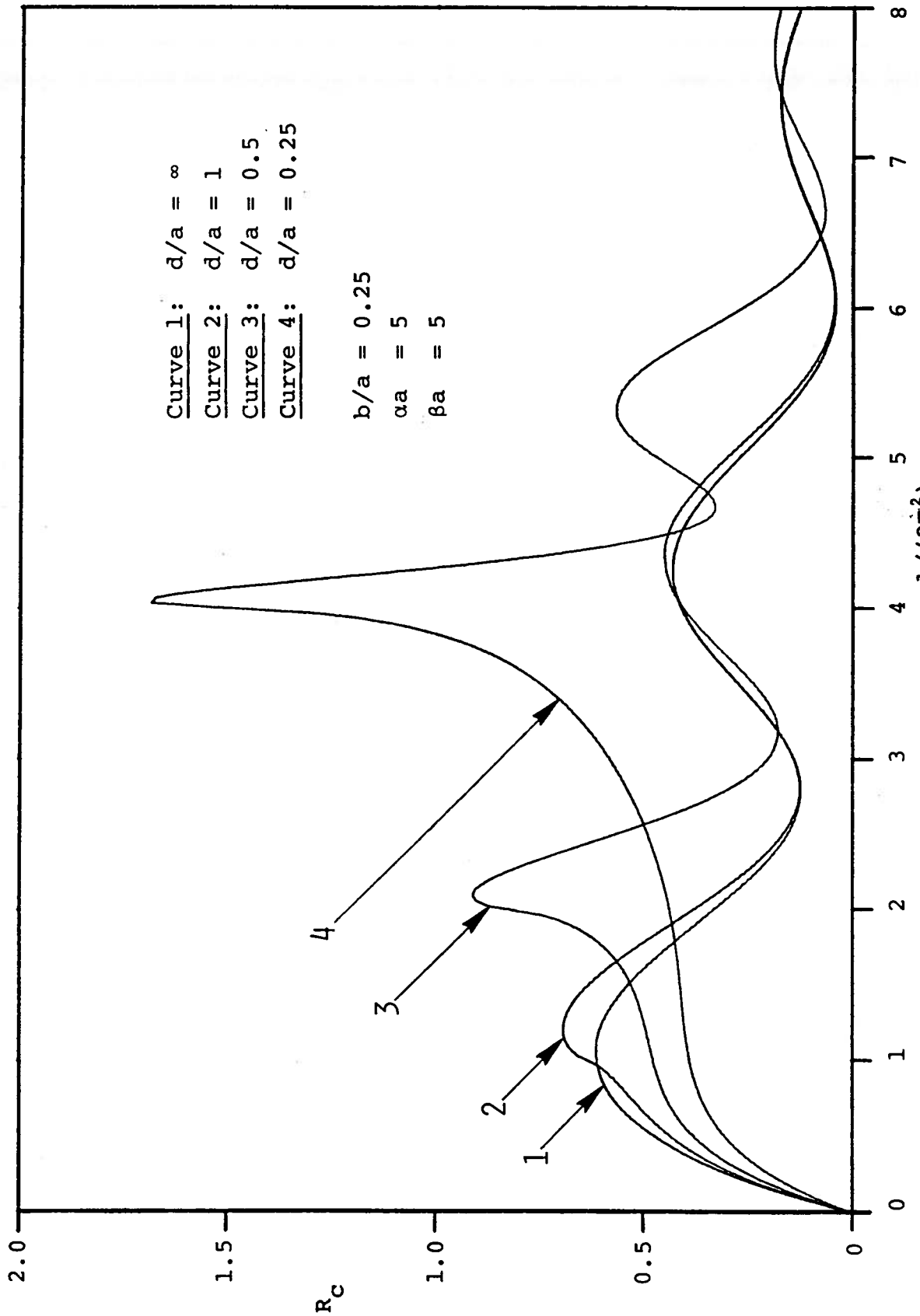

Figure 2.28: Wave Resistance Showing the Effect of Water Depth (B/L = 0.25)

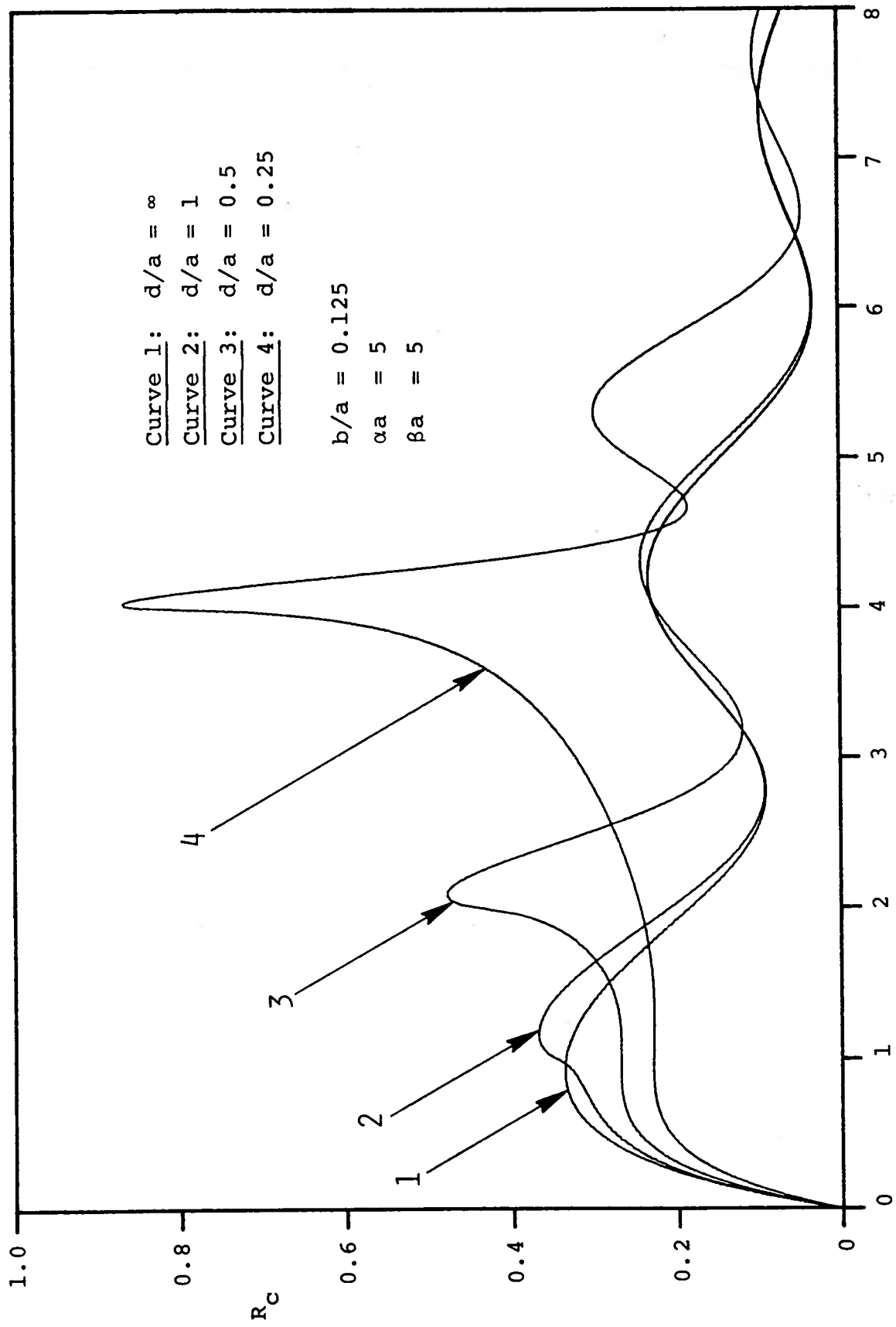

Figure 2.29: Wave Resistance Showing the Effect of Water Depth (B/L = 0.125)

$$F_d = V/\sqrt{gd} \qquad (2.47)$$

is equal to unity.

Comparison with Experiments. Some measured values of the wave resistance, taken from Everest and Hogben (1967) are shown in Fig. 2.30. Their resistance coefficient is equal to twice that of (2.42). In addition, they used an inverse-speed scale to highlight the low-speed effects.

These experiments tend to verify the general form of the wave-resistance curve at the speeds of interest. The main and secondary humps are confirmed, as well as the main hollow. The theory breaks down at lower speeds, because the steepness of the waves becomes greater than about 1/7, when they become nonlinear, thus violating the restrictions of the theory.

The generation of spray at low speeds also tends to cloud the issue of comparing analytic and experimental results. It is interesting to note that smoothing of the pressure at the edges (using finite values of αL and βL, referred to above) reduces the magnitude of the low-speed oscillations in the resistance curve -- more in keeping with these experimental results.

2.5.5. Skirt drag

The problem of calculating the drag of the skirts or seals (in the case of a sidehull ACV) is a very difficult one, and has not been achieved in a theoretical manner. Mantle (1975) showed how attempts have been made to split skirt drag into three simply additive components, as follows:

Skirt-Wetting Drag. This drag component refers to the frictional drag of the water on the skirts in calm water. The data that was analyzed gave the result:

From Everest and Hogben (1967, p. 311)

	MODEL WEIGHT	FAN SPEED
+	140 lb	4,500 rpm
×	140 lb	4,000 rpm
⊡	140 lb	3,500 rpm
⊙	140 lb	3,000 rpm
△	160 lb	4,500 rpm
▽	180 lb	4,500 rpm
●	200 lb	4,500 rpm
♂	220 lb	4,500 rpm
✱	220 lb	5,350 rpm

——— THEORETICAL RESULT (REF. 6.) RECTANGULAR PRESSURE DISTBN $L/B = 1.5$

– – – – LINE SUGGESTED FROM EXPERIMENTAL RESULTS, FOR CONDITIONS LESS PRONE TO WETTING. (CORRECTED FOR TRIM-UP AT HIGH SPEED)

-------- AS ABOVE UNCORRECTED

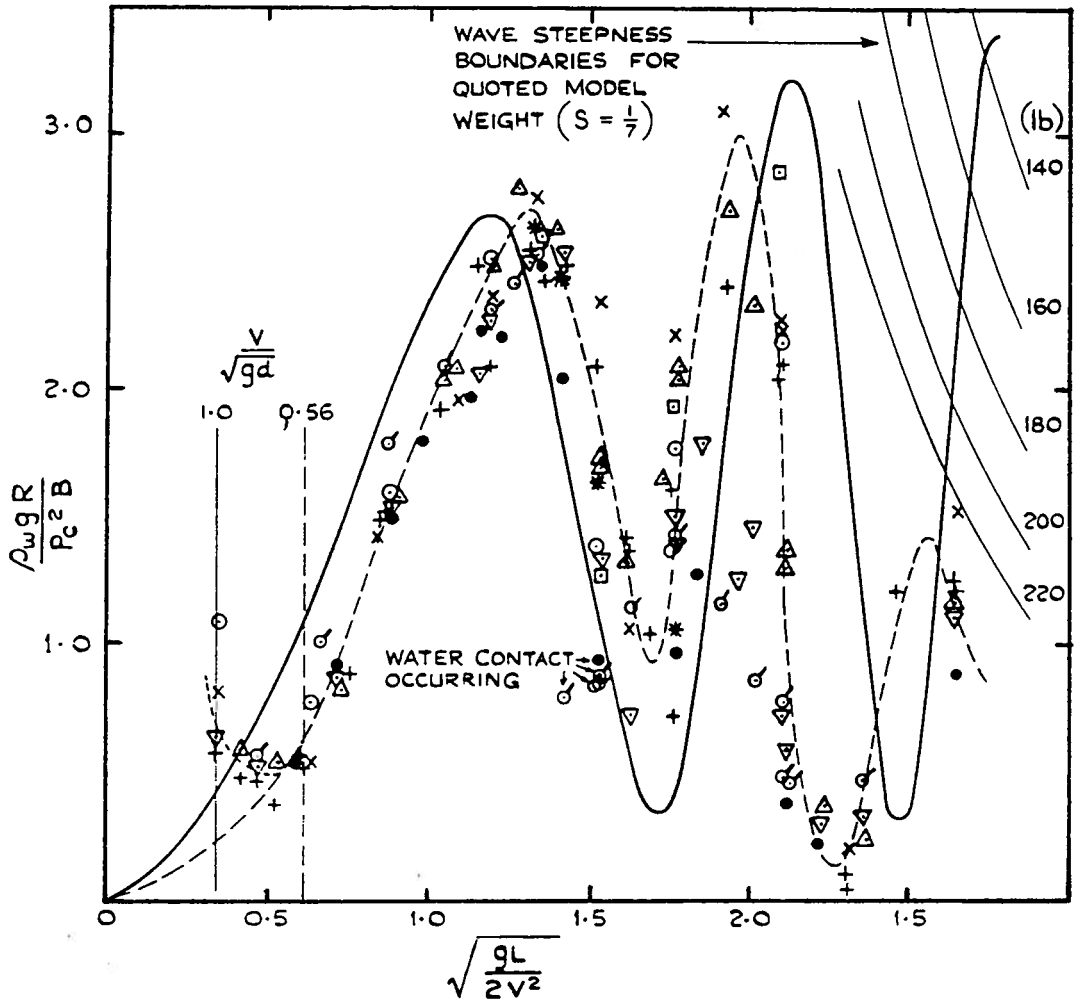

Figure 2.30: Comparison of Experimental and Theoretical Wave Resistance

$$D_{sk_w} = 3.46\times10^{-6}(h/L)^{-0.34} C\sqrt{S}\, q_w \quad , \tag{2.48}$$

where $$q_w = \frac{1}{2}\rho_w V^2 \tag{2.49}$$

is the dynamic head of the water. The equation is seen to include the effect of the dimensionless clearance h/L, the circumference of the skirt C and the water dynamic head. The planform shape is partly taken into account by the appearance of the area S. This equation can be expressed dimensionlessly as

$$D_{sk_w}/W = 0.0058\ (h/L)^{-0.34}\ \frac{1 + L/B}{(L/B)^{1/2}}\ k \quad , \tag{2.50}$$

where the pressure number is defined as

$$k = \frac{1}{2}\rho V^2/p_c \quad . \tag{2.51}$$

Eq. (2.50) has been derived from (2.48) assuming a rectangular planform and the ratio of water density to air density to be 838. The multiplicative constant in (2.50) is known only very roughly.

Skirt Wavemaking Drag. The suggestion is made that the wavemaking drag of the skirt is related to that of the cushion, already discussed, in the following way:

$$D_{sk_{wm}}/D_w = 0.468\ C_p^{-0.259} - 1 \quad , \tag{2.52}$$

where the cushion-density parameter has been given by (2.30). This formula can be critized for a number of reasons: it ignores the fact that with sufficient clearance all round, there would not be any skirt wave drag at all. Also ignored is the fact that wave resistance is not additive in this simple-minded way. At best, this formula gives reasonable results for typical ACVs.

The results of plotting (2.50) and (2.52) are shown in Fig. 2.31. The large scatter in the data is evident, but the equations do give a guide to the magnitude of these skirt forces.

Rough-Water Drag. Finally, Mantle suggested the following equation for the additional drag associated with operation in rough water:

$$D_r = 20\times10^{-5}\left[\frac{2h_w}{h_c + h_f}\right]^{5/3} \alpha\sqrt{S}\, q_w \quad , \tag{2.53}$$

where h_w is the wave height, h_c is the cushion height, and h_f is the height of the fingers. This equation can therefore be applied to a bag-and-finger skirt. The non-dimensional form of this result is

$$D_r/W = 0.34\left[\frac{2h_w}{h_c + h_f}\right]^{5/3} \frac{1 + L/B}{(L/B)^{1/2}}\, k \quad . \tag{2.54}$$

The rough-water skirt drag is plotted in Fig. 2.32. Even considering the logarithmic scales being used, most of the data for different craft do collapse quite well onto the suggested equation. This is true despite the fact that the skirt designs (and hence their stiffness) vary widely for the cases analyzed.

2.6. Powering Considerations

2.6.1. Introduction

The power required to drive an ACV essentially consists of that required to overcome the various resistance components discussed in Section 2.5. In addition, one must include the lift power. A further complication is that during operation over rough water, there is a tendency for the waves to deplete the cushion of its air. This air has to be replenished by the lift system. This phenomenon is called wave pumping.

From Mantle (1975, p. 3-58): L/B = 2.0

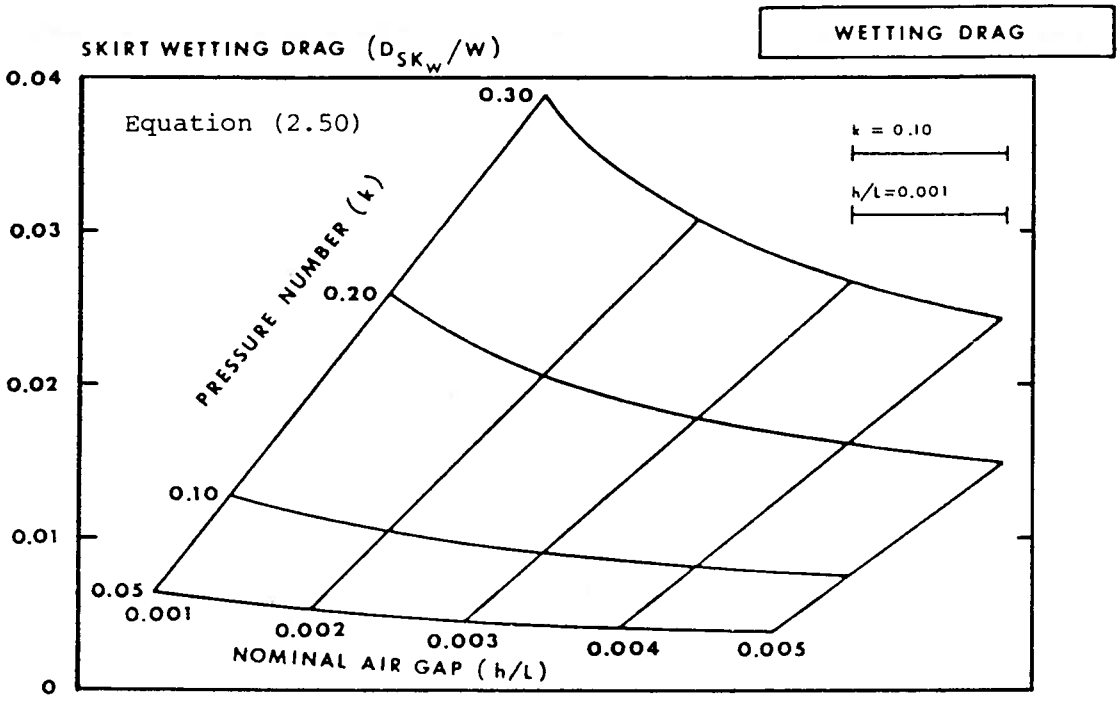

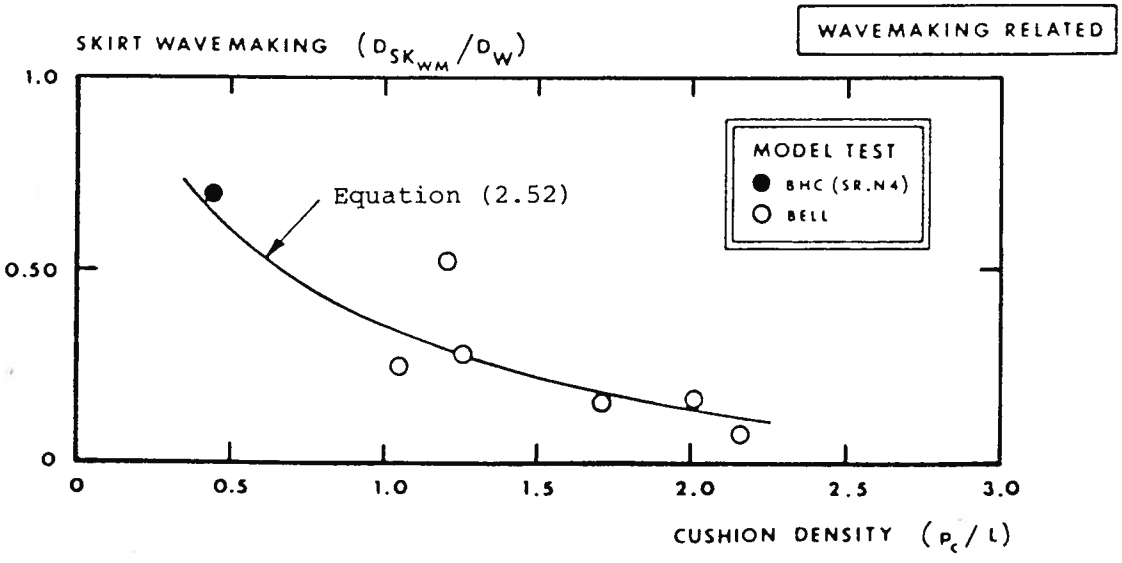

Figure 2.31: Empirical Calm-Water Skirt Drag

From Mantle (1975, p. 3-60)

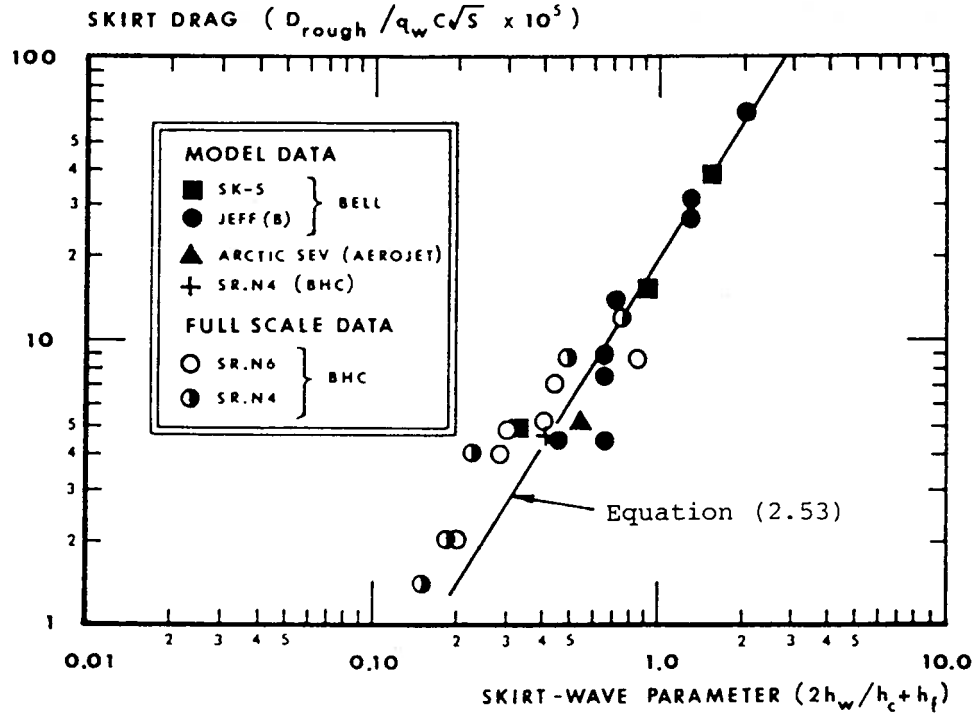

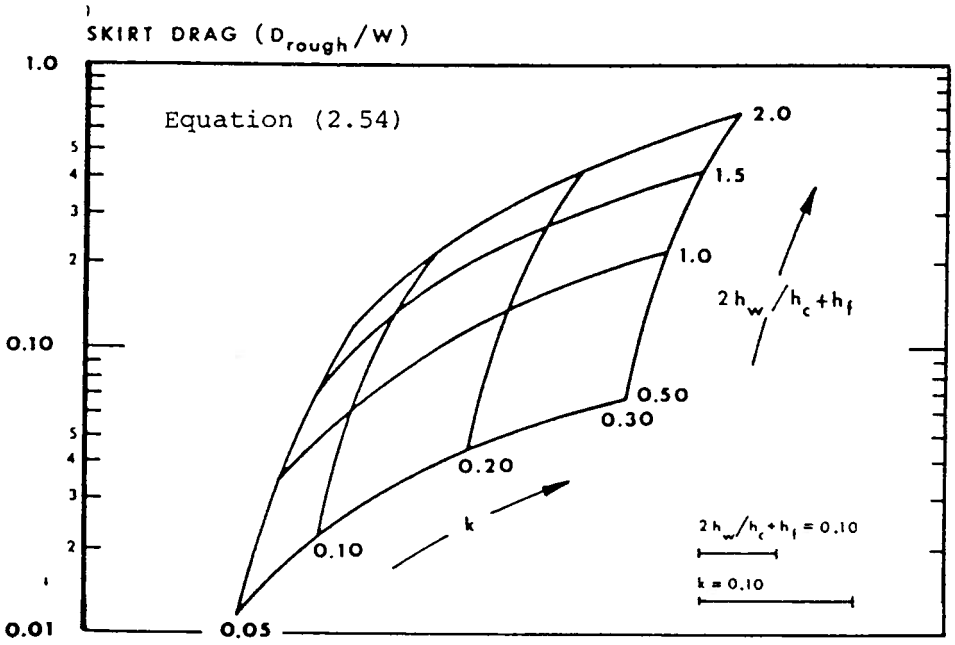

Figure 2.32: Empirical Rough-Water Skirt Drag

Another point to consider is the effect of forward speed on the lift-fan performance. Forward speed also results in some aerodynamic lift on the body of the craft which reduces the required cushion pressure and the corresponding lift air flow.

Summing the power components gives us the equation

$$P = \max(P_L, P_{wp}) + P_D \quad . \tag{2.55}$$

The first two components of power mentioned in this equation refer respectively to the lift and wave-pumping terms. The last term P_D is the power required to overcome all the resistance components referred to in Sec. 2.5.

2.6.2. Cushion pressure and ram pressure

We first note that the general speed of the air flow over the top surface of the craft will be greater than the forward speed of the vehicle. Bernoulli's equation states that there will be a corresponding drop in static pressure, causing an upward force, or lift, on the vehicle. We can therefore improve on (2.1) for the cushion pressure, by writing

$$p_c = W/S - C_L \frac{1}{2}\rho V^2 \quad , \tag{2.56}$$

where C_L is the lift coefficient due to the upper surface (based on cushion area). Typical values of C_L lie in the range 0.30 to 0.40.

A second point to note is that part of the dynamic pressure of the free air stream (related to the craft), namely

$$q = \frac{1}{2}\rho V^2 \quad , \tag{2.57}$$

can be recovered by the lift fan.

2.6.3. Lift power for a plenum chamber

When we consider the flow of energy from the atmosphere to the cushion, we obtain

$$p_c = p_f - k_D Q^2 + \varepsilon q \quad , \tag{2.58}$$

where k_D gives the diffuser losses, and ε is the intake recovery factor that represents the fraction of the ram pressure (2.57) that can be retrieved. Thus the fan pressure is given by

$$p_f = p_c + k_D Q^2 - \varepsilon q \quad . \tag{2.59}$$

Instead of using (2.5), the following equation is needed for the volume flow:

$$Q = Ch D_c \sqrt{2(W/S - C_L \cdot \tfrac{1}{2}\rho V^2)/\rho} \quad , \tag{2.60}$$

where use has been made of (2.56). Finally, the lift power is given by

$$P_L = p_f Q/\eta_L \quad , \tag{2.61}$$

where η_L is the fan efficiency.

2.6.4. Lift power for a peripheral jet

The total pressure in the air jet is represented by an expression similar to (2.58), namely

$$p_T = p_f - k_D Q^2 + \varepsilon q \quad , \tag{2.62}$$

where k_D now represents the diffuser loss for this type of vehicle.

Using (2.12), we obtain the fan pressure

$$p_f = p_c/(1-e^{-2x}) + k_D Q^2 - \varepsilon q \quad , \tag{2.63}$$

while (2.13) gives the volume flow as

$$Q = \frac{Ch}{1 + \cos\theta} \left(\frac{2p_c}{\rho}\right)^{1/2} \frac{1 - e^{-x}}{(1 - e^{-2x})^{1/2}} \quad . \tag{2.64}$$

The lift power for the peripheral jet is then

$$P_L = p_f Q/\eta_L \quad ,$$

as before.

2.6.5. Wave-pumping power

We start by considering a two-dimensional wave form given by

$$\zeta = \frac{1}{2} h_w \cos[2\pi(x - Vt)/\lambda] \quad , \tag{2.65}$$

where $h_w/2$ is the amplitude, λ is the wavelength, t is the time, and x is the longitudinal coordinate (moving with the ACV). The time-dependent part of the cushion volume between this wave and the craft is given by

$$\nabla_{wp} = -B \int_{-L/2}^{L/2} \zeta \, dx \quad ,$$

while the time-rate change of this volume gives the flow associated with cushion pumping:

$$\begin{aligned} Q_{wp} &= -B \int_{-L/2}^{L/2} \dot{\zeta} \, dx \\ &= -\frac{1}{2} h_w BV \Big[\cos[2\pi(x - Vt)/\lambda]\Big]_{x = -L/2}^{L/2} \\ &= -h_w BV \sin(\pi L/\lambda) \sin(2\pi Vt/\lambda) \quad . \end{aligned} \tag{2.66}$$

The maximum instantaneous value of this flow is just

$$Q_{wp} = h_w BV \sin(\pi L/\lambda) \quad . \tag{2.67}$$

The lift power required to supply the volume flow (in the case of a plenum chamber) is given by

$$P_{wp} = p_f Q_{wp}/\eta_L \quad , \tag{2.68}$$

with p_f given by (2.59).

The development of these equations assumes that the craft is traveling at a constant height above a fixed datum, with no pitching. We have also considered that the velocity of the wave is small compared to that of the ACV.

In addition, (2.68) represents an instantaneous maximum (positive) value of P_{wp}. At an instant equivalent to half a wave period later, when the wave pumping is actually negative, we would want to extract this power.

In most ACVs, this is not done, and the craft experiences vertical accelerations from the wave-pumping effect. In some experimental craft, however, such as the SES-100A and SES-100B, a special heave-alleviation system was installed. This system simply vented the excess cushion pressure to atmosphere, with a resulting improved ride in rough water.

2.6.6. Power required to overcome drag

The drag components are given by (2.28), (2.29), (2.43), (2.50), (2.52), and (2.54). Combining these, we have the total propulsion power as

$$P_P = (D_a + D_m + D_w + D_{sk_w} + D_{sk_{wm}} + D_r)V/\eta_p \quad , \tag{2.69}$$

where η_p is the efficiency of the propeller.

3. HYDROFOIL BOATS

3.1 Types of Hydrofoils

3.1.1 Introduction

Hydrofoil systems can be categorized in a number of different ways: the type of each foil element in the system (subcavitating, supercavitating, super-ventilated), the placement of the foil relative to the water free surface (surface-piercing or submerged), the grouping of the foils (laterally, longitudinally, and vertically), and the method of stabilization used (by geometric variations, proximity to the free surface, or by an automatic control system). We start by considering the first aspect, namely the foil type.

3.1.2 Type of Foil Element

Three types of foil sections are shown in Fig. 3.1. The subcavitating foil is the most efficient of these designs, because of its high lift-to-drag ratio. The section of this foil resembles that of an airfoil section. In fact, airfoil data is often used to assist in the design of hydrofoils. An excellent reference for this information is the work by Abbott and von Doenhoff (1959), in which a collection of information for the NACA-series foils is given. This data gives the lift and drag characteristics which can be applied directly to the hydrofoil, provided the appropriate fluid density is used. It is generally possible to ignore the relatively small effect of the Reynolds number on the lift, except near the stall condition.

The lift coefficient for a typical wing section is shown in Fig. 3.2, while the drag coefficient is shown in Fig. 3.3. These depend on the angle of attack α. The moment coefficient is plotted in the two figures in different ways. In the first figure, the moment is measured about the quarter-chord point ($x = c/4$, where c is the chord length), whereas in the second figure

From Eames (1971, p. 116)

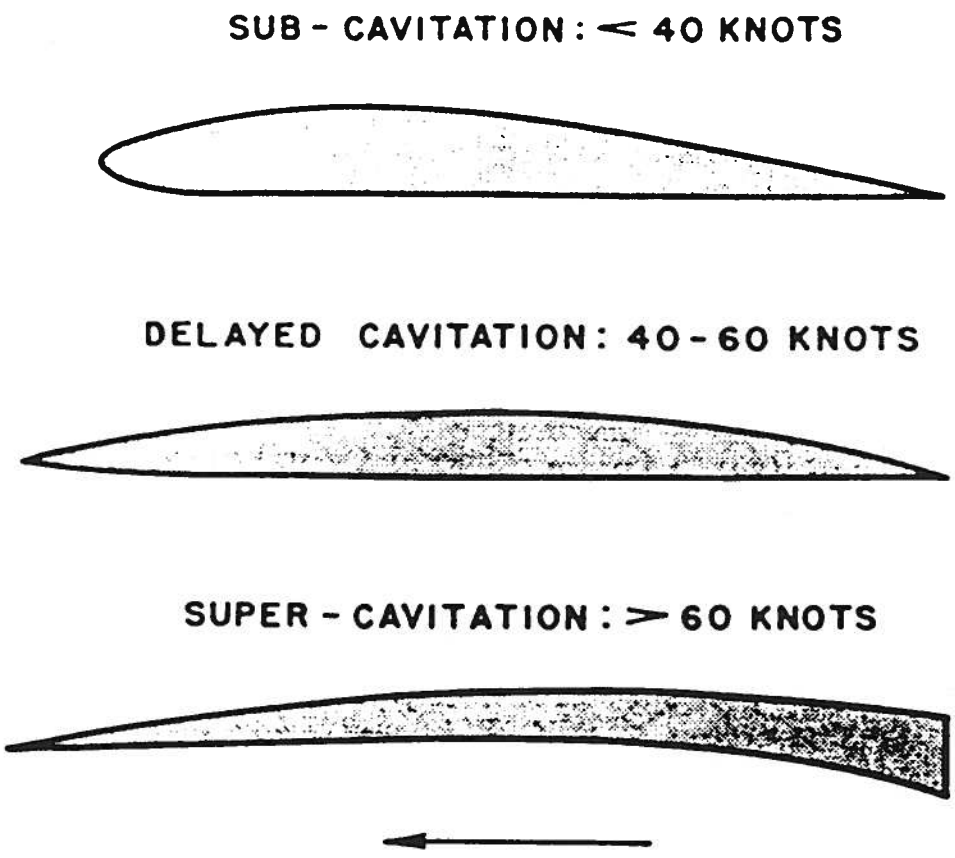

Figure 3.1: Typical Hydrofoil Sections

From Abbott and von Doenhoff (1959, p. 498)

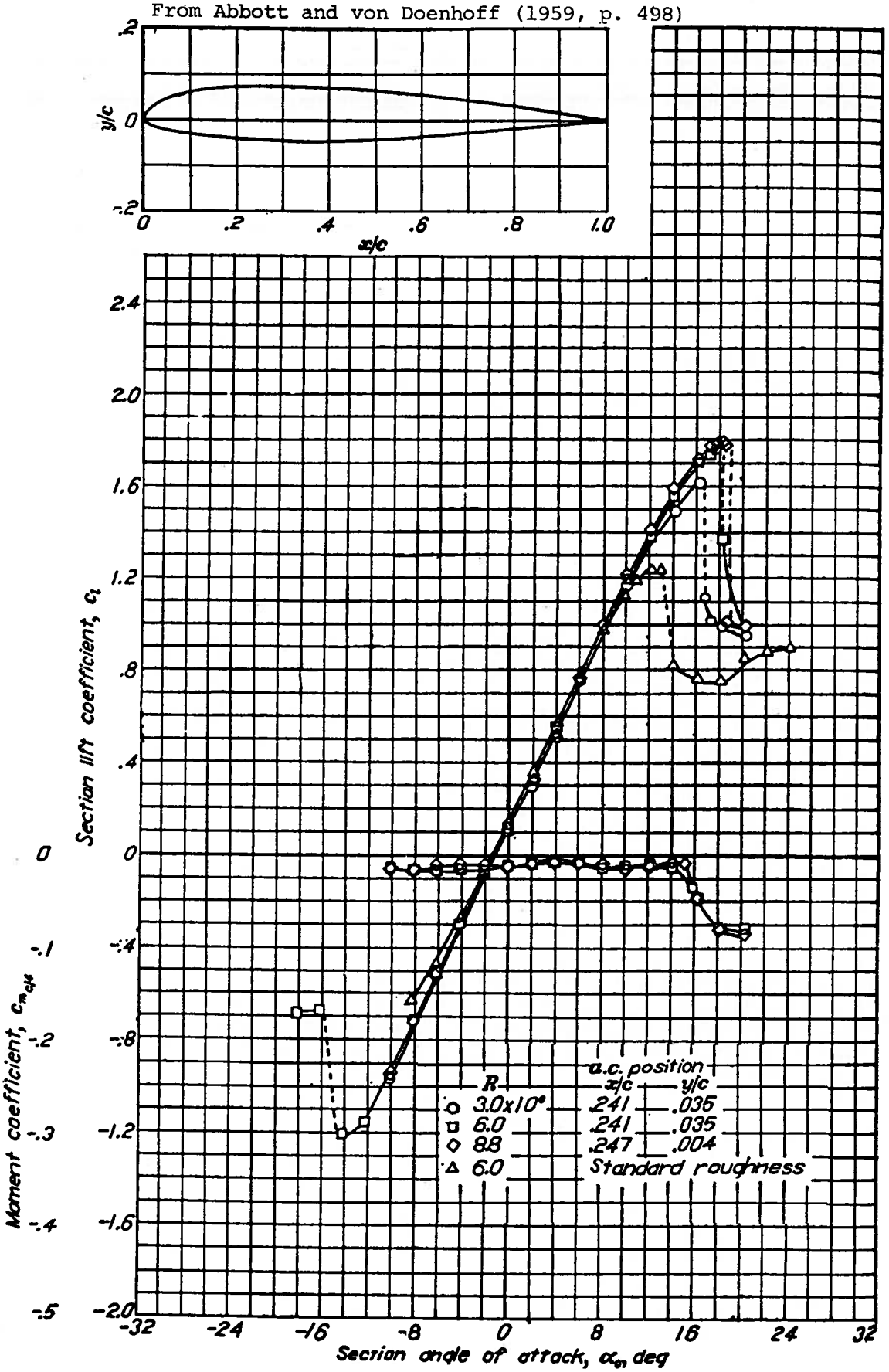

Figure 3.2: Lift and Moment Characteristics of NACA 23012 Wing Section

From Abbott and von Doenhoff (1959, p. 499)

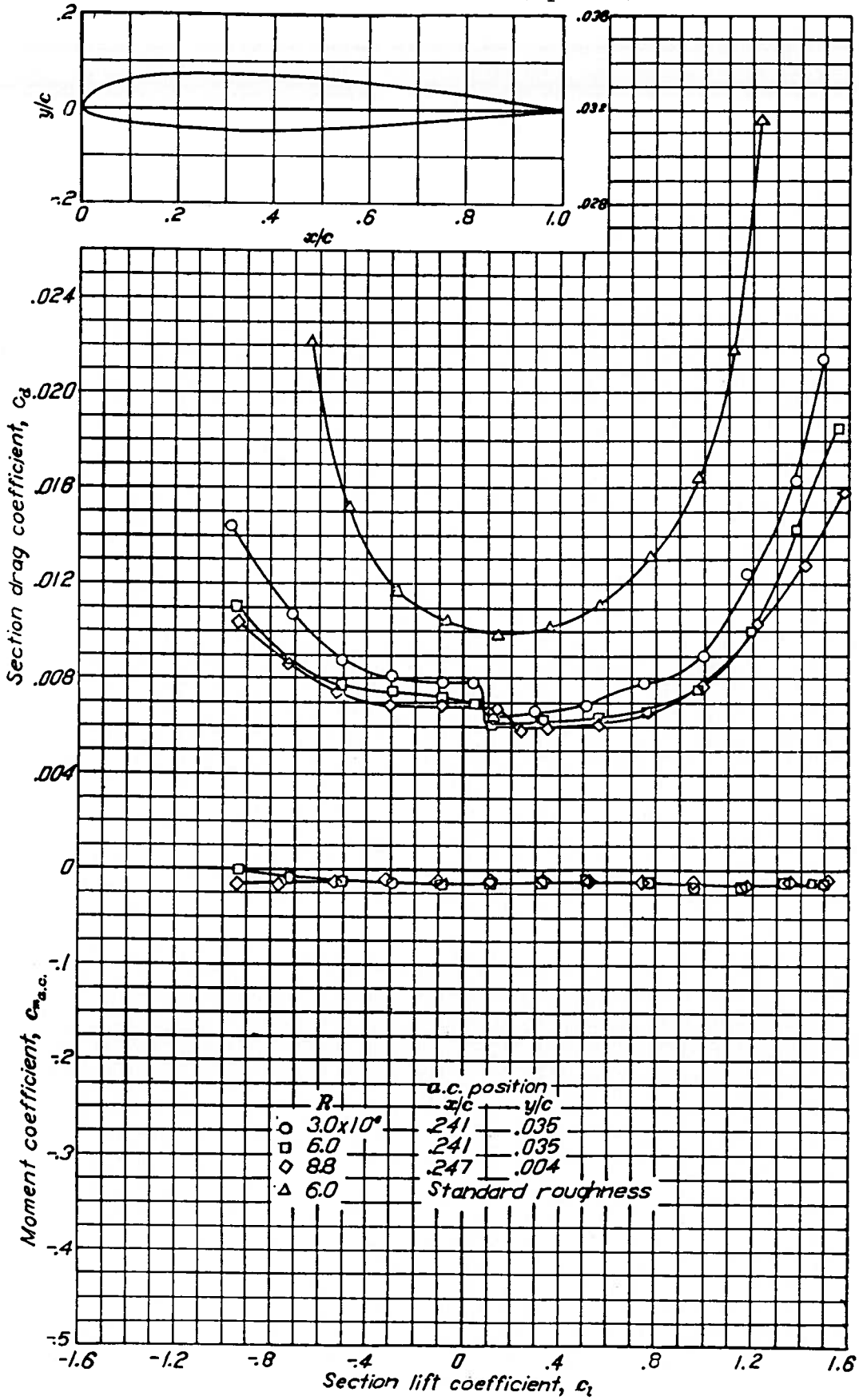

Figure 3.3: Drag and Aerodynamic Center of NACA 23012 Wing Section

it is referred to the aerodynamic center (which happens to be quite close to the quarter-chord point for this foil). The aerodynamic center is defined as that point about which the moment coefficient is essentially constant -- at least up to the stalling point. The section lift, drag, and moment coefficients are defined by the formulas

$$C_L = L/\frac{1}{2}\rho V^2 c \quad , \tag{3.1}$$

$$C_D = D/\frac{1}{2}\rho V^2 c \quad , \tag{3.2}$$

and $$C_M = M/\frac{1}{2}\rho V^2 c^2 \quad . \tag{3.3}$$

The numerator in each of these formulas refers to the two-dimensional lift, drag, and moment, respectively. The graphs of experimental results show that an increase in the Reynolds number delays stall, but otherwise has little effect on the lift. The effect of viscosity on drag, of course, is substantial because of skin friction. For this wing section, the center of pressure, defined by

$$\bar{x} = .M/L$$

$$= \frac{C_M}{C_L} c \quad , \tag{3.4}$$

basically coincides with the aerodynamic center.

Turning now to the question of cavitation, we first note that the pressure distribution on the foil can be approximately decomposed into three parts, as shown in Fig. 3.4. The graphs show the contributions to the three pressure coefficients. These pressures p_1 , p_2 , and p_3 are defined as the contributions due to thickness, due to camber at the ideal angle of attack, and due to any additional angle of attack. The pressure coefficients Cp_1

From Abbott and von Doenhoff (1959, p. 78)

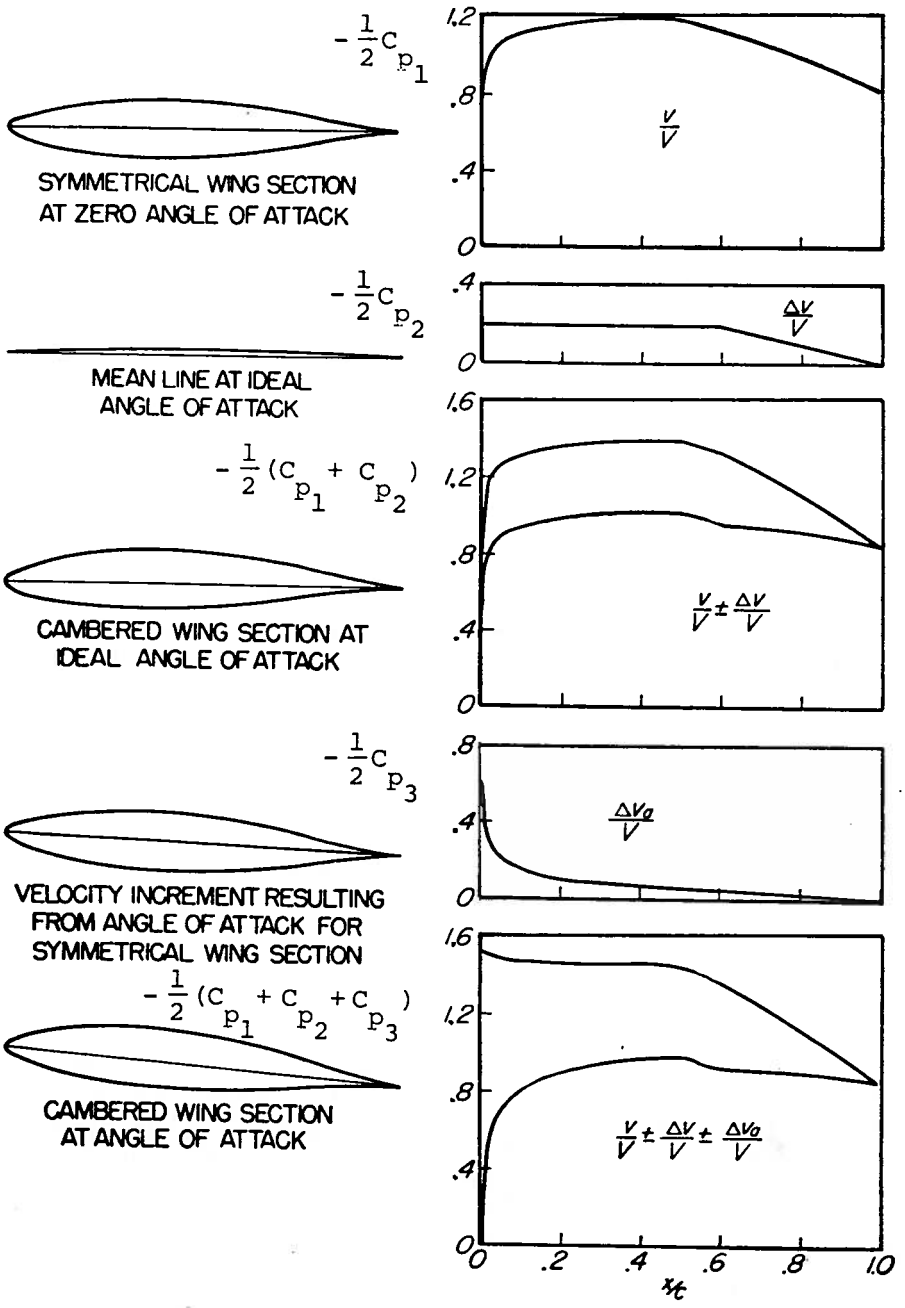

Figure 3.4: Superposition of Pressures on a Foil

Cp_2 , and Cp_3 are the ratios of the respective pressures to the dynamic pressure of the free stream $\frac{1}{2}\rho V^2$. Normally, an attempt is made to set the foil at the ideal angle of attack (also called the shock-free condition), when the forward stagnation point is at the leading edge. In this condition, the last coefficient Cp_3 is zero.

The pressure on the surface of the foil is given by the formula

$$p = p_a + \rho g d + (Cp_1 + Cp_2 + Cp_3)\frac{1}{2}\rho V^2 \quad , \tag{3.5}$$

where the contributions of the atmospheric (p_a) and the hydrostatic ($\rho g d$) pressures have been included. Under the assumption of thin-foil, or linear, theory the pressure coefficients are equal to minus twice the relative velocity increment due to the respective cause, as noted in Fig. 3.4.

As the pressure coefficients are approximately proportional to the respective causes, it can be seen that with sufficient thickness, camber or angle of attack, or at a great enough speed, the absolute pressure could drop to the vapor pressure p_v , at some point on the foil surface. (The pressure coefficients in (3.5) are all negative over most of the upper foil surface, due to the effect of the increased velocity on the pressure in the Bernoulli equation.)

To avoid cavitation at these higher speeds of operation, it is possible to utilize thinner foil sections. This reduces the thickness effect shown in Fig. 3.4. Another solution to the difficulty is to make use of a delayed-cavitation section, seen in Fig. 3.1. Such a section is also illustrated in Fig. 3.5. Here a comparison in both the section shape and the resulting distribution of the pressure coefficient is made. The peak pressure has been reduced, thus allowing some increase in the operating speed of the foil, without the onset of cavitation.

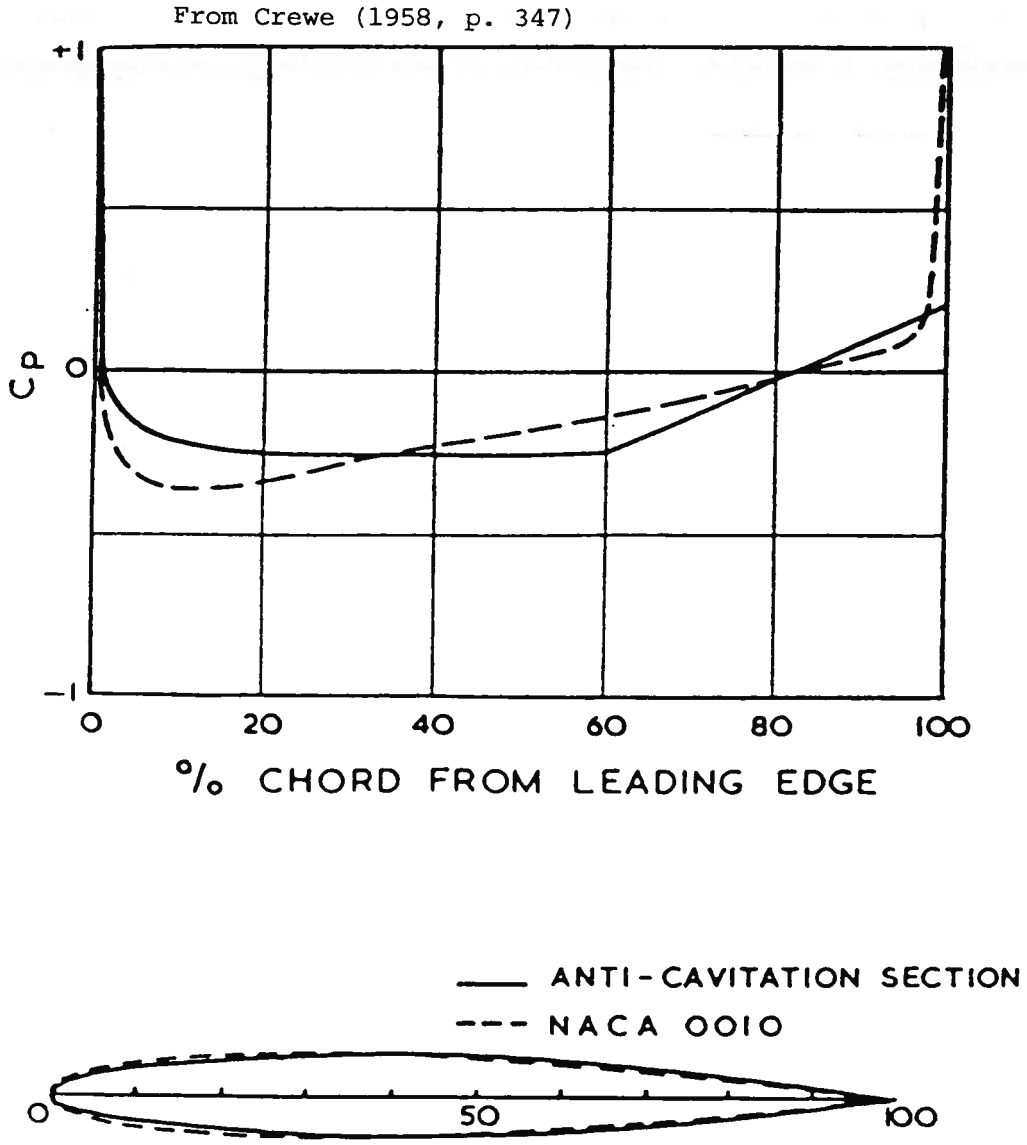

Figure 3.5: Comparison of Standard and Anti-Cavitation Sections

Unfortunately, there is a limit to our ability to prevent cavitation, because the foil section eventually becomes so thin as to be structurally too weak. Under this condition, it is very undesirable to have a partially-cavitating foil which would result in an unstable flow with unsteady lift and drag forces on the foil. Furthermore, the resulting cavitation causes rapid erosion over those parts of the surface where the cavitation bubbles collapse into water again.

A preferable solution is to employ a so-called supercavitating section shown at the bottom of Fig. 3.1. In this case, the whole of the upper surface is enveloped by the cavity so that very little erosion occurs. The cavity collapse occurs well behind the foil. Unfortunately, the lift-to-drag ratio of this section is much worse then that of a subcavitating section.

Yet another possibility in foil design is to use a super-ventilating section. This section is essentially the same as a supercavitating one, but is intended for use at relatively high speeds -- but not so high that full cavitation can be guaranteed. Air is led down from the atmosphere to the foil surface, where it is used to ventilate the resulting cavity, which resembles the vapor cavity already referred to.

3.1.3 Foil Placement

In early hydrofoil designs, the foils were of the surface-piercing type. That is, a portion of the foil (the tips) were designed to project through the water at the design speed of operation. Such an arrangement provides automatic heave stability, because a downward displacement (say) of the boat will result in an increase in submerged foil area, and a correspondingly greater lift force, which will return the craft to its equilibrium position.

Fitting the boat with foils such as these near the bow and the stern will also ensure static longitudinal (or pitch) stability. Natural roll stability

can also be ensured by suitable geometric shaping of the foil as seen in a bow-on view. This point is illustrated in Fig. 3.6. It is necessary to arrange the slope of the foil near the water surface so that the local normal vector intersects the centerplane of the boat above the center of gravity. This intersection point is equivalent to the metacenter. It is clear that as the boat travels faster, it will rise further out of the water. This means that the position of the intersection point will be a function of speed, in general. In other words, the roll stability varies with the speed. Because of the well-known $\frac{1}{2}\rho V^2$ factor in lift calculations (see (3.1)), there will be an additional influence of speed on roll stiffness -- as well as on the heave stiffness.

Fig. 3.6 also shows that the supports which connect the foil to the hull can provide additional roll stability when the boat is operating in the hull-borne mode.

More recently, attention has been devoted to the use of fully-submerged foils. The main advantage of this type is the much smaller response to waves -- thus giving rise to a smoother ride in rough water. In addition, the foil efficiency is somewhat better because of the lack of spray losses associated with the surface-piercing type. The better ride in rough water allows the pursuit of higher speed, and consequently, the use of supercavitating sections is often considered. Unfortunately, the lack of wave response also implies that the submerged foil does not always possess sufficient natural heave and roll stability. Thus, some means of automatic control system is required.

This control system is usually designed to adjust the angle of flaps set into the foils, or perhaps to alter the angle of attack of all-movable foils. A sophisticated system receives inputs from sensors which measure the craft's motion relative to an inertial frame of reference, as the sea surface cannot

From Crewe (1958, p. 351)

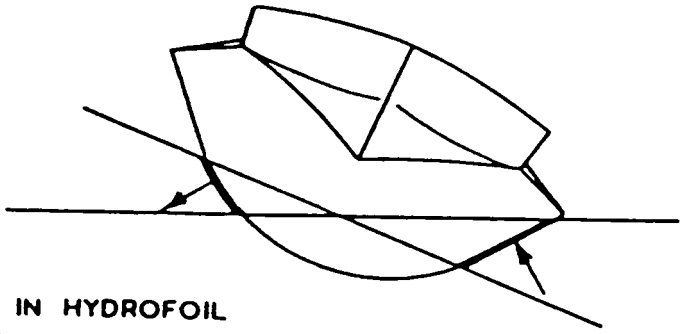

CHANGE IN HYDROFOIL
LOADING DUE TO ROLL.

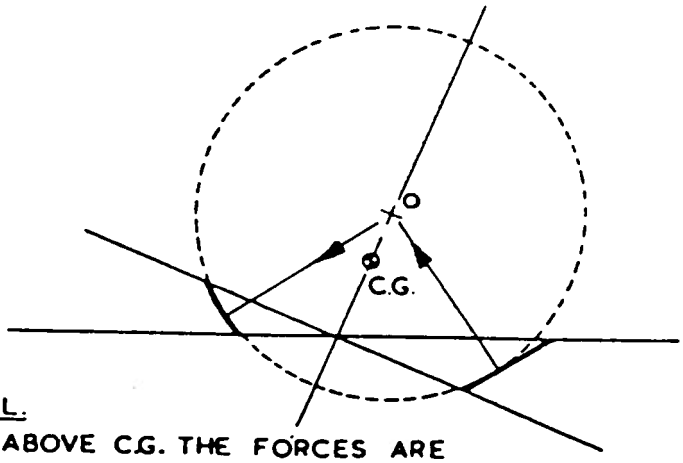

DIHEDRAL.
IF O IS ABOVE C.G. THE FORCES ARE
STABILISING I.E. CIRCLE TOUCHING ELEMENTS
MUST HAVE SUFFICIENTLY LARGE RADIUS.

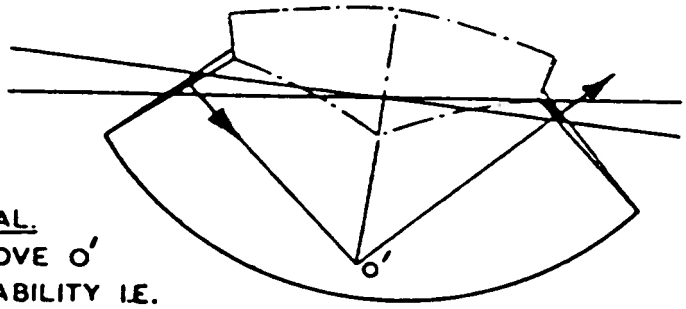

ANHEDRAL.
C.G. ABOVE O'
FOR STABILITY I.E.
ANHEDRAL ALWAYS STABILISING IN PRACTICE.

Figure 3.6: Natural Roll Stability with Surface-Piercing Foils

be used as a datum. Of course, the relative motion must also be continuously monitored so that in the event of a very heavy sea, the boat will not be forced to fly through the waves. Different types of responses, depending on the sea state are therefore required. This is illustrated in Fig. 3.7. The fully-submerged system has been the subject of research and development by the US Navy.

A very common design philosophy is to use a main bow foil of the surface-piercing type, which supports most of the boat's weight. An auxiliary, smaller, fully-submerged foil, carrying the remainder of the load is fitted at the stern. This combination of the two systems can provide positive longitudinal (heave and pitch) stability, while roll stability is still derived from the surface-piercing foil alone. This design is illustrated in Fig. 3.8(c). It is desirable for a downward heave disturbance of the boat to result in an upward lift force as well as a bow-up moment. In addition, a longitudinal moment should result in a counteracting moment with little change in lift. Both these properties are possessed by this arrangement and choice of foils, which is the most popular one in the western world. It is often called the Supramar system.

A third system is the so-called Alexeyev design which is in common use in Russia. This makes use of the fact that there is a small loss in lift on the foil as it approaches the water surface. It is therefore possible to obtain the necessary stability -- in heave, roll, and pitch, by placing the foils very close to the surface at the design speed of operation. Because the stiffness of this system is minimal, it can only be used in relatively calm water, and at speeds very close to the design speed. It is therefore suitable for use on inland rivers, as opposed to coastal routes, or the open sea.

A fourth design is that developed by the Defence Research Establishment

From Du Cane (1974, p. 16)

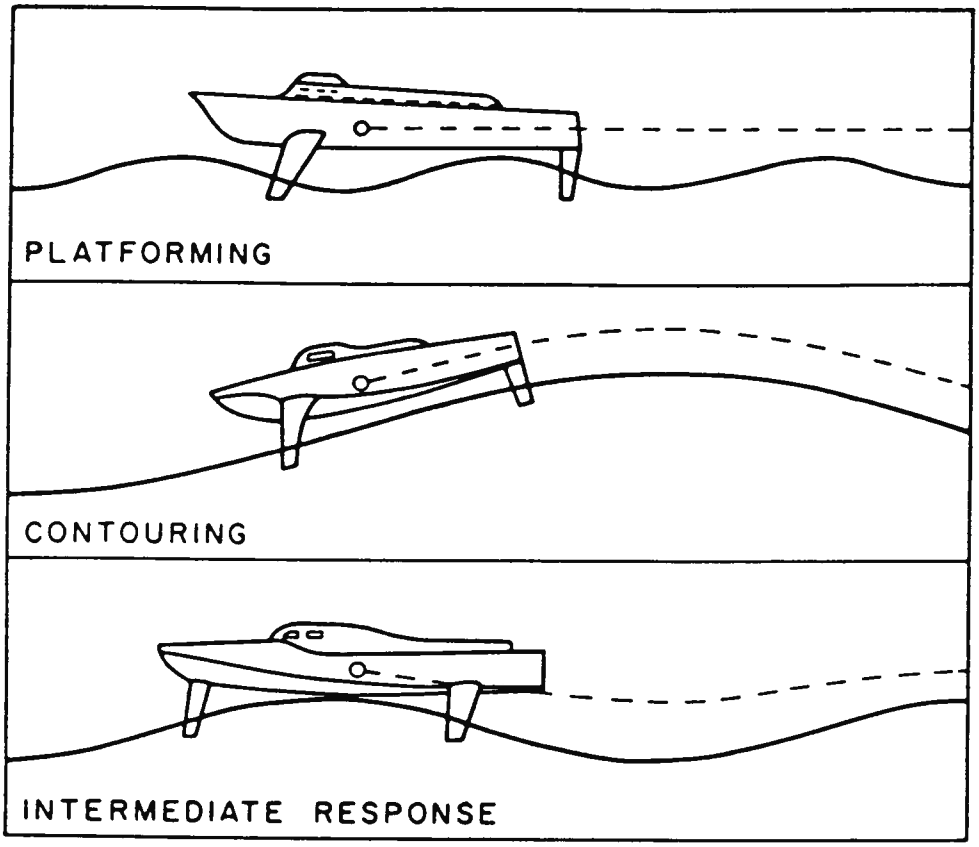

Figure 3.7: Modes of Operation in Waves

From Crewe (1958, p. 353)

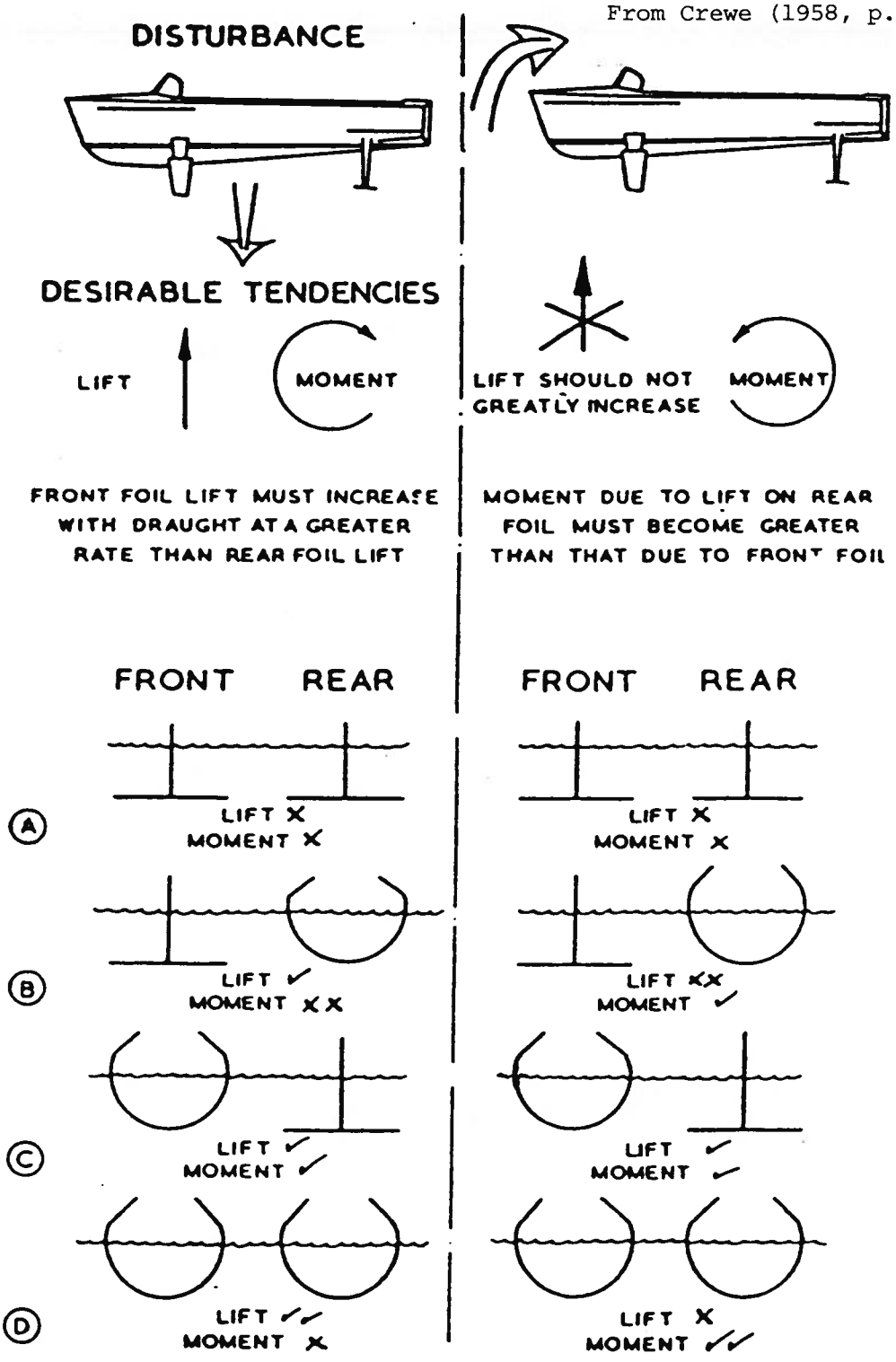

Figure 3.8: Longitudinal Stability Using Surface-Piercing and Fully-Submerged Foils

Atlantic (DREA) in Canada. Here, a main subcavitating foil carrying about ninty percent of the boat weight is located slightly aft of midships. A smaller surface-piercing superventilated foil is used at the bow to provide the longitudinal stability. It is said that this arrangement provides good behavior in a following sea.

The main features of the four systems discussed here are summarized in Table 3.1. A comparison is made on the basis of hydrodynamic performance, seakeeping, and other features. It is noted that the Canadian system is well suited to operation in severe seas, while the Alexeyev system is better suited for the other extreme, namely calm water. The US Navy system gives excellent maneuverability and behavior in heavy seas. On the other hand, the Supramar system has an acceptable performance in most areas, and is particularly favored for its engineering simplicity.

3.1.4 Foil Grouping

The question of the disposition of the foils around the craft will now be briefly addressed. Fig. 3.9 shows the basic arrangement possibilities in the horizontal plane. Regarding the longitudinal disposition of the foils, one can make use of aeroplane, canard, and tandem systems. Early hydrofoil designs were of the tandem arrangement, with the center of gravity located amidships. It is more common now, however, to adopt the aeroplane design because of its better longitudinal stability characteristics. However, as noted in Sec. 3.1.3, the canard system can be made to work well in very rough water.

Regarding the lateral arrangement, the choice is basically between split and non-split foils as shown in Fig. 3.9. One can get greater foil area, and hence lift, using the non-split style. Where the lift is adequate (for example, at higher speeds), but additional roll stability is desired, then the

From Du Cane (1974, p. 51)

NOTES: (1) Blanks do not imply zero capability; merely that this feature is not noteworthy. (2) Many existing craft do not exploit the full potential of their type.		*Fully Submerged*		*Surface-Piercing*	
		Russian	*U.S. Navy*	*Supramar*	*Canadian*
Performance	High maximum speed	✓			✓
	Low take-off speed			✓	✓
	Low foil system drag	✓	✓✓		
	High rates of turn		✓✓		
Seakeeping	Comfort in moderate seas (Fig. 9)		✓✓	✓	✓
	Ability in heavy seas (Fig. 9)		✓		✓
	Ability in extreme seas (Fig. 9)				✓
	Hullborne seakeeping ability			✓	✓✓
Other features	Foil retraction or mooring convenience	✓	✓		
	Low foil system weight	✓	✓		
	Capacity for load and C.G. variations			✓✓	✓
	Engineering simplicity	✓✓		✓✓	✓

Table 3.1: Effect of Foil Position Relative to the Water Surface

From Du Cane (1974, p. 15)

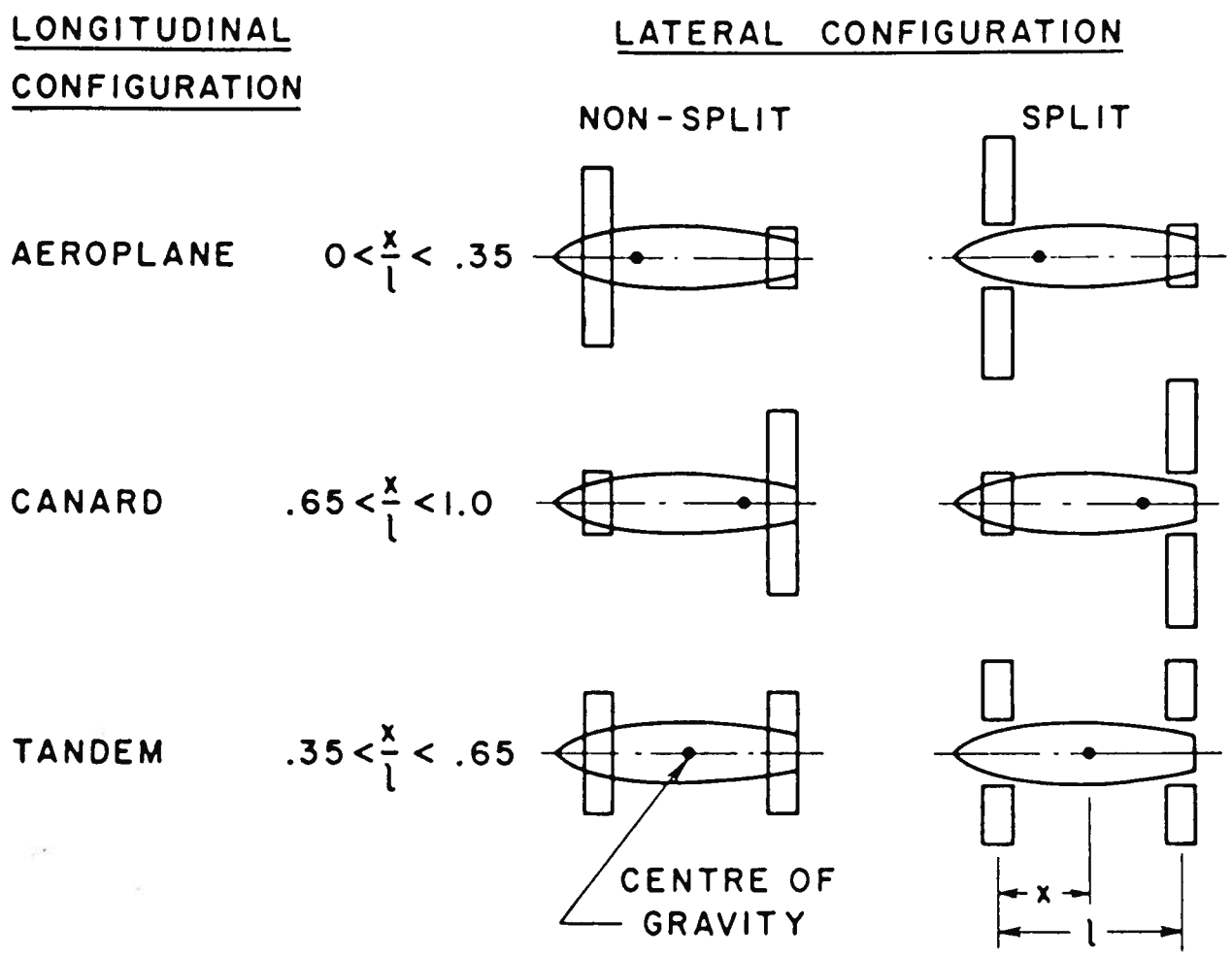

Figure 3.9: Longitudinal and Lateral Arrangement of Foils

split arrangement is chosen because of its relatively larger track and hence righting moments that are generated when rolling. The last comment would apply to both the surface-piercing and the fully-submerged types.

3.1.5 Method of Stabilization

Some methods of achieving stability have already been referred to. Other possibilities are shown in Fig. 3.10, which shows, in a more comprehensive way, the different basic designs that were being tested in 1958. One arrangement that was seriously considered at that time was the ladder-foil on the Canadian boat Baddeck (ex Bras d'Or). That was a development of an original craft built earlier in the century by Alexander Graham Bell (the inventor of the telephone), and his associate Frederick Baldwin. Their work led to the HD-4 hydrodome (the early term for a hydrofoil boat) which achieved a record water speed of 70.86 mph on September 9, 1919. A detailed description of their work on hydrofoils was reported by Parkin (1964).

Yet another method of obtaining stabilization is the Aquavion system in Fig. 3.10. This idea utilizes a pair of planing surfaces projected ahead of the boat. These act as feelers and sense the heave and roll of the craft relative to the water surface. One version of a mechanical sensor is called the Hydrofin, and is depicted in Fig. 3.11. The system requires a mechanical linkage between the feelers and the incidence control on the fully-submerged foils. This design attempts to take advantage of the main favorable characteristic of fully-submerged foils -- their relatively low sensitivity to the waves on the water surface. This advantage is partly lost by the feeler arrangement. As mentioned in Sec. 3.1.3, a better method of stabilization of fully-submerged foils uses a system which essentially relies on position measured in an inertial frame of reference.

From Crewe (1958, p. 344)

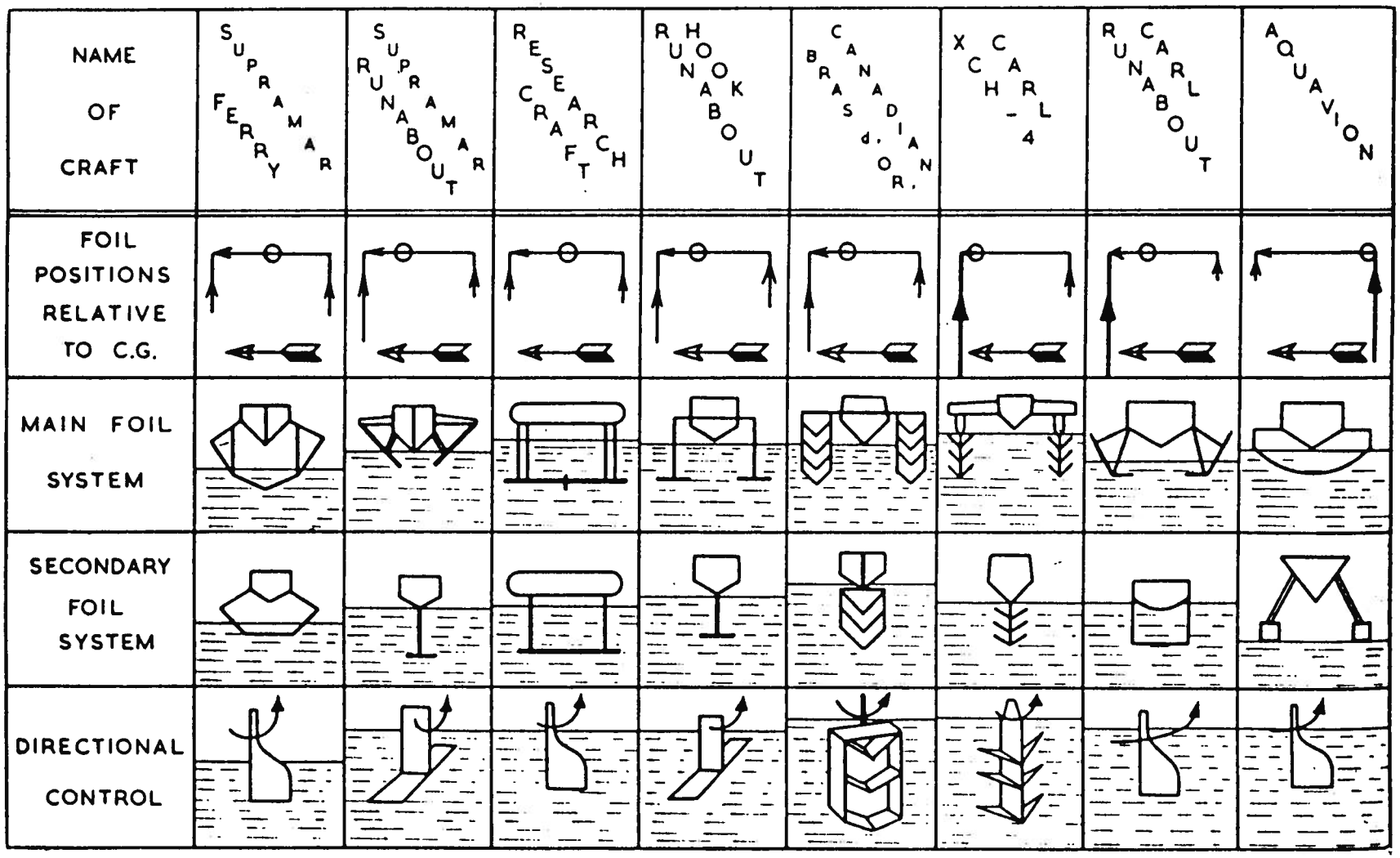

Figure 3.10: Typical Foil Configurations

From Du Cane (1974, p. 25)

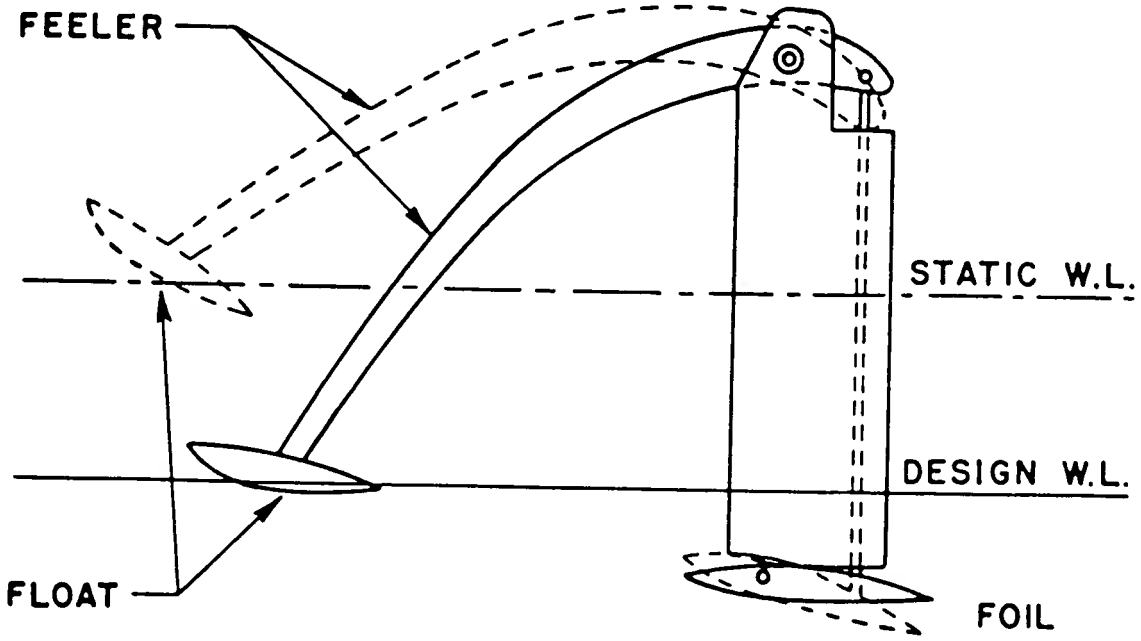

Figure 3.11: The Hydrofin Principle

The chief techniques of stabilization which have been developed are displayed in Table 3.2.

3.2 Comparison with Other Marine Vehicles

Fig. 3.12 compares the resistance-speed curves for hydrofoil boats, hard-chine and round-bilge planing craft, and displacement ships. The curves in Fig. 3.12(b) show that at low speeds, the displacement boat has the least resistance, but the upward trend of the resistance curve is so great, as to make it impractical for a large Froude number. A round-bilge boat (particularly a fine one with a large length-to-beam ratio) has a form which delays the eventual very rapid increase in resistance, and is therefore more suitable for a higher speed.

For still higher speeds, one is led to a hard-chine design -- although this would be unsuitable at a lower speed. Fig. 3.12(b) indicates that a hydrofoil boat generally has a relatively high resistance at low speeds. However, for sufficiently high speeds, its resistance is lower than that of the other types of marine vehicles shown.

The question of designing hydrofoils with different displacements and for different speeds is raised in Fig. 3.13. It is well known that the lift on a foil is proportional to its area, other factors being equal. This property is stated by (3.1). Thus for geometrically similar foils traveling at the same speed, the lift is proportional to the square of the foil span S :

$$L \propto S^2 \quad , \tag{3.6}$$

while for geometrically similar boats, the weight depends on the cube of the craft length ℓ :

$$W \propto \ell^3 \quad . \tag{3.7}$$

Thus, for the foils to support the weight of the boat, $L = W$, and we have

$$S \propto \ell^{3/2} \quad \text{for a fixed speed.} \tag{3.8}$$

From Du Cane (1974, p. 14)

Fully Submerged Systems	Control of lift curve slope	Free surface effect—U.S.S.R.: Alexeyev Ventilation control—Supramar
	Control of flaps or foil angle	Surface sensing— Hook Motion sensing— U.S. Navy
Surface-Piercing Systems	Control of immersed area	Ladder principle— Bell-Baldwin Dihedral foils— Supramar
	Control of trim and area	Grunberg principle—Aquavion SV bow foil— Canadian

Table 3.2: Summary of Stabilization Techniques

From Crewe (1958, p. 338)

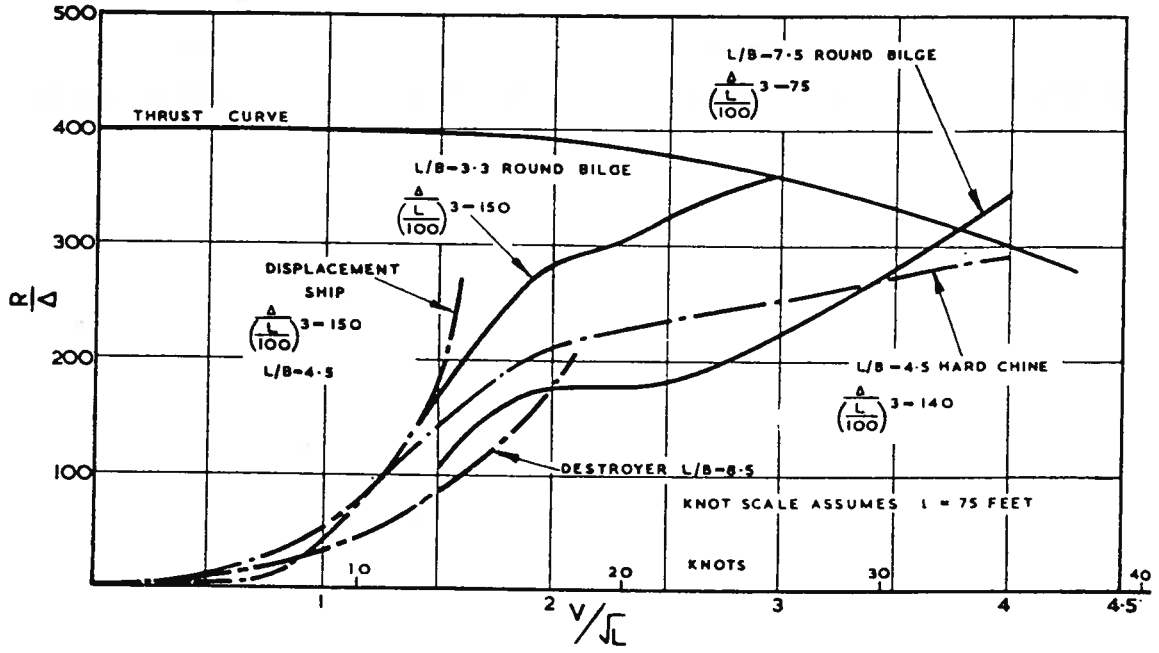

(a) Drag Curves of Orthodox Displacement and Planing Craft

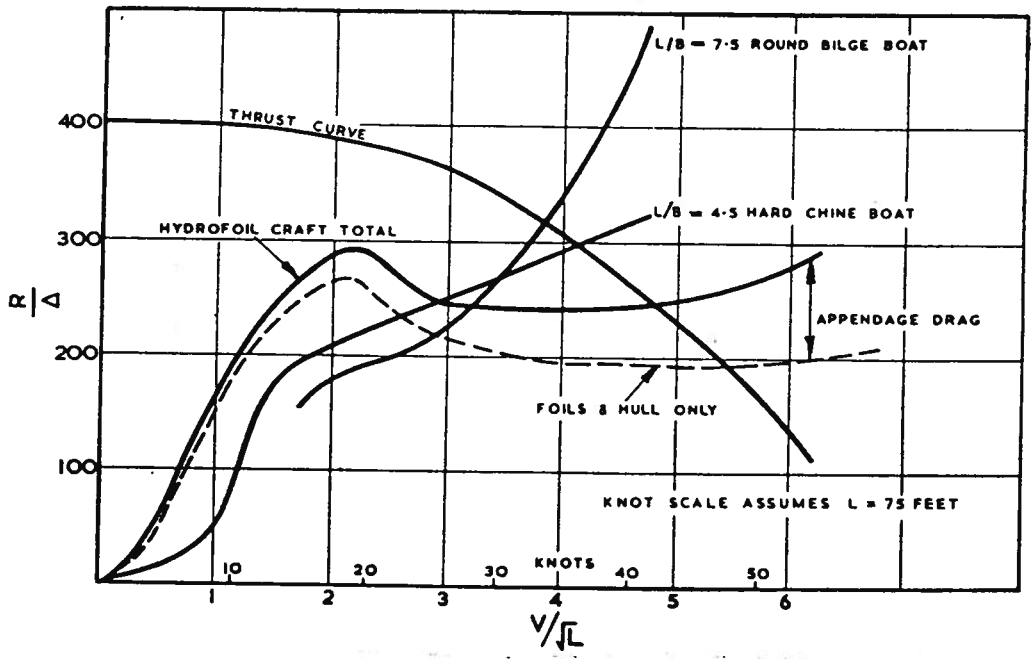

(b) Comparison of the Drag of a Hydrofoil Boat with Orthodox Craft of Approximately the Same Length

Figure 3.12: Drag Characteristics of Hydrofoil and Orthodox Craft

From Du Cane (1974, p. 49)

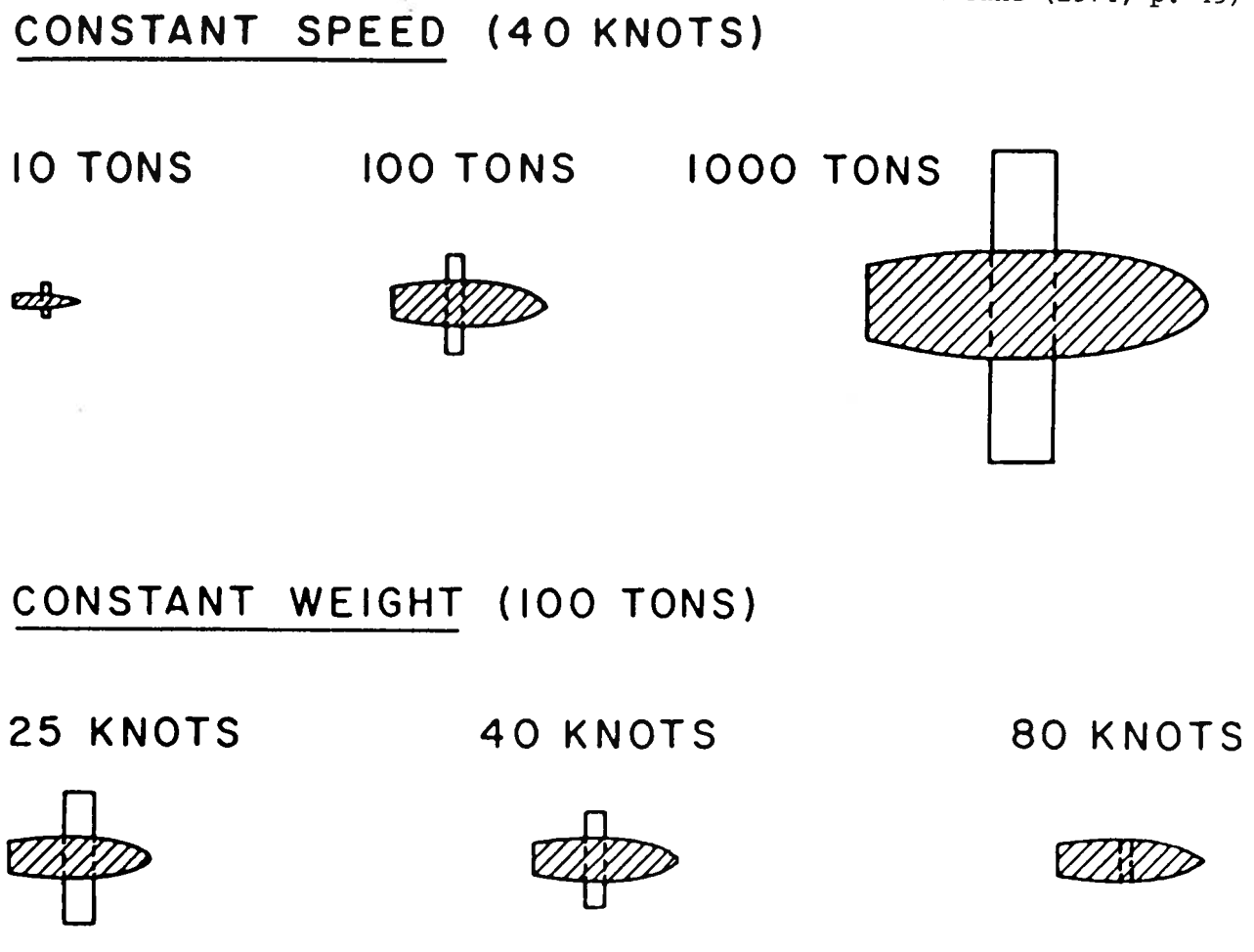

Figure 3.13: Hydrofoil Scaling Problems

Fig. 3.13 illustrates graphically that (3.8) requires the span of the foils to grow much faster than the linear dimension of the hydrofoil. Eventually, for a large enough boat, the foils would weigh more than the hull!

Of course, by adopting Froude scaling for the speed, we would require that the speed increases with the length of the boat. That is

$$V \propto \ell^{1/2} \quad . \tag{3.9}$$

Under this condition, we should replace (3.8) by

$$S \propto \ell \quad \text{for a fixed Froude number.} \tag{3.10}$$

This shows that geometric similarity could be preserved by observing Froude scaling. In practice, however, this cannot be done. Firstly, extremely high speeds are not desirable for economic and safety reasons. Secondly, cavitation becomes important at the higher speeds (above 40 kt), so that (3.9) cannot be obeyed.

A similar problem is raised if we wish to design a hydrofoil of a particular weight to operate over a range of speeds. Because the lift in (3.1) depends on the square of the speed, that is

$$L \propto V^2 \quad , \tag{3.11}$$

we require much smaller foils at higher speeds, as illustrated in Fig. 3.13. The ladder-foil system is one successful attempt at a design which provides a variable foil area to cope with different speeds. (The main deficiency of the ladder-foil, apart from its complexity, is the lower hydrodynamic efficiency of a multiplane arrangement.)

3.3 Thin-Foil Theory

3.3.1 Introduction

The computation of the lift developed by a two-dimensional foil is commonly based on three inviscid theories. The most general method utilizes a distribution of mathematical sources and vortices around the surface of the

foil. This is often called the panel method.

If we assume the surface to be divided into, say, n panels, with the source strength constant on each panel, then there will be n unknown source strengths, together with the requirement that there is no normal velocity at the collocation point (or center) of each panel. The discretization of the surface into panels is shown in Fig. 3.14. As stated, this method will generate a flow similar to that shown in Fig. 3.15(a): the pressure distribution around the foil will generate no lift.

The solution to this difficulty is found by applying the Kutta condition. This states the experimental fact that the flow should separate smoothly from the trailing edge, as shown in Fig. 3.15(b). This can be achieved in our mathematical model by adding a constant vortex density, of equal strength on each panel, to the sources already referred to. The additional unknown quantity is balanced by the requirement that the tangential velocity on the first panel must be equal in magnitude to that on the last panel. This statement, which represents the Kutta condition, is also equivalent to saying that the pressure is the same on the first and last panels. Results in Fig. 3.14(b) taken from Doctors and Kelly (1983) show the convergence rate of the lift on a Joukowski foil based on an integration of the pressure distribution. It is also known that the lift on a two-dimensional foil is given by

$$L = \rho V \Gamma \quad , \tag{3.12}$$

where Γ is the circulation per unit span around the foil. In the figure, the results are dimensionless, in the sense that ρ and V have both been set to unity. Three different source-distribution elements have been tested here, and are referred to as the constant, linear, and tent elements. These have been given the code numbers 30, 40, and 50, respectively. The figure shows the slightly better convergence behavior of the tent element compared to

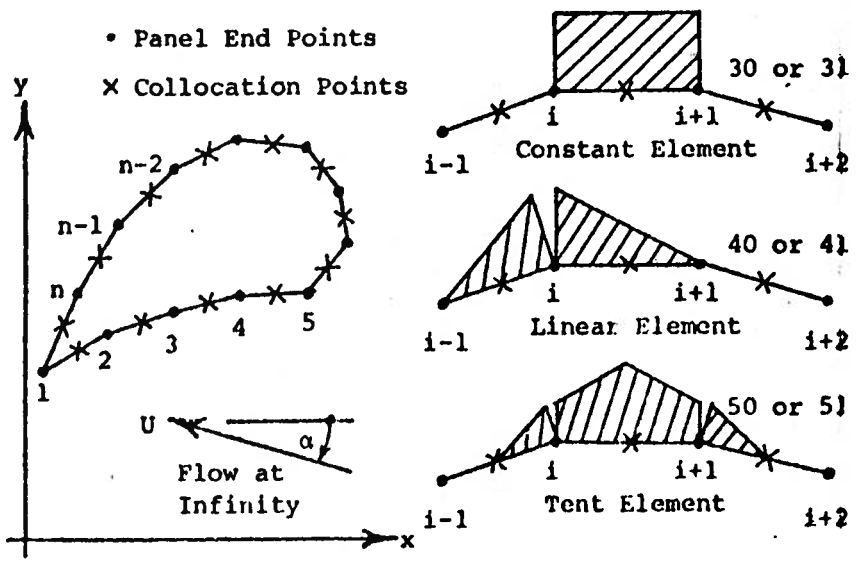

(a) Discretization of Body Surface into Flat Panels

From Doctors and Kelly (1983)

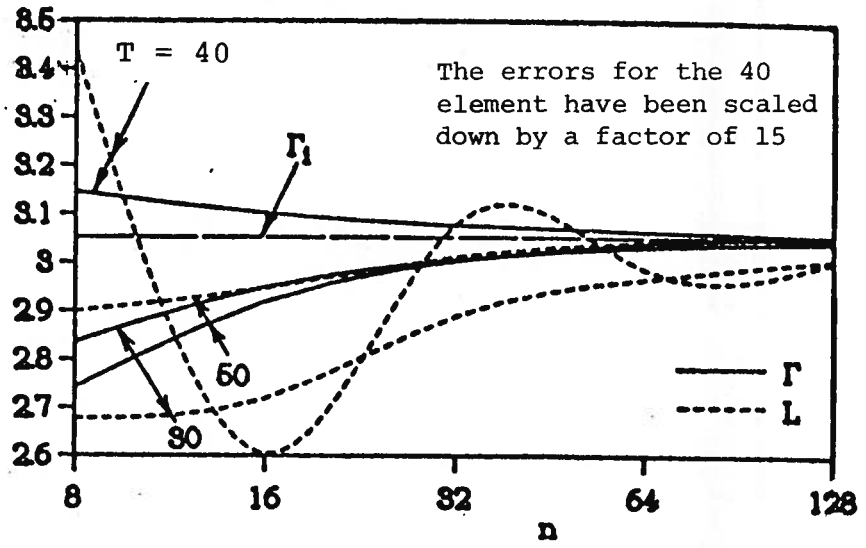

(b) Circulation and Lift

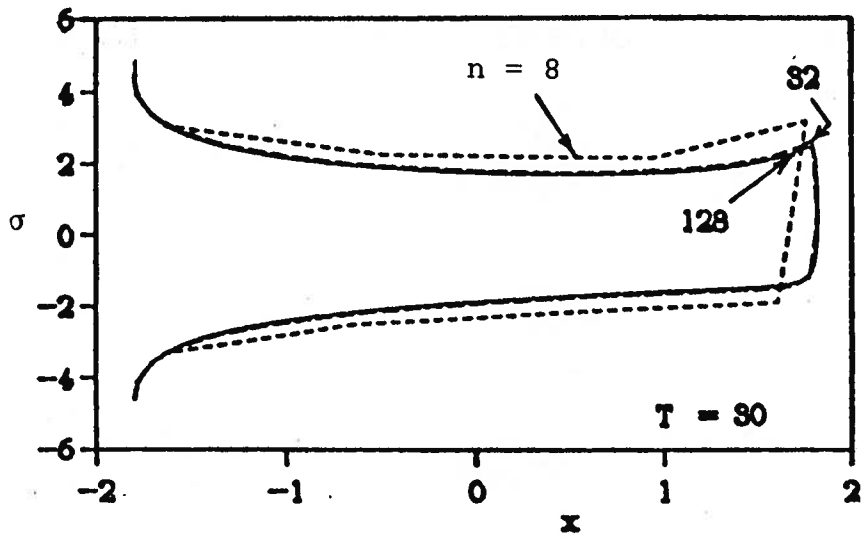

(c) Source Distribution

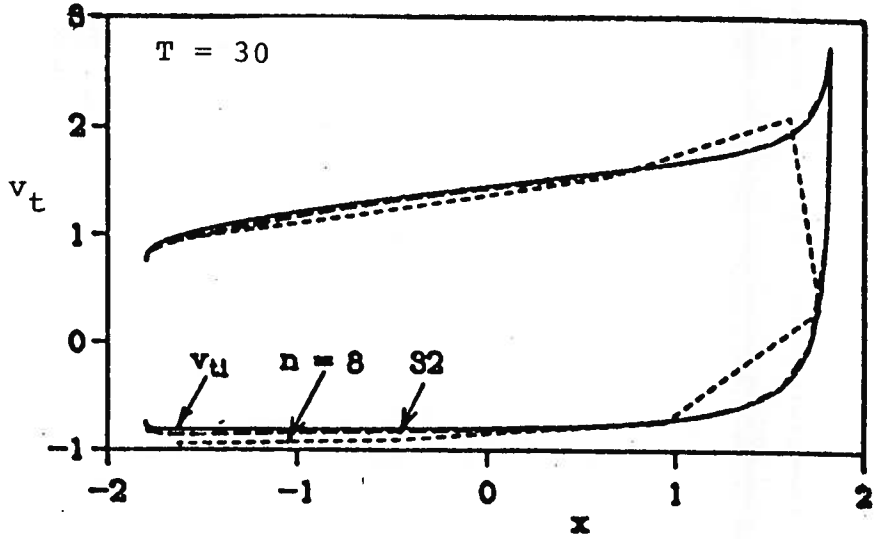

(d) Tangential Velocity

Figure 3.14: The Panel Method Applied to a Joukowski Airfoil

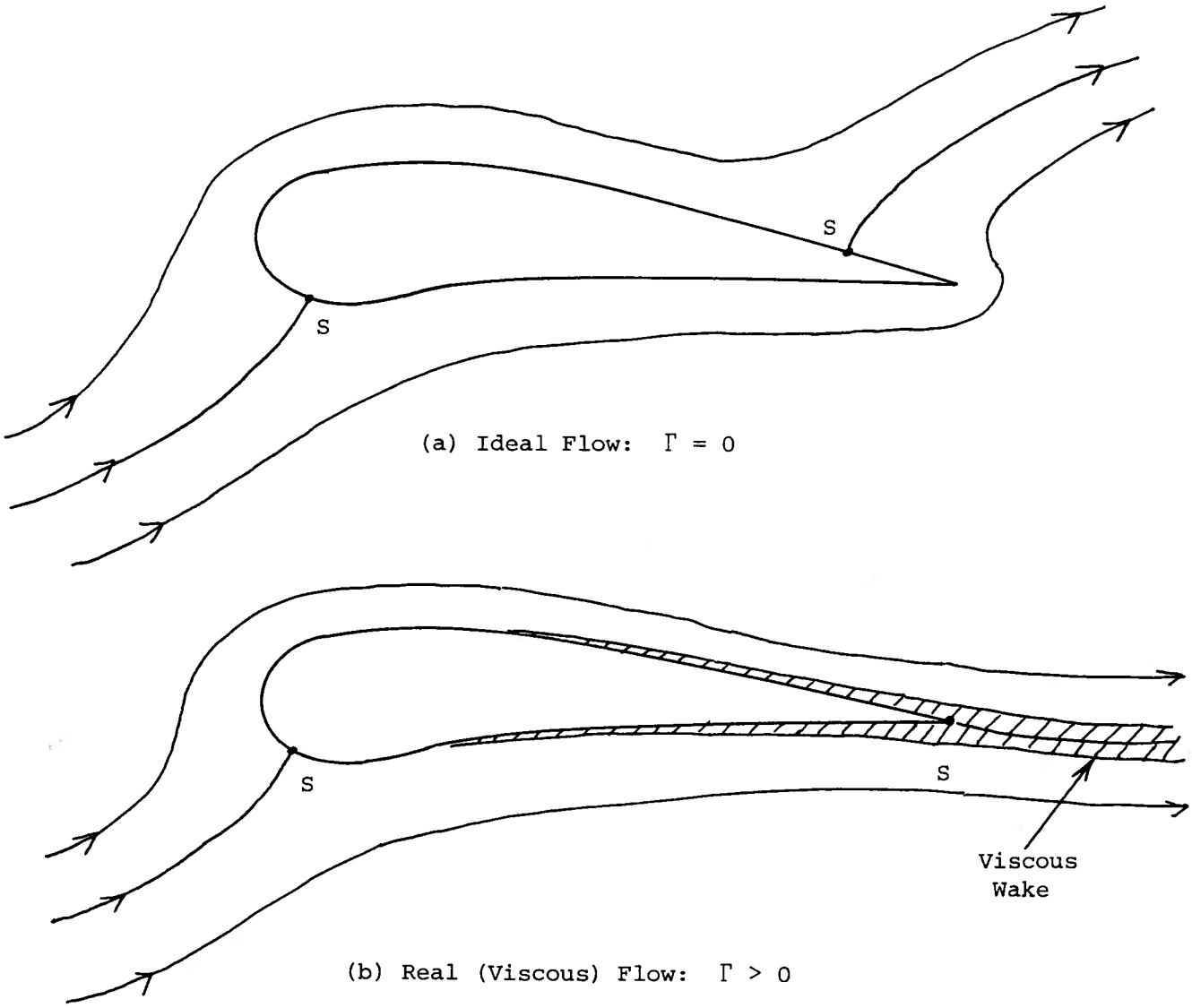

Figure 3.15: Application of the Kutta Condition

the more popular constant element. All three elements converge in the sense that as the number of elements n becomes large, the computed value of lift L and circulation Γ approach the ideal value Γ_i for the foil.

The resulting source distribution and tangential-velocity distribution are shown for the constant-source element. There is little difference between the case of 32 elements and the ideal result based on conformal mapping (see Abbott and von Doenhoff (pp 46-63).

The next section deals with thin-foil theory which is adequate for many of the calculations required in hydrofoil design. This is because of the thin sections and the small camber and angles of attack that are generally used.

3.3.2 The Singularity Distribution

The assumptions of thin-foil theory allow us to represent the foil by a combined source and vorticity distribution along the chord line, as shown in Fig. 3.16. More details of the method can be found in Abbott and von Doenhoff (pp 64-79), and in Parsons (1980, pp 93-122). We first note that the upper and lower surface of the foil z_U and z_L, respectively, are given in terms of the mean line $g(x)$ and the local thickness $t(x)$, as follows:

$$z_U(x) = g(x) + \frac{1}{2}t(x)$$

$$\text{and} \quad z_L(x) = g(x) - \frac{1}{2}t(x) \quad . \tag{3.13}$$

Secondly, we utilize the fact that a point vortex of strength Γ will generate a tangential velocity given by

$$v_t = \Gamma/2\pi r \quad , \tag{3.14}$$

where r is the distance from the vortex. One of the features of thin-foil theory, is that the effects of thickness $t(x)$, and of camber $g(x)$, in (3.13) can be considered separately.

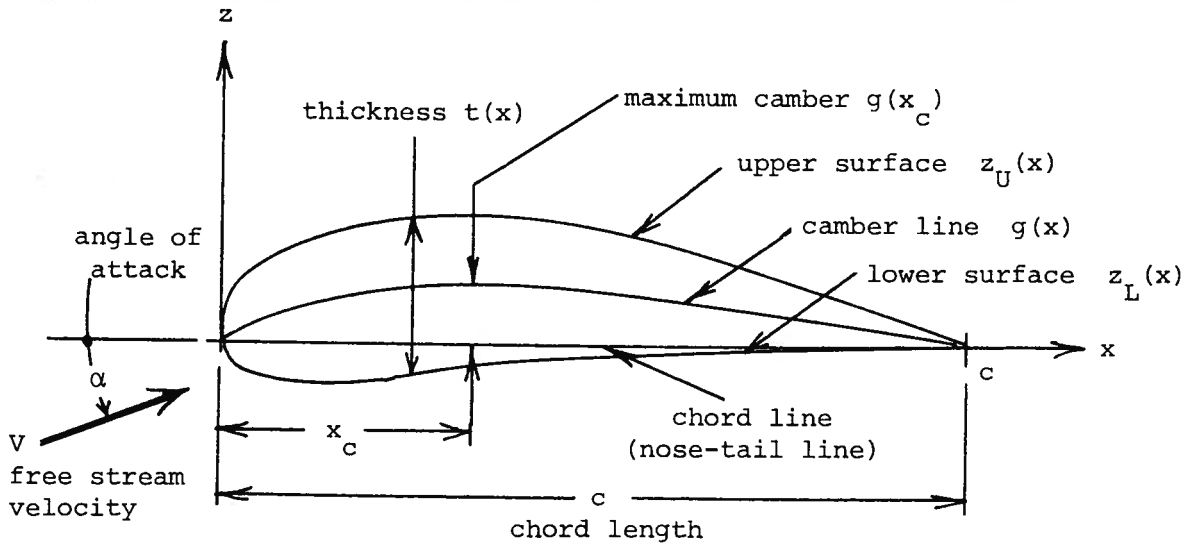

(a) Nomenclature for Foil Section

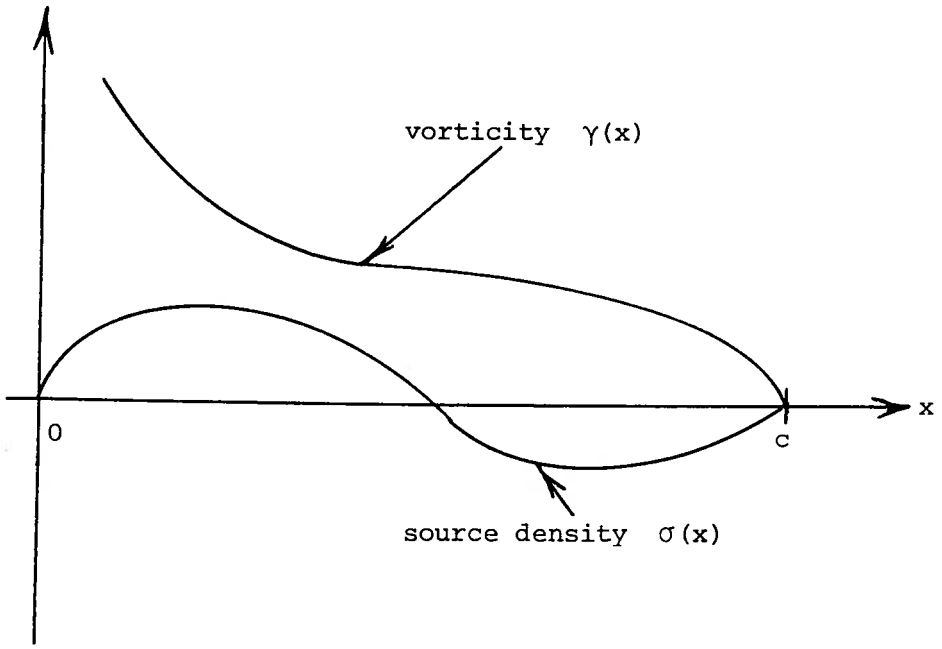

(b) Representation by Singularity Distributions

Figure 3.16: Thin-Foil Theory

It is clear that a source distribution on the chord line will produce a profile that is symmetric about that line, and can therefore be used to generate the required value of $t(x)$. The pressure distribution over the shape will be symmetric, and consequently, no lift is generated. In order to generate lift, the profile should possess some asymmetry relative to the free stream. There must be an angle of attack and/or some camber. The problem is therefore split up into a thickness (source distribution) and mean-line (vorticity distribution) problem. This is illustrated in Fig. 3.17, in which the mean-line problem is further split into the camber and angle-of-attack effects.

The vertical velocity on the mean line $w(x)$ can now be equated to the induced velocity for the entire vorticity distribution:

$$w(x) = V[\alpha - g'(x)] = -\frac{1}{2\pi}\int_0^c \frac{\gamma(\xi)}{x - \xi}\, d\xi \quad . \tag{3.15}$$

The right-hand side of (3.15) represents the integration of (3.14) over the foil, taking Γ and γ to be positive counter-clockwise. Care has been taken in (3.15) to distinguish between the "field point" x (where the boundary condition is applied), and the "source point" ξ (representing a typical location of the elementary vortex).

The solution of (3.15) is somewhat involved. Furthermore, it should be carried out with the requirement that the vorticity approaches zero at the trailing edge. Thus

$$\gamma(c) = 0 \quad . \tag{3.16}$$

This ensures that the type of lifting flow illustrated in Fig. 3.15(b) is obtained.

As already noted, the lifting solution represented by (3.15) can be decomposed into the influences of angle of attack and camber. Some important solutions are given in Table 3.3. The effect of an incident flow angle α

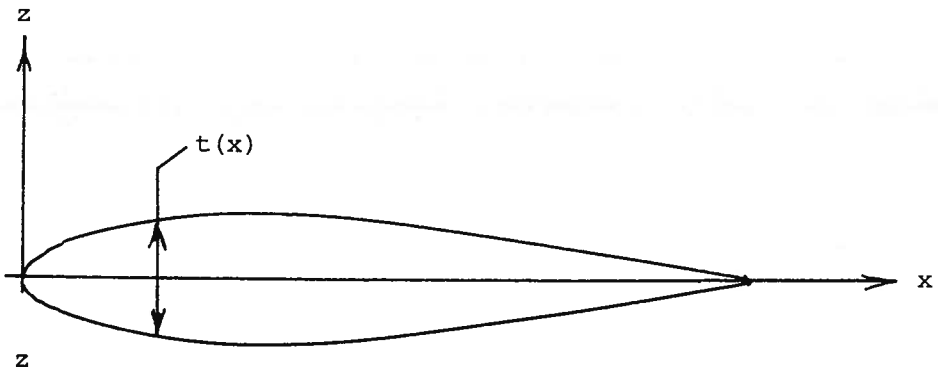

(a) The Thickness Problem

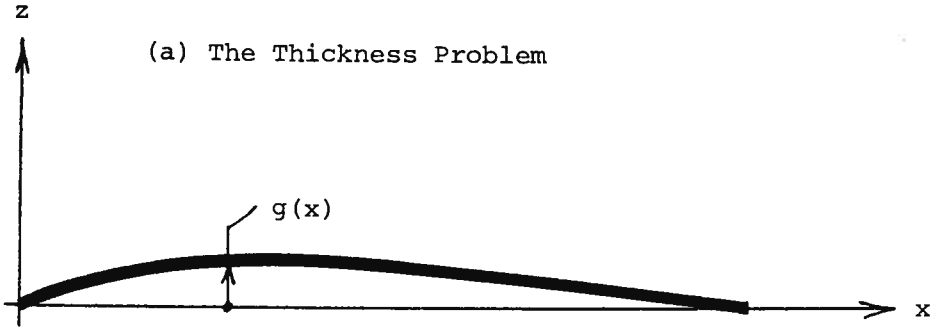

(b) The Camber Problem

(c) The Angle-of-Attack Problem

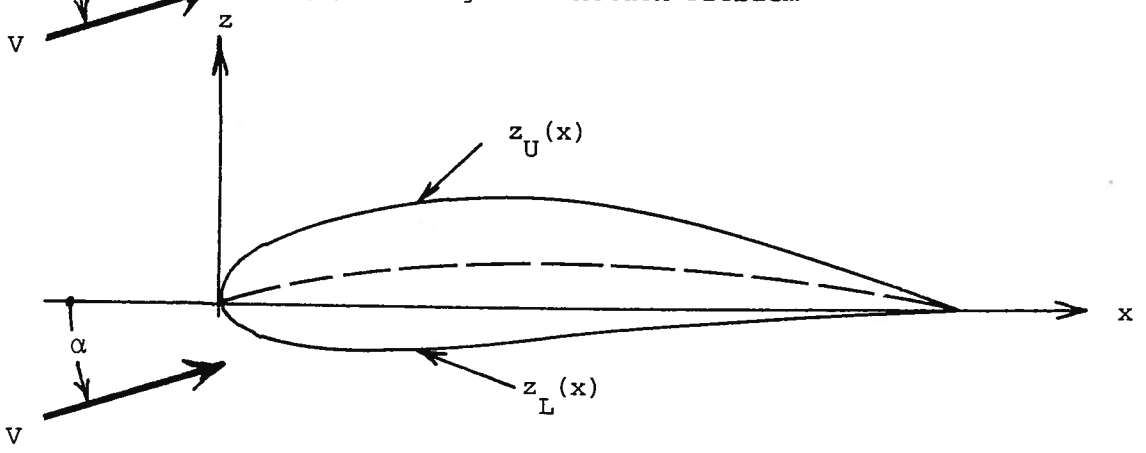

(d) The Complete Problem

Figure 3.17: Decomposition of the Foil into Components

has been incorporated by considering, in addition to parabolic and cubic shapes, a flat plate at an angle α_1 . That is $\alpha_1 \equiv \alpha$.

Table 3.3 Elementary Solutions for a Thin Subcavitating Foil

Case	Equation of Mean Line $g(x)$	Vorticity Distribution $\gamma(x)/V$	Lift Coefficient $L/\frac{1}{2}\rho V^2 c$	Moment Coefficient $M/\frac{1}{2}\rho V^2 c^2$
Flat	$-\alpha_1 x$	$-2\alpha_1\sqrt{(c-x)/x}$	$2\pi\alpha_1$	$\frac{1}{2}\pi\alpha_1$
Parabolic	$-\alpha_2 x^2/c$	$-4\alpha_2\sqrt{(c-x)/x}(1/2+x/c)$	$3\pi\alpha_2$	$\pi\alpha_2$
Cubic	$-\alpha_3 x^3/c^2$	$-6\alpha_3\sqrt{(c-x)/x}(3/8+x/2c+x^2/c^2)$	$\frac{15}{4}\pi\alpha_3$	$\frac{45}{32}\pi\alpha_3$

Examination of this table shows that the vorticity is zero at the trailing edge ($x = c$) in each of these cases. The foils contain a square-root singularity at the leading edge ($x = 0$), where the theory breaks down. This breakdown affects the validity of the results in that region, but has only a small effect on the lift and moment which are shown in the last two columns of Table 3.3. Furthermore, it is customary to design foils so that the vorticity does not become unbounded (according to the linear theory) at the leading edge. This is achieved by appropriate combinations of the elementary profiles, by employing a judicious choice of the constants α_1 , α_2 , α_3 , etc.

This desired situation is referred to as the shock-free condition, because the front stagnation point is at the leading edge, and the resulting flow is smooth.

The lift and moment coefficients on such a composite foil will be given by

$$C_L = C_{L_1} + C_{L_2} + C_{L_3} + \cdots \quad , \tag{3.17}$$

and $$C_M = C_{M_1} + C_{M_2} + C_{M_3} + \cdots \quad , \tag{3.18}$$

and the center of pressure is given by

$$\bar{x}/c = C_L/C_M \quad . \tag{3.19}$$

In concluding this section on thin-foil theory, it can be observed from (3.17) that a straight line will result from plotting the lift coefficient against the angle of attack α. Thus, we may write

$$dC_L/d\alpha = 2\pi \quad . \tag{3.20}$$

On the other hand, the exact (that is, nonlinear) inviscid-flow result for a flat-plate foil is

$$dC_L/d\alpha = 2\pi \cos \alpha \quad . \tag{3.21}$$

It can therefore be stated that for the usual range of angles of interest (say $\alpha < 10°$), the linear theory is within 2% of the nonlinear theory.

A greater difficulty is caused by the neglect of viscosity. This point is demonstrated in Fig. 3.18, in which it is seen that the lift falls short of the theory by about 22% at an angle of attack of 12° relative to the no-lift condition. A modified theory which makes an allowance for viscosity is seen to produce an improvement in the results. Fig. 3.19 shows the pressure distribution for the same foil. This figure also illustrates how the simple theory overpredicts the circulation, and hence the lift.

3.4 The Influence of the Free Surface

As already mentioned in Sec. 3.1.3, the lift on a foil drops off as it is brought near the free surface. This means that the efficiency of the foil is reduced, and consequently an increased surface area is needed. This problem was examined by Hough and Moran (1969) for two-dimensional foils, within the

From Abbott and von Doenhoff (1959, p. 61)

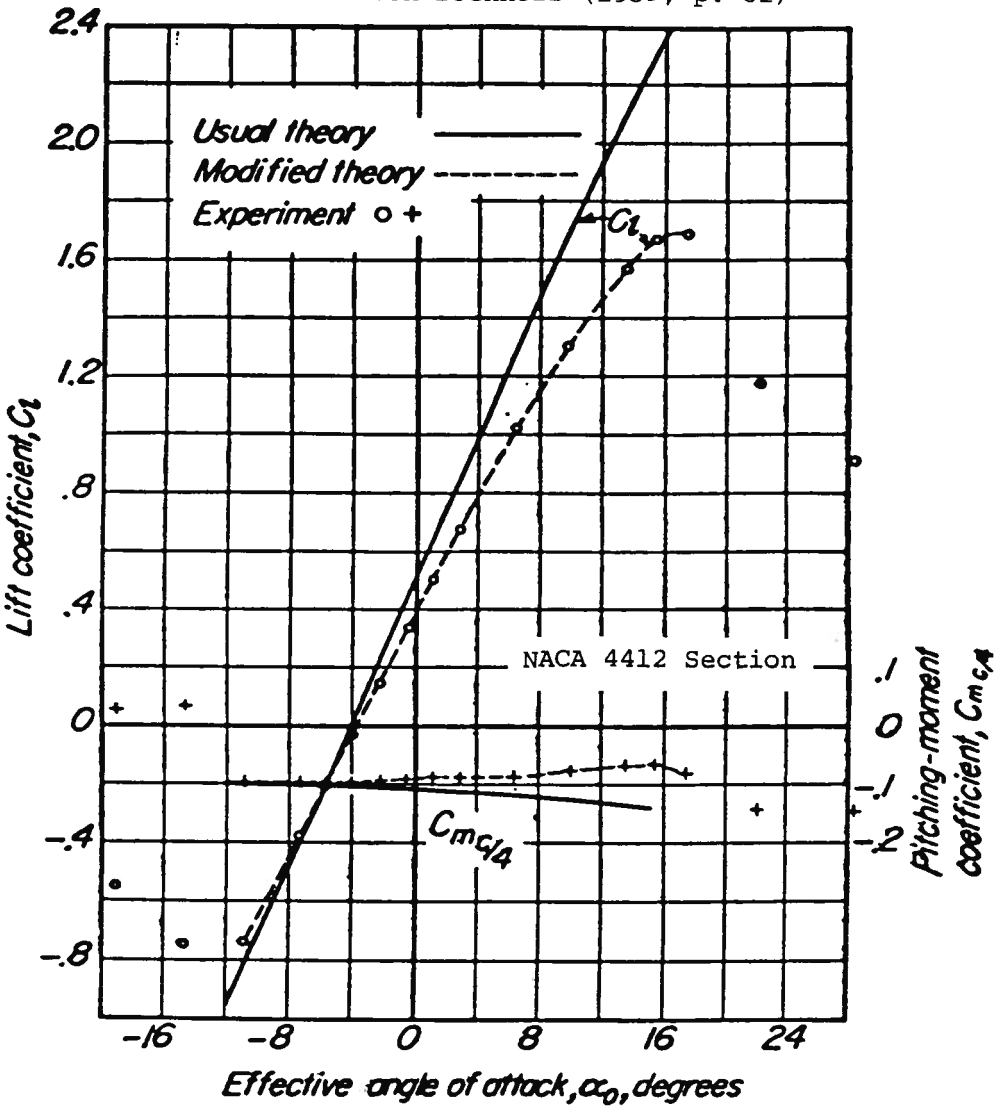

Figure 3.18: Effect of Viscosity on Lift and Moment

From Abbott and von Doenhoff (1959, p. 62)

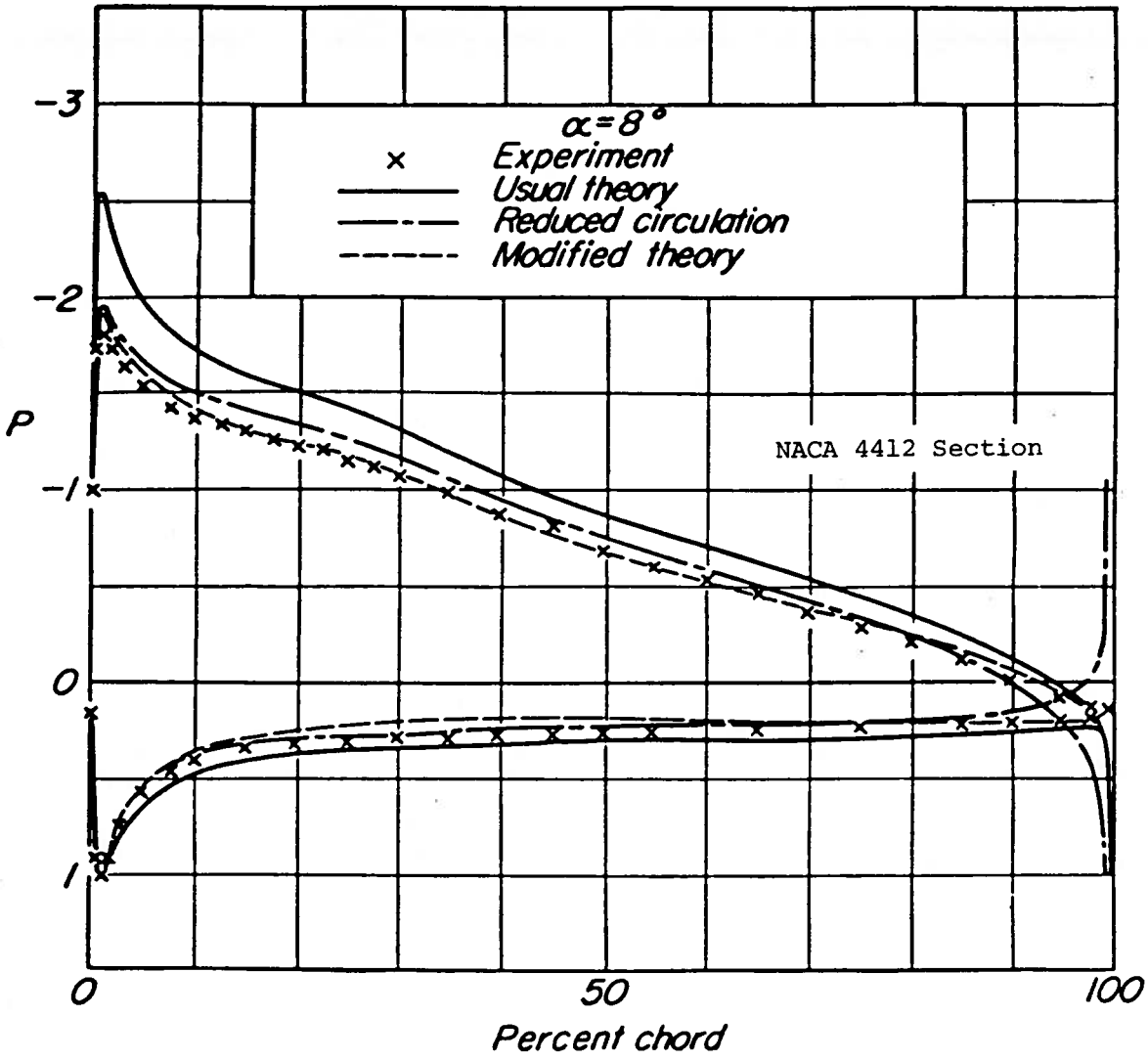

Figure 3.19: Measured and Theoretical Pressure Distributions

framework of linearized theory, already discussed in Sec. 3.3.2. Although expressed in a different manner, their method basically uses equations related to (3.14) and (3.15). These formulas have to be modified because the presence of the free surface alters the simple inverse relationship between tangential velocity and distance as expressed by (3.14).

Results of their work are displayed in Figs 3.20 through 3.22. Three foils are considered. The first is a flat plate at an angle of attack α, corresponding to the first case of Table 3.3. The second foil is a parabolic-arc at zero angle of attack, corresponding to a combination of the first two cases in Table 3.3, with $\alpha_2 = -\alpha_1$. The third foil is a flat horizontal foil with a flap set at an angle of attack. The flap represents the last fraction of the foil given by either E = 0.3 or 0.5, as noted in the figures. In these foils, the lift and moment will be proportional to the angle of attack, or the camber, as the case may be. However this dependence is not immediately apparent in the method of presentation of the data: the lift and moment coefficients are all plotted as a ratio to their values in an unbounded fluid. Figs 3.20 through 3.22 can therefore be conveniently used to apply correction factors to the formulas in Table 3.3.

Turning first to Fig. 3.20, we see that the effect of the free-surface is always to reduce the lifting capacity of the foil -- particularly for lower Froude numbers. It is interesting to note that at an infinite Froude number, the reduction in lift is exactly 50% when the depth of submergence d, approaches zero. Upon examining the effects displayed in Fig. 3.21, it should be noted that in the cruise condition for most hydrofoils, the Froude number (which is based on the chord length) is extremely high, and can often be approximated as being infinite.

The effect on the moment is shown in Fig. 3.22. This figure is mainly of

From Hough and Moran (1969, p. 57)

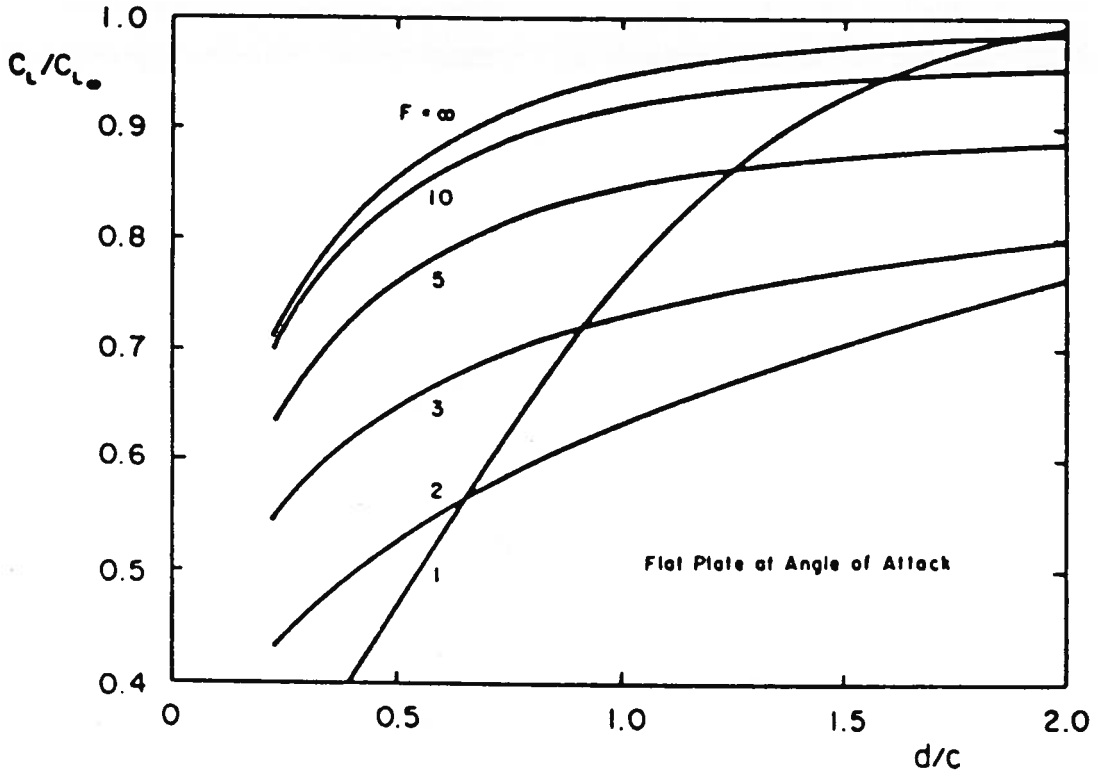

(a) Flat-Plate Foil

From Hough and Moran (1969, p. 56)

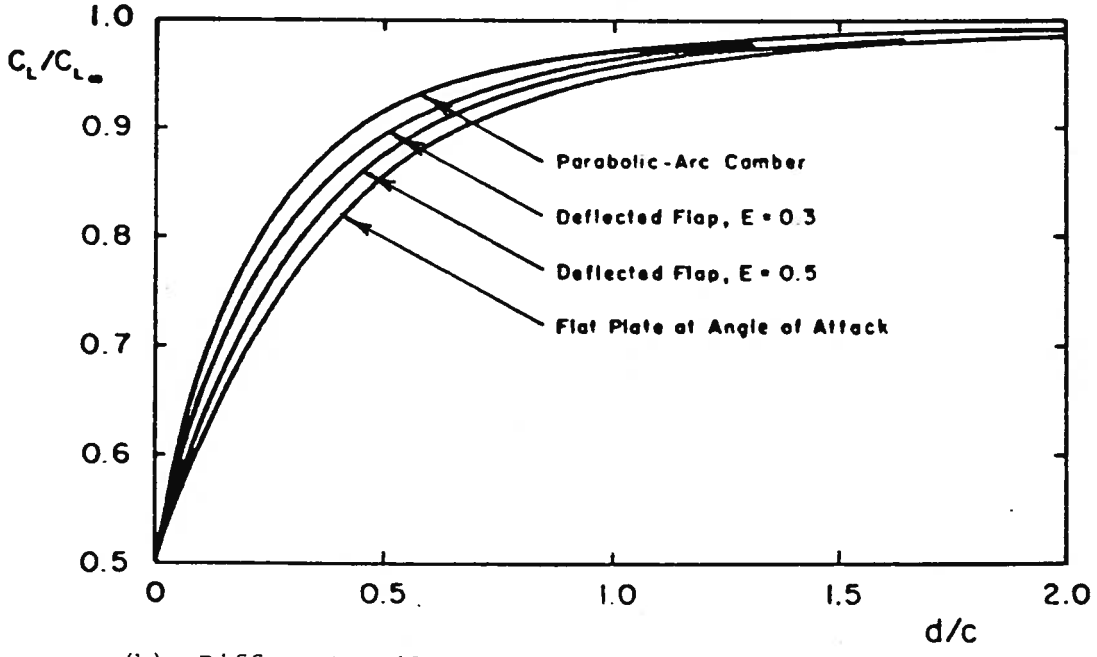

(b) Different Foils at Infinite Froude Number

Figure 3.20: Effect of Submergence on Hydrofoil Lift

From Hough and Moran (1969, p. 57)

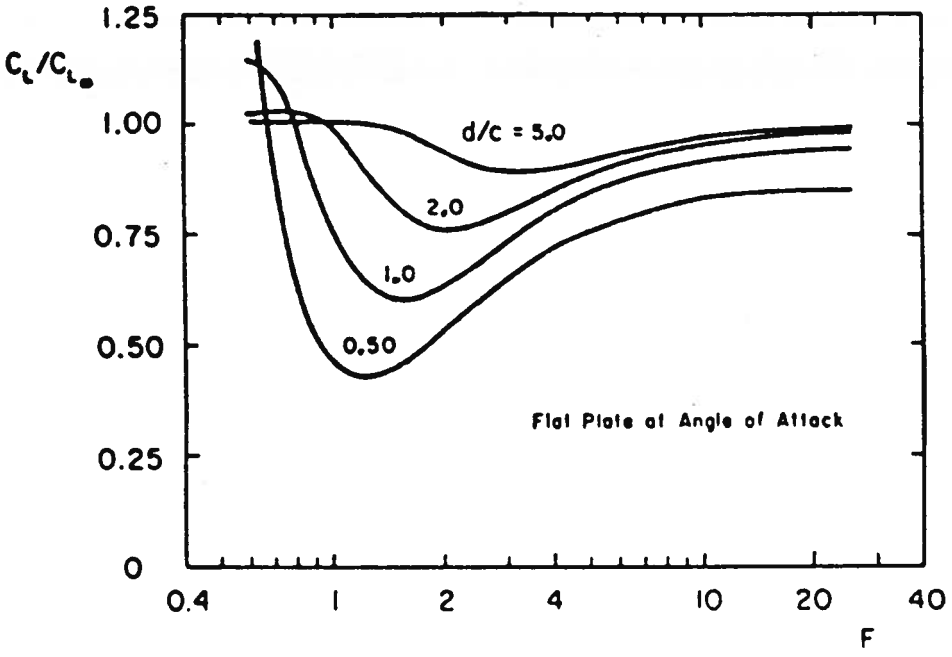

(a) Flat Plate

From Hough and Moran (1969, p. 57)

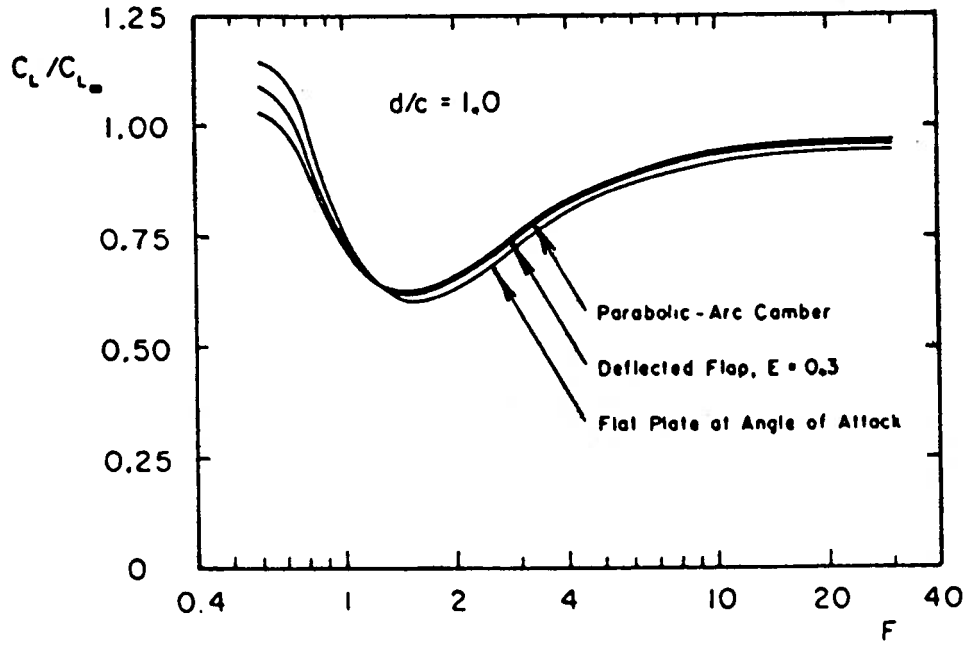

(b) Different Foils

Figure 3.21: Effect of Froude Number on Hydrofoil Lift

From Hough and Moran (1969, p. 58)

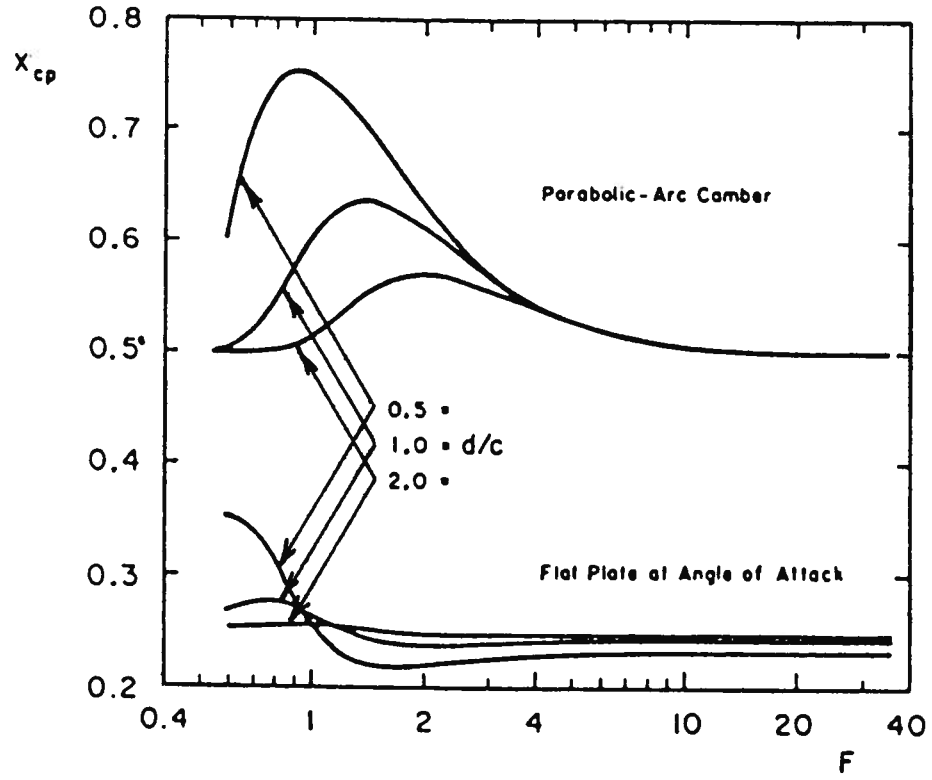

(a) Center of Pressure

From Hough and Moran (1969, p. 59)

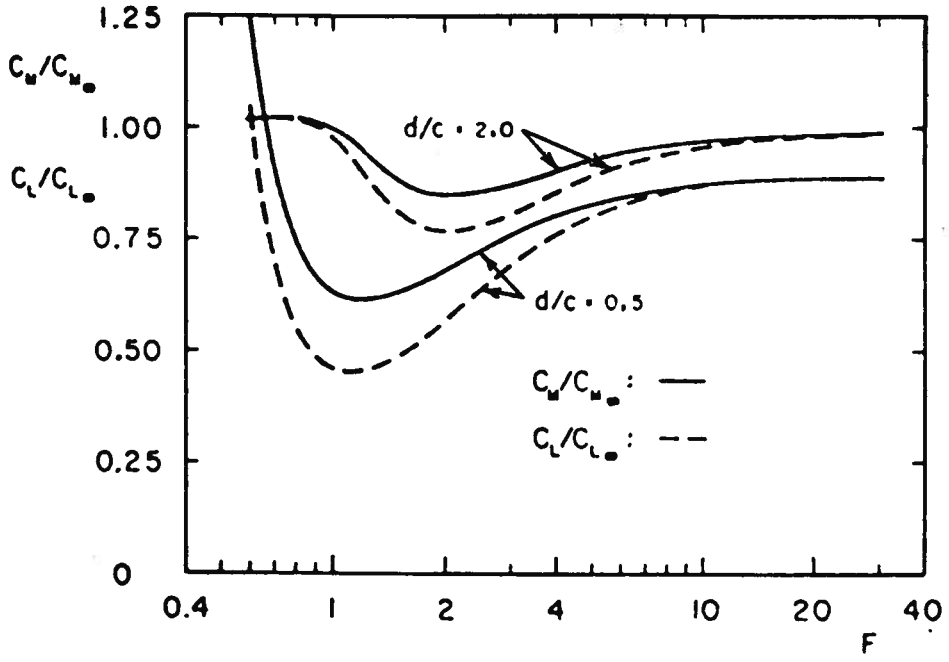

(b) Pitching Moment for Flapped Foil with E = 0.3

Figure 3.22: Effect of Froude Number on Center of Pressure and Pitching Moment

scientific interest, as most of the longitudinal moment on a hydrofoil craft arises from the relative forces on the bow and stern foils, and not from any relatively small absolute shifts in the center of pressure on the individual foils.

The graphical results for lift are also presented numerically in Table 3.4.

Regarding the pressure distribution over the foil surface, and its influence on the inception of cavitation, the method of Hough and Moran cannot be used, except at the shock-free condition. This is because the linearized theory breaks down at the leading edge, as already mentioned in Sec. 3.3.3. A method proposed by Giesing and Smith (1967) overcomes this difficulty by satisfying the kinematic condition on the foil surface exactly. This technique is an extension of the method used to generate Fig. 3.14 to include the free-surface effect. (In the same way, the method of Hough and Moran was an extension of the linearized theory to include the influence of the free surface.)

Examples of computed pressure distributions on a foil near a free surface are presented in Fig. 3.23. It is seen that the measured form of the pressure is correctly predicted. However, the pressures are generally high by about 18%. The main cause of this discrepancy is viscosity, which also affects the lift performance of an airfoil without a free surface. This point was referred to already in Sec. 3.3.3, and was shown in Figs. 3.18 and 3.19. The theoretical pressure distribution can be brought into line with the experimental one by reducing the angle of attack in order to give the same lift coefficient. Further confirmation of the method of Giesing and Smith is provided by Fig. 3.24.

From Hough and Moran (1969, p. 58)

F \ d/c	Flat Plate at Angle of Attack			Parabolic-Arc Camber			Deflected Flap $E = 0.3$		
	0.5	1.0	2.0	0.5	1.0	2.0	0.5	1.0	2.0
∞	0.855	0.947	0.985	0.915	0.972	0.992	0.893	0.963	0.990
20	0.851	0.942	0.979	0.911	0.967	0.986	0.890	0.958	0.983
10	0.833	0.918	0.954	0.894	0.944	0.962	0.872	0.934	0.959
7	0.799	0.888	0.928	0.863	0.915	0.937	0.840	0.905	0.933
5	0.760	0.846	0.887	0.820	0.872	0.896	0.799	0.862	0.893
4	0.723	0.802	0.850	0.782	0.830	0.860	0.761	0.820	0.856
3	0.648	0.732	0.799	0.711	0.762	0.810	0.688	0.751	0.806
2.5	0.594	0.685	0.774	0.657	0.716	0.784	0.635	0.704	0.780
2	0.526	0.634	0.764	0.589	0.664	0.771	0.566	0.653	0.768
1.7	0.480	0.610	0.782	0.542	0.637	0.784	0.520	0.627	0.783
1.4	0.442	0.613	0.840	0.494	0.627	0.833	0.476	0.622	0.836
1.2	0.433	0.652	0.911	0.467	0.647	0.894	0.457	0.650	0.901
1	0.466	0.764	0.991	0.453	0.718	0.967	0.462	0.737	0.976
0.8	0.639	0.994	1.029	0.486	0.888	1.010	0.552	0.930	1.017
0.7	0.889	1.109	1.028	0.570	0.995	1.013	0.702	1.040	1.019
0	1.191	1.057	1.015	1.103	1.029	1.008	1.134	1.040	1.012

Table 3.4: Effect of the Free Surface on Hydrofoil Lift

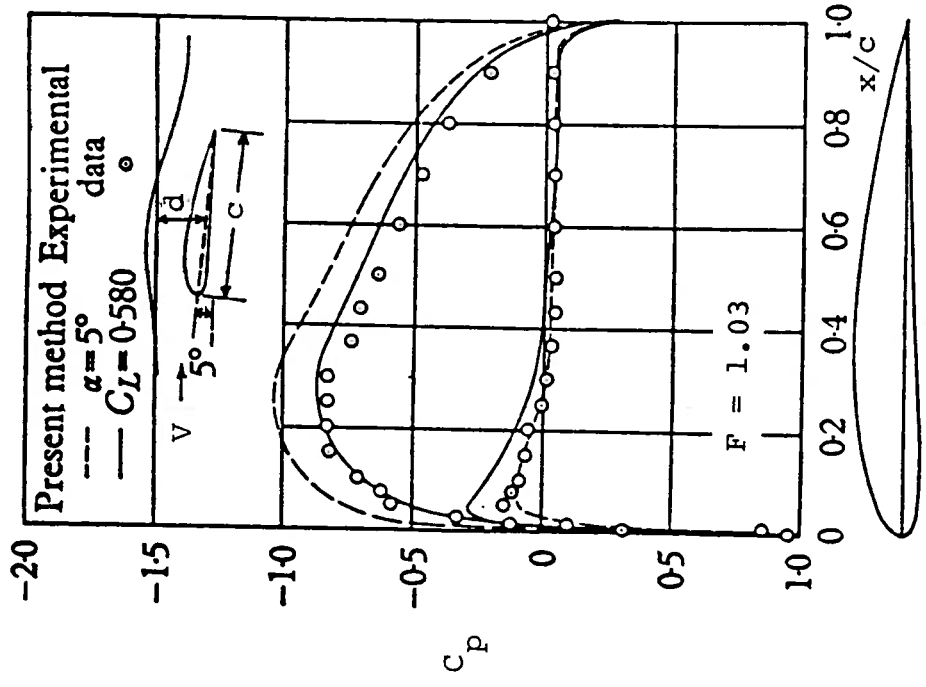

(a) d/c = 0.94 and $\alpha = 5^\circ$ or $C_L = 0.58$

From Giesing and Smith (1967, p. 125)

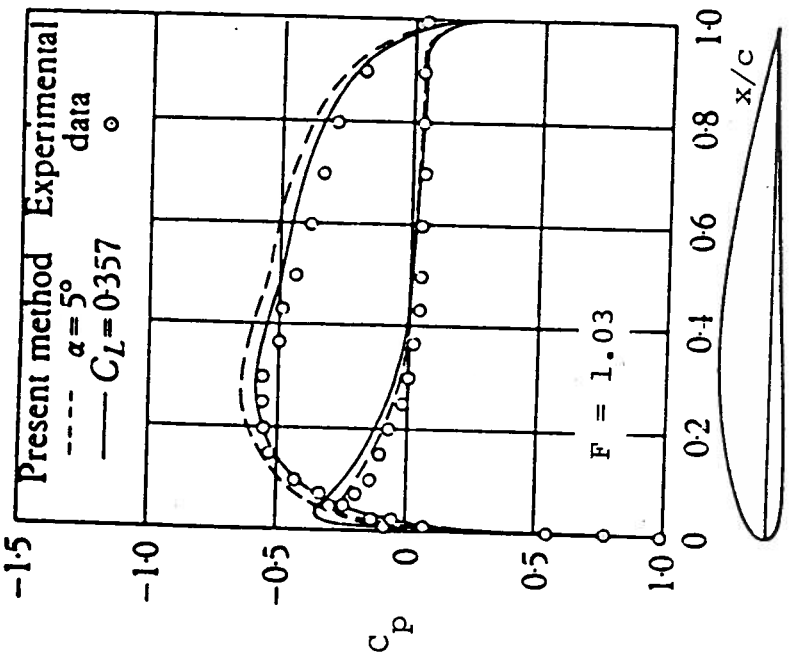

(b) d/c = 0.60 and $\alpha = 5^\circ$ or $C_L = 0.357$

Figure 3.23: Influence of the Free Surface on the Pressure on an NACA 4412 Section

From Giesing and Smith (1967, p. 126)

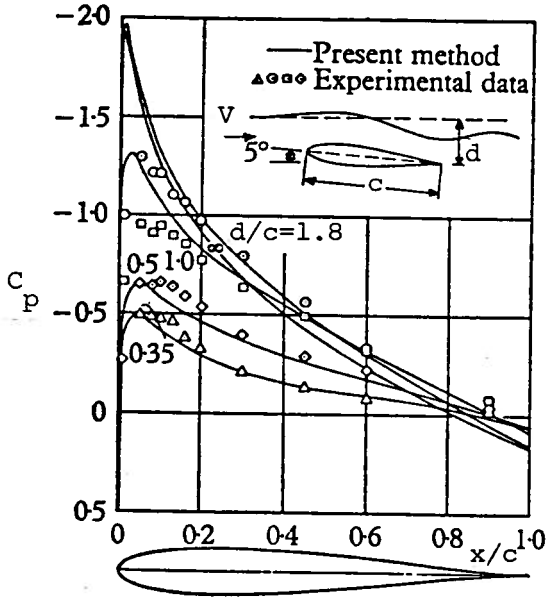

(a) F = 0.95 and $\alpha = 5^o$

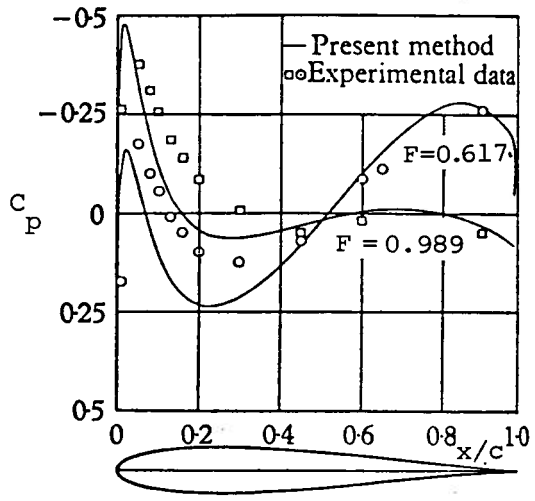

(b) d/c = 0.20 and $\alpha = 5^o$

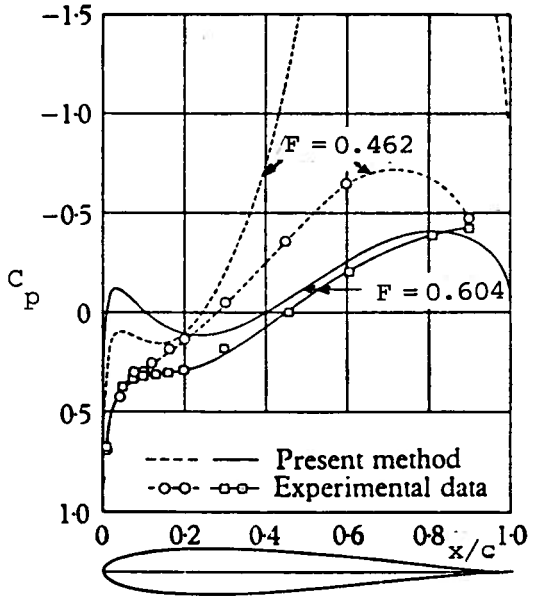

(c) d/c = 0.25 and $\alpha = 5^o$

Figure 3.24: Influence of the Free Surface on the Pressure on a 12%-Thick Joukowski Hydrofoil

3.5 Supercavitating Foils

3.5.1 Introduction

It was mentioned in Sec. 3.1.2 that it becomes necessary to utilize supercavitating sections at high speeds of operation. Such sections provide a more efficient, and stable performance than a section designed for subcavitating operation. Fig. 3.25 shows how a subcavitating section begins to cavitate. The cavitation starts to occur at the point on the surface where the pressure is lowest. The location of this point depends on the angle of attack of the foil, among other things.

Fig. 3.26 illustrates the flow around a supercavitating section. The analysis of this flow is extremely difficult -- even within the restrictions of potential-flow theory. This is because of the cavity-collapse region, which is critical in determining the flow pattern. Obviously, the role of viscosity and turbulence cannot be ignored in this area. However, results of great practical use can be obtained under the assumption of an infinite cavity length -- where the collapse phenomenon does not influence the foil. This corresponds to a zero cavitation number. The cavitation number is defined by

$$\sigma_N = (p_a + \rho g d - p_v)/\frac{1}{2}\rho V^2 \quad . \tag{3.22}$$

Assuming that σ_N is zero would be valid for the case of extremely high speed, or Froude number.

3.5.2 Linearized Solution

A further simplification results from the assumptions of linearized flow. This requires that the angle of attack and camber are both small as in Sec. 3.3.2. This theory was described by Newman (1980, pp 215-220). The performance for three elementary foil shapes is given in Table 3.5.

From Du Cane (1974, p. 45)

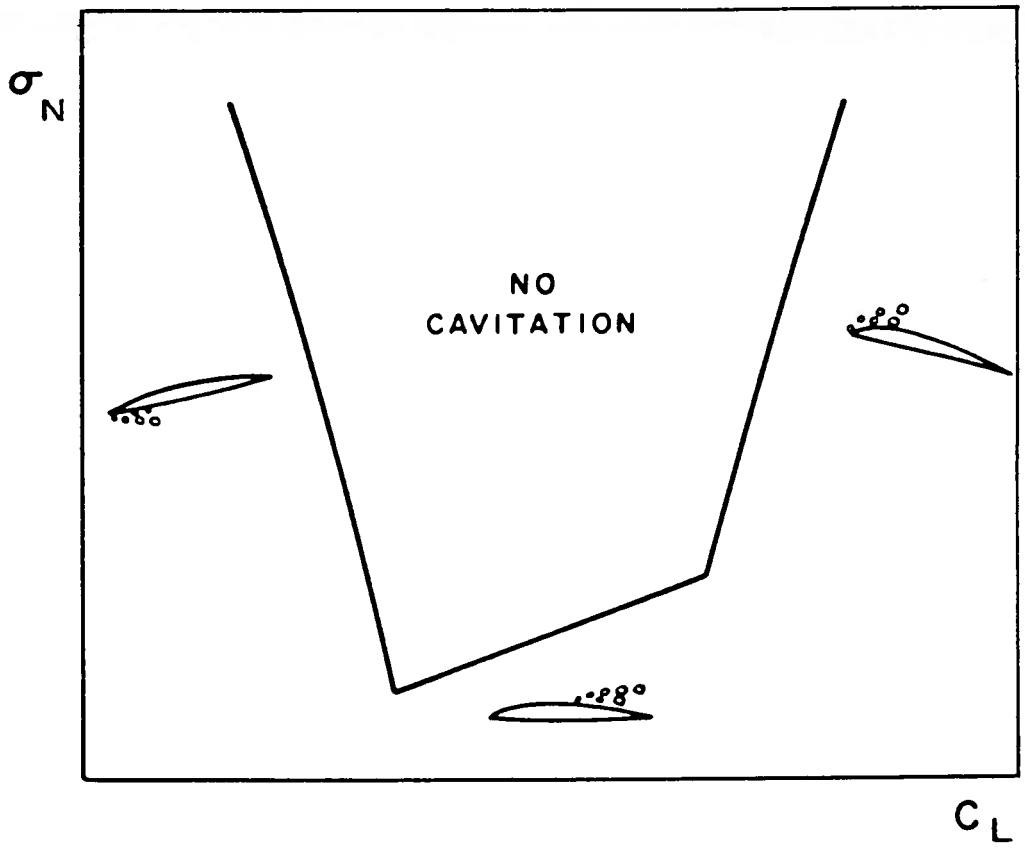

Figure 3.25: Typical Cavitation Bucket Diagram

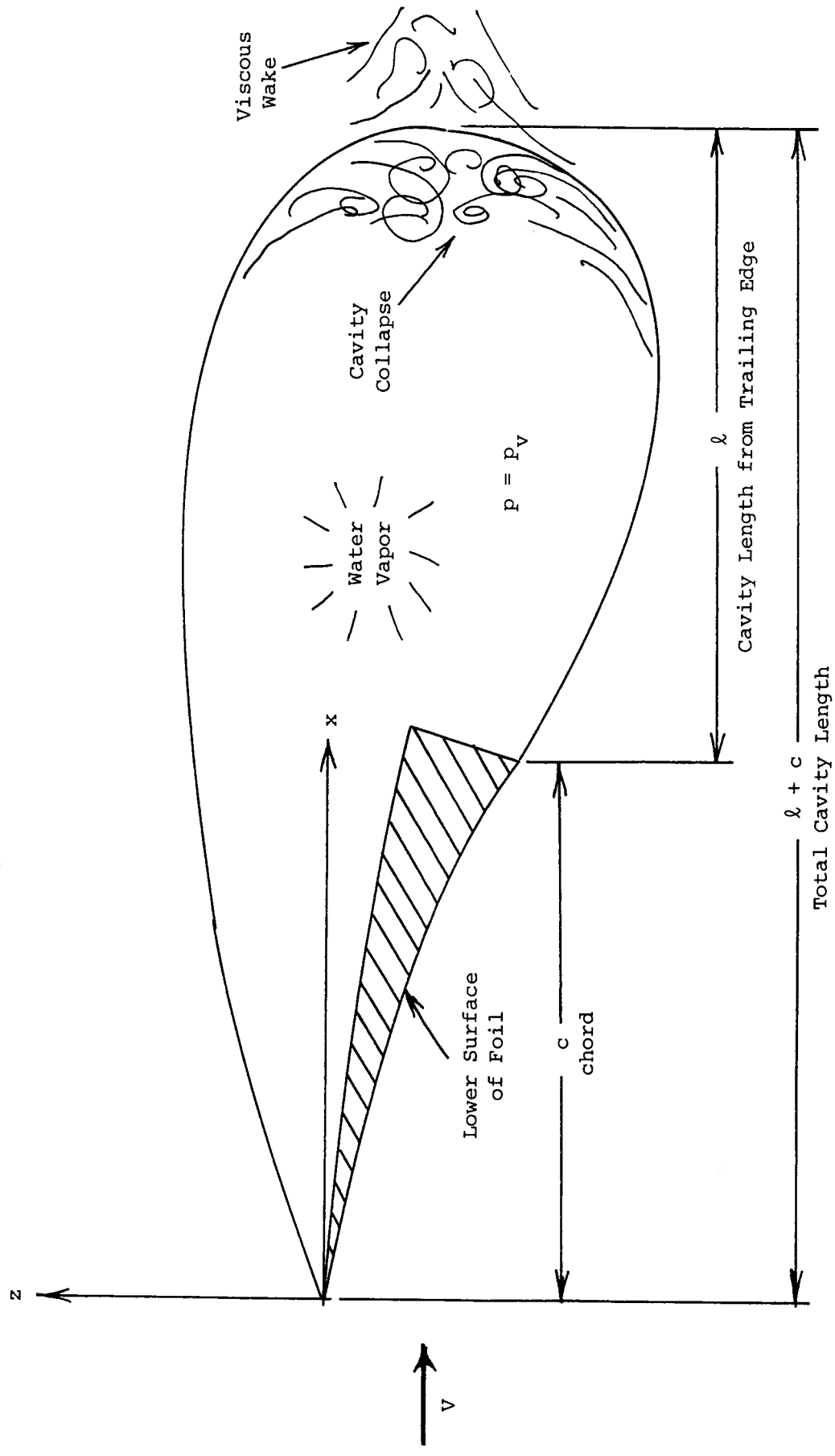

Figure 3.26: The Flow past a Supercavitating Foil

Table 3.5. Elementary Solutions for a Thin Supercavitating Foil

Case	Equation of Lower Surface of Foil $g(x)$	Lift Coefficient $L/\frac{1}{2}\rho V^2 c$	Moment Coefficient $M/\frac{1}{2}\rho V^2 c^2$	Drag Coefficient $D/\frac{1}{2}\rho V^2 c$
Flat	$-\alpha_1 x$	$\frac{1}{2}\pi\alpha_1$	$\frac{5}{32}\pi\alpha_1$	$\frac{1}{2}\pi\alpha_1^2$
Parabolic	$-\alpha_2 x^2/c$	$\frac{15}{16}\pi\alpha_2$	$\frac{25}{64}\pi\alpha_2$	$\frac{25}{32}\pi\alpha_2^2$
Cubic	$-\alpha_3 x^3/c^2$	$\frac{315}{256}\pi\alpha_3$	$\frac{4725}{8192}\pi\alpha_3$	$\frac{35721}{32768}\pi\alpha_3^2$

It is instructional to compare these results with those of Table 3.3 for the corresponding subcavitating foil. That table does not contain a column for the drag, as there is no drag on a two-dimensional fully-wetted foil in inviscid flow. (The horizontal component of the pressure distribution around the foil integrates to zero.) Of course one must add the frictional drag on both sides of the foil for the subcavitating case, and on just one side of the foil in the supercavitating case.

Regarding the lift for the flat plate, it is seen that this is one-quarter of that for the subcavitating case. When one also considers the pressure-drag contribution (in the last column of Table 3.5), it is clear that the supercavitating foil is less efficient.

Just as for the subcavitating foil, we may generate a composite supercavitating foil for the elementary solutions, as noted by Tulin (1964):

$$C_L = C_{L_1} + C_{L_2} + C_{L_3} + \cdots \quad , \tag{3.23}$$

$$C_M = C_{M_1} + C_{M_2} + C_{M_3} + \cdots \quad , \tag{3.24}$$

$$\bar{x}/c = C_L/C_M \quad , \tag{3.25}$$

and $$C_D = \left[(C_{D_1})^{1/2} + (C_{D_2})^{1/2} + (C_{D_3})^{1/2} + \ldots\right]^2 \quad . \tag{3.26}$$

In the last formula, the sign of the square roots is that of the corresponding value of the coefficient α in Table 3.5. That the section drag coefficients in (3.26) are not simply additive should be clear from the fact that while we can obviously add the elementary pressure distributions to give (3.23) and (3.24), the horizontal components of these are affected by the foil profile.

3.5.3 The Influence of the Free Surface

One would anticipate that the proximity of the water surface must affect the lift and drag characteristics of a supercavitating foil just as the behavior of subcavitating foils is altered. This problem has been examined by Doctors (1984). The angle of attack and curvature of the foil were considered to be small so that a linearized approach to the solution could be made. As a result of the linearizing process, many of the quantities of interest are proportional to the angle of attack α (the same is true even for a cambered foil, if the camber is proportional to α). Such quantities include the upper and lower elevations of the cavity y_U and y_L, seen in Figs 3.27 and 3.28, the lift coefficient C_L in Figs 3.29(a) and 3.30(a), and the cavitation number σ_N in Figs 3.29(b) and 3.30(c). The latter was defined in (3.22). The drag coefficient C_D, on the other hand, is proportional to α^2, as noted in Figs 3.29(a) and 3.30(b).

Figs 3.27 and 3.28 illustrate the rather strong influence of the Froude number and depth of submergence on the cavity shape, which can suffer large distortions, as the free surface is approached.

In order to use this data one must first compute the reduced cavitation number σ_N/α, using (3.22). This assumes that the required depth of opera-

From Doctors (1984, p. 37)

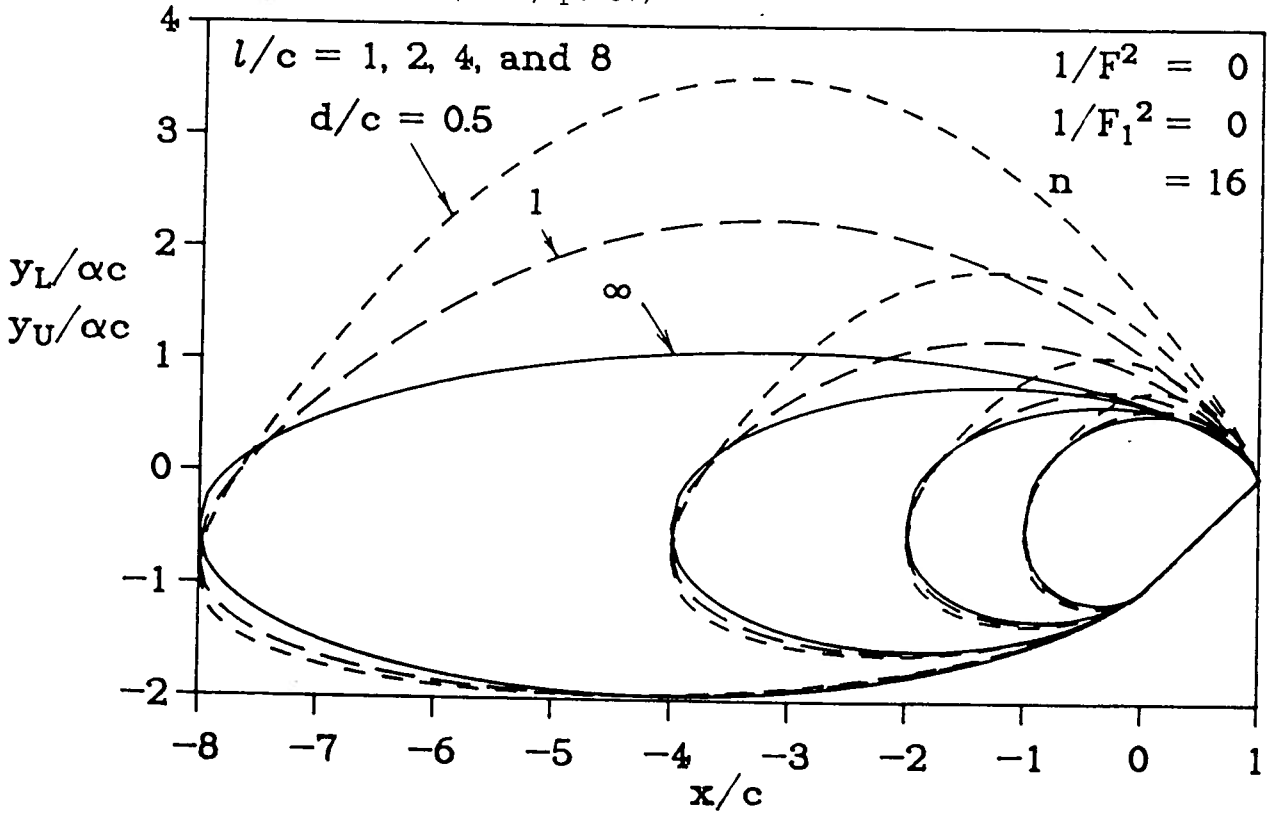

(a) Infinite Froude Number

From Doctors (1984, p. 38)

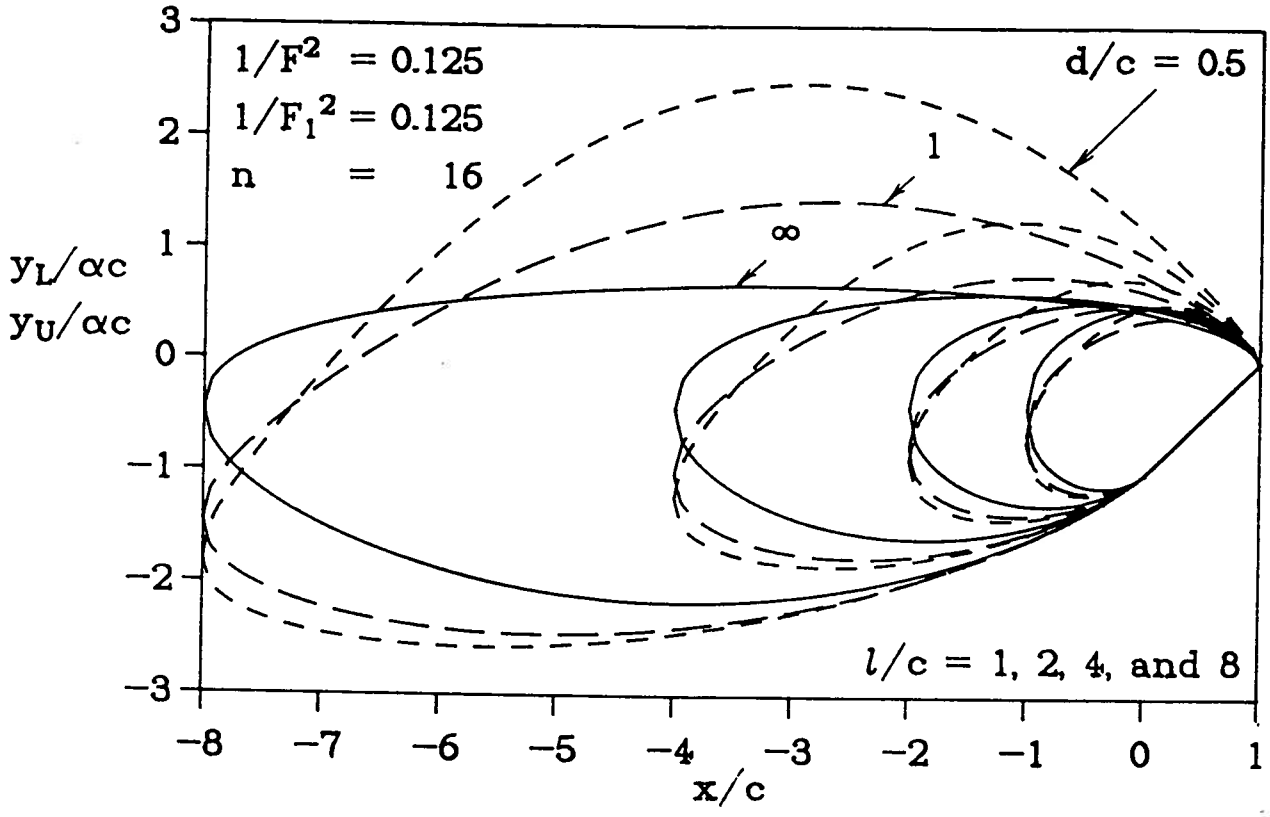

(b) Finite Froude Number

Figure 3.27: Cavity Shapes for a Flat Supercavitating Foil

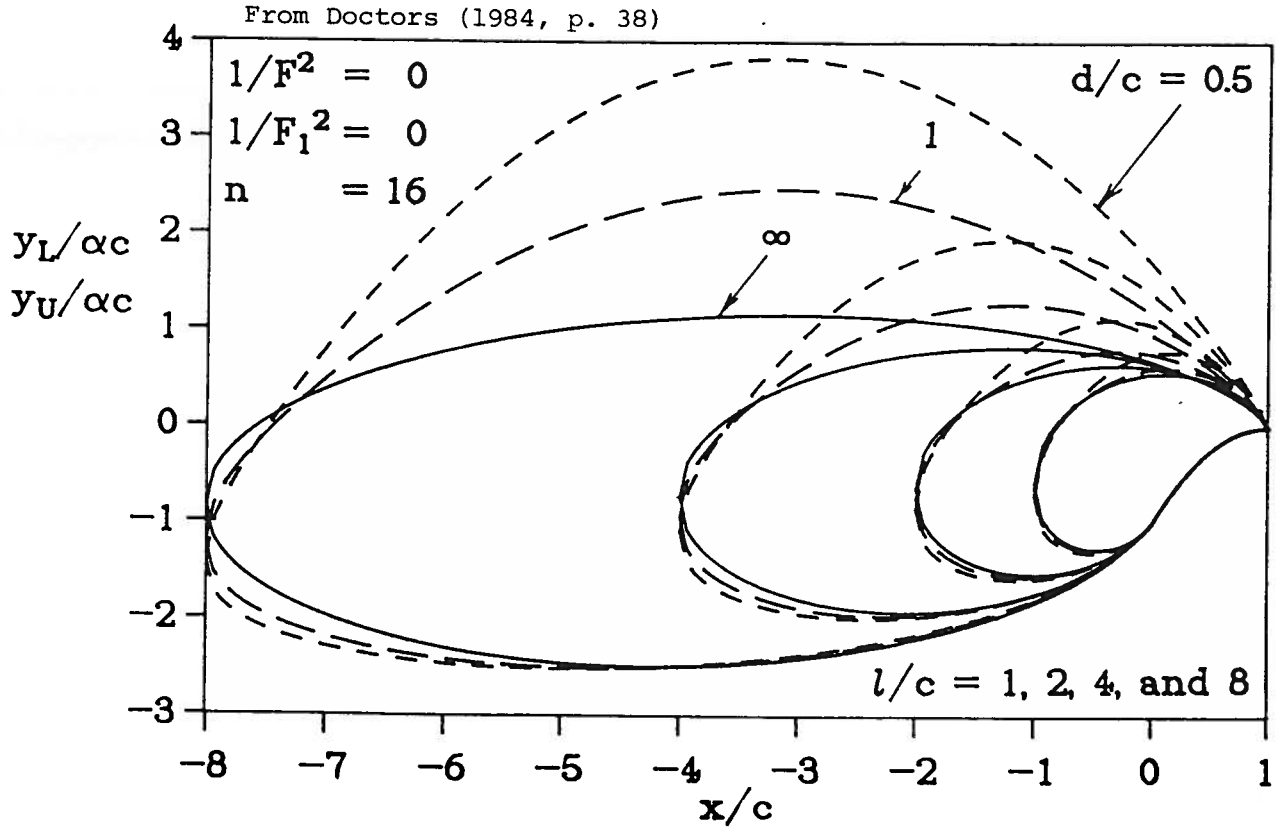

(a) Infinite Froude Number

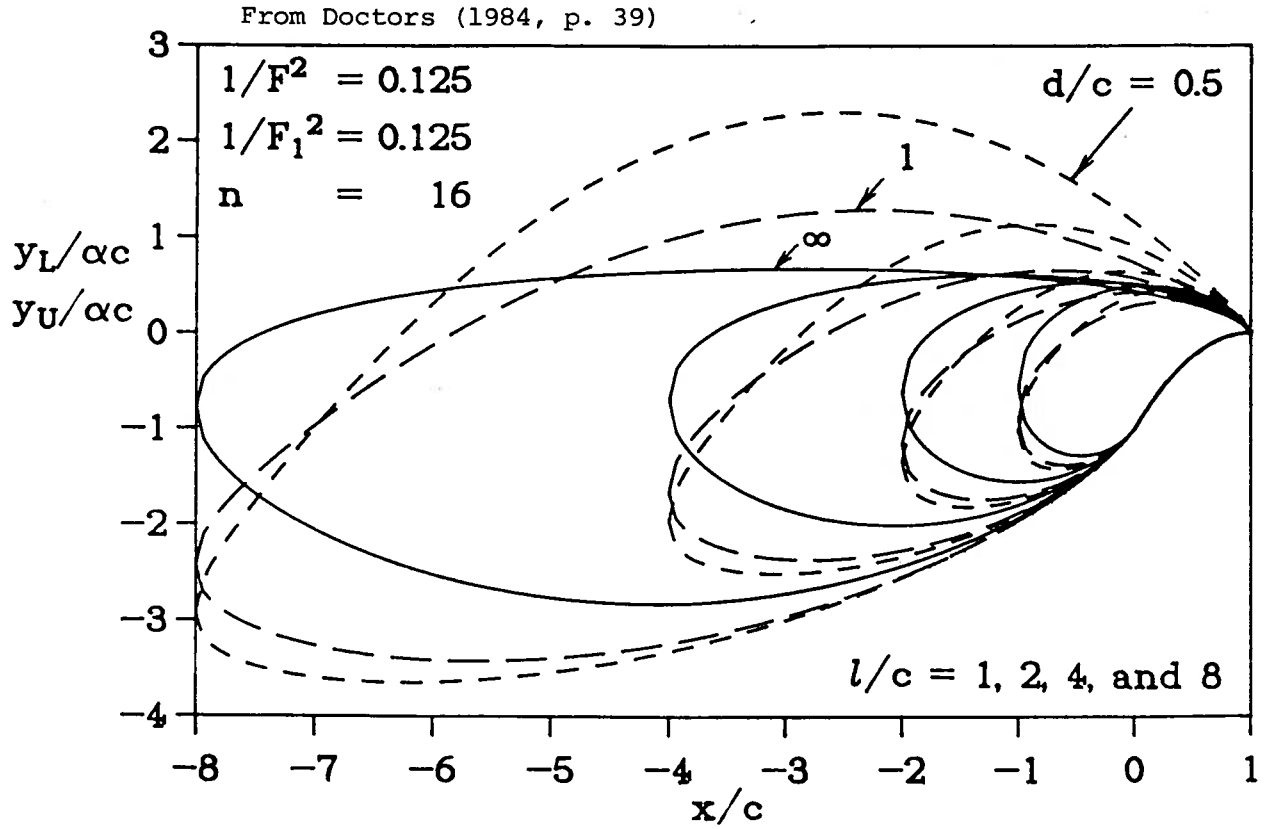

(b) Finite Froude Number

Figure 3.28: Cavity Shapes for a Parabolic Supercavitating Foil

From Doctors (1984, p. 39)

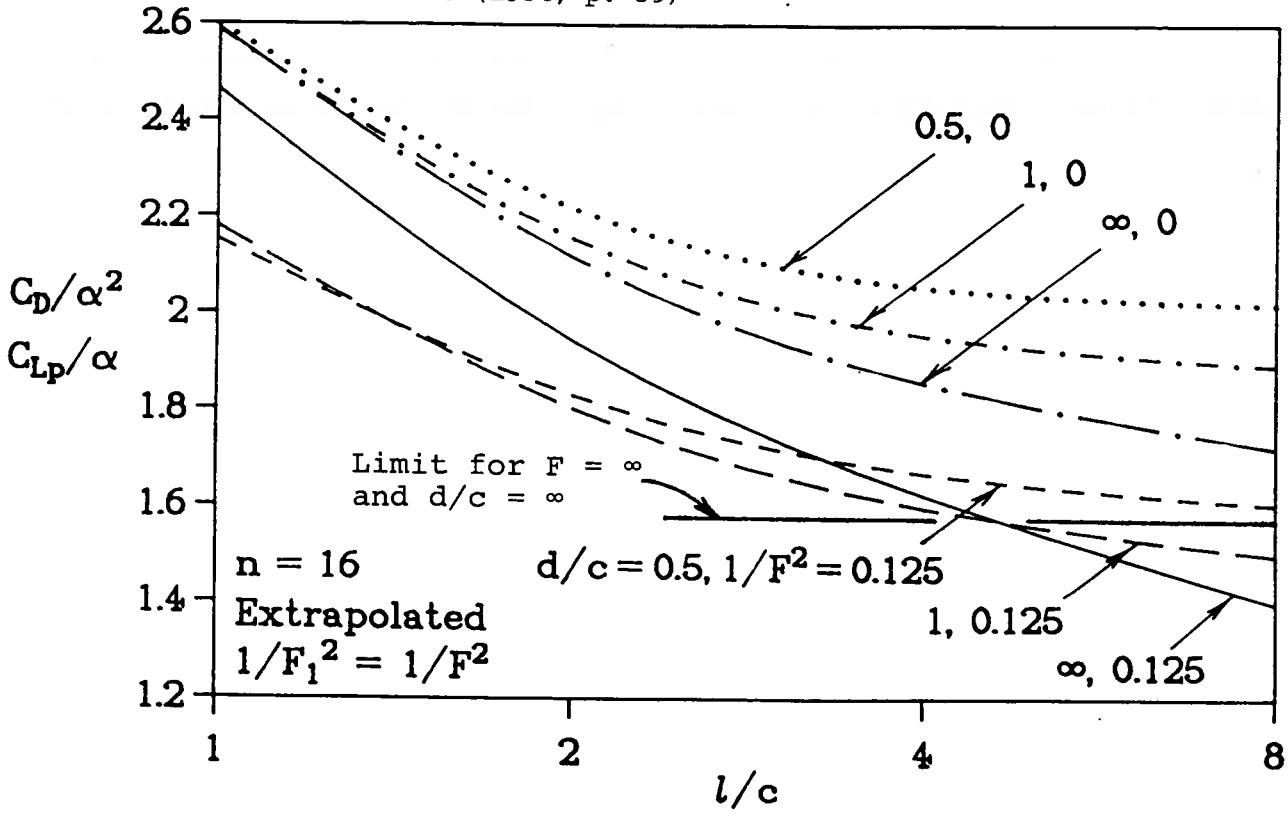

(a) Lift and Drag Coefficients

From Doctors (1984, p. 40)

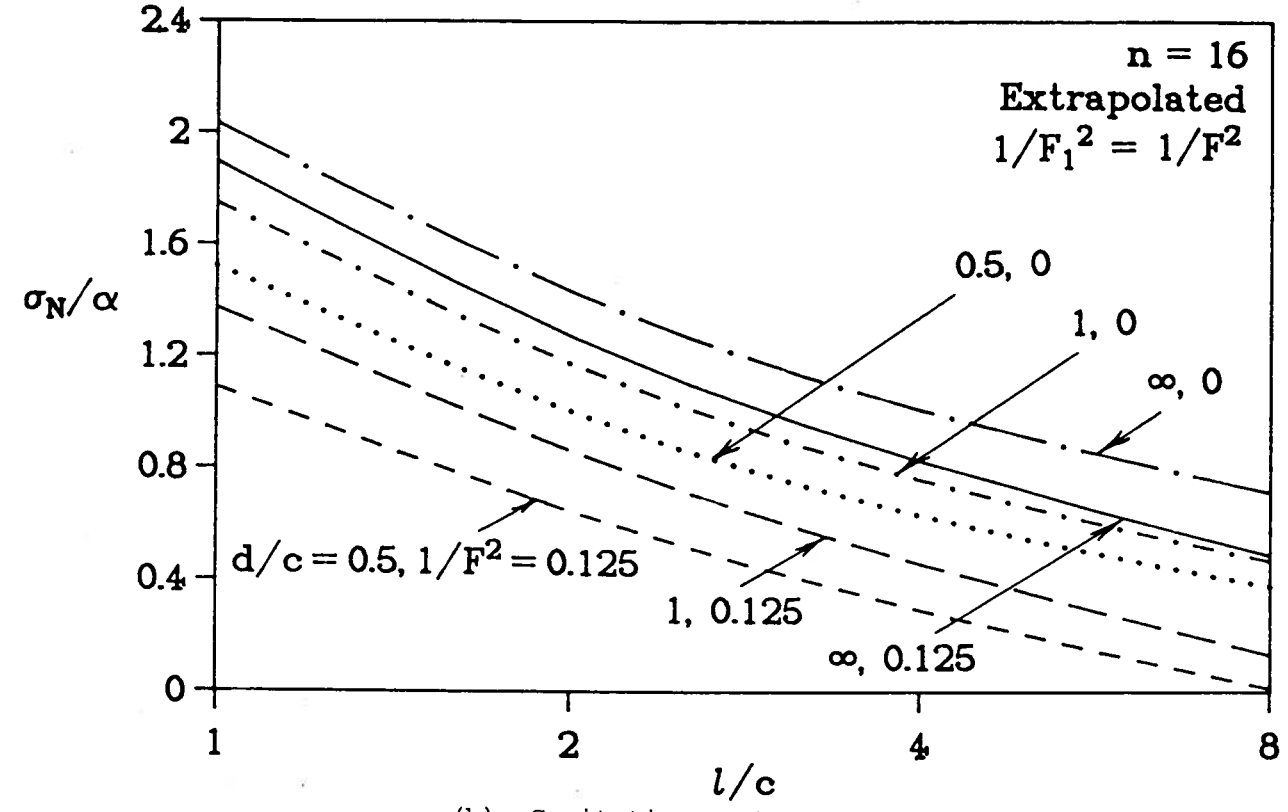

(b) Cavitation Number

Figure 3.29: Performance of a Flat Supercavitating Foil

From Doctors (1984, p. 40)

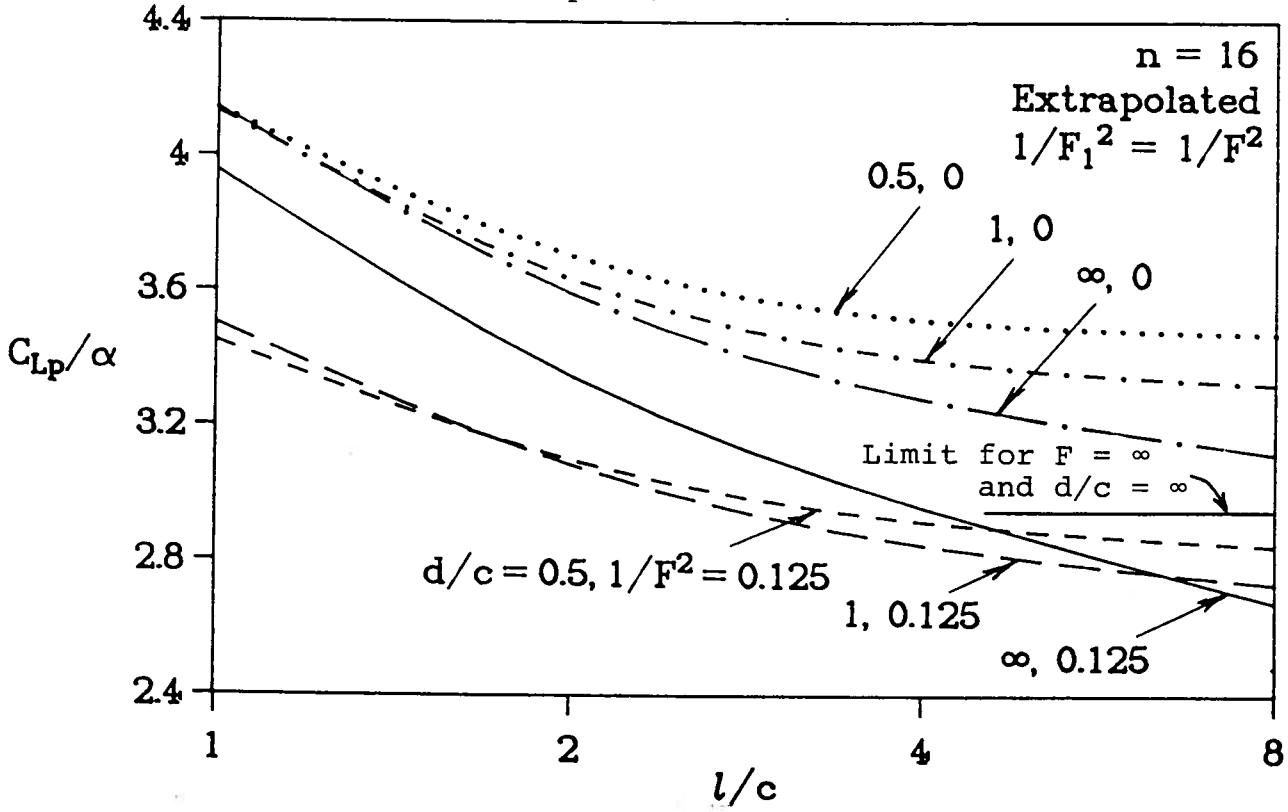

(a) Lift Coefficient

From Doctors (1984, p. 41)

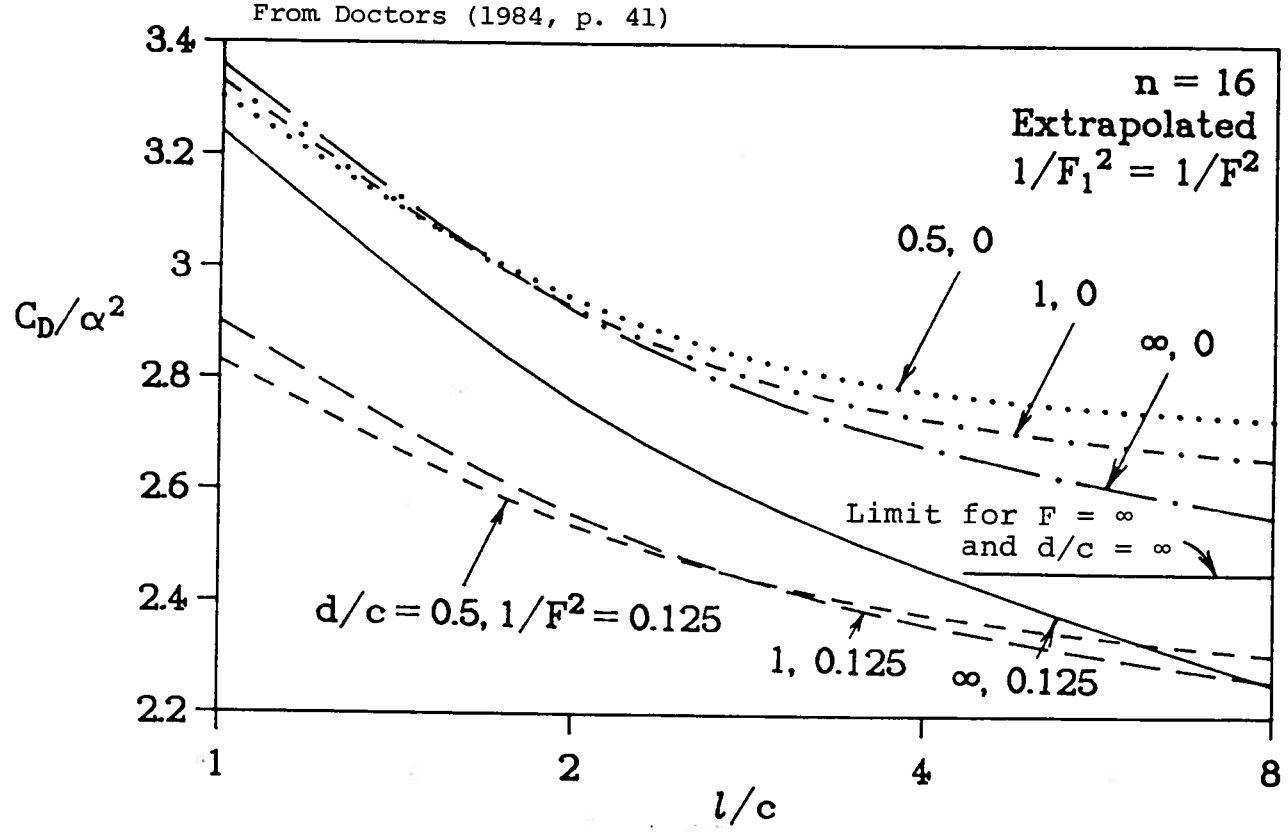

(b) Drag Coefficient

Figure 3.30: Performance of a Parabolic Supercavitating Foil

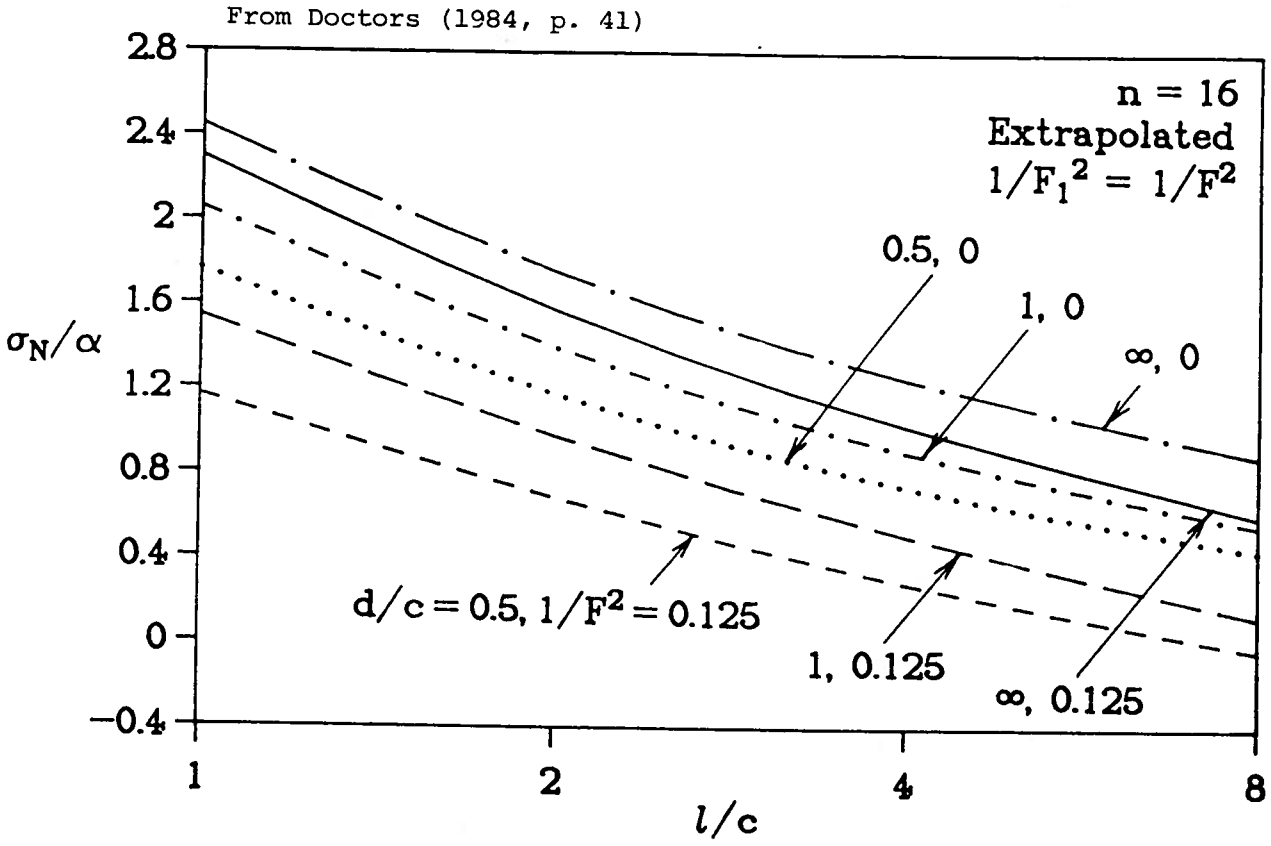

(c) Cavitation Number

Figure 3.30: (Continued)

tion d, and the angle of attack α have been chosen. The cavity length ℓ is then obtained using Fig. 3.29(b) for the flat foil, or Fig. 3.30(c) for the parabolic foil.

The second stage is to use the cavity length to find the lift and drag coefficients from Fig. 3.29(a) for the flat foil, or Figs 3.29(a) and (b) for the parabolic foil.

It should be noted that the superposition laws for lift and moment given by (3.23) through (3.25) hold for the present case (where the cavity length is finite and the influence of the free surface is included). In the same manner, the cavitation number can be constructed from a linear combination of the contributions from elementary foils. Unfortunately, the law for combining the contributions to the drag coefficient (3.26) does not apply here, being somewhat more complicated in the present case.

Finally, it may be noted that the limiting values of the lift and drag coefficient for infinite values of the Froude number, depth-to-chord ratio, and cavity-length-to-chord ratio have been indicated on Figs 3.29(a), 3.30(a), and 3.30(b). These were obtained from Table 3.5.

3.6 Three-Dimensional Effects

3.6.1 Subcavitating Foils

We consider here the problem of extending the results of Sec. 3.3.2 for a thin two-dimensional foil to the three-dimensional case. Such a foil can be represented by a vortex pattern as shown in Fig. 3.31. The vortex pattern effectively consists of a line of bound vortices on the wing and a distribution of trailing, or free, vortices behind the wing. This is referred to as the lifting-line model.

Details of this theory can be found in Abbott and von Doenhoff (1959),

From Abbott and von Doenhoff
(1958, p. 9)

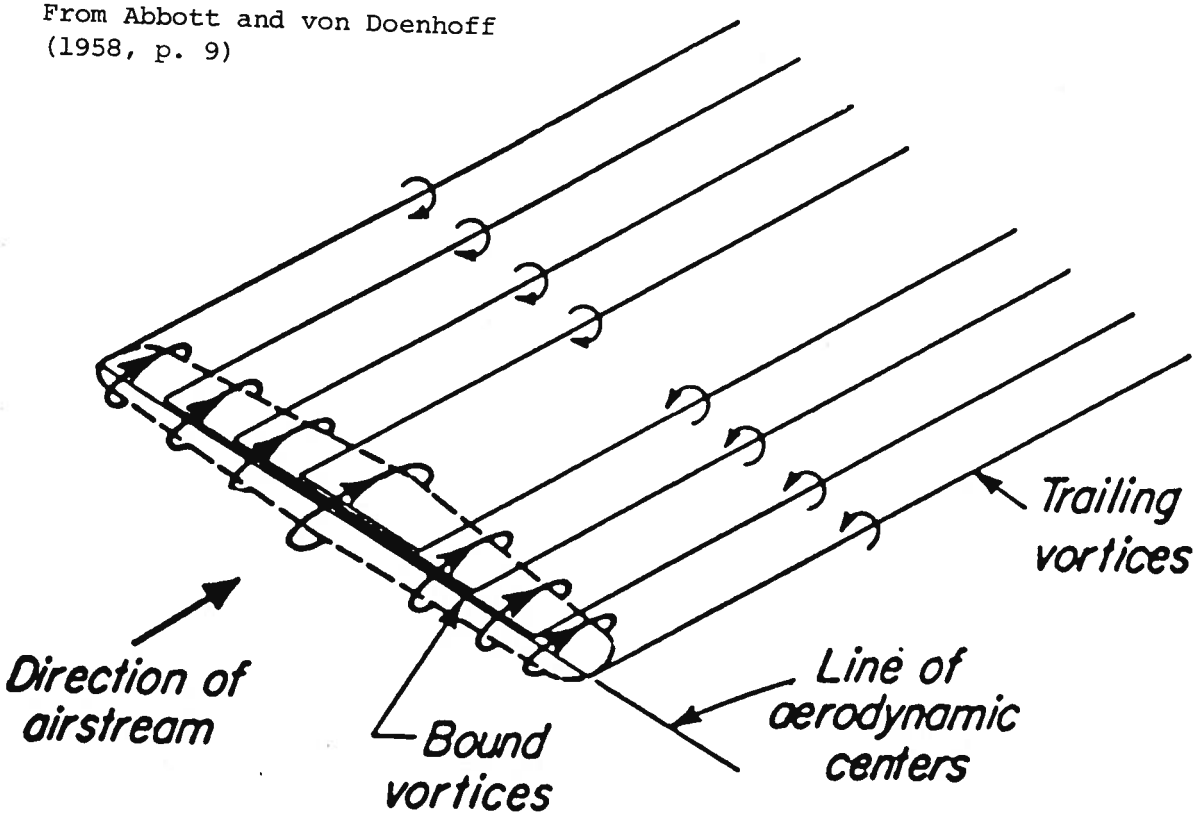

Figure 3.31: Vortex Pattern Representing a Lifting Wing

Glauert (1944, pp 137-155), and in Parsons (1980, pp 123-142). While lifting-line theory can be applied to a wing with arbitrary spanwise loading, particularly simple results are obtained if it is assumed that the loading varies from zero at one tip to a maximum in the center and back to zero at the other tip in an elliptic fashion.

For the elliptic load distribution, the vortices shown in Fig. 3.31 induce a constant downwash velocity over the span of the wing, resulting in a spanwise-constant induced angle-of-attack correction, given by

$$\alpha_I = - C_L/\pi A \quad , \tag{3.27}$$

where C_L is the three-dimensional lift coefficient, and A is the aspect ratio of this wing. Now, the force generated by the wing acts normal to the resulting flow (not the free-stream in this case). Thus, as a result of the induced downwash, a three-dimensional wing has a drag (even in inviscid flow) -- in contrast to the case of two dimensions. We may now write for the lift coefficient:

$$C_L = 2\pi\alpha_0 = 2\pi(\alpha - \alpha_{L0} + \alpha_I) \quad , \tag{3.28}$$

where α_0 is the effective angle of attack in three-dimensions, α is the actual angle of attack measured from the chord line as usual, and α_{L0} is the angle of attack at which there is no lift (usually negative).

We can combine the above results to give

$$C_L = m(\alpha - \alpha_{L0}) = 2\pi A(\alpha - \alpha_{L0})/(A + 2) \quad . \tag{3.29}$$

This equation shows that the lift-curve slope, namely $dC_L/d\alpha = m$, is less than the ideal two-dimensional result of 2π, but it approaches that value as the aspect ratio becomes large.

This formula is plotted in Fig. 3.32, together with other theories and some numerical results based on lifting-surface theory. This theory assumes a distribution of vortices over the wing surface rather than simply using a con-

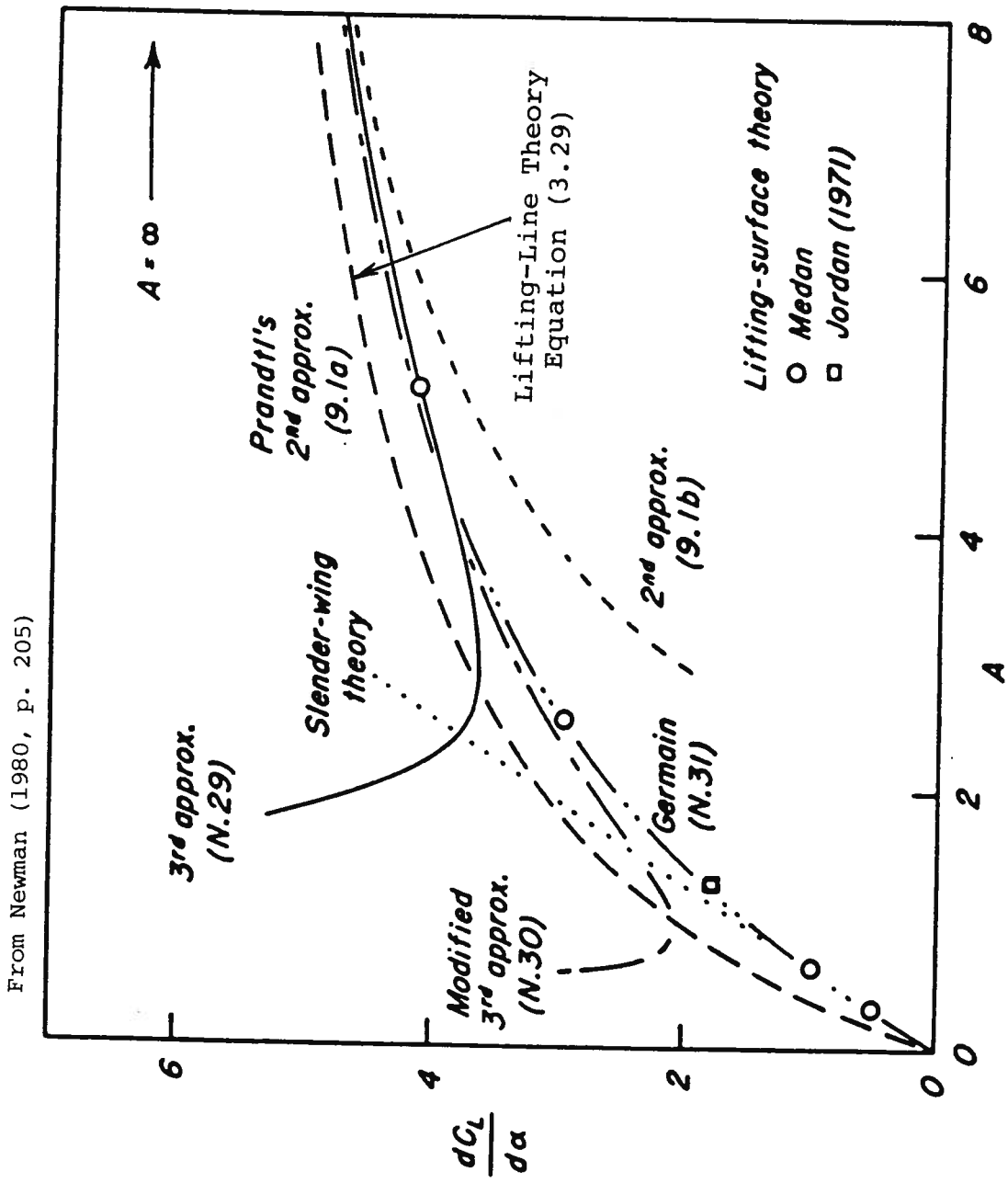

Figure 3.32: The Lift-Curve Slope of an Elliptic Wing

centrated bound vortex. The lifting-line theory becomes progressively better as the aspect ratio is increased.

In some cases, the two-dimensional lift-curve slope is given by m_0, that is, different from the ideal value of 2π for an inviscid flow without a free surface. (See Fig. 3.18, for example.) Then (3.28) has to be adjusted, and consequently (3.29) becomes:

$$m = m_0/(1 + m_0/\pi A) \quad . \tag{3.30}$$

3.6.2 Non-Elliptic Loadings

As noted above, computations for other loading cases can be made by the lifting-line method. A common example, of interest to hydrofoil designers, is the rectangular-planform wing. Details of this case can be found in Glauert (p. 150). A comparison of the efficiency of a rectangular wing to an elliptic one is given in Table 3.6. It can be seen that although the elliptic distribution is known to be the most efficient (because of the uniform induced downwash), other practical shapes are not markedly inferior to it.

Table 3.6. Comparison of Rectangular to Elliptic Load Distributions

Aspect Ratio	2	4	6	8	10	∞
$\frac{C_{L,\text{Rectangular}}}{C_{L,\text{Elliptic}}}$	0.968	0.967	0.966	0.964	0.962	1

3.6.3 Combined Influence with the Free Surface

The question of the three-dimensional effect in combination with the proximity of the free surface is an important one. It applies to both subcavitating and supercavitating foils. A full investigation of the problem

has been carried out by very few workers, and is beyond the scope of this course. The correct answer must involve, at the minimum, a lifting-line approach in which the vortex whose behavior satisfies the free-surface condition is used.

An expedient solution is to apply the three-dimensional correction factors presented in Sec. 3.6.1 to the relevant two-dimensional data covered in Sec. 3.4 for the subcavitating foil near a free surface, and in Sec. 3.5 for the supercavitating foil near a free surface. The use of correction factors in the latter case would be most justified when the Froude number is infinite (the case of practical interest), as there is no vorticity in the cavity then, and the foil can be accurately represented by a lifting-line.

3.7 Calculation of Foil Resistance

3.7.1 Subcavitating Foils

The drag coefficient of a fully-wetted hydrofoil can be approximately decomposed into a number of contributions as follows:

$$C_D = C_{D_0} + C_{D_I} + C_{D_W} + C_{D_T} \quad , \tag{3.31}$$

in which the terms on the right-hand side are the viscous, induced, wave, and tip-loss drag coefficients, respectively.

The viscous drag is a result of the frictional drag on the foil, together with the pressure drag caused by the lack of complete pressure recovery toward the trailing edge of the foil. This coefficient has been measured for the NACA sections, for example, already discussed in Sec. 3.1.2. If such data is lacking for the section of interest, then one could utilize a suggestion mentioned by Du Cane (1974, p. 34), namely:

$$C_{D_0} = 2C_F(1 + 1.2\ t/c) + 0.11(C_L - C_{L_i})^2 \quad , \tag{3.32}$$

where C_F is the flat-plate friction coefficient, t is the maximum thickness of the foil, and C_{L_i} is the coefficient of lift at the ideal angle of attack, that is, the shock-free condition, already discussed in Sec. 3.3.2.

The first term of (3.32) is seen to include the friction on both sides of the foil, as well as a correction for the effect of thickness. The second term accounts for the lack of pressure recovery -- assumed to be a minimum at the ideal angle of attack. As a test, this equation can be compared with the experimental results of Fig. 3.3.

Regarding the frictional drag, one can consult the information presented by Schlichting (1962), which is reproduced in Fig. 3.33. If we assume that the flow is fully turbulent, then Curve 2 on this figure (the one-seventh power law) may be used in the low-Reynolds-number region:

$$C_F = 0.074\ R^{-1/5} \quad \text{for} \quad 5\times10^5 < R < 10^7 \quad , \tag{3.33}$$

where R is the Reynolds number based on the chord of the foil:

$$R = \rho V c/\mu \quad , \tag{3.34}$$

in which μ is the viscosity of the water. An approximation suitable for a larger range of Reynolds numbers (the logarithmic law) is given by

$$C_F = 0.455/(\log_{10}R)^{2.58} \quad \text{for} \quad 10^5 < R < 10^9 \quad , \tag{3.35}$$

and is referred to as Curve 3 in Fig. 3.33.

The induced drag has already been discussed, and can be calculated as the horizontal component of the "lift" force on the wing. As noted in Sec. 3.6.1, the force acts at an angle α_I to the vertical. Thus, we may write

$$C_{D_I} = C_L|\alpha_I| \quad , \tag{3.36}$$

and using (3.27), we have

$$C_{D_I} = C_L^2/\pi A \quad . \tag{3.37}$$

The next term in (3.31) is the wave resistance. This can be computed by

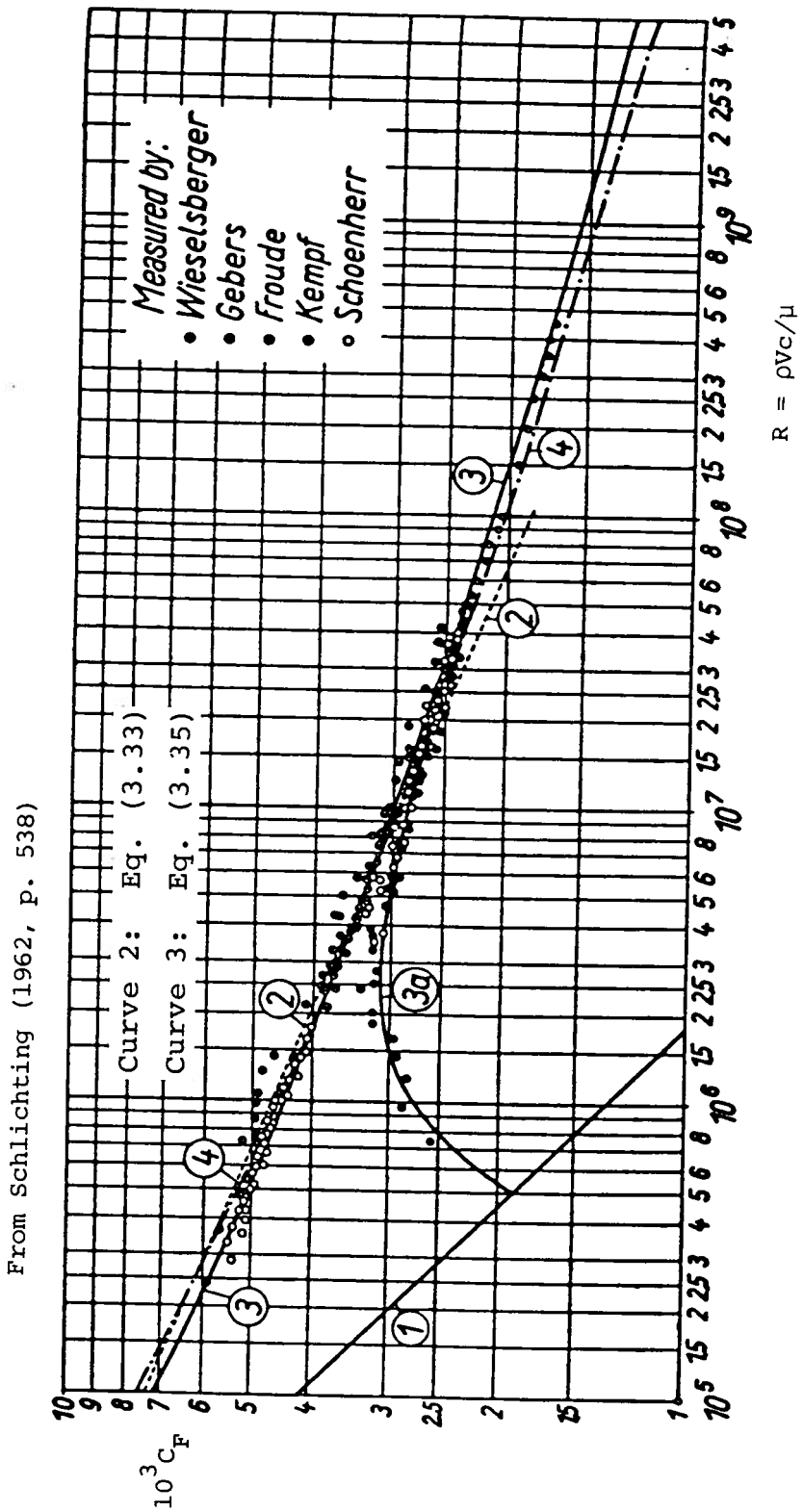

Figure 3.33: The Friction on a Smooth Flat Plate

means of the amplitude of the downstream waves generated by an equivalent lifting line. It can also be calculated on the basis of the induced downwash velocity experienced by the foil. Adopting the second approach, it can be shown (for example, Doctors (1984, Eq. (31)), that the downwash velocity at the foil is given by

$$w_W = k_0 \Gamma \exp(-2k_0 d) \quad , \tag{3.38}$$

where k_0 is the wave number given by

$$k_0 = g/V^2 \quad . \tag{3.39}$$

Now, we have the wave-induced angle of attack:

$$\alpha_W = -w_W/V$$

$$= -\frac{k_0 \Gamma}{V} \exp(-2k_0 d) \quad . \tag{3.40}$$

The circulation can be expressed in terms of the lift by means of (3.12), so that (3.40) becomes

$$\alpha_W = -\frac{k_0 L}{\rho V^2} \exp(-2k_0 d)$$

$$= -\frac{1}{2} k_0 c \, C_L \exp(-2k_0 d) \quad . \tag{3.41}$$

Lastly, the wave resistance is given by a formula similar to (3.36):

$$C_{D_W} = C_L |\alpha_W| \tag{3.42}$$

$$= \frac{1}{2} k_0 c \, C_L^2 \exp(-2k_0 d)$$

$$= \frac{1}{2F^2} C_L^2 \exp(-2d/cF^2) \quad . \tag{3.43}$$

This formula is identical to that given by Du Cane (p. 36, Eq. (8)). An inspection of (3.43) shows that at a high Froude number F (which is based on the foil chord), the wave resistance becomes negligible. This analysis is a

two-dimensional one but should give reasonably accurate results in a typical three-dimensional case.

A detailed discussion of the last term in (3.31) is beyond the scope of these notes. The tip losses result from a number of effects including the finite thickness of the foil at the tips t_{tip}. For the case of zero lift, the contribution from two wing tips to the total drag coefficient might be approximated, as pointed out by Parsons (p. 138), by

$$\begin{aligned} C_{D_T} &= 0.11(t_{tip}/c)^2 \quad \text{for square ends} \quad , \\ &= -\,0.04(t_{tip}/c)^2 \quad \text{for round ends} \quad . \end{aligned} \tag{3.44}$$

The question of tip losses when the wing generates lift is more complicated and will not be discussed here.

3.7.2 Supercavitating Foils

We may write the resistance of a supercavitating foil as

$$C_D = C_{D_0} + C_{D_p} \quad . \tag{3.45}$$

The terms on the right-hand side represent the viscous- and the pressure-drag components, respectively. The wave drag is included in the pressure-drag term, as is the induced drag. The tip losses have been ignored here.

Regarding the viscous drag, this can be estimated as the frictional drag on one side of a flat plate. Thus we write

$$C_{D_0} = C_F \quad , \tag{3.46}$$

where C_F has been approximated by (3.33) and (3.35), and is plotted in Fig. 3.33. In contrast to the subcavitating case, where (3.32) is applicable, there are negligible thickness and pressure-loss effects on the viscous drag in the present case.

The main component of drag on the foil is due to the pressure distribution on the lower (wetted) surface. For the simplest case, we can write

$$C_{D_p} = \alpha C_L \quad \text{for a flat supercavitating foil.} \tag{3.47}$$

For foils with a curved surface, one has to resort to more involved calculations. The results of these are shown in Table 3.5 and are applicable to the case when free-surface and cavity-length effects are ignored. More complete information is presented in Figs. 3.29 and 3.30.

3.8 Calculation of Inception of Cavitation

Assuming one had access to detailed pressure distributions on the foil, such as those shown in Fig. 3.4, then we could rewrite (3.5) as

$$p_v = p_a + \rho g d + (C_{p_1} + C_{p_2})\tfrac{1}{2}\rho V^2 \quad , \tag{3.48}$$

since cavitation would start when $p = p_v$. We have assumed that the foil is set at the ideal angle of attack, and thus $C_{p_3} = 0$. We may rearrange (3.48) using the definition of the cavitation number in (3.22):

$$\sigma_N = -(C_{p_1} + C_{p_2}) \quad . \tag{3.49}$$

Note that both C_{p_1} and C_{p_2} are negative, and that one is interested in their maximum absolute values. (This assumes that these occur at approximately the same place on the surface of the foil.)

Thus, for example, we first select the speed and depth of operation of the foil. The cavitation number is then calculated from (3.22) and substituted into (3.49). This method yields the maximum angle of attack α before cavitation occurs.

If detailed pressure coefficients are lacking, then an approximate procedure can be used. First, values of the pressure coefficient due to the thickness effect C_{p_1} can be extracted from Table 3.7, on the assumption that these are proportional to the foil-section thickness. The pressure coeffi-

From Du Cane (1974, p. 46)

For $t/c < 0.2$

Foil Section	$-C_{p_1}$
Ellipse (Ideal but not practical)	2.00 t/c
D.T.M.B.–E.P.H. (Submerged struts only)	2.15 t/c
N.A.C.A. 16 Series	2.28 t/c
Warren 45°	2.36 t/c
N.A.C.A. 66 Series	2.42 t/c
Circular Arc (Bi-ogival)	2.55 t/c
N.A.C.A. 65 Series	2.58 t/c
N.A.C.A. 64 Series	2.65 t/c
N.A.C.A. 63 Series	2.67 t/c
N.A.C.A. 4 and 5 Digit. (For $t/c > 0.08$)	3.50 t/c

Table 3.7: The Pressure Coefficient due to the Thickness Effect

cient due to the camber can be computed by assuming that the load is distributed equally between the upper and lower surfaces of the foil, and that it is uniform over the leading fraction a of the foil, and then tapers to zero at the trailing edge. This type of foil is called a NACA "a" series section. This gives

$$C_{L_I} = -2C_{p_2}\left[a + \frac{1}{2}(1 - a)\right]$$

$$\text{or} \quad -C_{p_2} = C_{L_i}/(1 + a) \quad . \tag{3.50}$$

This formula only applies to the ideal case, at the shock-free condition. At larger angles of attack, a strong suction is created on the upper surface near the nose. At smaller angles of attack, a strong suction is created on the lower surface near the nose. Either of these two possibilities invalidates (3.50).

The best value of $-C_{p_2}$ is $\frac{1}{2}C_{L_i}$ and would occur if the loading were completely uniform, that is $a = 1$. This is practically impossible to achieve. In practice, a value of $-C_{p_2}$ such as $\frac{2}{\pi}C_{L_i}$ is a goal that can be achieved.

4. PLANING CRAFT

4.1. Introduction

4.1.1. Types of Planing Hulls

Two basic hull forms are shown in Figs. 4.1 and 4.2. These illustrate typical round-form and hard-chine designs that are in common use. Both of these designs possess the two principal characteristics of an essentially vertical and flat transom stern, together with an approximately flat and horizontal bottom. The idea behind these two features is to promote the planing behavior. The chine, shown in Fig. 4.1 is the discontinuity in the hull surface.

Planing is generally said to occur when the boat is traveling fast enough for the major part (say 50 to 90%) of its weight to be supported by hydrodynamic forces -- rather than hydrostatic forces alone. The speed at which this occurs depends on the details of the hull shape and, of course, the development of the pheonomenon of planing is a gradual one. In fact, at very low speeds, the hydrodynamic effect is a negative one. The speed of the water over most of the hull surface is greater than that of the forward speed of the boat, and this causes a drop in pressure. The suction forces the boat to squat, and also to assume a trim.

It is only when the speed increases sufficiently for the flow to separate cleanly from the bottom of the transom, that the form of the pressure distribution on the hull surface changes markedly and generates an upward force and a bow-up moment. For this reason, planing is commonly associated with the transom of the stern becoming dry.

The speed of a planing boat is generally defined by means of the beam Froude number, that is

$$F_B = V/\sqrt{gB} \quad , \tag{4.1}$$

From Du Cane (1974, pp 4 and 5)

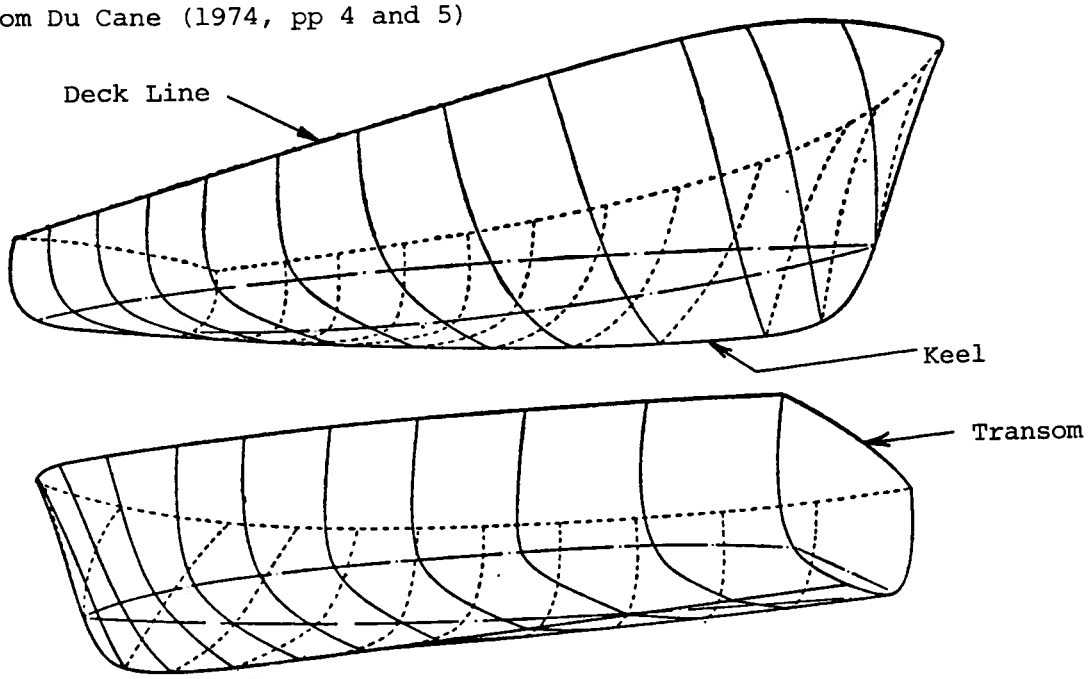

(a) Round-Form Type

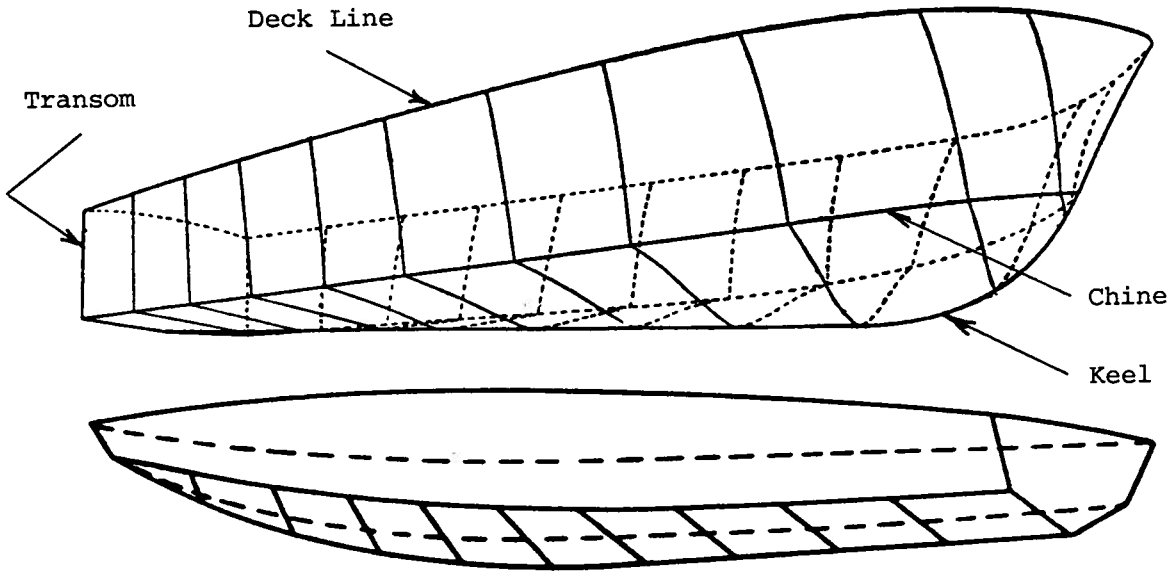

(b) Hard-Chine Type

Figure 4.1: Types of Planing Hulls

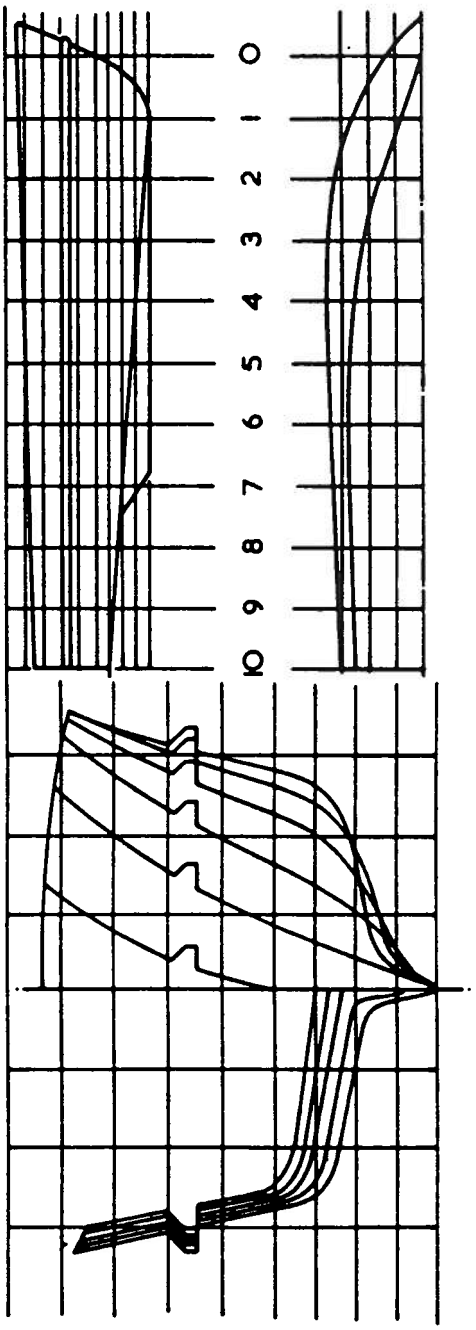

From Du Cane (1974, p. 405)

(a) Round-Form Type

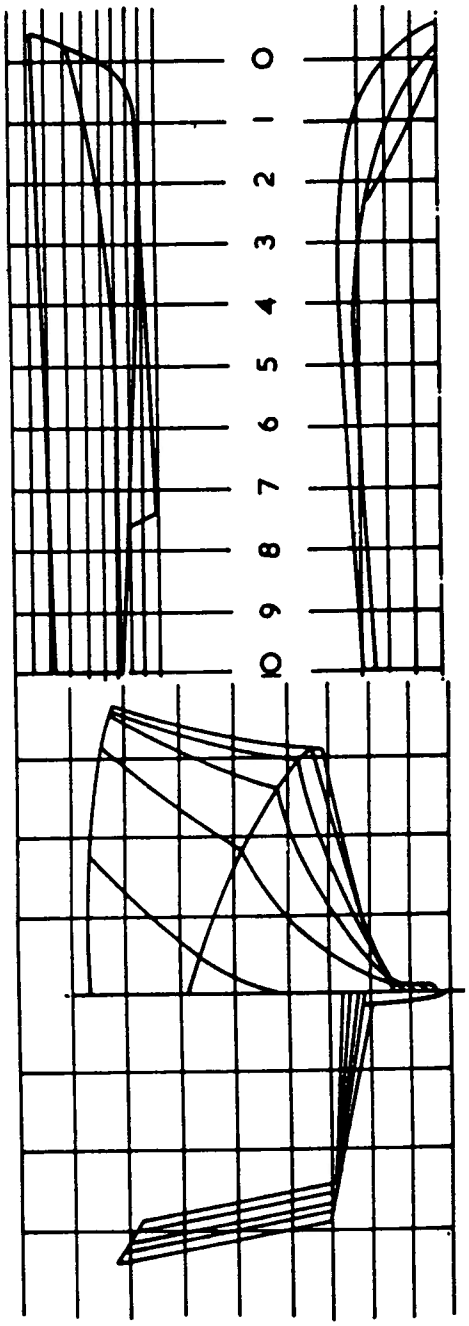

(b) Hard-Chine Type

Figure 4.2: The Lines of Two Planing Hulls

where V is the forward speed, g is the acceleration due to gravity, and B is the beam (preferably measured at the transom). The Froude number based on the beam, is often called the speed coefficient, and is a better measure than the Froude number based on the craft length at rest, namely

$$F_0 = V/\sqrt{gL_0} \quad , \tag{4.2}$$

where L_0 is the wetted length of the stationary boat. The stationary Froude number has little hydrodynamic significance, because the wetted length varies with speed.

A third possibility is to use the dynamic wetted length L, when underway. That is,

$$F = V/\sqrt{gL} \quad . \tag{4.3}$$

This Froude number is hydrodynamically meaningful like the beam Froude number. Unfortunately it is not so convenient to use because the Froude number defined this way is not proportional to the speed. Finally, it should be pointed out that a volume Froude number is also popularly used in connection with planing boats:

$$F_\nabla = V/\sqrt{g\nabla^{1/3}} \quad , \tag{4.4}$$

where ∇ is the at-rest displaced volume of the craft.

The lift force is less on a round-form boat because of the Bernoulli effect already referred to. The hard-chine form is therefore preferred if very high speeds are desired. A further advantage of a hard-chine design is that the wetted surface is more clearly defined. A disadvantage of the hard-chine boat is the pounding and generally worse motions that this type experiences in rough water. As a guide, Saunders (1957, p. 424) suggested that planing occurs when F_0 lies in the range of 0.62 to 0.89.

Fig. 4.3 depicts a racing boat with a rounded (in plan view) transom stern. An important feature of this particular craft is the series of longi-

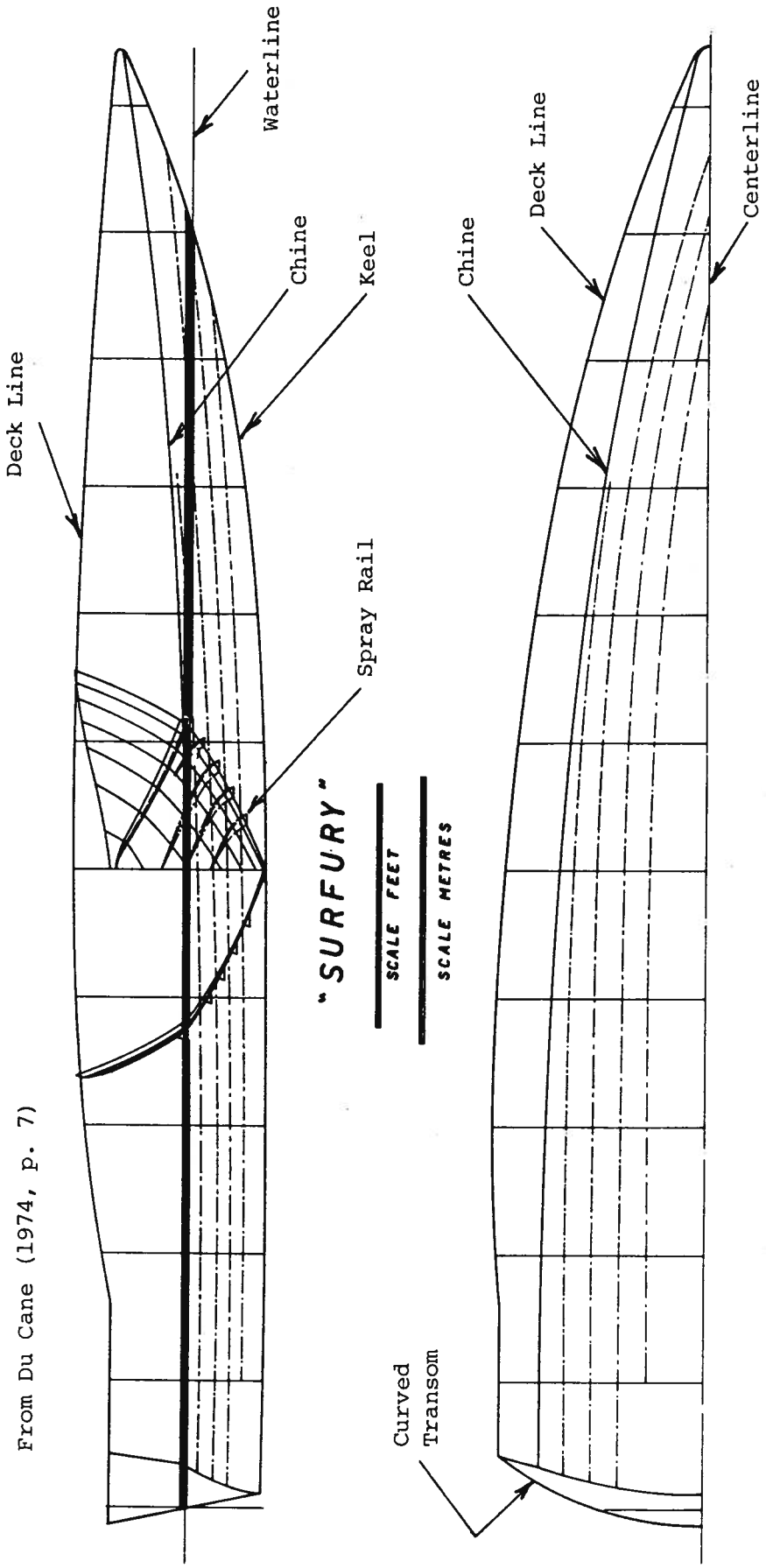

From Du Cane (1974, p. 7)

Figure 4.3: Example of a Deep-Vee Racing Hull

tudinal spray rails (or spray strips). In addition to reducing the spray, rather like miniature chines, they help to define the actual wetted surface when under way. As the boat accumulates speed, it rises out of the water, and successive spray rails come into play. The only two spray rails that materially influence the water flow in this way are the last ones on each side that are still submerged. Spray rails are also fitted at the chine itself in order to increase its effect. Occasionally, as shown in Fig. 4.2(a) a spray rail may be attached to the hull at some point above the under-way waterline. The only purpose of those rails is to keep the deck dry -- they do not affect the planing behavior.

The discussion so far has concentrated on simple hulls. These are hulls with one planing surface. Some hulls are constructed with a number of steps in order to promote better longitudinal stability (pitching). Another variation is a hull fitted with sponsons, as shown in Fig. 4.4. When running at speed, the boat is supported by three planing surfaces. One is near midships under the main hull, and the other two are aft under the two sponsons. As the extent of the wetted surface is very small at speed, the hydrodynamic action is often called three-point planing.

4.1.2. Simple Planing Surfaces

The simplest planing surface is a flat one. This is illustrated in Fig. 4.5(a). The principal feature of the flow is the rise in the water level ahead of the line of intersection between the undisturbed water surface and the plane. Consequently, the dynamic wetted-surface length L is greater than the submerged length L_i. Both of these lengths are different from the stationary length L_0, previously mentioned. The leading edge of the wetted surface is nominally defined to coincide with the location of the spray-root line. The slight curvature that this line possesses (when projected onto the

From Du Cane (1974, p. 10)

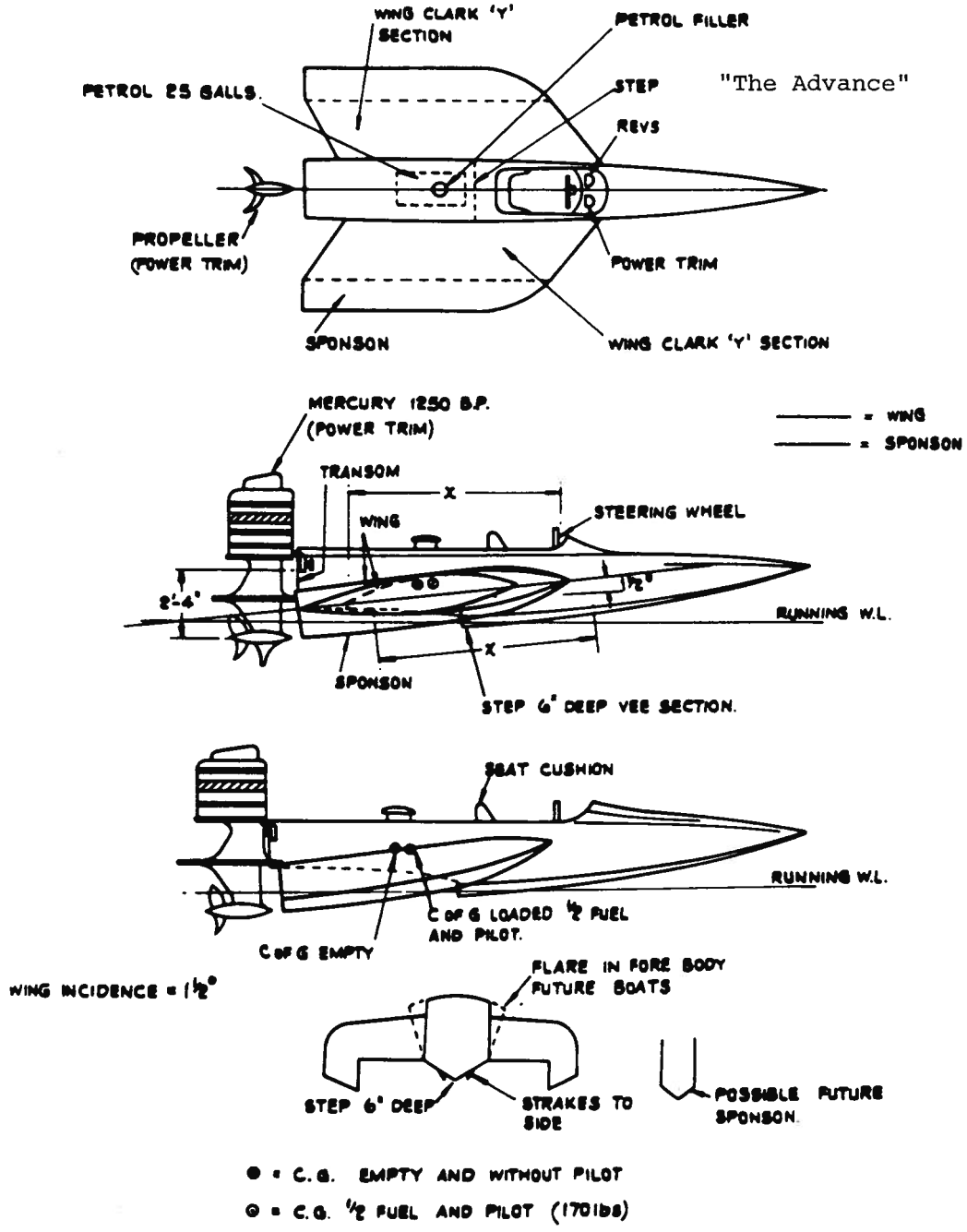

Figure 4.4: Ram-Wing Planing Racing Boat

plane) is usually ignored in any calculations.

The plane is wetted ahead of the spray-root line. This is more clearly indicated in Fig. 4.5(b). However, it can be shown that the thickness of the spray δ is closely proportional to the square of the trim angle τ, for the usual range of trims of interest. Since this is generally quite small, one can ignore the lift of the pressure distribution on the plane ahead of the spray-root region. The pressure distribution is seen to have its stagnation value near the spray root. It falls off to zero at the trailing edge of the plate.

Fig. 4.6 shows the main features of a prismatic planing surface. This differs from the flat surface in that a deadrise angle β is included in the description of its shape. The use of deadrise results in a decrease in the lifting capacity of the surface. This will be discussed later in these notes. However, a deadrise surface has two main advantages: less motion in waves and better directional stability.

Experiments show that there is almost no build-up or water rise under the keel. Thus, contrary to the case of the flat planing surface, the spray root starts at the intersection of the undisturbed water surface and the keel. This is referred to as point 0 in Fig. 4.6. There is, however, a rise in water level away from the keel. As noted in Fig. 4.6, the dynamic half-wetted beam is given by $\frac{\pi}{2}b_1$, where b_1 is the half-wetted beam computed on the basis of the intersection of the undisturbed water surface with the hull. This factor of $\pi/2$ is an outcome of a simple two-dimensional theory which assumes that the body is slender. It has been experimentally verified for prismatic planing surfaces with various aspect ratios and deadrise angles, and operating at different Froude numbers.

From Savitsky (1964, pp 72 and 73)

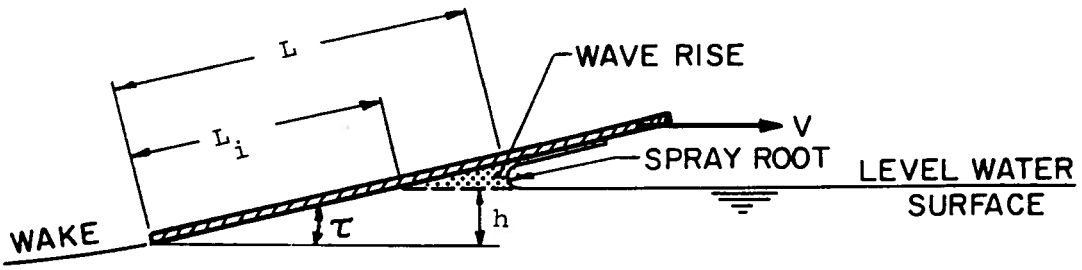

(a) The Geometry

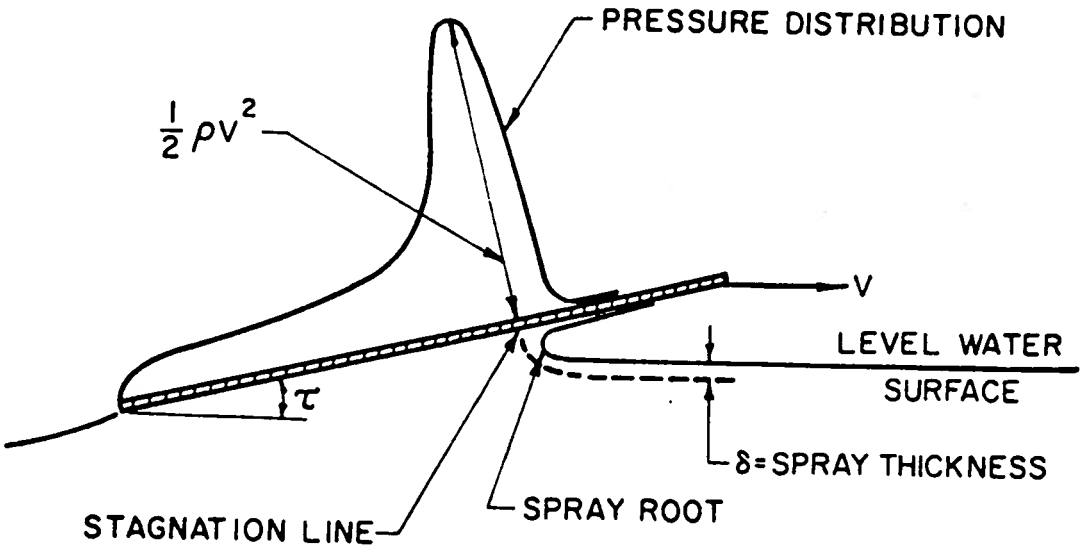

(b) Pressure Distribution

Figure 4.5: A Flat Planing Surface

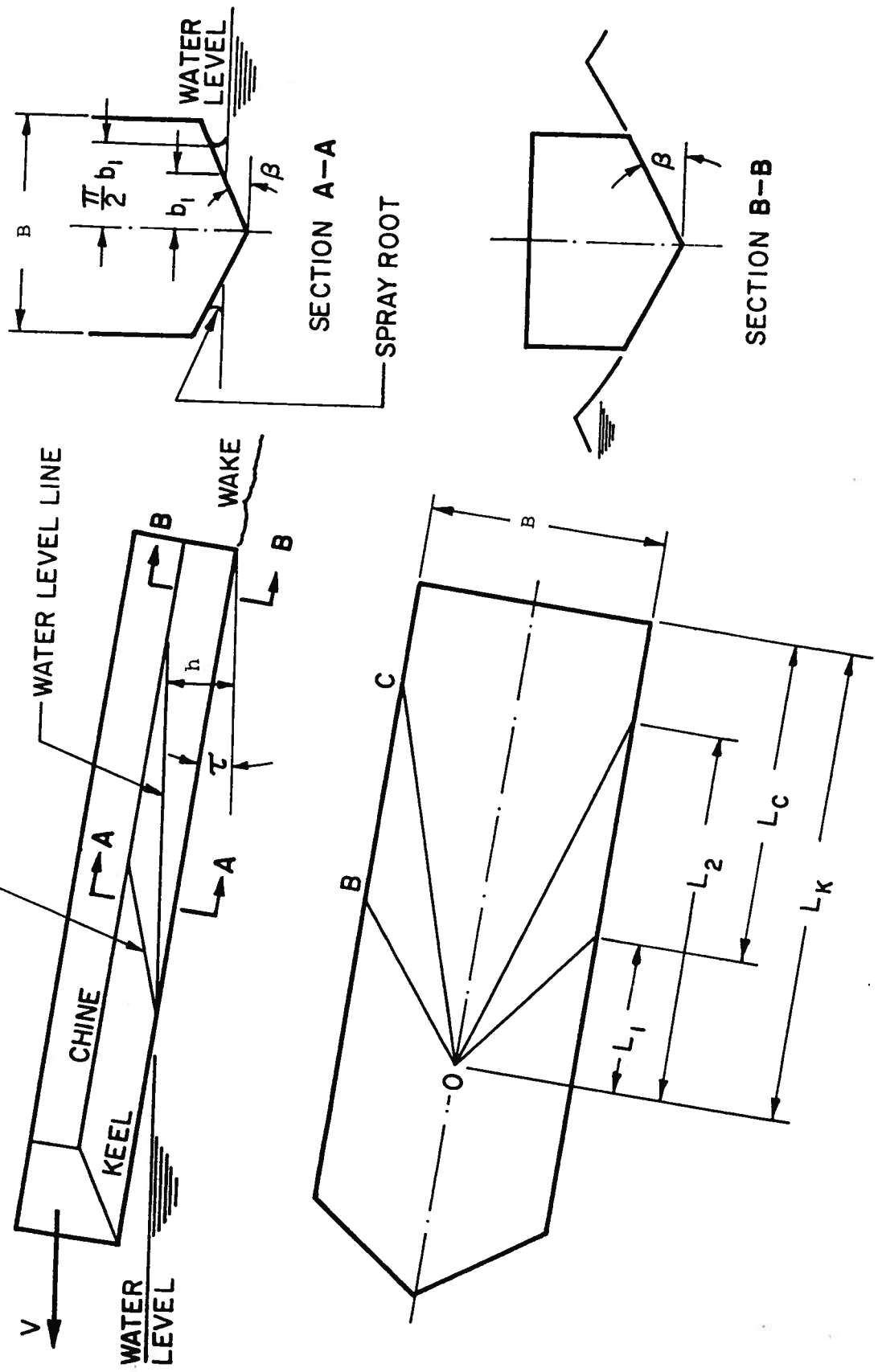

From Savitsky (1964, p. 74)

Figure 4.6: A Prismatic Planing Surface

4.1.3. Other Features of Planing Surfaces

Some refinements to the basic prismatic form are illustrated in Fig. 4.7. Thus warp, or twist, is defined in Fig. 4.7(a). Warp is reflected by the fact that the deadrise angle is greater at the bow than at the stern. The particular body plan shown possesses a relatively large deadrise angle, and this is referred to as a deep-vee design. The main advantage of warp is to reduce the problem of motions in waves.

Fig. 4.7(b) illustrates the feature of buttock-line convexity, or rocker. The lifting qualities of the hull are diminished by rocker. In fact, from the point of view of the resulting lift-to-drag ratio of the boat, it would be desirable to build the hull with a negative rocker. The hydrodynamic effect is similar to that of camber in the case of a lifting airfoil or hydrofoil. Unfortunately, it would be difficult to use negative rocker in practice, particularly with regard to behavior in waves.

A shock-absorbing bow is shown in Fig. 4.7(c). Such a bow usually has a deep-vee section with a non-constant deadrise angle. Details of this are given in Fig. 4.8(a). The bow section is convex near the keel and concave near the chine. Fig. 4.8(b) represents a typical history of bow-upward acceleration during an impact. The shock-free bow produces a more nearly uniform force during the impact, and is therefore preferable from this aspect.

Finally, Fig. 4.9(a) illustrates the influence on wetted surface of a combination of a deep-vee with a warped bottom, as compared to Fig. 4.9(b) for a shallow vee with a small degree of warp. The first design results in a wetted surface with a forward-facing "finger". Small changes in trim can cause large variations in the length of the finger, which are considered to be undesirable from the point of view of pitch motions.

The sections of this deep-vee design posses some concavity. Convex sec-

From Du Cane (1974, pp 88, 118, and 119)

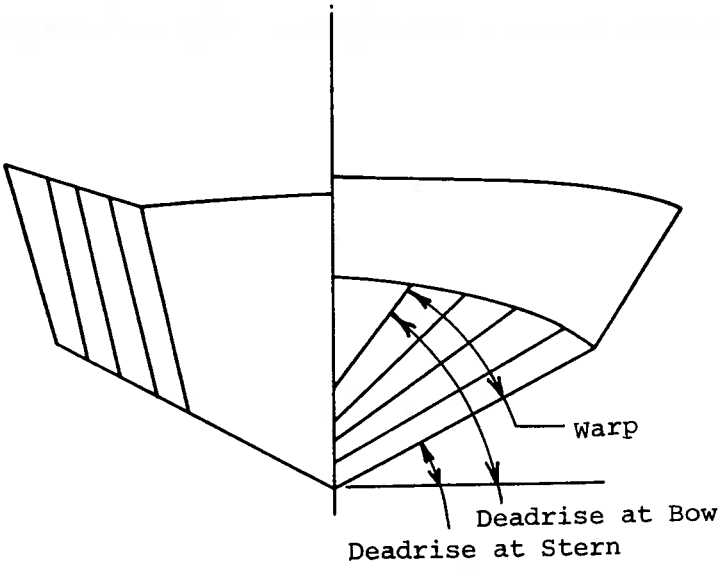

(a) Deep-Vee Body Plan

(b) Buttock-Line Convexity or Rocker Slope

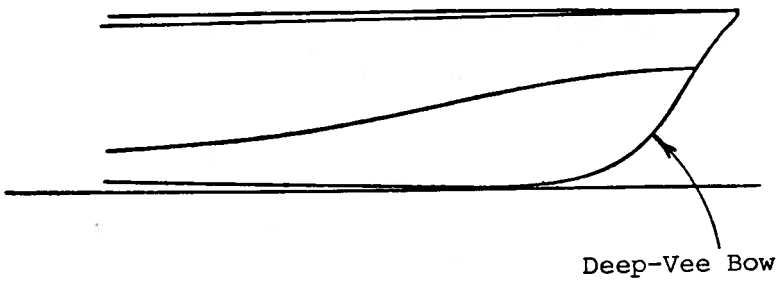

(c) Shock-Absorbing Bow

Figure 4.7: Other Features of Planing Surfaces

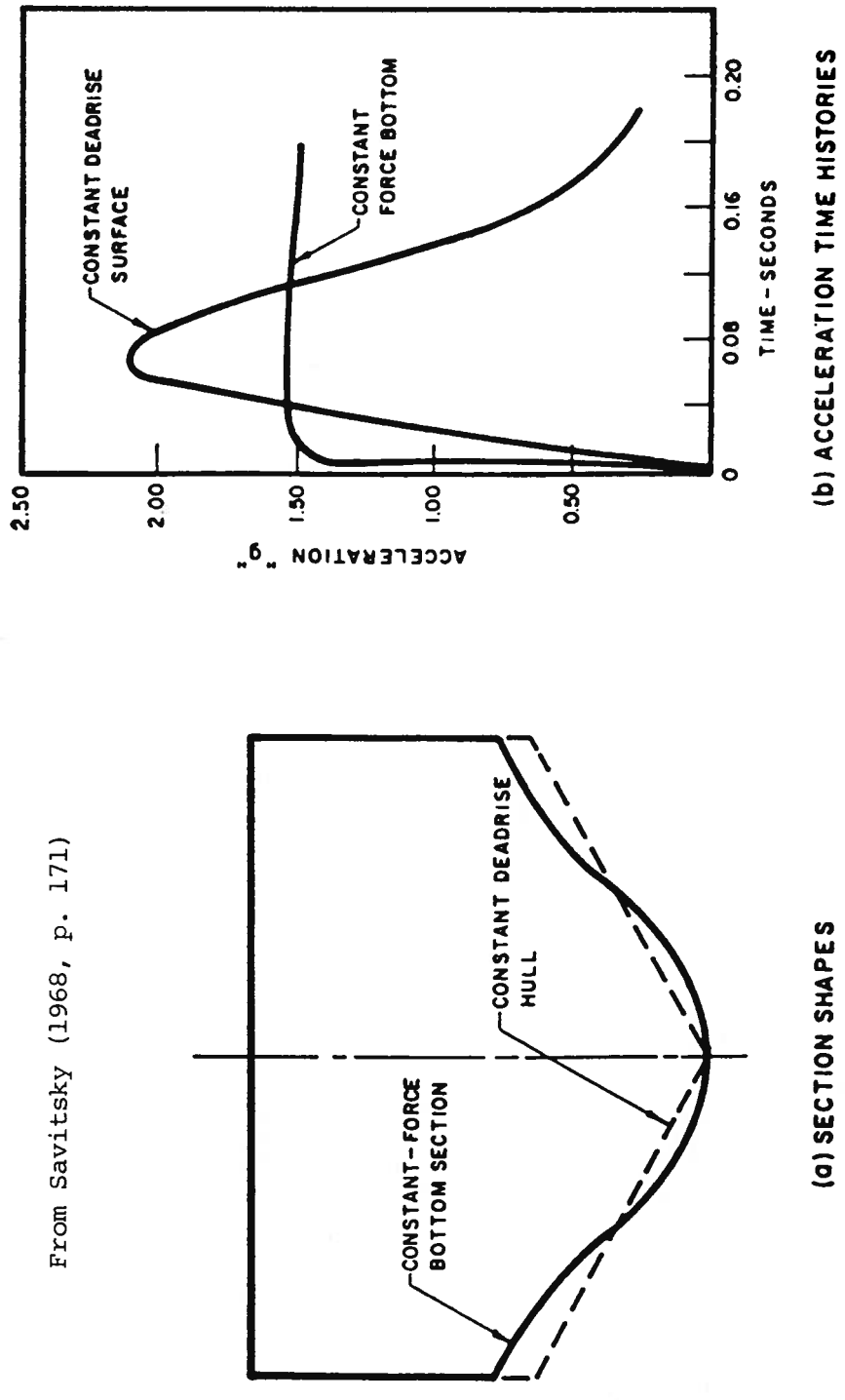

From Savitsky (1968, p. 171)

Figure 4.8: Typical Impact Characteristics of Two Bottom Sections

From Du Cane (1974, p. 437)

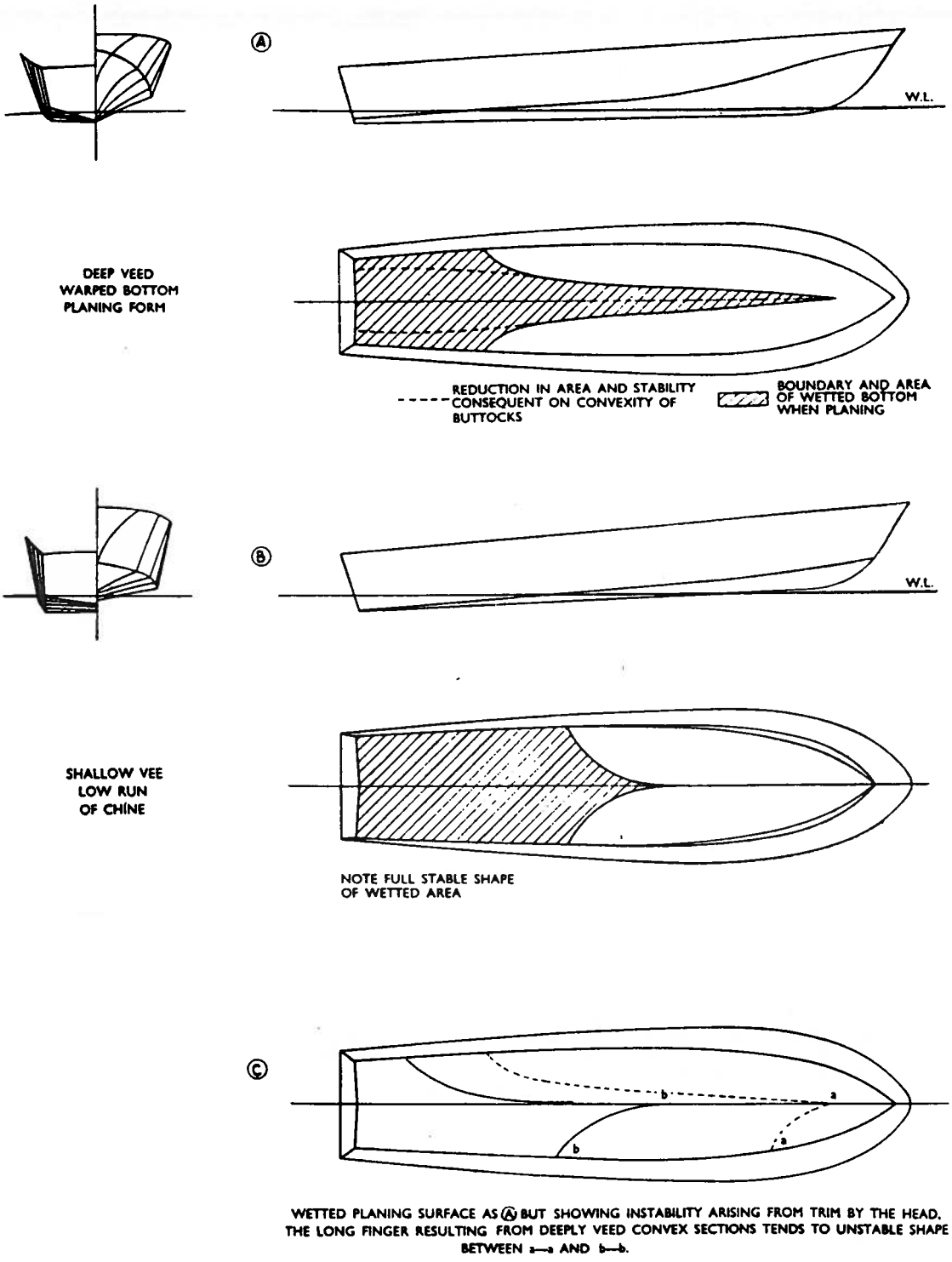

Figure 4.9: Influence of Hull Shape on Wetted Surface

tions are also frequently used. An example is presented in Fig. 4.3.

4.2. Two-Dimensional Planing Theory

We first approach the theoretical problem of computing the behavior of planing in calm water by studying the two-dimensional problem. In this case, the beam B is infinite. A number of researchers have worked on this problem. A simple panel method was developed by Doctors (1974), and will be discussed here.

Fig. 4.10 defines the problem and the nomenclature. An interesting difficulty encountered in the course of the solution, is that the wetted length is not known beforehand. This difficulty is bypassed by assuming a dynamic wetted length. If the resulting lift does not match the weight of the boat, then the solution can be repeated by means of a iterative technique. In a similar way, the depth of the trailing edge below the free surface h is unknown. (In principle, it must be chosen so that the wetted length is equal to the given value c.)

As viscosity is ignored, the planing surface can be represented by a pressure distribution, which is decomposed into a series of overlapping triangular pressure elements as shown in Fig. 4.10(a). The nominal length of an element is $2a$, so that we have

$$c = 2an \quad , \tag{4.5}$$

where n is the number of spaces. The number of elements is actually $n - 1$. The profile of the planing surface is defined as $z(x)$.

Now, the disturbance generated at x_i by a pressure element of strength p_j and centered at x_j can be computed using the methods outlined by Lamb (1932), and can be written as

$$\zeta_{ij} = \frac{p_j}{\rho g} K_{ij}\left((x_i - x_j)k_0,\ ak_0\right) \quad , \tag{4.6}$$

From Doctors (1974, pp 482 and 483)

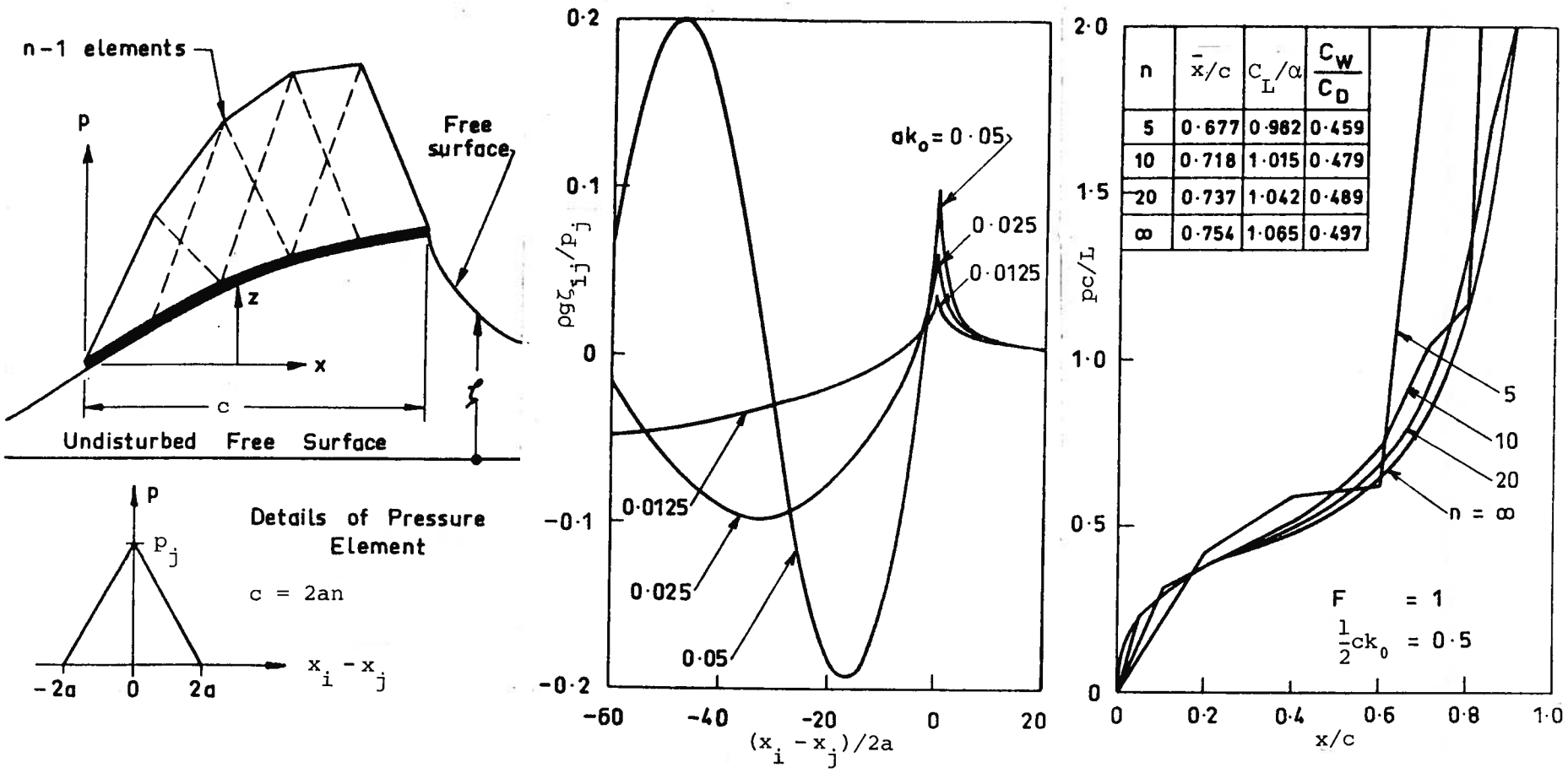

(a) Nomenclature (b) The Influence Function (c) Convergence

Figure 4.10: Two-Dimensional Planing

where ρ is the water density, and k_0 is the circular wave number given by

$$k_0 = g/V^2 \quad . \tag{4.7}$$

Being a linear theory, (4.6) predicts that the disturbance ζ is proportional to the strength of the pressure element. The dimensionless influence is plotted in Fig. 4.10(b) for six different values of the parameter ak_0 (which is effectively the inverse of the square of the Froude number based on the element length). In each case, the pressure element generates a rise in the water level followed by the development of a downstream harmonic wave, whose elevation is given by

$$\frac{\rho g \zeta_j}{p_j} = \frac{4}{ak_0} \sin^2(ak_0) \sin[(x - x_j)k_0] \quad . \tag{4.8}$$

The second stage of the solution is to combine the influence of the elements, so that the total water elevation at the i'th point matches the profile of the planing surface, plus the effect of the trailing-edge submergence h. Thus we can write

$$\sum_{j=2}^{n} K_{i-j}\, p_j = \rho g(z_i - h) \text{ for } i = 1 \text{ to } n \quad . \tag{4.9}$$

This set of equations contains n conditions, and has n unknowns ($n - 1$ values of p_j and one value of h). The inversion of the equations can be done in the usual way, and then the lift, moment, and drag computed by means of summations of the pressure distribution:

$$L = 2a \sum_{i=2}^{n} p_i \quad , \tag{4.10}$$

$$M = 2a \sum_{i=2}^{n} p_i\, x_i \quad , \tag{4.11}$$

and

$$D = 2a \sum_{i=2}^{n} p_i\, z'(x_i) \quad . \tag{4.12}$$

Fig. 4.10(c) shows an example of the convergence of the pressure distribution as the number of elements is increased. Typically 80 elements are sufficient to give an accuracy of about one percent. The pressure shows the expected singularity at the leading edge, similar to that experience in thin-airfoil theory.

The drag in (4.12) is experienced by the plate as the horizontal component of the pressure force. It is also equal to the sum of the momentum flux in the leading-edge spray jet (shown in Fig. 4.5), and the wave resistance. We can express the latter in terms of the downstream wave amplitude (see Newman (1980, pp 266-270)):

$$D_W = \frac{1}{4}\rho g A^2 \quad . \tag{4.13}$$

The wave amplitude A can be obtained by summing the individual wave components generated by each pressure element. The effect of the appropriate phase shifts, caused by the origin of each element being different is included in (4.8). Thus

$$\zeta = \frac{4}{ak_0\rho g} \sin^2(ak_0) \sum_{i=2}^{n} p_i \sin[(x - x_i)k_0]$$

$$= \frac{4}{ak_0\rho g} \sin^2(ak_0)[P \sin(xk_0) - Q \cos(xk_0)] \quad , \tag{4.14}$$

where $\begin{matrix} P \\ Q \end{matrix} = \sum_{i=2}^{n} p_i \begin{matrix} \cos \\ \sin \end{matrix} (x_i k_0) \quad .$ (4.15)

Thus, the downstream wave amplitude is

$$A = \frac{4}{ak_0\rho g} \sin^2(ak_0) \sqrt{P^2 + Q^2} \quad , \tag{4.16}$$

and the wave resistance from (4.13) is

$$D_W = \frac{4}{\rho g(ak_0)^2} \sin^4(ak_0)(P^2 + Q^2) \quad . \tag{4.17}$$

Results for the pressure distribution are shown for three elementary planing profiles in Fig. 4.11. These profiles are given in the following table.

Table 4.1: Elementary Planing Profiles

Case	Equation of Profile $z(x)$
Flat	$\alpha_1 x$
Parabolic	$\alpha_2 x^2/c$
Cubic	$\alpha_3 x^3/c^2$

In each case of Fig. 4.11, the correct hydrostatic pressure is predicted when the Froude number is zero. When the Froude number is greater than zero, the singularity in the pressure at the leading edge is developed. This corresponds to the splash jet.

The lift, drag, wave-drag, and moment coefficients are defined in the usual way as

$$C_L = L/\frac{1}{2}\rho V^2 c \quad , \tag{4.18}$$

$$C_D = D/\frac{1}{2}\rho V^2 c \quad , \tag{4.19}$$

$$C_W = D_W/\frac{1}{2}\rho V^2 c \quad , \tag{4.20}$$

and $$C_M = M/\frac{1}{2}\rho V^2 c^2 \quad , \tag{4.21}$$

while the center of pressure is just

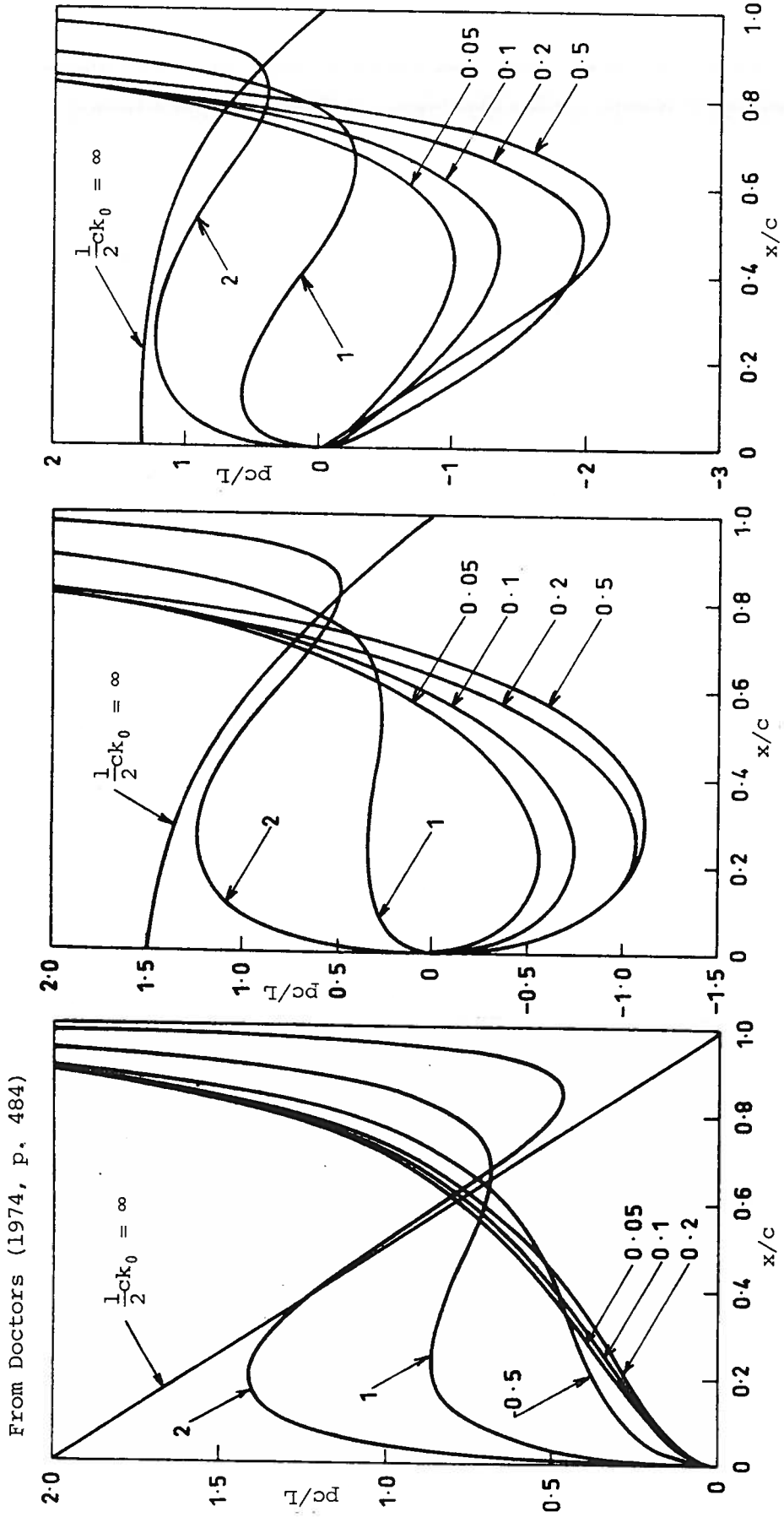

Figure 4.11: Two-Dimensional Planing Pressure Distributions

$$\bar{x}/c = C_M/C_L \quad . \tag{4.22}$$

Some of these coefficients are plotted in Fig. 4.12(a). The curves demonstrate that the wave resistance approaches zero at a high Froude number, while the lift coefficient increases, and eventually, at infinite Froude number, equals one half of the corresponding values for an airfoil with the same profile. Fig. 4.12(b) shows that the center of pressure approaches the airfoil results at infinite Froude number. The curves of trailing-edge depth indicate that the planing surface continues to rise as the Froude number increases.

Finally some attempts at determining optimum planing forms are displayed in Fig. 4.13. Combinations of the elementary profiles in Table 4.1 were generated as follows:

$$\begin{aligned} z(x) &= \alpha_1 x + \alpha_2 x^2/c + \alpha_3 x^3/c^2 \\ &= \alpha_1 (x + rx^2/c + sx^3/c^2) \quad . \end{aligned} \tag{4.23}$$

This combination is referred to as a three-term profile, while setting $s = 0$ creates a two-term profile. The lift and moment coefficients for these combinations are obtained by the principle of superposition:

$$C_L = C_{L_1} + C_{L_2} + C_{L_3} + \cdots \tag{4.24}$$

and

$$C_M = C_{M_1} + C_{M_2} + C_{M_3} + \cdots \quad . \tag{4.25}$$

Fig. 4.13(a) gives the values of r and s as a function of the Froude number for the two- and three-term profiles which minimize the drag. The asterisked curves represent the values of r and s if the spray jet is eliminated. Fig. 4.13(b) highlights two interesting points. The first is that there is not much gain to be had by using all three terms. Secondly, elmination of the spray jet is seen to generate the optimum form for $F > 1$. Very high values of the ratio C_L^2/C_D can be obtained by this optimizing method -- such as 17.9 at a Froude number of 3, compared to only 2.48 for a

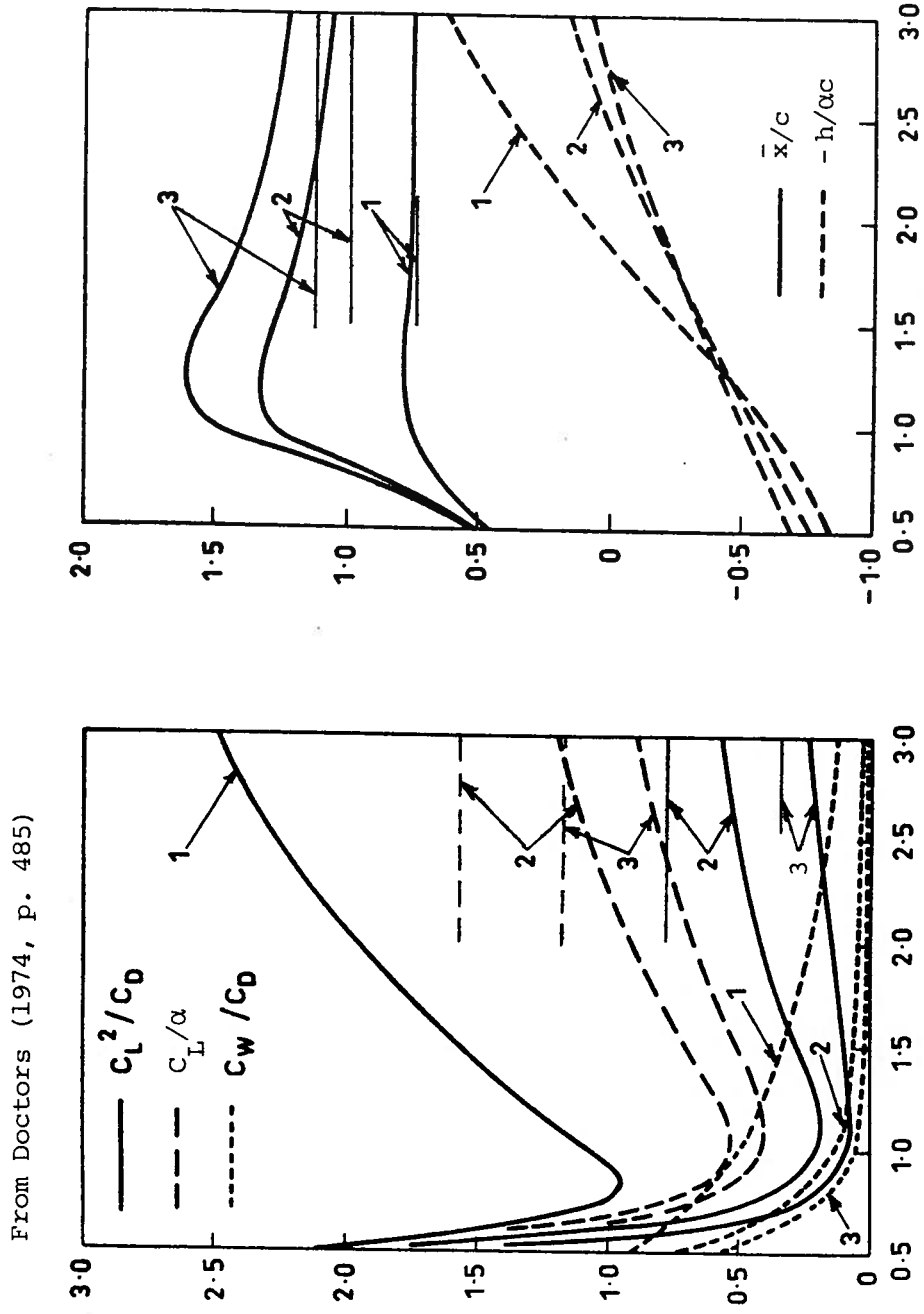

(a) Lift and Drag Coefficients (b) Center of Pressure and Stern Submergence

Figure 4.12: Two-Dimensional Planing Performance

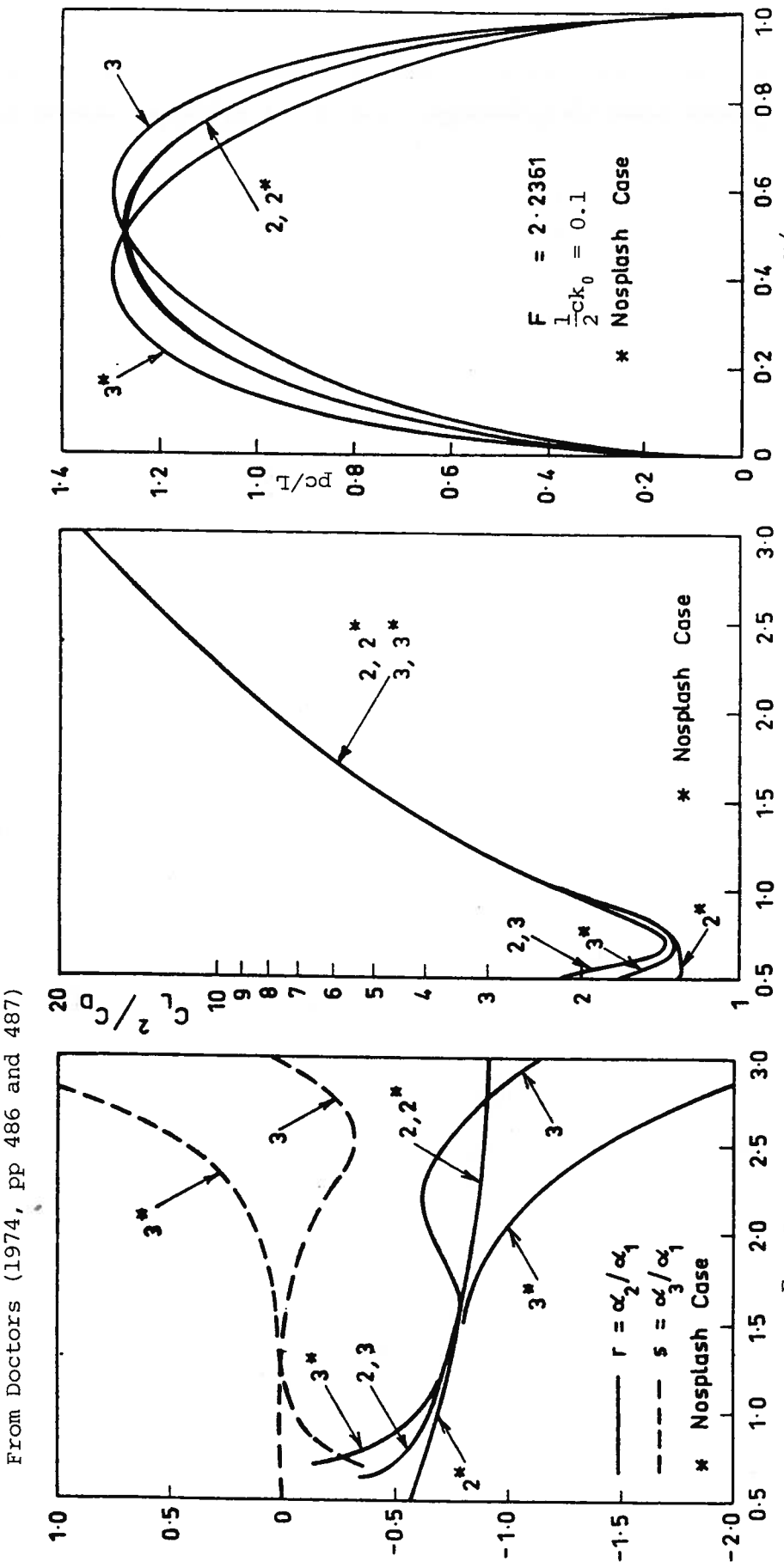

(a) Shape Coefficients (b) Lift-Squared-to-Drag Coefficients (c) Pressure Distributions

Figure 4.13: Two-Dimensional Optimum Planing Performance

flat plate (in Fig. 4.12(a)). Unfortunately, the optimum form is obtained by using a negative value of r (positive camber), which is not a practical shape to use -- as noted in Sec. 4.1.3. It does point out, though, that an attempt should be made to avoid negative camber (or rocker). Lastly, Fig. 4.13(c) displays examples of the pressure distributions which nearly possess fore-and-aft symmetry.

4.3. Three-Dimensional Planing Theory

The theory of three-dimensional planing can be approached in the same way as for the two-dimensional case. In constrast to the two-dimensional case, however, there are only a couple of publications which are devoted to the true three-dimensional situation -- that is, without making the assumption of either a low-aspect ratio ($B/L \ll 1$), or a large-aspect ratio ($B/L \gg 1$). The work of Doctors (1975) will be cited in this section.

Fig. 4.14(a) presents the problem definition for both the flat plate (similar to Fig. 4.5), and the prismatic shape (as in Fig. 4.6). The overlapping triangular pressure elements used in Sec. 4.2, have now been replaced by their three-dimensional equivalent -- a type of tent function. These are shown in Fig. 4.14(b). The tents have a rectangular base with a nominal length 2a and a nominal width 2b. They overlap both longitudinally and transversely to give a pressure distribution which varies bi-linearly between control points (the element centroids). An obvious difficulty is that one cannot exactly model the curved shape of the wetted surface at the leading edge. This shape is approximated by what is essentially a staircase representation.

The three-dimensional equivalent of the kinematic condition (4.9) for the prismatic surface is

$$\sum_{j=1}^{n} K_{ij}\, p_j = \rho g(\alpha x_i + 2dy_i/B - h) \text{ for } i = 1 \text{ to } n \quad , \tag{4.26}$$

From Doctors (1975, p. 520)

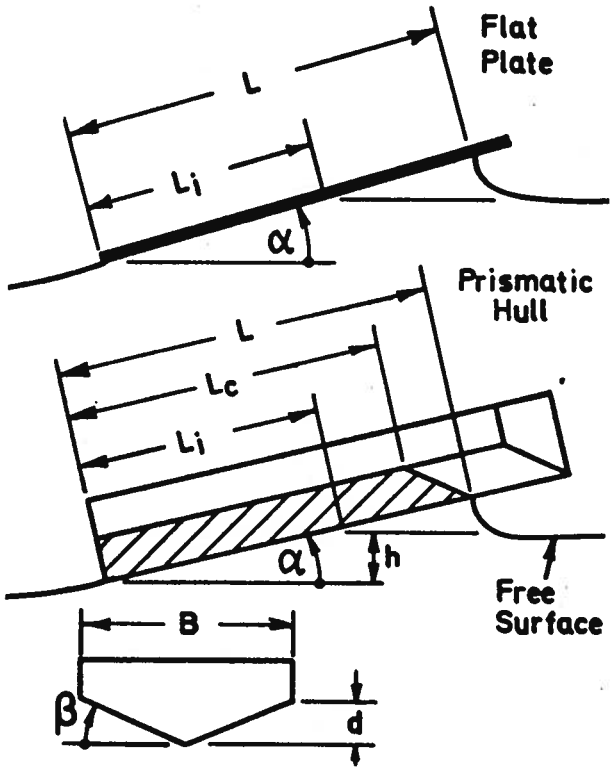

(a) Nomenclature

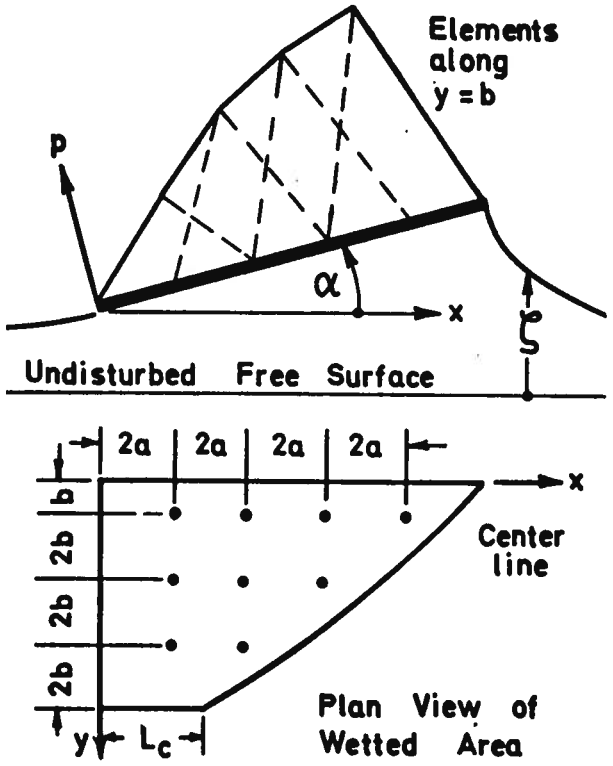

(b) Use of Pressure Panels

Figure 4.14: Three-Dimensional Planing

where n is the number of elements on one side of the centerplane, and K_{ij} is the dimensionless free-surface elevation generated at the i'th field point (x_i, y_i) by a unit pressure element at the j'th source point (x_j, y_j), together with its image at $(x_j, -y_j)$. The effect of deadrise d is included in (4.26). The set of equations (4.26) represents n conditions (one for each field point), but $n + 2$ unknowns (one for each pressure, together with α and h).

Two additional equations are supplied by noting that the weight and its moment are given by

$$\frac{1}{2}W = S \sum_{j=1}^{n} p_j \qquad (4.27)$$

and

$$\frac{1}{2}W\bar{x} = S \sum_{j=1}^{n} p_j x_j \quad , \qquad (4.28)$$

where S is the nominal area of each panel, and is given by the relation

$$S = 4ab \quad . \qquad (4.29)$$

The set of simultaneous equations (4.26), (4.27), and (4.28) were solved by first assuming the extent of the wetted surface. From this, the paneling could be carried out. The calculation of the coefficients K_{ij} , is rather difficult to execute accurately, as they are represented by integrals of oscillatory functions. Once the solution has been found, it is necessary to check the Kutta condition. In the present technique, the Kutta condition was satisfied by adjusting the extent of the wetted surface until the kinematic condition was fulfilled at the trailing edge -- in addition to the interior points already included in (4.26).

Fig. 4.15 displays a comparison of results obtained by this theory for a flat plate ($\beta = 0$) with experimental results determined by Savitsky (1964). The relationship between the stationary length L_0 with the average dynamic length L_m is first shown in Fig. 4.15(a). The agreement is good to within

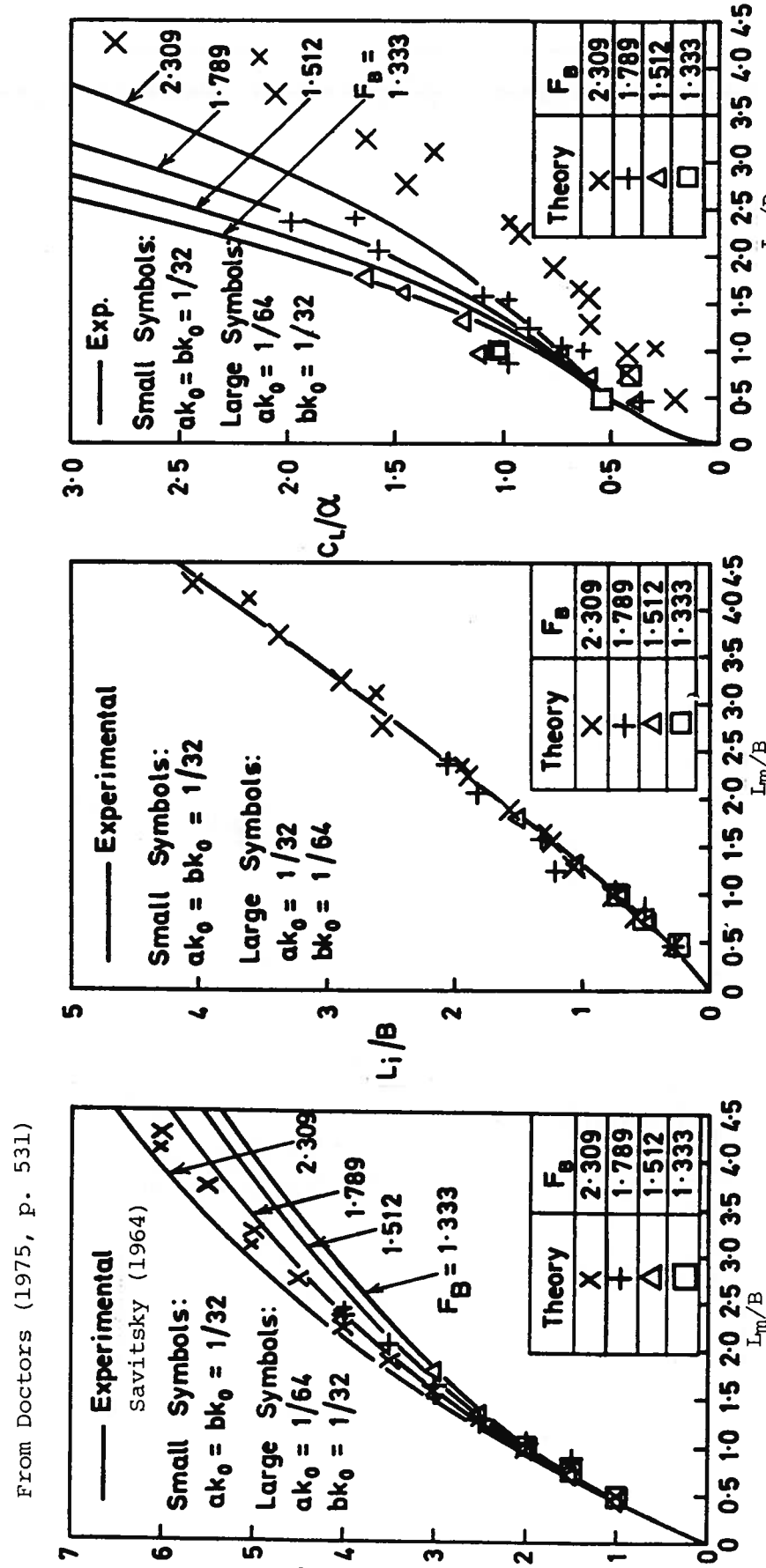

(a) Hydrostatic Length (b) Immersed Length (c) Lift Coefficient

Figure 4.15: Three-Dimensional Planing of a Flat Plate

4%. The small effect of Froude number is predicted by the theory. Fig. 4.15(b) examines the variation of the immersed wetted length L_i with the mean dynamic length L_m. The predictions are seen to be even better here. The negligible influence of Froude number on L_i is also demonstrated by the theory. Finally, the lift coefficient is plotted in Fig. 4.15(c). The general variation of the lift with both the dynamic wetted length and the Froude number are correctly predicted. However, the predicted lift is low by up to 30%.

The case of deadrise is shown in Fig. 4.16. Three amounts of deadrise are considered: $d/h_0 = 0.25$, 0.5, and 0.75, where h_0 is the stationary submergence of the transom. In addition, two different beam Froude numbers are taken into consideration.

Fig. 4.16(a) displays good correlation for the relationship between stationary and dynamic wetted lengths. The small influence of the deadrise is correctly predicted too. The immersed wetted length in Fig. 4.16(b) is not so well predicted, compared to the case of the flat plate in Fig. 4.15(b) -- although the correct trends are indicated. Finally, the overall trends for the lift coefficient in Fig. 4.16(c) are demonstrated by the technique. This includes the lack of influence of deadrise in the linear theory. However, the large scatter of the computed points emphasizes the difficulties encountered in the calculation of the K_{ij} in (4.26).

4.4. Empirical Methods for Prismatic Forms

4.4.1. Zero Deadrise Angle

We first consider the case of a flat plate, as shown in Fig. 4.5. A number of experiments have been carried out by Savitsky and Neidinger (1954) for this case. Results of their experiments for the wave rise are plotted in Fig. 4.17. The dimensionless wetted length (or dynamic length), and the

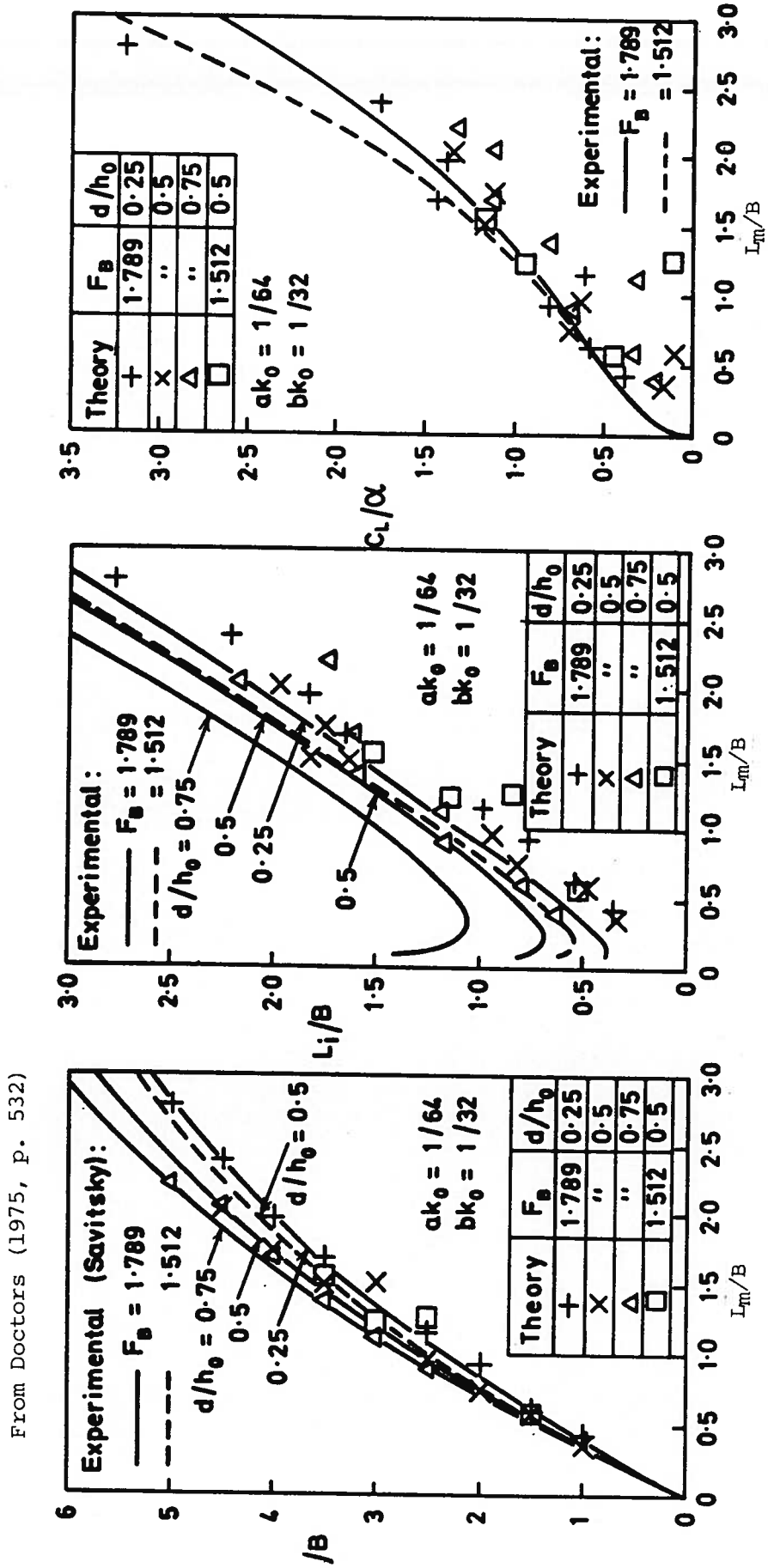

(a) Hydrostatic Length (b) Immersed Length (c) Lift Coefficient

Figure 4.16: Three-Dimensional Planing of a Prismatic Surface

From Savitsky and Neidinger (1954, p. 37)

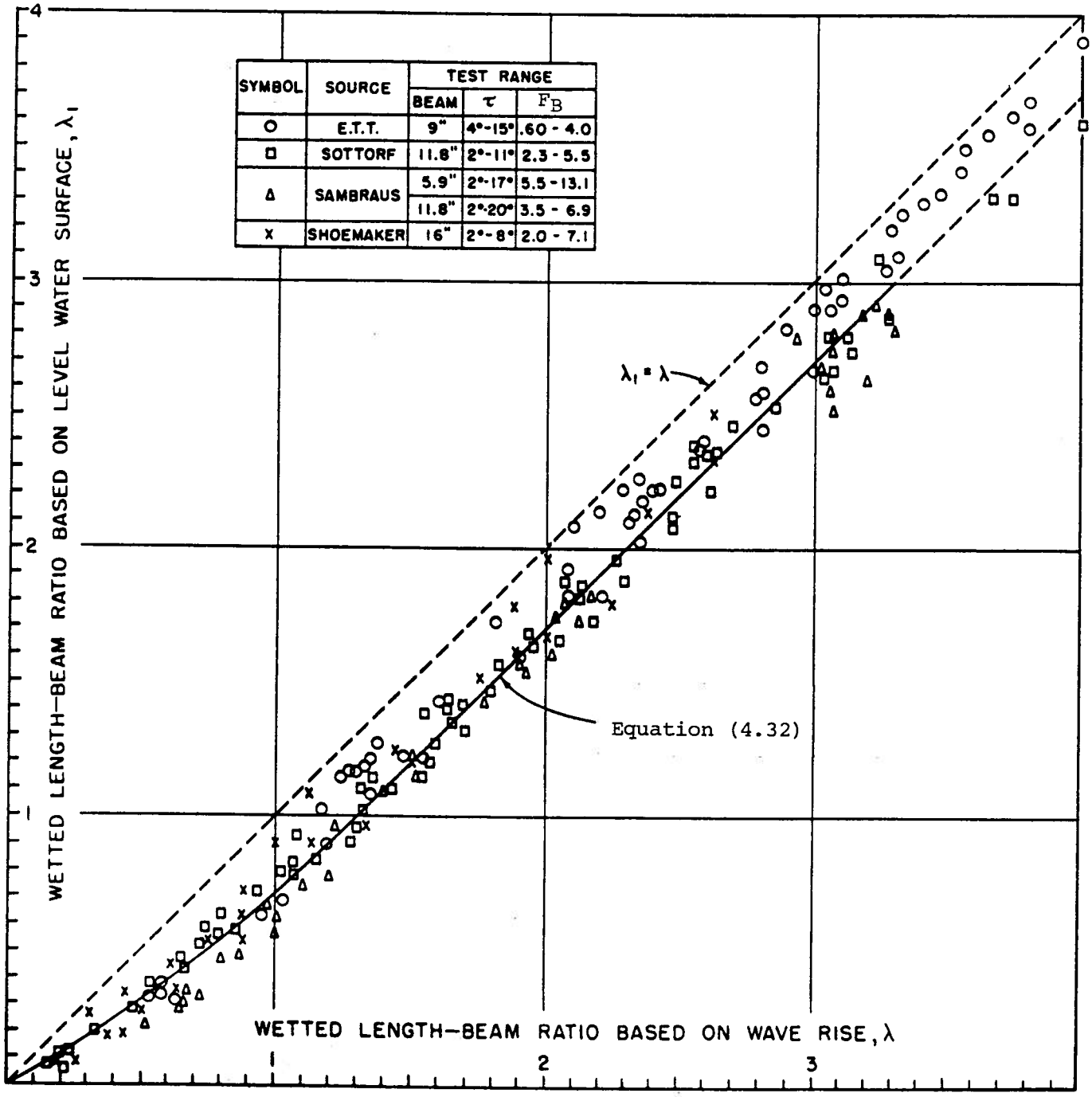

Figure 4.17: Wave Rise for a Flat Planing Plate

immersed length are defined in terms of the beam:

$$\lambda = L/B \tag{4.30}$$

and $$\lambda_i = L_i/B \quad . \tag{4.31}$$

The experimental results are seen to collapse about a curve defined by

$$\lambda = \left\{ \begin{array}{ll} 1.60\,\lambda_i - 0.30\,\lambda_i^2 & \text{for } 0 \leq \lambda_i \leq 1 \\ \lambda_i + 0.30 & \text{for } 1 \leq \lambda_i \leq 4 \end{array} \right\} \text{ for } 2° \leq \tau \leq 24° \text{ and } 0.60 \leq F_B \leq 25.0 \ , \tag{4.32}$$

where τ is the trim angle in degrees. It can be added that the wetted length was found to be practically constant across the width of the plate: that is, the spray-root line is almost straight.

The weight W supported by the plate was found to be approximated well by the formula

$$C_{L_0} = W/\tfrac{1}{2}\rho V^2 B^2 \tag{4.33}$$

$$= \tau^{1.1}(0.0120\,\lambda^{1/2} + 0.0055\,\lambda^{5/2}/F_B^2) \text{ for } 2° \leq \tau \leq 15° \ , \ 0.60 \leq F_B \leq 13.0 \ , \text{ and } \lambda \leq 4.0 \quad . \tag{4.34}$$

This function is plotted in Fig. 4.18. It shows how the lift drops off with increasing beam Froude number, if the trim and wetted-length ratio are fixed. Fig. 4.19 is included as a test of accuracy of (4.34). The best agreement occurs when the trim angle is greater than or equal to 4°. It is interesting to note that the linear theory expounded in Secs 4.2 and 4.3 indicates that the lift is proportional to the angle of trim. The experimental data shows that the dependence on trim is slightly stronger than that.

4.4.2. Non-Zero Deadrise Angle

We now consider the extension to the case of a constant-deadrise surface. Fig. 4.20 is a plot of the difference between the keel wetted length L_K and the chine wetted length L_C, which are illustrated in Fig. 4.6. This length

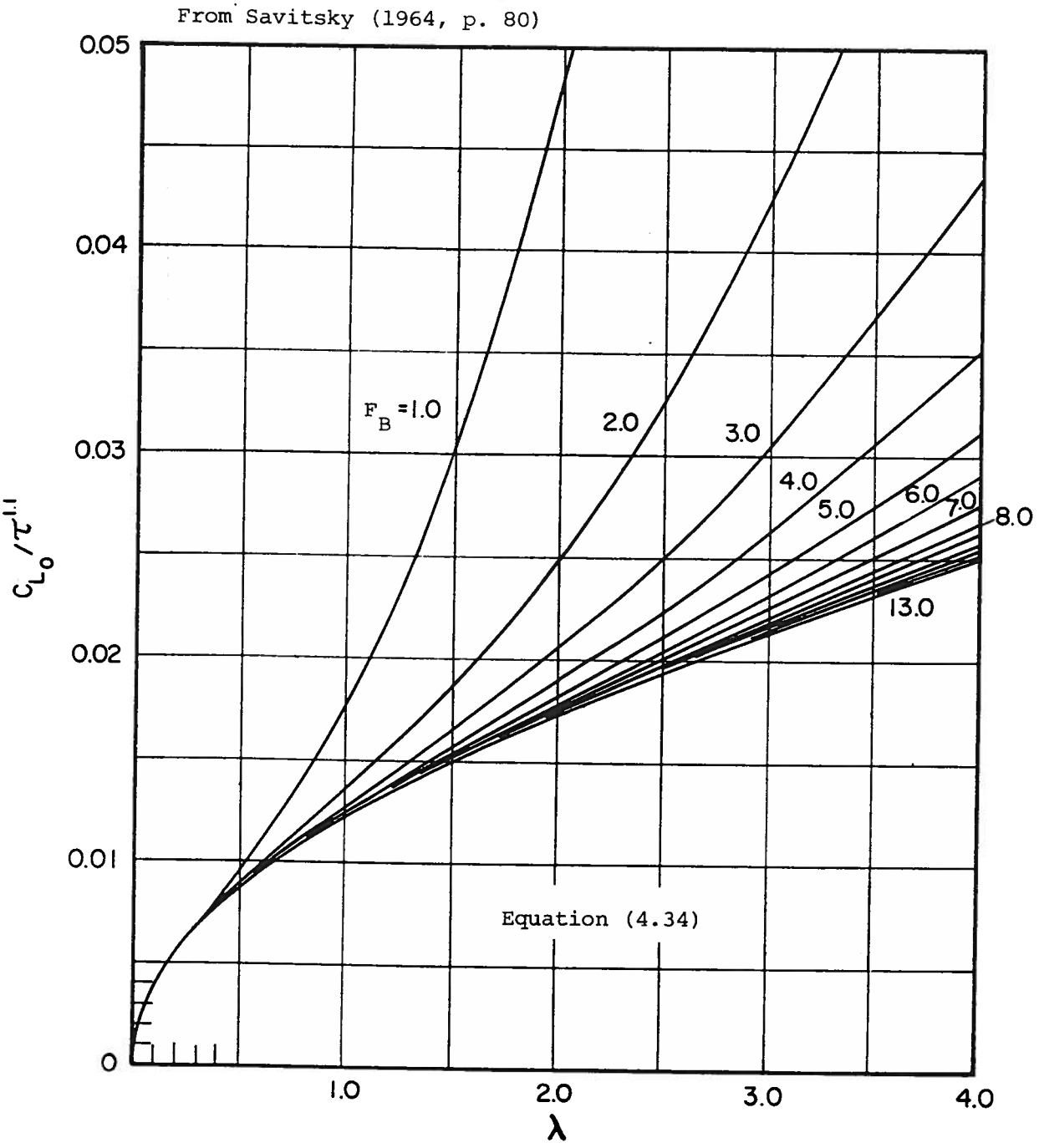

Figure 4.18: Lift Coefficient for a Flat Planing Surface

From Savitsky and Neidinger (1954, p. 39)

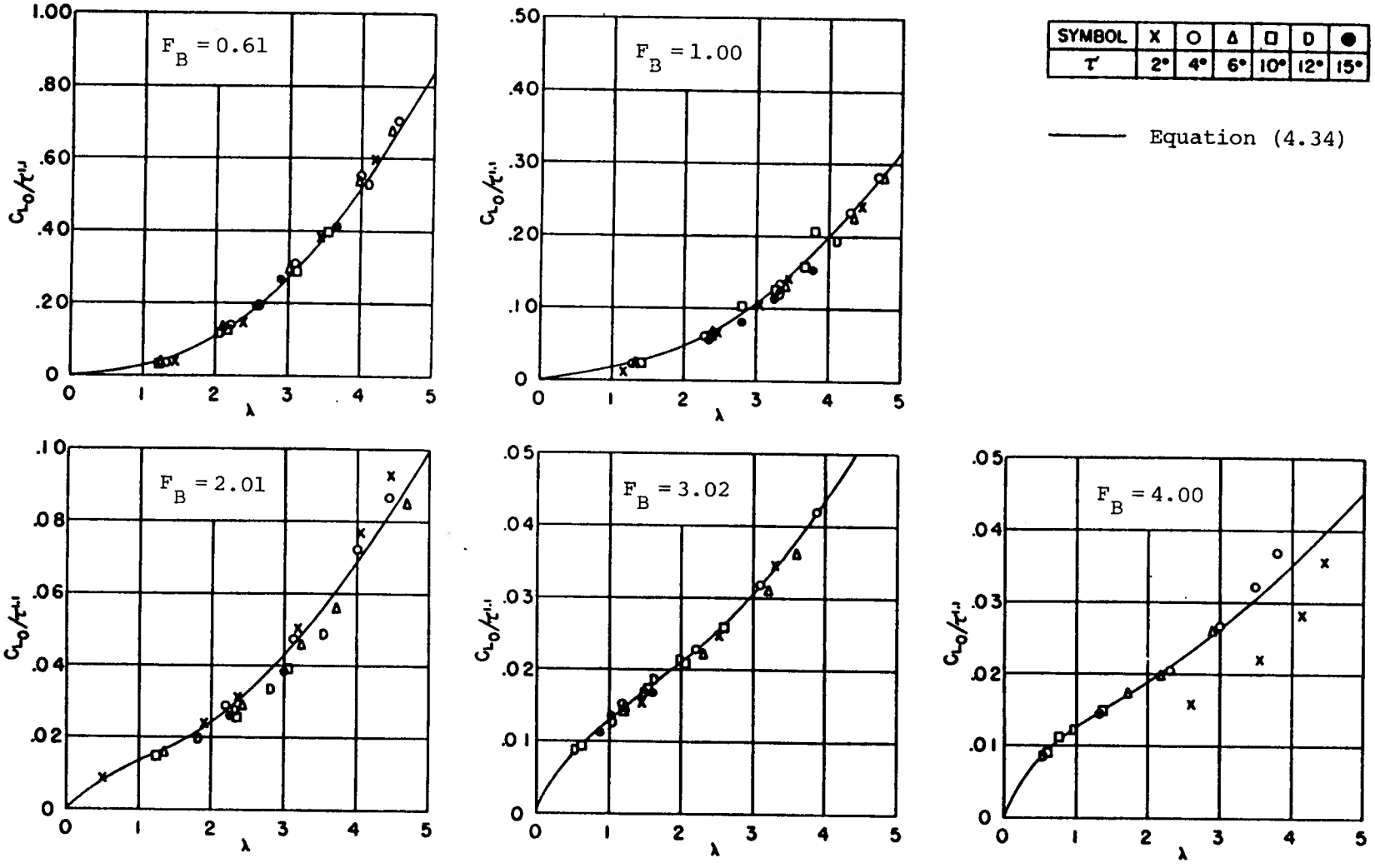

Figure 4.19: Verification of Lift Coefficient for a Flat Planing Surface

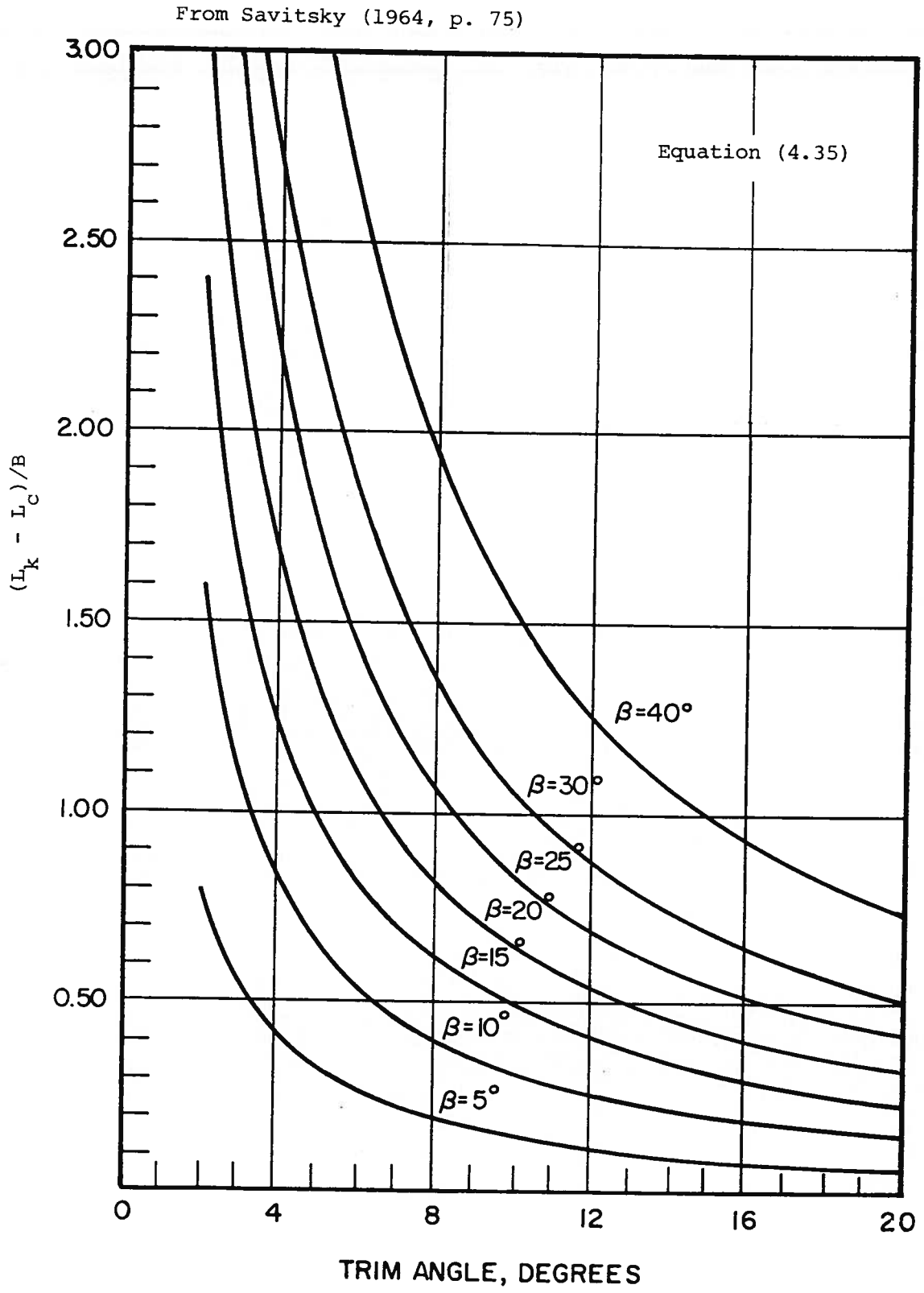

Figure 4.20: Chine Wetting for a Prismatic Planing Surface

difference can be computed on the basis of the discussion in Sec. 4.1.2, and is given by

$$L_1 = L_k - L_c = \frac{B}{\pi} \frac{\tan \beta}{\tan \tau} \text{ for } F_B > 2.0 \quad . \tag{4.35}$$

Not unexpectedly, the length difference is greater for larger deadrise angles. The mean wetted-length ratio is now defined as

$$\lambda = L_m/B \tag{4.36}$$

$$= \frac{1}{2}(L_k + L_c)/B \tag{4.37}$$

$$= \left(\frac{h}{\sin \tau} - \frac{B}{2\pi} \frac{\tan \beta}{\tan \tau}\right)/B \quad . \tag{4.38}$$

The last formula can be derived by a considering the geometry shown in Fig. 4.6, together with (4.35) and (4.37). It should be noted that the mean wetted length L_m only refers to the load-bearing part of the prism. The spray area ahead of the spray-root line basically contributes only to the drag.

The lift of a prismatic surface has been approximated by the formula

$$C_{L_\beta} = W/\frac{1}{2}\rho V^2 B^2 \tag{4.39}$$

$$= C_{L_0} - 0.0065\, \beta\, C_{L_0}^{0.60} \text{ for } F_B > 1.0 \quad , \tag{4.40}$$

in which the deadrise angle β is measured in degrees. This formula is plotted in Fig. 4.21. It shows that a prismatic surfaces suffers a small loss in lifting capacity compared to a flat surface with the same beam and mean wetted length. A test of (4.40) is provided by Fig. 4.22 which shows good correlation with the experimental points.

It is important to know the center of pressure when considering the equilibrium of the craft. Savitsky and Neidinger pointed out that the first term in (4.34) represents a dynamic lift that acts at a point $\frac{3}{4}L_m$ ahead of

From Savitsky (1964, p. 81)

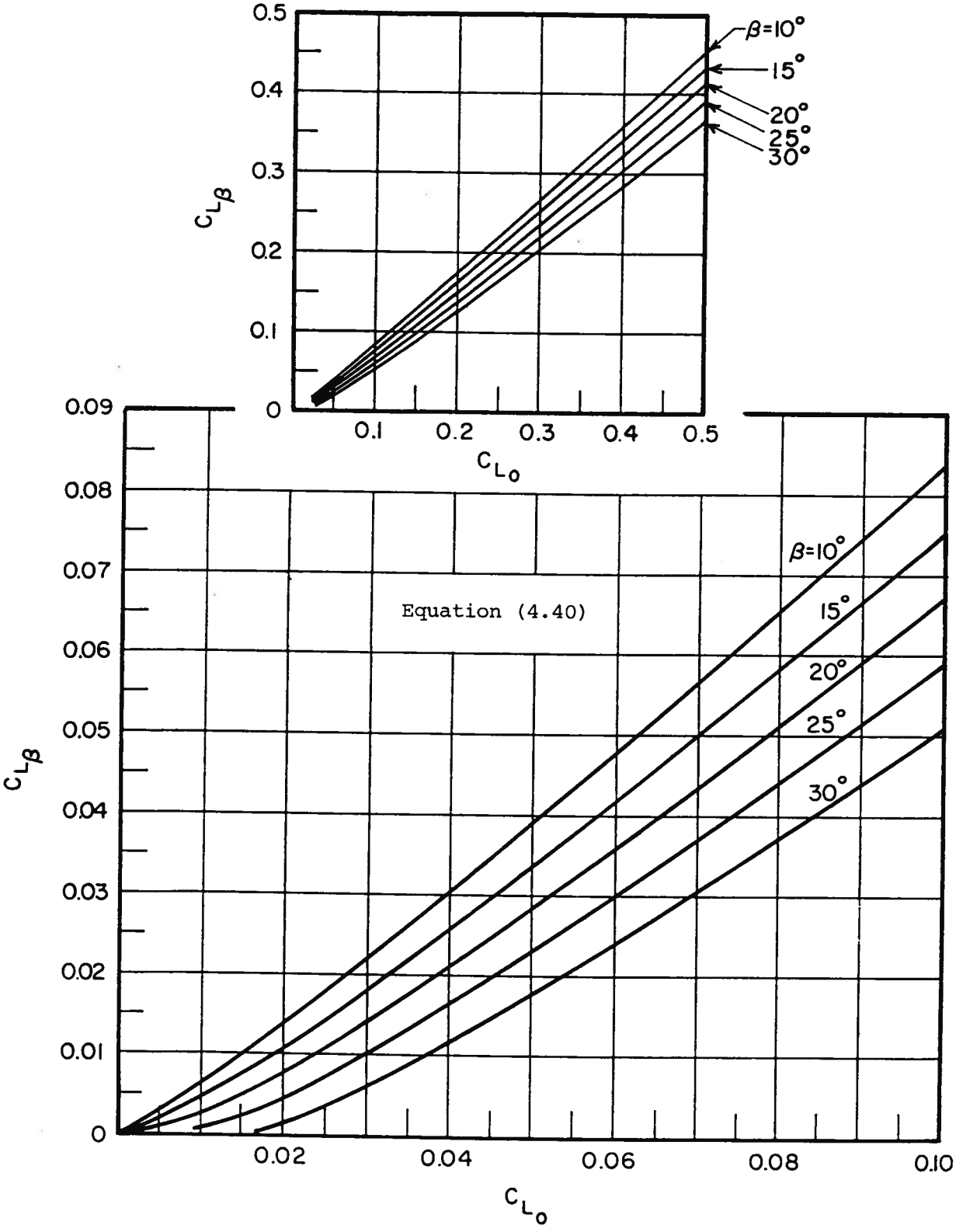

Figure 4.21: Lift Coefficient for a Prismatic Planing Surface

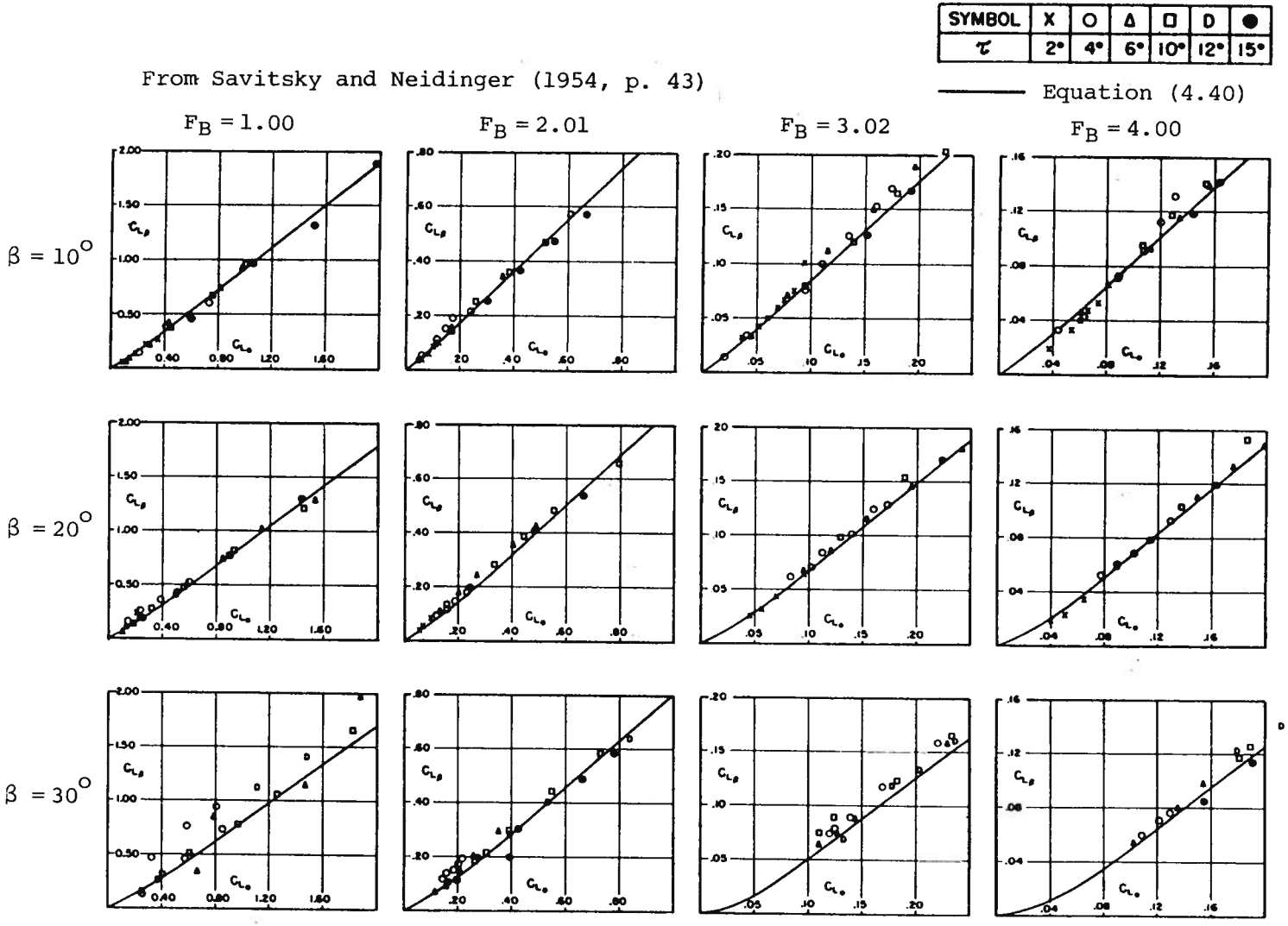

Figure 4.22: Verification of Lift Coefficient for a Prismatic Planing Surface

the transom, while the second term represents a hydrostatic force that would act $\frac{1}{3}L_m$ ahead of the transom. The moments can now be used to compute the location of the center of pressure:

$$L_p/L_m = \frac{\tau^{1.1}\left(\frac{3}{4}\times 0.0120\ \lambda^{1/2} + \frac{1}{3}\times 0.0055\ \lambda^{5/2}/F_B{}^2\right)}{\tau^{1.1}(0.0120\ \lambda^{1/2} + 0.0055\ \lambda^{5/2}/F_B{}^2)} \quad .$$

This analysis ignores the effect of deadrise, which would influence the numerator and the denominator of this equation in the same direction, but by different amounts. This result may be simplified to give

$$L_p/L_m = 0.75 - 1/(5.21\ F_B{}^2/\lambda^2 + 2.39) \text{ for } 0.60 \leq F_B \leq 13.0 \text{ and } \lambda \leq 4.0 \quad . \tag{4.41}$$

This result is plotted in Fig. 4.23. The center of pressure is seen to approach a point $\frac{3}{4}L_m$ ahead of the stern as the beam Froude number approaches infinity. The formula is tested against experimental data in Fig. 4.24. The fact that the trim and the deadrise angle do not play a role in (4.41) is justified by these results.

4.4.3. Calculation of Drag

The normal pressure force N and the frictional force D_F that act on a planing surface are shown in Fig. 4.25. The force diagram shows that the drag can be written as

$$D = W \tan\tau + D_F/\cos\tau \quad . \tag{4.42}$$

The first term in (4.42) is straightforward. The frictional force in the second term can be written approximately as

$$D_F = \frac{1}{2}\rho V_m{}^2 S_F C_F \quad , \tag{4.43}$$

where V_m is the average velocity of the fluid over the bottom, S_F is the effective frictional area, and C_F is the coefficient of friction.

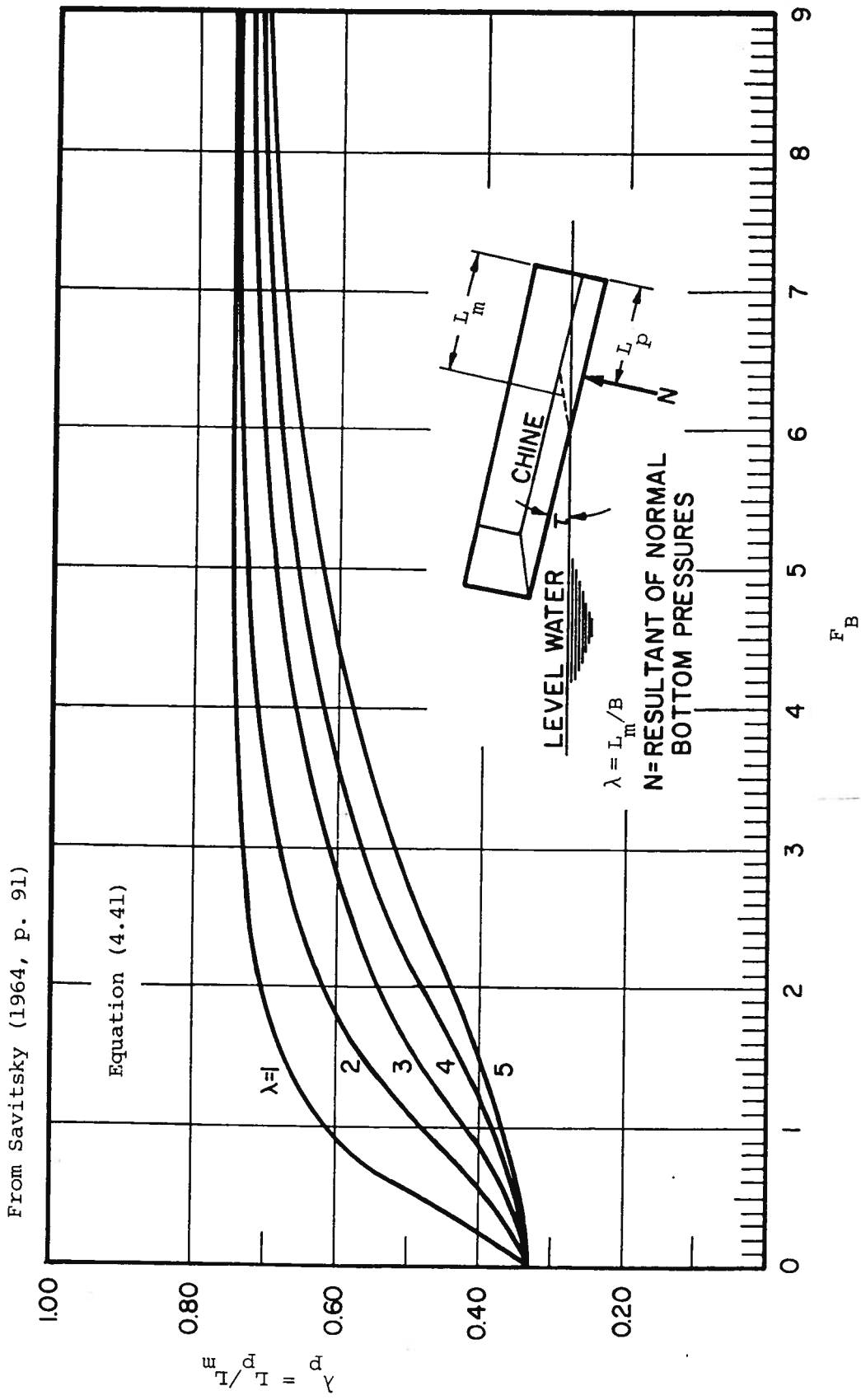

Figure 4.23: Location of Center of Pressure

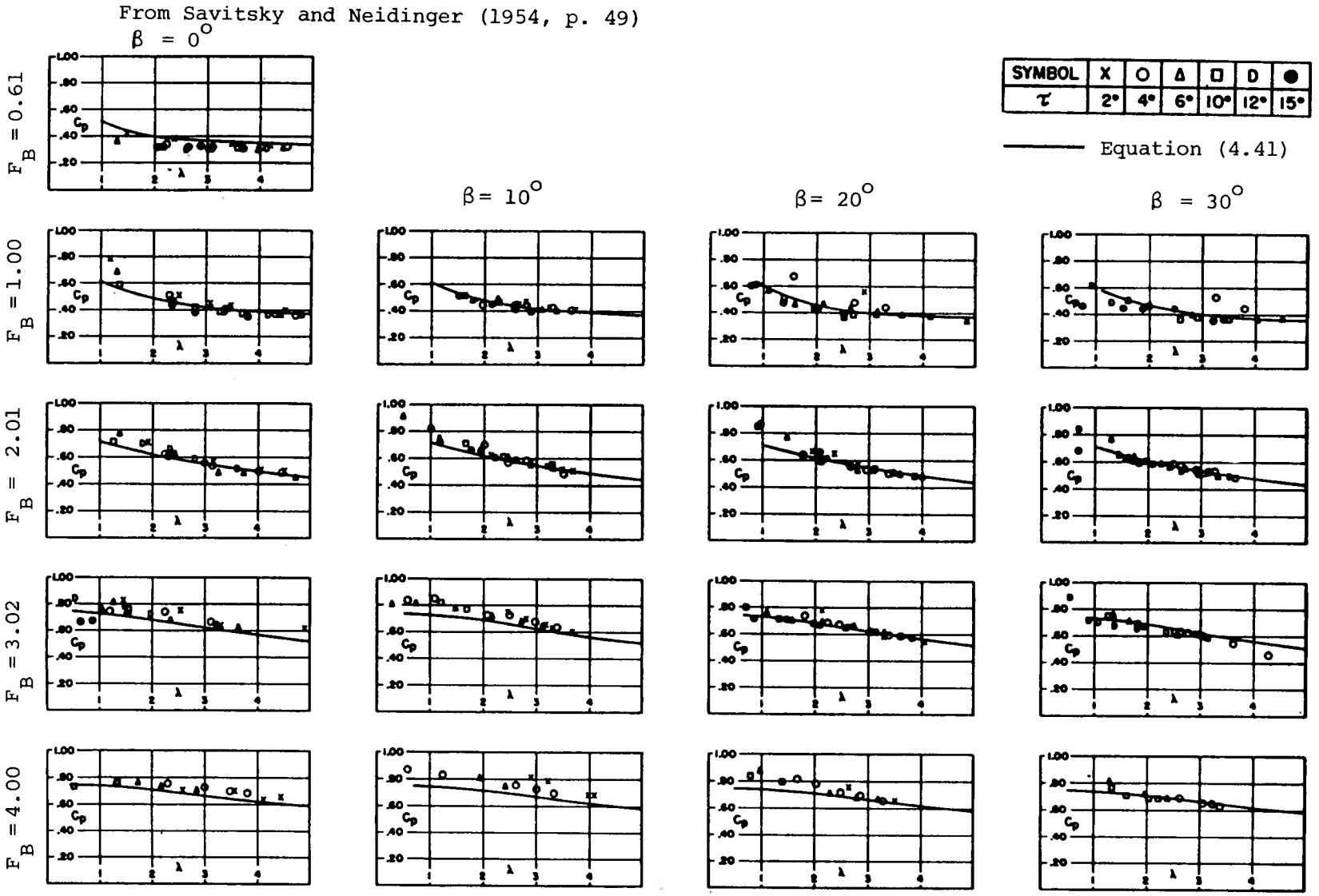

Figure 4.24: Verification of Location of Center of Pressure

From Savitsky (1964, p. 83)

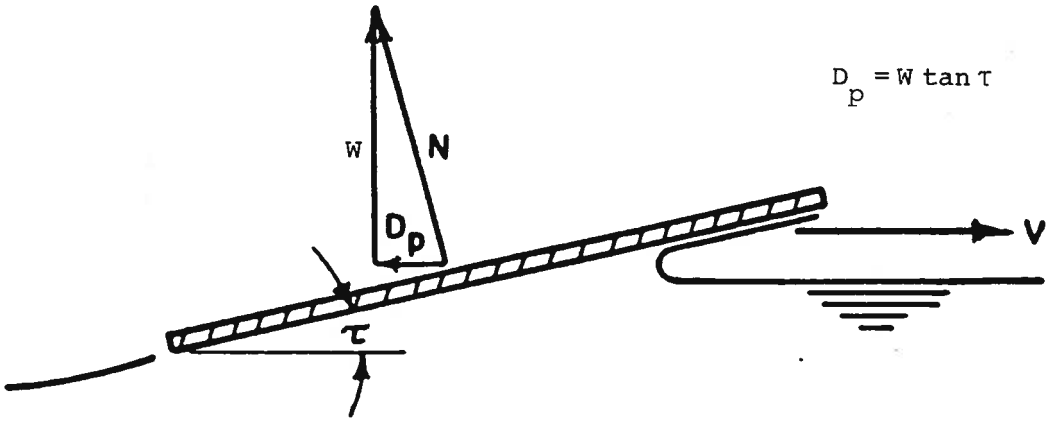

a) FRICTIONLESS FLUID

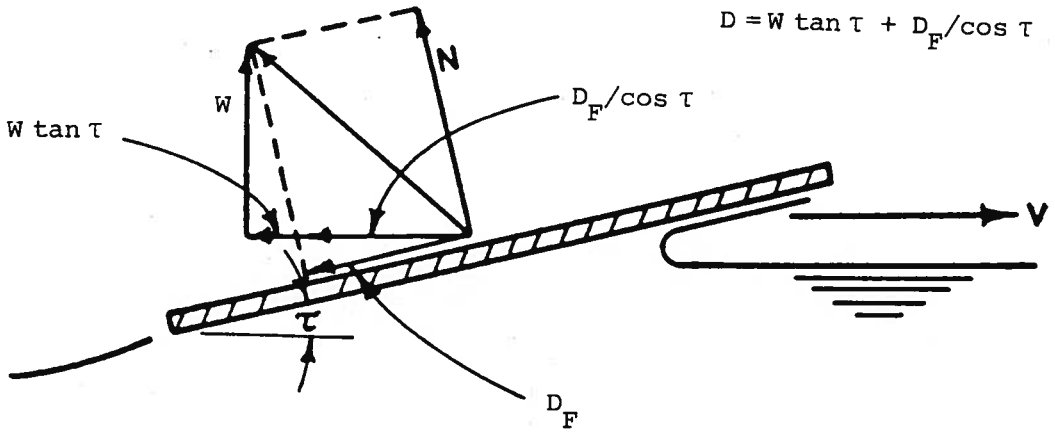

b) VISCOUS FLUID

Figure 4.25: Drag Components on a Planing Surface

The average velocity can be estimated by considering the dynamic lift component of (4.34), together with the deadrise correction (4.40):

$$C_{L_d} = 0.0120\,\lambda^{1/2}\tau^{1.1} - 0.0065\,\beta(0.0120\,\lambda^{1/2}\tau^{1.1})^{0.6} \quad , \tag{4.44}$$

which can be used to compute the dynamic part of the load:

$$W_d = \frac{1}{2}\rho V^2 B^2 C_{L_d} \quad . \tag{4.45}$$

Thus the average dynamic pressure is

$$\begin{aligned} p_d &= W_d/\lambda B^2 \cos\tau \\ &= C_{L_d}\rho V^2/2\lambda \cos\tau \quad . \end{aligned} \tag{4.46}$$

Savitsky's analysis ignores the $\cos\beta$ factor which should properly be included in the denominator of (4.46). Finally, we can apply the Bernoulli equation between some point upstream where the velocity is V, and an average point on the planing surface, where the velocity V_m is presumed to exist. The height of this point relative to the datum is ignored in this calculation, since the hydrostatic part of the lift was deliberately excluded from (4.44). Hence,

$$\begin{aligned} V_m &= V\left(1 - p_d/\frac{1}{2}\rho V^2\right)^{1/2} \\ &= V\left(1 - C_{L_d}/\lambda \cos\tau\right)^{1/2} \quad . \end{aligned} \tag{4.47}$$

This formula has been plotted in Fig. 4.26. The graphs show how decreasing the wetted-length ratio or increasing the deadrise angle both reduce the value of the average velocity on the bottom.

Returning to (4.43), we note that S_F can be computed from the relationship

$$S_F = \lambda_F B^2/\cos\beta \quad , \tag{4.48}$$

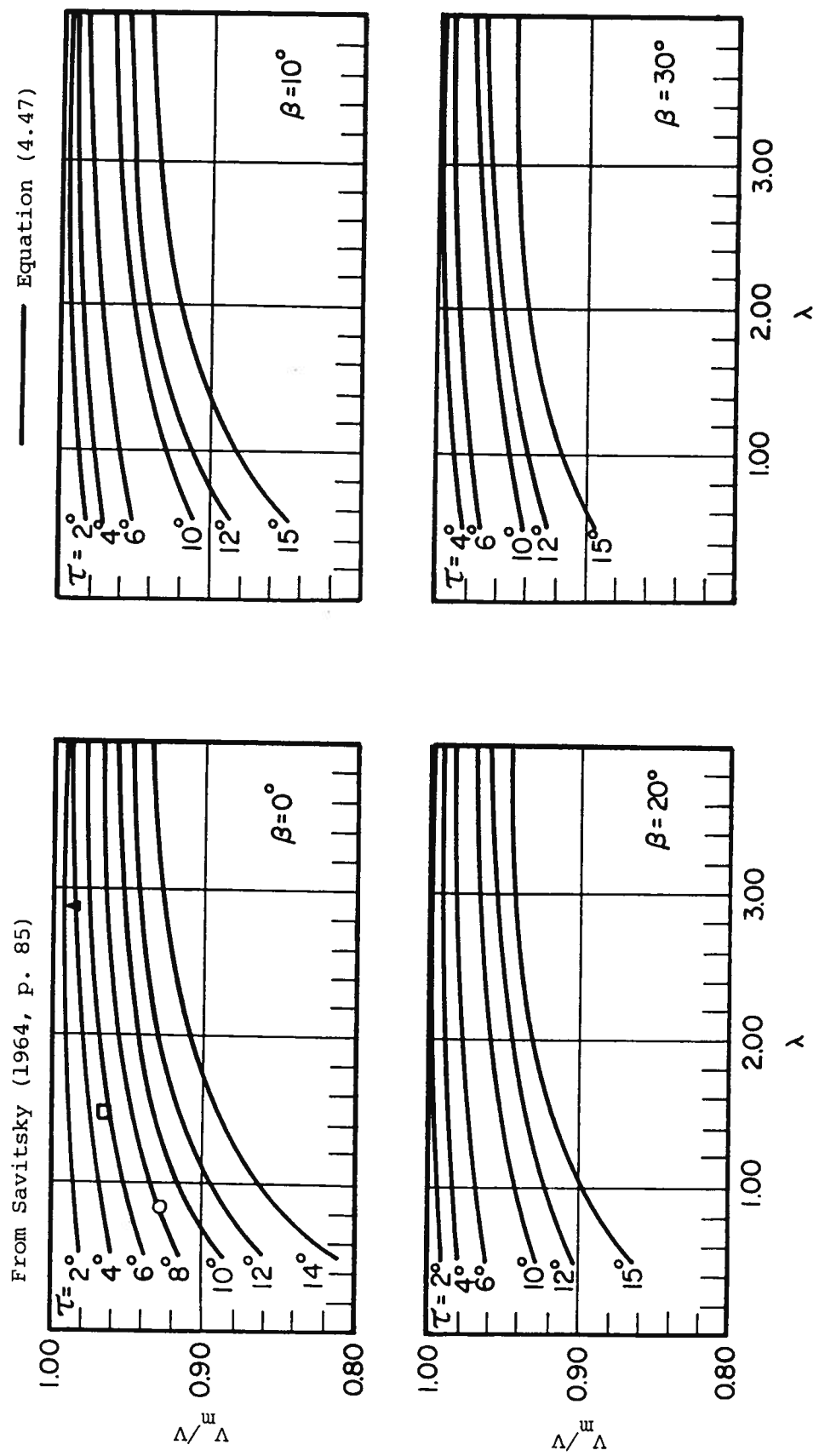

Figure 4.26: Magnitude of Average Bottom Velocity for a Prismatic Surface

where λ_F is the friction-wetted-length-to-beam ratio. It takes into account the frictional forces on the spray area, seen in Fig. 4.27. Savitsky and Neidinger suggested that it could be calculated from the formula

$$\lambda_F = \lambda + \Delta\lambda \quad , \tag{4.49}$$

in which the correction $\Delta\lambda$ is plotted in Fig. 4.28. However, in his later paper, Savitsky (1964) indicated that the figure should not be used for τ less than 4°. For τ less than 4°, he advised that $\Delta\lambda$ should be set to zero.

Finally, the coefficient of friction in (4.43) can be computed using one of the standard formulas for the drag on a flat plate. These formulas require the value of the Reynolds number based on the frictional length and the average velocity. That is

$$R = \rho V_m (B\lambda_F)/\mu \quad , \tag{4.50}$$

where μ is the water viscosity. A recommended pair of approximations for the coefficient of friction is the one-seventh-power-law formula:

$$C_F = 0.074\ R^{-1/5} \text{ for } 5\times10^5 < R < 10^7 \quad , \tag{4.51}$$

and the logarithmic-law formula:

$$C_F = 0.455/(\log_{10}R)^{2.58} \text{ for } 10^5 < R < 10^9 \quad , \tag{4.52}$$

which were given by Schlichting (1962). In addition, the standard American Towing Tank Committee (ATTC) roughness should be included:

$$\Delta C_F = 0.0004 \quad . \tag{4.53}$$

4.5. Calculation of the Equilibrium Condition

In this section, we will apply the information presented in Sec. 4.4 to the problem of determining the performance of a planing boat in which the following data is supplied: the beam B, the deadrise angle β, the weight W, propeller shaft-line inclination ε and its displacement from the center

From Savitsky (1964, p. 78)

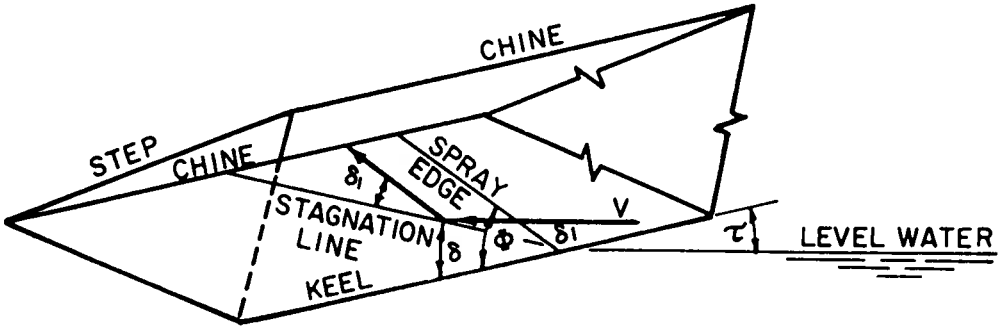

$$\tan\theta = \tan\Phi \cos\beta$$

$$\tan\alpha = \frac{\pi}{2} \frac{\tan\tau}{\tan\beta}$$

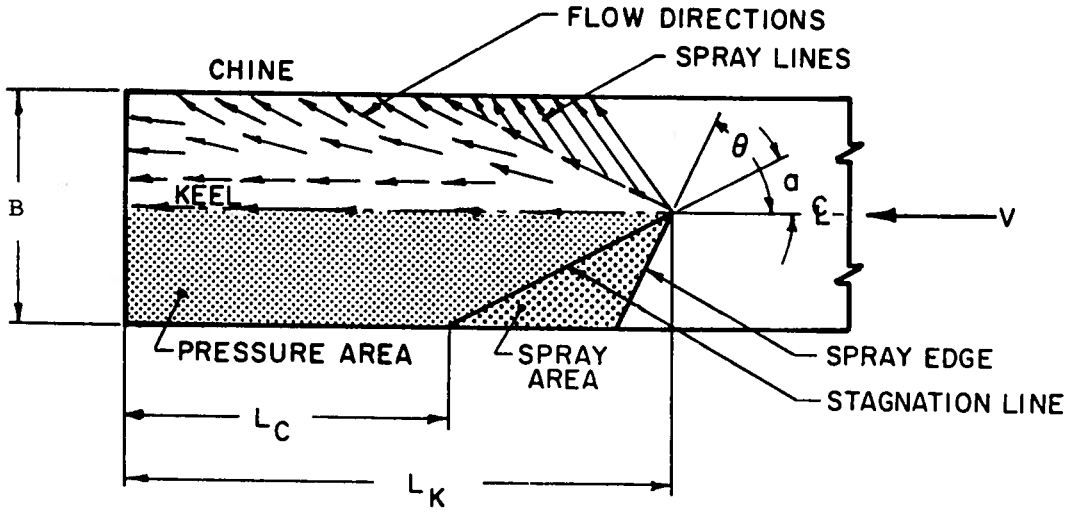

VIEW OF BOTTOM ON PLANE PARALLEL TO KEEL

Figure 4.27: Flow Direction along Planing Prism

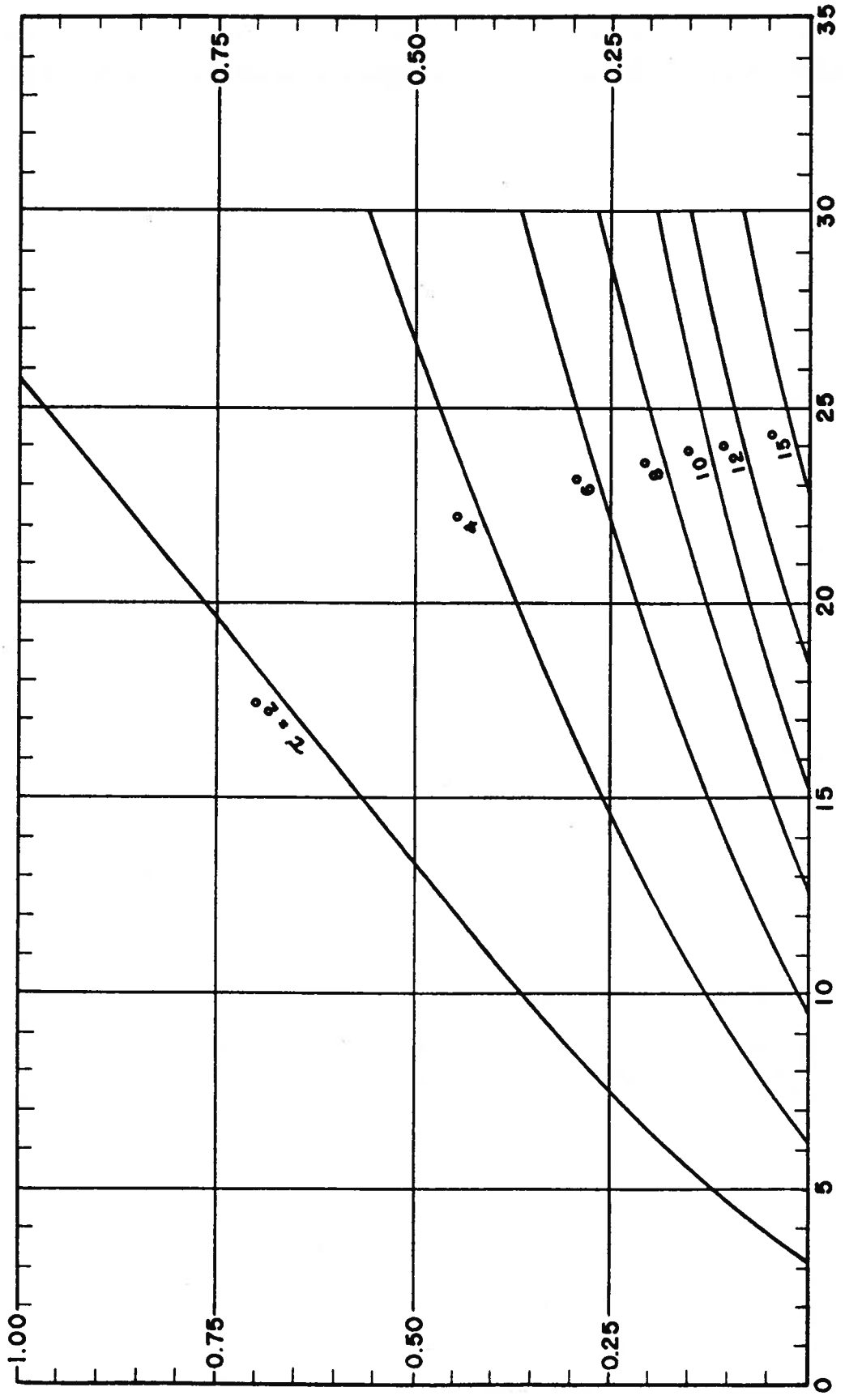

From Savitsky and Neidinger (1954, p. 47)

Figure 4.28: The Spray Increase in Effective Friction Length

of gravity f, the location of the center of gravity ahead of the transom L_G, and above the keel H_G, and the speed of the boat V. We are interested in determining the running trim angle τ, the wetted length at the keel L_k and at the chine L_c, the total resistance D, the keel draft h, and the required propeller thrust T. These quantities are shown in Fig. 4.29(a).

We can resolve the forces on the boat parallel to the keel to obtain

$$T \cos \varepsilon - W \sin \tau - D_F = 0 \quad , \tag{4.54}$$

and normal to the propeller-shaft line to get

$$N \cos \varepsilon - W \cos(\tau + \varepsilon) + D_F \sin \varepsilon = 0 \quad . \tag{4.55}$$

For equilibrium of the moments about the center of gravity, we have

$$M = Tf - Nc - D_F a = 0 \quad . \tag{4.56}$$

In these equations, f is the moment arm for the thrust, N is the normal force on the hull, and c is the arm for its moment about the center of gravity, which is given by

$$c = L_G - L_p \quad . \tag{4.57}$$

The arm for the moment of the frictional force is simply

$$a = H_G - \frac{1}{4} B \tan \beta \quad . \tag{4.58}$$

The effective power is given by the formula

$$P_e = DV \quad . \tag{4.59}$$

The draft of the keel at the transom is just

$$h = L_k \sin \tau \quad . \tag{4.60}$$

The difficulty in solving these equations lies in the fact that the trim angle is not known beforehand; it must be chosen to satisfy the equations of equilibrium. The Savitsky long-form method for the solution is listed in Table 4.2. It starts with an assumed value of τ, from which the moment M in (4.56) can be computed directly. If M is not sufficiently close to zero,

From Savitsky (1964, pp 89 and 90)

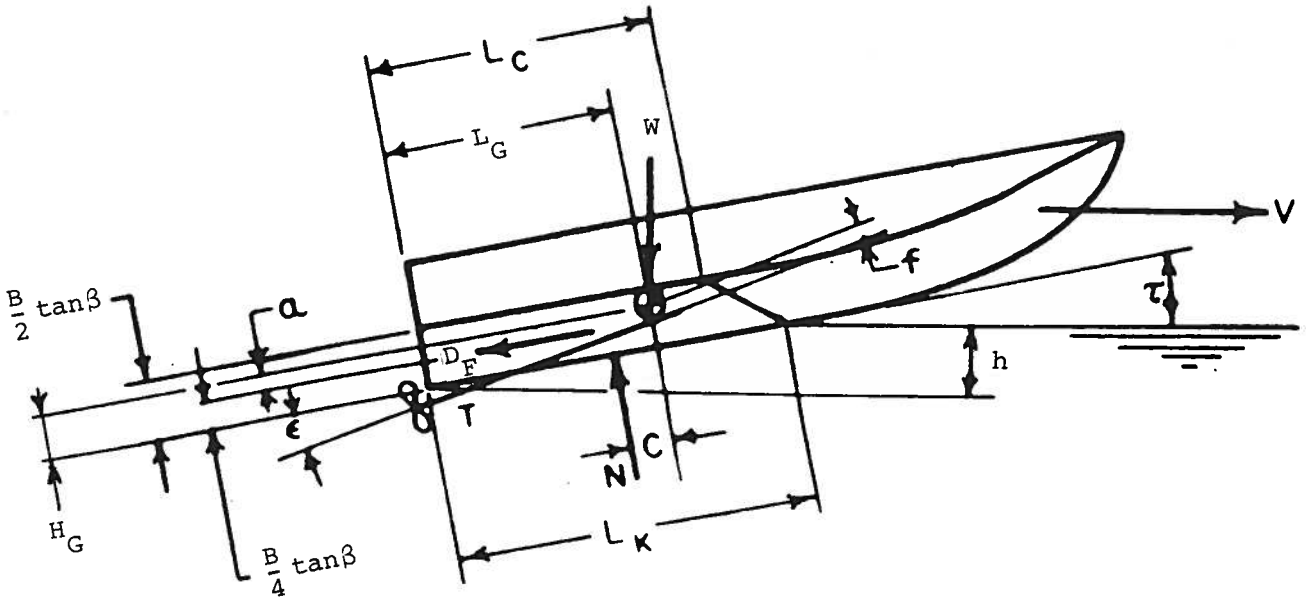

(a) The General Case

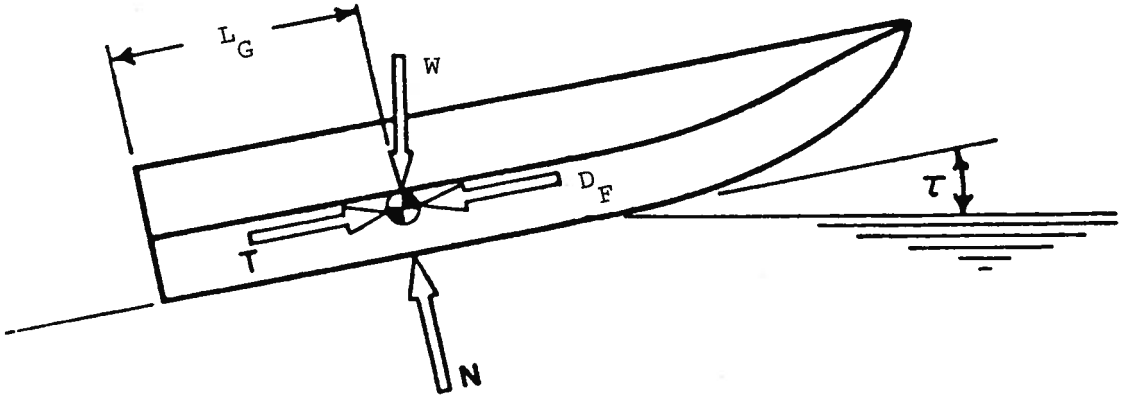

(b) The Case of Concurrent Forces

Figure 4.29: Equilibrium of a Planing Boat

then the value of τ should be adjusted, and the calculation iterated.

A modification which is more suitable for hand calculations is to use two trial values of τ, and to employ linear interpolation to find the value corresponding to zero moment.

In Step 4 of the process, (4.40) must be inverted. That is, C_{L_0} is required from the other variables in that equation. The value of C_{L_0} can be obtained from Fig. 4.21. Alternatively, (4.40) can be solved using either the Newton-Raphson method, or the method of repeated substitution. The latter is easily programmed by writing the (n + 1)'th estimate as

$$C_{L_0}^{(n+1)} = C_{L_\beta} + 0.0065\ \beta [C_{L_0}^{(n)}]^{0.6} \quad ,$$

where the superscript (n) refers to the n'th estimate. A good starting procedure is to take $C_{L_0}^{(1)} = C_{L_\beta}$. This iterative technique converges to four significant figures in about five iterations.

Similarly, at Step 5, we need to invert (4.34). This time, Fig. 4.18 can be used. A method suitable for numerical computation, is to rewrite the equation as

$$\lambda^{(n+1)} = \left\{F_B^2\left(C_{L_0}/\tau^{1.1}[\lambda^{(n)}]^{1/2} - 0.0120\right)/0.0055\right\}^{1/2} \quad ,$$

with the first estimate taken as $\lambda^{(1)} = \left(F_B^2 C_{L_0}/0.0055\ \tau^{1.1}\right)^{2/5}$.

A simplification to this method is to assume that all the forces on the boat act through the center of gravity. The situation is shown in Fig. 4.29(b). In this case, no iteration is required, as the moment equation (4.56) is automatically solved. However, (4.41) has to be inverted. That is, we need to find λ in terms of F_B and L_p/B. The procedure has been simplified by the production of a nomogram in Fig. 4.30. This technique is called the Savitsky short-form method, and is listed in Table 4.3.

Table 4.2: Savitsky Long-Form Method

Step	Quantity	Meaning	Source
1	τ	Running Trim	Estimate
2	F_B	Beam Froude number	(4.1)
3	C_{L_β}	Deadrise lift coefficient	(4.39)
4	C_{L_0}	Flat-plate lift coefficient	(4.40) or Fig. 4.21
5	λ	Mean-wetted-length ratio	(4.34) or Fig. 4.18
6	C_{L_d}	Dynamic-lift coefficient	(4.44)
7	V_m	Average bottom velocity	(4.47) or Fig. 4.26
8	$\Delta\lambda$	Spray correction to wetted length	Fig. 4.28
9	λ_F	Frictional-wetted-length ratio	(4.49)
10	R	Reynolds number	(4.50)
11	C_F	Coefficient of Friction	(4.51) or (4.52)
12	ΔC_F	ATTC standard roughness	(4.53)
13	S_F	Frictional wetted area	(4.48)
14	D_F	Frictional drag	(4.43)
15	D	Drag	(4.42)
16	T	Propeller thrust	(4.54)
17	N	Normal force	(4.55)
18	L_p	Center of pressure	(4.41) or Fig. 4.23
19	c	Arm for normal force	(4.57)
20	a	Arm for frictional force	(4.58)
21	M	Moment on boat	(4.56)
22	τ	Repeat (1) through (21) until M=0, or use interpolation, to find τ	
23	P_e	Effective power	(4.59)
24	L_k	Keel wetted length	(4.35)
25	L_c	Chine wetted length	(4.35)
26	h	Draft of keel at transom	(4.60)

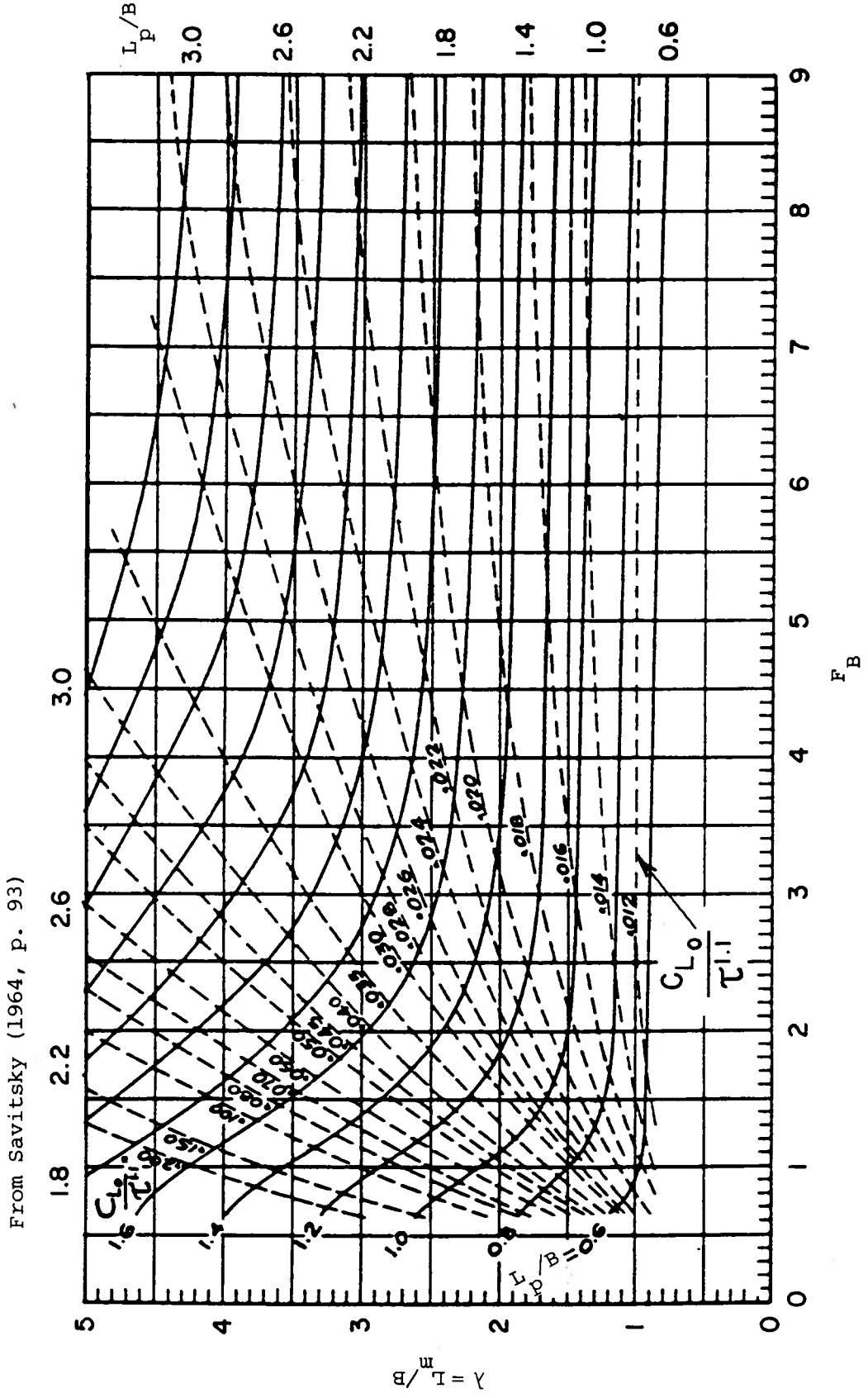

Figure 4.30: Nomogram for the Case of Concurrent Forces

Table 4.3: Savitsky Short-Form Method

Step	Quantity	Meaning	Source
1	F_B	Beam Froude number	(4.1)
2	C_{L_β}	Deadrise lift coefficient	(4.39)
3	C_{L_0}	Flat-plate lift coefficient	(4.40) or Fig. 4.21
4	L_p/B	Center of Pressure	(4.57) with c = 0
5	λ	Mean-wetted-length ratio	(4.41) or Fig. 4.30
6	$C_{L_0}/\tau^{1.1}$	Reduced flat-plate coefficient	(4.34) or Fig. 4.30
7	τ	Running trim	Steps 3 and 6
8	C_{L_d}	Dynamic-lift coefficient	(4.44)
9	V_m	Average bottom velocity	(4.47) or Fig. 4.26
10	$\Delta\lambda$	Spray correction to wetted length	Fig. 4.28
11	λ_F	Frictional-wetted-length ratio	(4.49)
12	R	Reynolds number	(4.50)
13	C_F	Coefficient of Friction	(4.51) or (4.52)
14	ΔC_F	ATTC standard roughness	(4.53)
15	S_F	Frictional wetted area	(4.48)
16	D_F	Frictional drag	(4.43)
17	D	Drag	(4.42)
18	T	Propeller thrust	(4.54)
19	P_e	Effective power	(4.59)
20	L_k	Keel wetted length	(4.35)
21	L_c	Chine wetted length	(4.35)
22	h	Draft of keel at transom	(4.60)

Again, the graphical aspects can be avoided in a numerical procedure. The solution for C_{L_0} at Step 3 is identical to Step 4 in the long-form method, and has already been described.

At Step 5, we can rewrite (4.41) as

$$\lambda^{(n+1)} = \frac{L_p}{B}/\left[0.75 - 1/\left(5.21\ F_B^2/[\lambda^{(n)}]^2 + 2.39\right)\right] \quad ,$$

with the first estimate being $\lambda^{(1)} = (L_p/B)/0.75$. This method also converges rapidly.

4.6. Modifications to the Basic Prismatic Form

4.6.1. Warp

Many planing craft possess a certain amount of warp or twist, so that the deadrise angle increases from the transom stern toward the bow. This feature is shown in Fig. 4.7(a). A small amount of experimental work has been carried out on models, and was reported by Savitsky and Brown (1976). They suggested that the formulas presented in Sec. 4.4 could still be used, but with a change of interpretation given to the symbols.

For the lift formula (4.34), an effective trim angle should be used. This is defined as

$$\tau_e = \tau + 0.12\ \theta \text{ in (4.34)} \quad , \tag{4.61}$$

where τ is still the trim angle, but now measured at the keel only, while θ is the angle of the run of the chine (the chine therefore has a running trim of $\tau + \theta$). The deadrise angle β is now the deadrise angle only at the transom. The fact that (4.61) increases the effective trim angle by only 12% of the chine-run angle, even though the average geometric trim has been increased by 50% of the chine-run angle, implies that the lion's share of the load is carried by the surface of the bottom near the keel. The effect of increased deadrise is ignored in (4.40), however.

Regarding the calculation of the drag in (4.42), it is advised that the average geometric values of the trim and deadrise angles should be used. That is

$$\tau_e = \tau + \frac{1}{2}\theta \quad \text{in (4.42)} \quad . \tag{4.62}$$

and $\beta_e = \tan^{-1}(\tan\beta + \lambda \tan\theta)$ in (4.48) . (4.63)

It will be noted that the use of warp will increase the lift slightly, and the drag somewhat more, so that the lifting efficiency of the planing surface is reduced.

4.6.2. Variable Beam

Hadler, Hubble, and Holling (1974) carried out a number of computations comparing the predictions of the formulas given in Sec. 4.4 with the experimental results on the Series 65 planing-hull forms. They stated that the best agreement was achieved when the following were used: (a) the mean beam B over the chines, and (b) the deadrise β at half the chine length ahead of the transom. Their comment regarding the deadrise is compatible with the advice given in Sec. 4.6.1.

4.6.3. Transom Flaps

The use of flaps was investigated by Savitsky and Brown (1976). The nomenclature together with some results of their use are shown in Fig. 4.31. Their study showed that the flap lift is given by

$$\Delta W = 0.046\, cs\delta\, \frac{1}{2}\rho V^2 \quad , \tag{4.64}$$

where c is the chord of the flap, s is its span, and δ is the flap deflection in degrees. This increment in lift will be part of the total boat weight W in (4.42). The flap experiences a form of drag given by

$$\Delta D = 0.0052\, \Delta W(\tau + \delta) \quad , \tag{4.65}$$

From Savitsky and Brown (1976, p. 385)

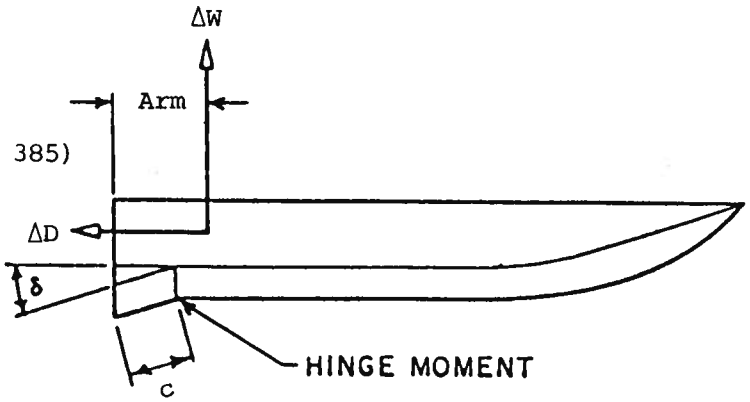

(a) Nomenclature

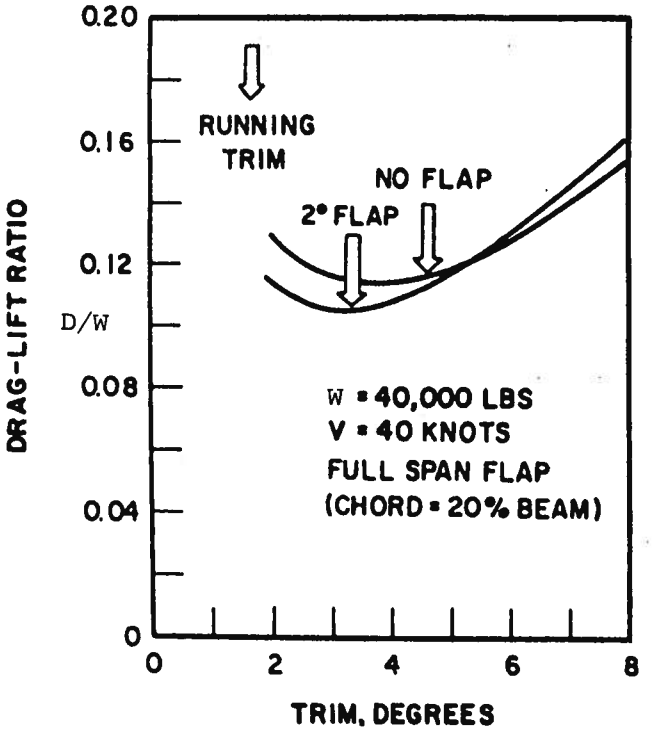

(b) Effect of Flaps on Performance

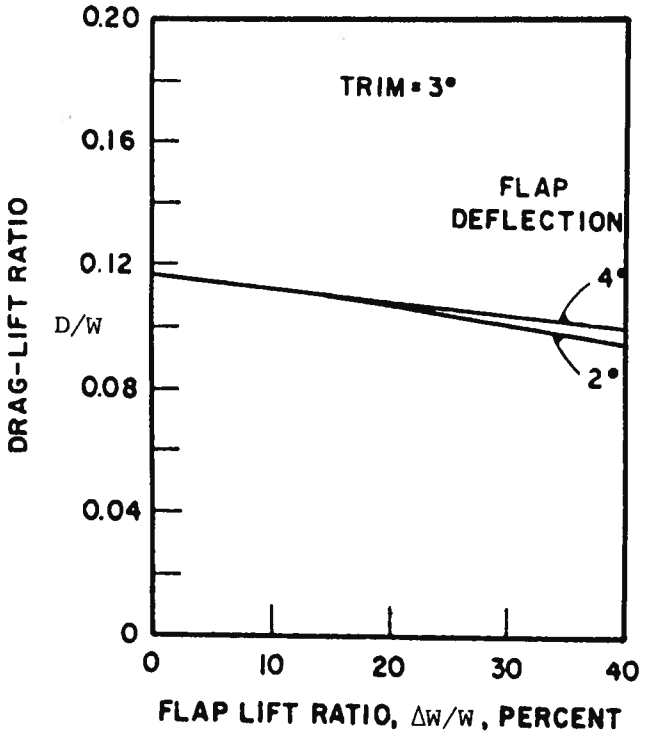

(c) Effect of Flap-Lift on Total Drag-Lift Ratio

Figure 4.31: The Use of Transom Flaps

while the frictional force has already been included in the calculation (4.48), since the flap is assumed to be made of part of the original hull. The bow-up moment exerted on the boat, about its center of gravity is

$$\Delta M = [0.6\ B + c(1 - s/B) - L_G]\Delta W \quad , \tag{4.66}$$

where L_G is the longitudinal center of gravity ahead of the transom. Finally, the torque required to keep the flap deflected against the hydrodynamic moment (the hinge moment) is given by

$$H = 0.139\ c\ \Delta W \quad . \tag{4.67}$$

Formulas (4.64) through (4.67) have been validated for the following ranges of the relevant variables: $0 \leq c/L_m \leq 0.10$, $0 \leq \delta \leq 15°$, $0 \leq \tau \leq 10°$, and $2 \leq F_B \leq 7$. Additionally it was found that the transverse location of part-span flaps ($s < B$) was unimportant.

When performing the equilibrium calculations with flaps, the drag increment ΔD (4.65) must be added to the frictional drag D_F in (4.42), (4.54), (4.55), and (4.56). The moment increment ΔM (4.66) must be included in (4.56). The craft weight W must be decremented by the amount ΔW (4.64) for the purpose of computing the lift coefficient C_L in (4.33) or (4.39). Similarly, the center-of-gravity calculation (4.57) must take into account the flap moment (4.66).

Fig. 4.31(b) shows that the full-span flap at a deflection of 2°, used in the example, reduces the overall drag by 10%. The optimum trim angle is also reduced. Fig. 4.31(c) shows the effect of increasing the flap area, for two different flap deflections. While both flaps reduce the drag, the larger one with a smaller angle is superior.

It should be remarked that the use of flaps is hydrodynamically equivalent to adding negative rocker, or positive camber. As noted in Sec. 4.2, this feature can improve the lift-to-drag ratio.

4.6.4. Appendages

Skegs. A thin skeg will generate a negligible lift. According to Hadler (1966), its drag can be estimated from the formula

$$\Delta D = \frac{1}{2}\rho V_m^2 (2S) C_F \quad , \tag{4.68}$$

where S is the area of one side of the skeg, and C_F is the coefficient of friction based on the skeg length and the mean bottom velocity V_m, given by (4.47). This drag component acts in a direction parallel to the keel of the boat.

Propeller Shaft and Strut Bossing. The drag is assumed to act parallel to the keel and is given by

$$\Delta D = \frac{1}{2}\rho V^2 \ell d (1.1 \sin^3\varepsilon + \pi C_F) \quad , \tag{4.69}$$

where ℓ and d are the length and diameter of the shaft, while ε is its inclination relative to the keel. This formula takes into account both profile and frictional forces. The latter can be estimated from the coefficient of friction for the shaft C_F, which depends on the Reynolds number calculated on the basis of boat speed and shaft diameter.

Equation (4.69) is claimed to be valid if this Reynolds number lies in the range 10^3 to 5.5×10^5. The lift, which acts normal to the shaft is given by

$$\Delta W = \frac{1}{2}\rho V^2 \ell d (1.1 \sin^3\varepsilon \cos\varepsilon) \quad . \tag{4.70}$$

For the purpose of computing the moment in the equilibrium equation (4.56), these two forces can be assumed to act at the midpoint of the shaft.

Fully-Wetted Struts and Rudders. The drag may be calculated from the formula

$$\Delta D = \frac{1}{2}\rho V^2(2S)C_F[1 + 2(t/c)^2 + 60(t/c)^4] \quad , \tag{4.71}$$

where S is the area on one side and t/c is the thickness-to-chord ratio. The coefficient of friction C_F depends on the Reynolds number based on the boat speed V and the rudder chord c. The formula can be used if the Reynolds number is greater than 5×10^5.

If the rudder penetrates the water surface, an additional drag due to spray must be included:

$$\Delta D = 0.24\ \frac{1}{2}\rho V^2 t_w^2 \quad , \tag{4.72}$$

in which t_w is the maximum rudder thickness at the water surface.

Ventilated-Wedge Rudder. A surface-piercing wedge rudder with a trailing cavity has a drag which can be estimated from the formula:

$$\Delta D = [2C_F + A(t/c)^2(1 + gh/V^2) + 0.24\ t_w^2/S + B]\frac{1}{2}\rho V^2 S \quad , \tag{4.73}$$

where C_F is the frictional-drag coefficient for one side of the rudder, which depends on the Reynolds number based on the boat speed and the rudder chord c, t is the maximum thickness, g is the acceleration due to gravity, and S is the area on one side of the rudder. The second term accounts for the cavity drag, in which $A = 2/\pi$ for a simple wedge section, and $A = 8/9\pi$ for a convex-parabolic section whose sides are parallel at the end. The second term also contains a correction for the cavitation number being a function of the rudder height h. The third term represents the spray drag (4.72). The fourth term is an additive correction which should be applied if the aspect ratio is less than 2.5:

$$B = (2.5 - h/c)^2/150 \text{ if } h/c < 2.5 \quad . \tag{4.74}$$

Strut Palms. If struts are attached to the hull by means of non-flush palms, then one can approximate the additional drag as

$$\Delta D = 0.75\, C_D (h/\delta)^{1/3} wh \tfrac{1}{2}\rho V^2 \quad , \tag{4.75}$$

where C_D is a drag coefficient whose value would be 0.65 for a rectangular shape with rounded edges, h and w are the height and width of the palm, and δ is the boundary-layer thickness at the location of the palm. The latter can be estimated, from Schlichting (1962, p. 537), as

$$\delta = 0.37\, x(\rho V_m x/\mu)^{-1/5} \quad , \tag{4.76}$$

where x is the distance from the palm to the spray root.

Interference Drag. Finally, an additional component of drag arises from the flow distortion where struts and rudders meet the planing surface. These can be estimated as

$$\Delta D = \tfrac{1}{2}\rho V^2 t^2 [0.75(t/c) - 0.0003/(t/c)^2] \quad , \tag{4.77}$$

and are seen to depend primarily on the strut (or rudder) thickness t and chord c.

Effect on the Equations of Equilibrium. The Savitsky long-form method can easily be modified to include the effect of the appendages and flaps. We replace (4.54) through (4.56) by the three equations:

$$T \cos \varepsilon - W \sin \tau - (D_F + \textstyle\sum \Delta D_i) = 0 \quad , \tag{4.78}$$

$$(N + \textstyle\sum \Delta W_i)\cos \varepsilon - W \cos(\tau + \varepsilon) + (D_F + \textstyle\sum \Delta D_i)\sin \varepsilon = 0 \quad , \tag{4.79}$$

and $$M = Tf - Nc - D_F a + \textstyle\sum \Delta M_i = 0 \quad . \tag{4.80}$$

In these equations, the ΔD_i are the contributions to the drag parallel to the keel from the appendages, while the ΔW_i are the contributions to the lift normal to the keel. The ΔM_i are the bow-up moments. For a flap, this is given by (4.66). For the other appendages, one must multiply the relevant

lift and drag increments by the appropriate lever arms.

4.7. Other Aspects of Planing Boats

4.7.1. Porpoising

Porpoising is defined as the combined nonlinear oscillations of a boat in pitch and in heave of sustained or increasing amplitude, which occurs while planing in smooth water. The energy for driving this unwanted motion is derived from the forward momentum of the boat. Porpoising is peculiar to high-speed planing hulls. The motions can be so severe as to throw the boat completely out of the water and to cause severe structural damage.

During part of the cyclic behavior, the boat might assume a nose-down attitude which could lead to the craft diving, or tripping over the bow.

Porpoising limits are plotted in Fig. 4.32. The experiments showed that for any particular deadrise angle, there is a trim angle (as a function of the lift coefficient), at which porpoising will begin. Lowering the trim angle always increases the margin against porpoising. It is also seen that increasing the deadrise angle increases the margin against porpoising.

As pointed out by Savitsky (1964), the optimum trim angle from the point of view of lift-to-drag ratio is usually higher than the safe angle from the viewpoint of porpoising. Thus it is generally necessary to run the boat at a somewhat unfavorable trim angle. This problem can be partly alleviated by the use of deadrise.

It should also be emphasized that the pitch moment of inertia does not affect the porpoising limits in Fig. 4.32. The moment of inertia will, of course, affect the frequency of any resulting motion.

From Savitsky (1964, p. 92)

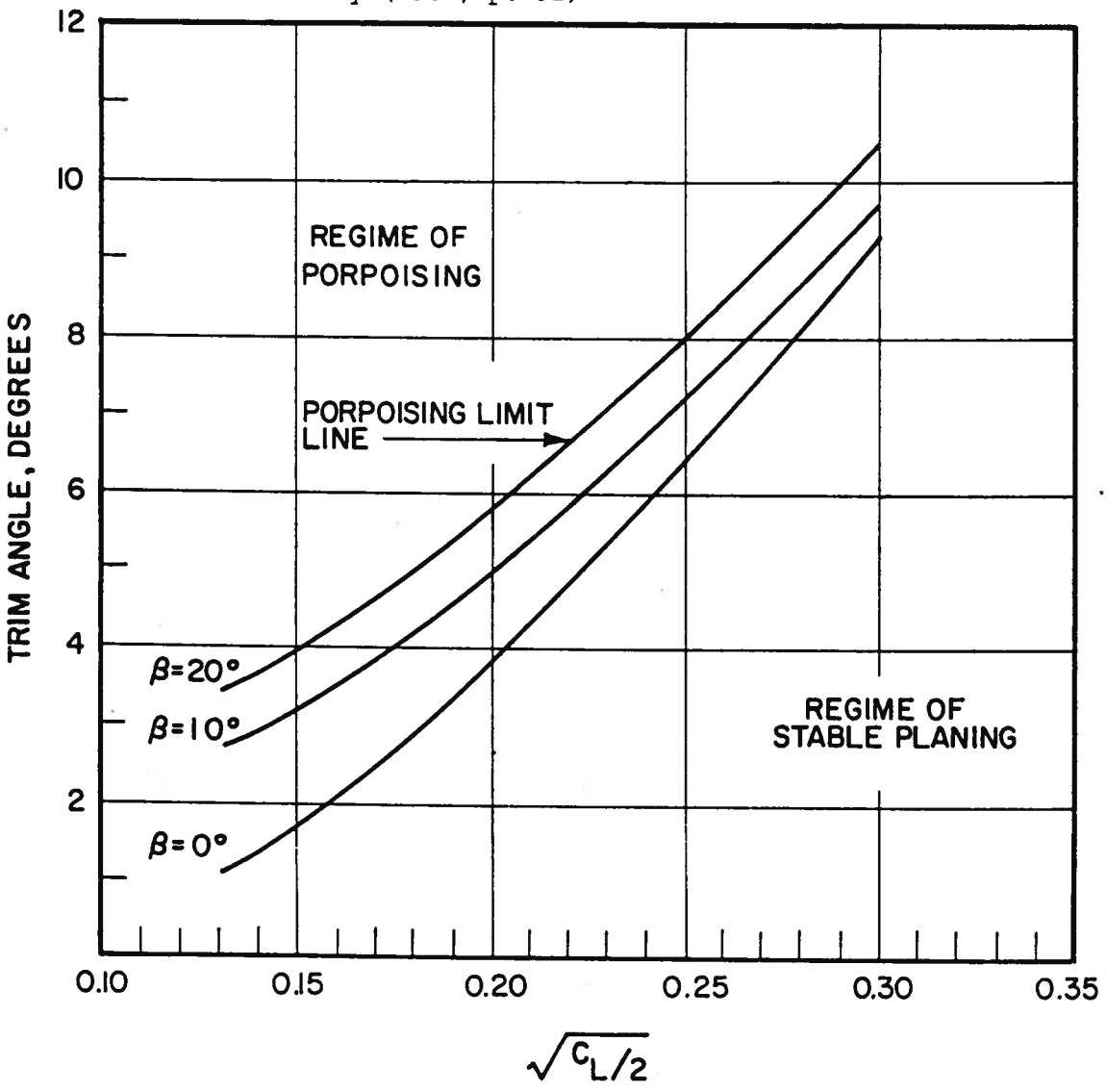

Figure 4.32: Porpoising Limits for Prismatic Planing Hulls

4.7.2. Motions and Accelerations in Waves

Savitsky and Brown (1976) presented formulas for computing the added resistance of a planing boat at three different Froude numbers. These results were obtained from a series of tests on models. The chief outcome of these experiments was to illustrate the nonlinearity of the phenomenon of planing-boat motions: the motions are not proportional to the wave height.

For the added resistance in waves, the results are:

$$\frac{\Delta D}{\rho g B^2} = 66\times10^{-6}\left(\frac{H_{1/3}}{B} + 0.5\right)\frac{L^3}{\nabla} + 0.0043(\tau - 4) \text{ at } F = 0.60 \quad , \tag{4.81}$$

where $H_{1/3}$ is the significant wave height, and L is the boat length. This formula indicates that deadrise has no effect. The precision is ± 20%.

$$\frac{\Delta D}{W} = \frac{0.3\ H_{1/3}/B}{1 + 2H_{1/3}/B}\left(1.76 - \frac{\tau}{6} - 2\tan^3\beta\right) \text{ at } F = 1.19 \quad , \tag{4.82}$$

where W is the boat weight. At this speed, there is an effect of deadrise, but the length is seen to be unimportant. The precision is also ± 20%.

$$\frac{\Delta D}{\rho g B^3} = \frac{0.158\ H_{1/3}/B}{1 + (H_{1/3}/B)[0.12\ \beta - 21(\nabla/B^3)(5.6 - L/B) + 7.5(6 - L/B)]} \text{ at } F = 1.79 \ , \tag{4.83}$$

where ∇ is the stationary displaced volume of the boat. This formula ignores any influence of trim or deadrise angle. It has an accuracy of ± 10%.

A single formula for the average impact acceleration at the center of gravity, for a range of speeds, was found. It is

$$\bar{a}_{CG} = 0.117\left(\frac{H_{1/3}}{B} + 0.084\right)\frac{\tau}{4}\left(\frac{5}{3} - \frac{\beta}{30}\right)\frac{V^2B^2}{\nabla} \quad , \tag{4.84}$$

in which the precision claimed is ± 20%.

The average impact accleration at the bow is

$$\bar{a}_{bow} = \bar{a}_{CG}[1 + 1.13(L/B - 2.25)/F] \quad , \tag{4.85}$$

with a precision of ± 20%.

Equations (4.81) through (4.85) have been validated for the following ranges of the variables: $3.5\times10^{-3} < \nabla/L^3 < 8.75\times10^{-3}$, $3 < L/B < 5$, $3° < \tau < 5°$, $10° < \beta < 30°$, $0.2 < H_{1/3}/B < 0.7$, and $0.60 < F < 1.79$.

4.7.3. Series Tests

Some systematic series of planing-hull forms have been tested. Three important ones are the Series 62, 63, and 65 of the David Taylor Model Basin (now the David Taylor Naval Ship Research and Development Center, in Bethesda, Maryland). These are reproduced in Figs. 4.33 through 4.37.

Details of the Series 62 are shown in Fig. 4.33. They are a hard-chine boat whose beam varies along the length. The figure shows that the models differ only in the length-to-beam ratio: other geometric properties, such as deadrise angle, buttock shape, and percentage beam variation are the same for all models. Length-to-beam ratios of 2 to 7 were tested. Information on the results for this series can be found in Hadler and Hubble (1971) and Hubble (1974).

Beys (1963) carried out tests on the round-bottom Series 63. The length-to-beam ratio of this series varies between 2.5 and 6. As indicated in Fig. 4.34, these are all geometrically similar and can therefore be represented by a single body plan.

Series 65 (see Hubble (1974) and Holling and Hubble (1974)) was divided into two sub-series, both being suitable as hulls for hydrofoil boats. Series 65-A in Fig. 4.35 is recommended for the airplane-type configuration, while Series 65-B in Fig. 4.36 was designed for the canard-type arrangement. These are both hard-chine forms, but some of the sections are seen to possess convexity -- in contrast to Series 62. (Series 63 is the softest of the three series considered here.)

Fig. 4.37 is included in order to point out the fact that Series 65 do not only incorporate variations in length-to-beam ratio. Inspection of the figure shows that there are a total of six different variations of the dead-rise angle over the boat length.

These series were tested over a number of different Froude numbers F_∇ , length-to-beam ratios L/B , longitudinal center of gravity L_G/L , and slenderness ratios $L/\nabla^{1/3}$. A designer can use the tabulated results for other values of the parameters by interpolating between the appropriate sets of data.

From Hadler and Hubble (1971, p. 368)

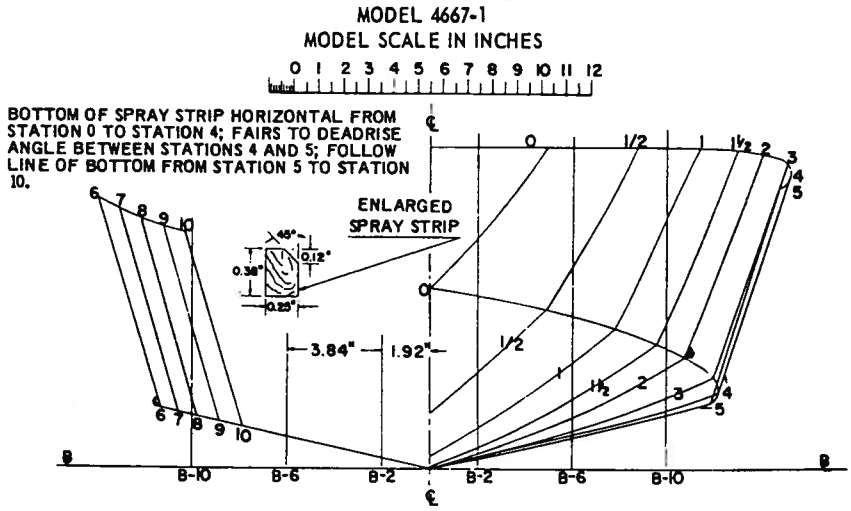

Body Plan of Series 62 Parent Hull

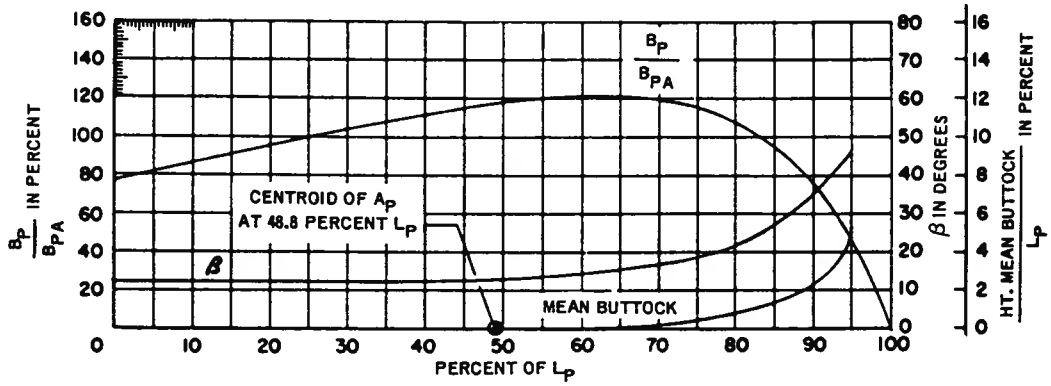

Form Characteristics Curves for Parent Hull

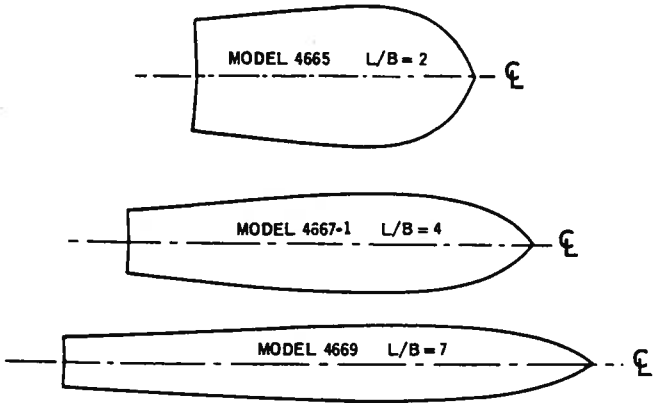

Chine Lines in Plan View of Three Series 62 Hulls

Figure 4.33: Hard-Chine Planing-Hull Form Series 62

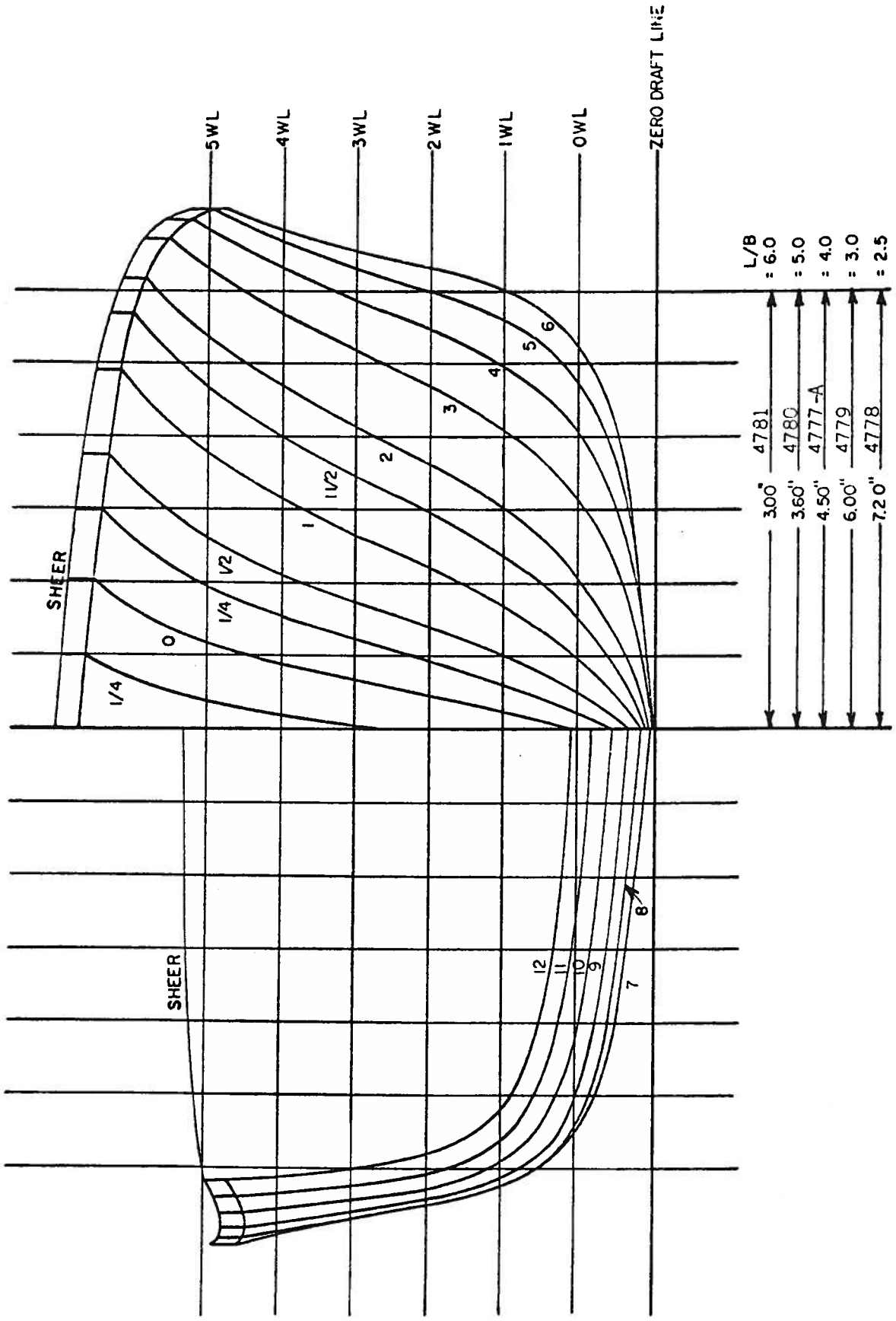

From Beys (1963, p. 8)

Figure 4.34: Round-Bottom Boat Series 63

From Hadler, Hubble and Holling (1974, p. 24)

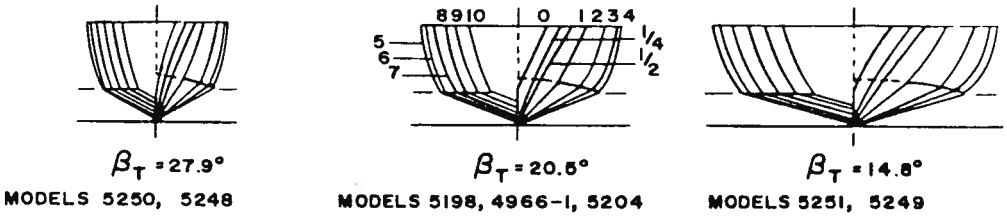

MODEL 5204: $L_P/B_{PX} = 9.34$, $L_P/d_c = 45.0$

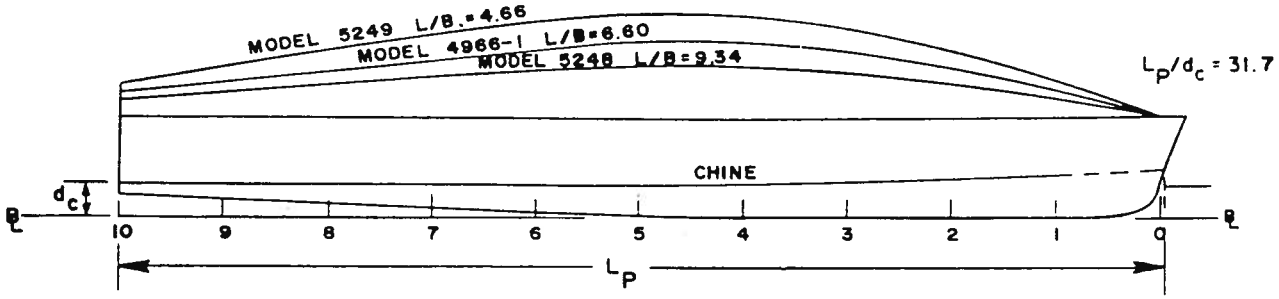

Note: $L/B = L_P/B_{PX}$

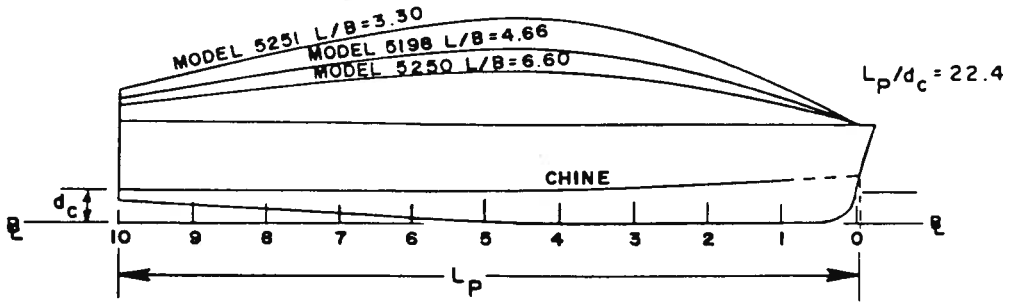

Figure 4.35: Hydrofoil Craft Hull (Airplane-Type) Series 65-A

From Hadler, Hubble and Holling (1974, p. 25)

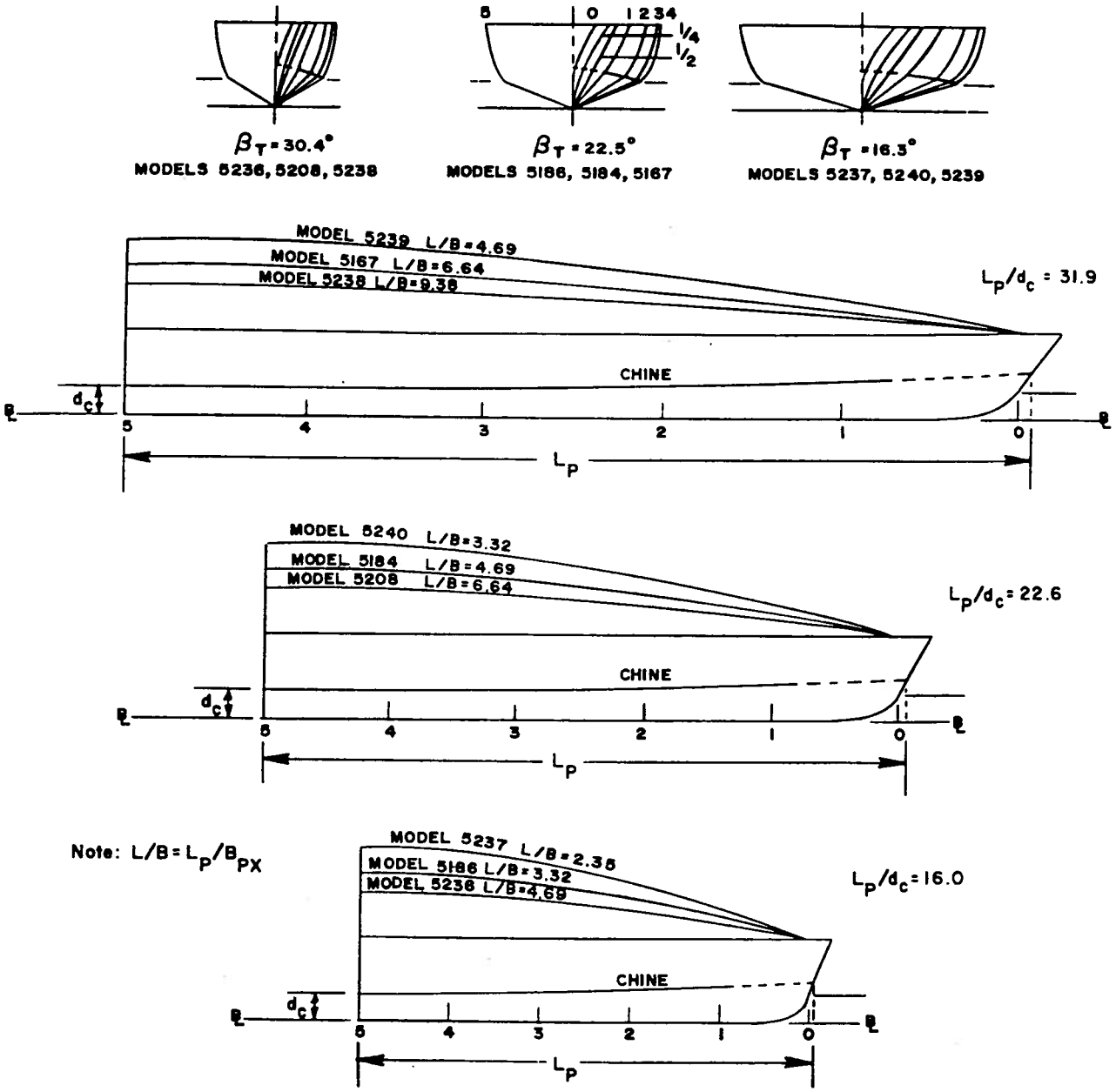

Figure 4.36: Hydrofoil Craft Hull (Canard-Type) Series 65-B

From Hadler, Hubble and Holling (1974, p. 27)

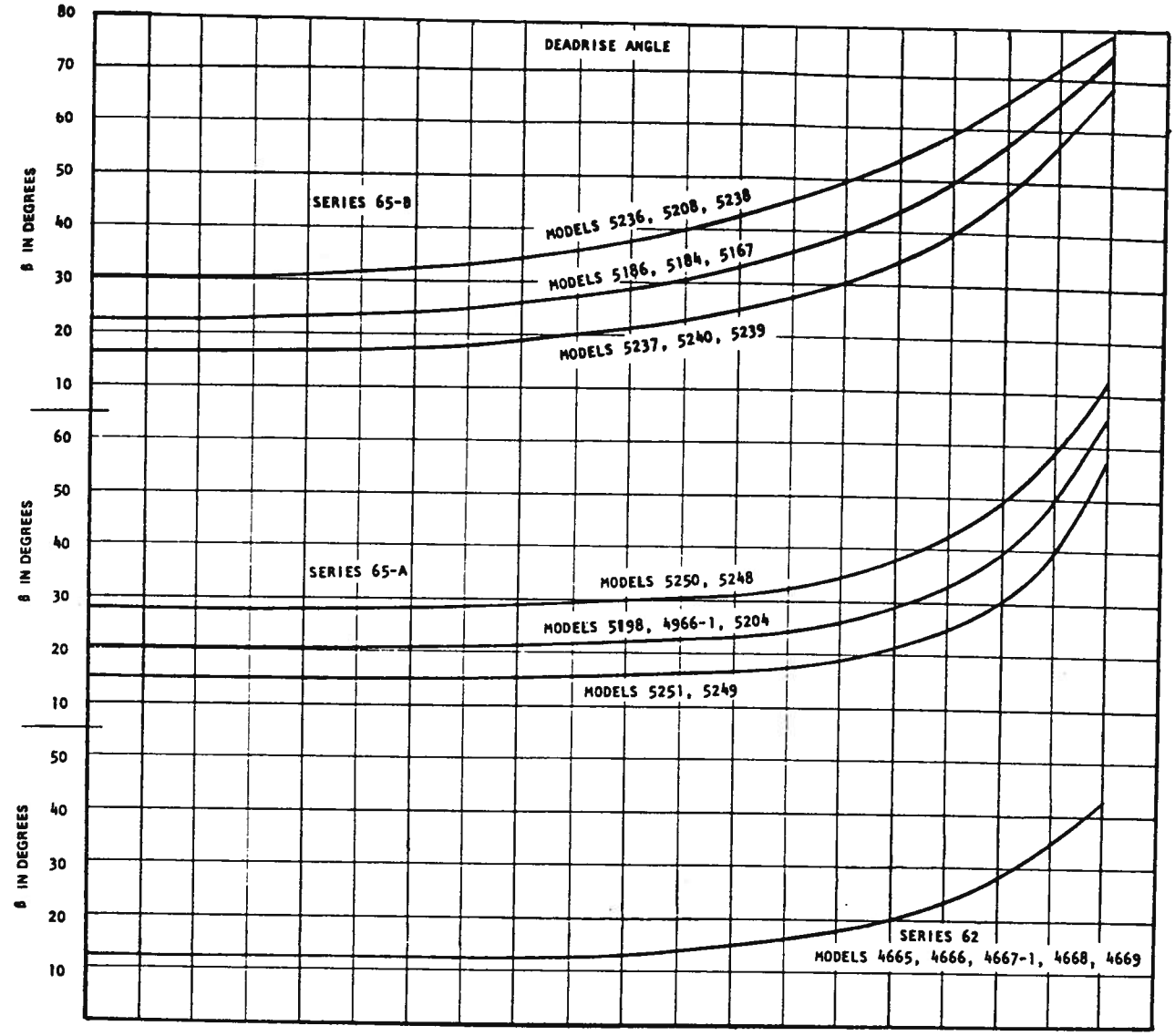

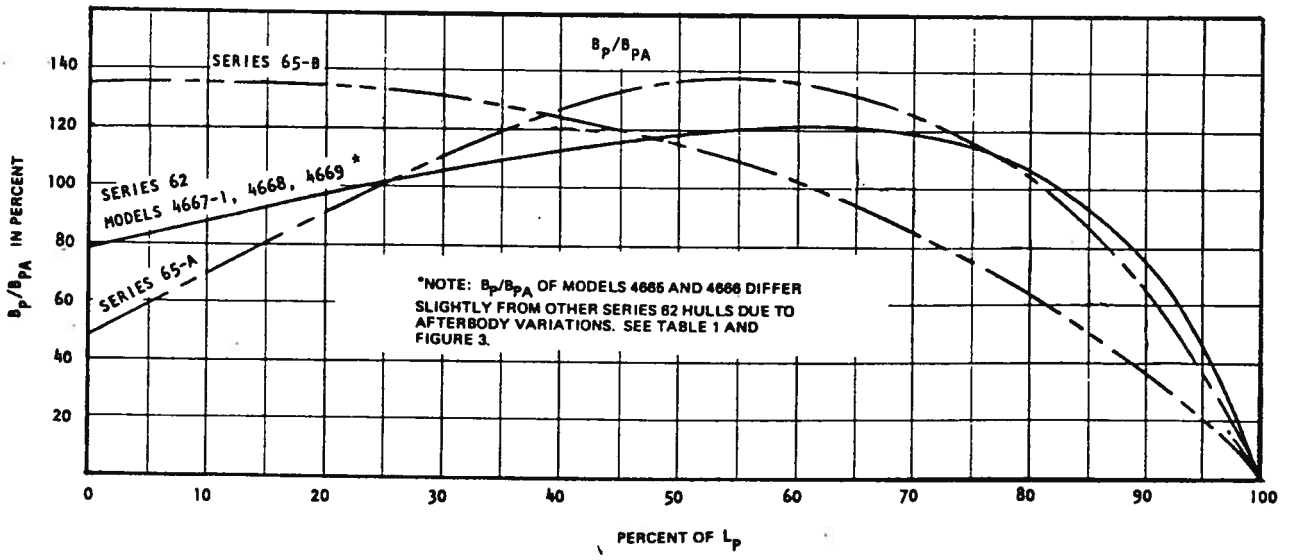

Figure 4.37: Form Characteristic Curves of Series 62 and 65

5. PROPULSION

5.1. Introduction

The three most common propulsors for small craft are subcavitating propellers, supercavitating propellers and water jets. Fig. 5.1, taken from Alison (1978) indicates how the efficiency of these three devices might be expected to vary with forward speed. It is seen that the subcavitating propeller is the most efficient in the low-speed range. At higher speeds, where a subcavitating propeller begins to cavitate, its efficiency drops off rapidly. In this situation, a supercavitating propeller will give a better performance -- though not as good as that of a subcavitating propeller at low speeds.

Ideally, one might expect waterjets to be more efficient, since with good duct design, the flow can be decelerated before encountering the pump, which can therefore be made to operate in the subcavitating mode. In addition, the problem of propeller-shaft inclination is avoided. However, the frictional losses in the duct are always very large. Waterjets are also inconvenient from the point of view of the installation, as a large part of the boat is wasted in order to accommodate the ducting.

A fourth possibility shown in the figure is a surface-piercing propeller. This is also called a partly-submerged propeller. In the proposed high-speed mode of operation, this propeller would be ventilated.

Fig. 5.2 illustrates most of the propulsion arrangements that have been tried out in the last century. An example of the operation of the vertical-axis propeller (Voith-Schneider) is shown in Fig. 5.3. Its main advantage is the ability to develop thrust in any direction because of the available cyclic control of the pitch angle of the individual blades. However, it has a lower efficiency than a standard propeller. For the sake of completeness, Fig. 5.4

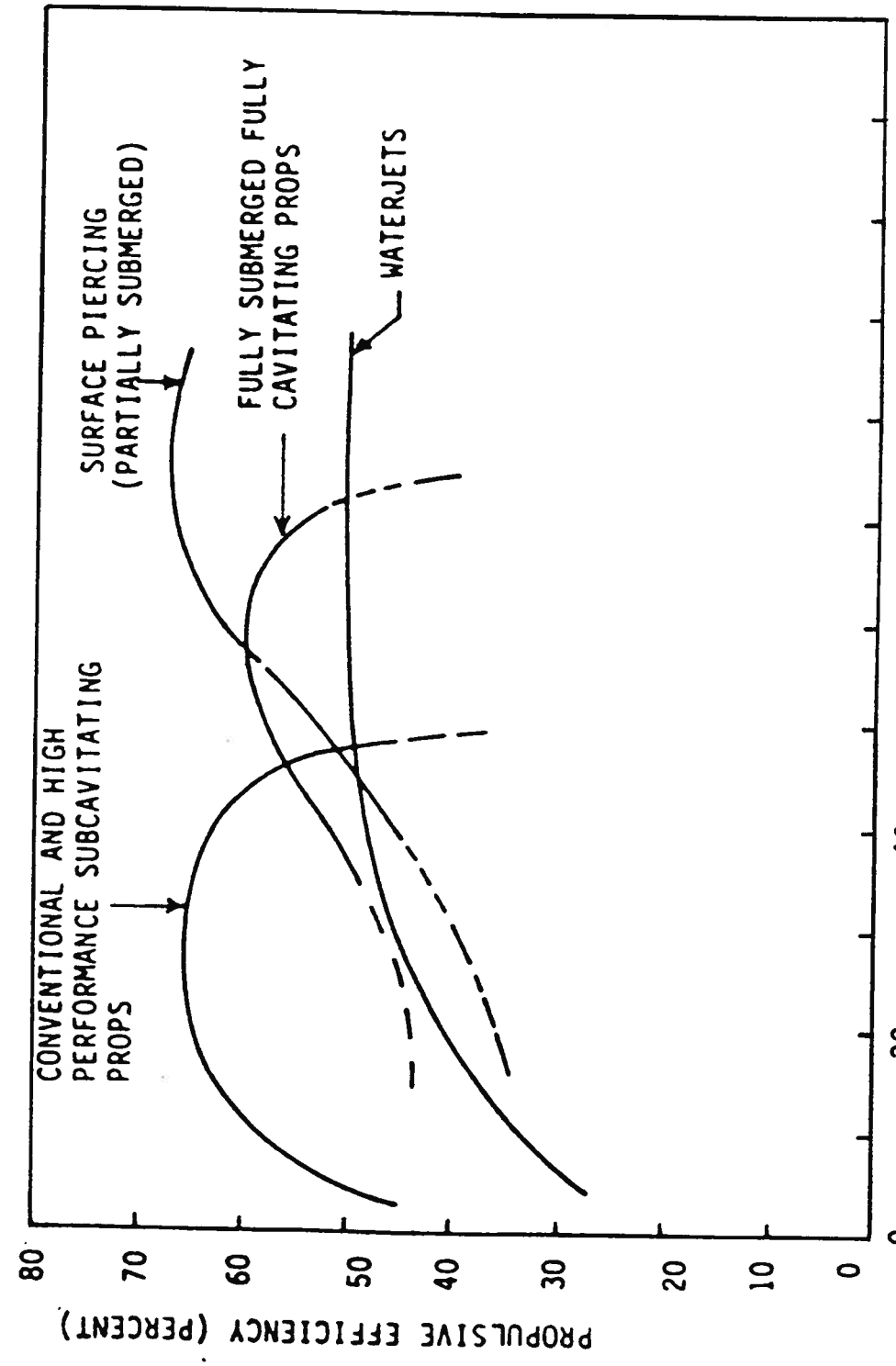

From Allison (1978, p. 339)

Figure 5.1: Approximate Maximum Installed Efficiency Envelopes

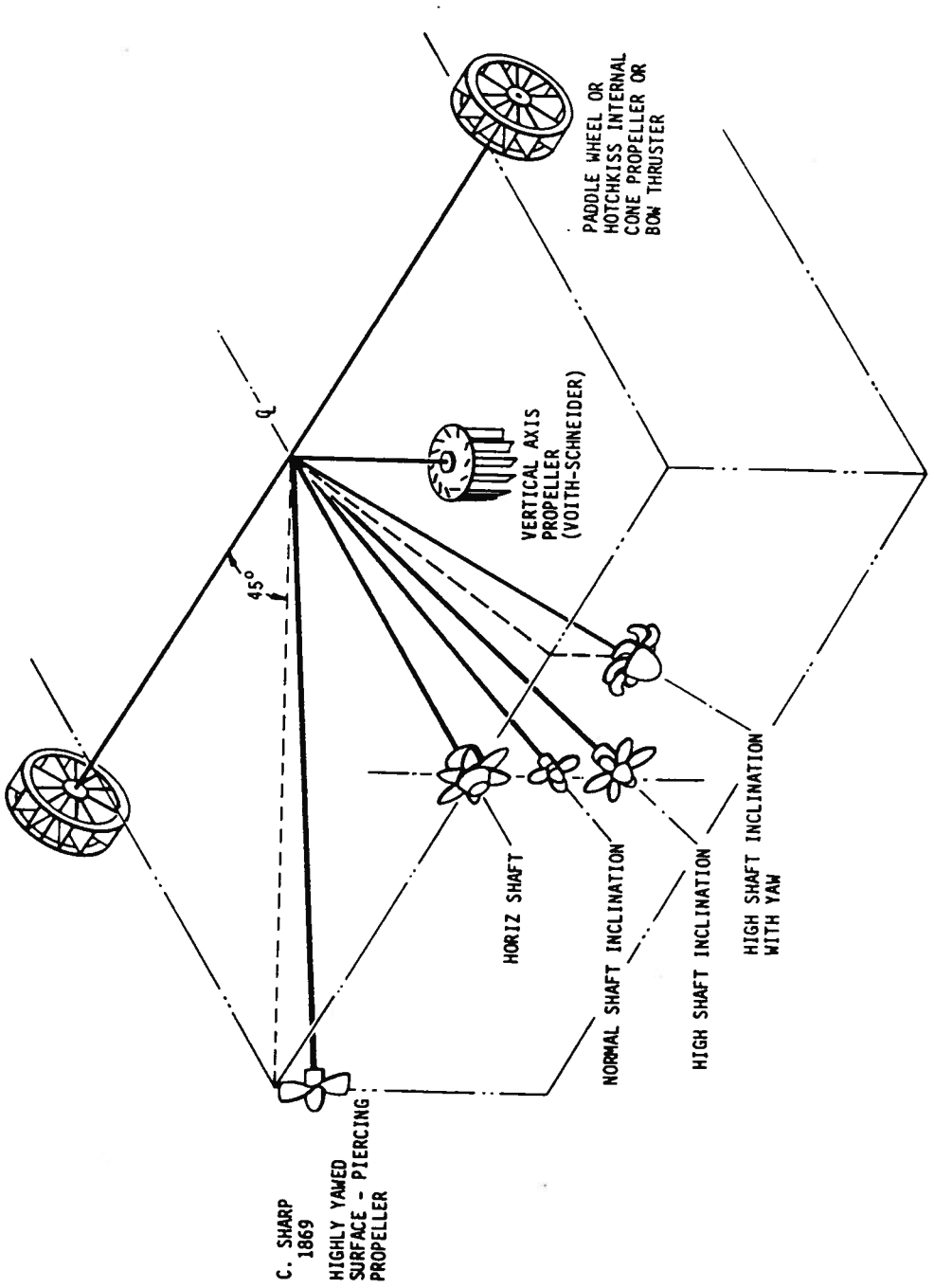

From Allison (1978, p. 378)

Figure 5.2: Orientations for Various Ship Propulsors

From Harvald (1983, p. 221)

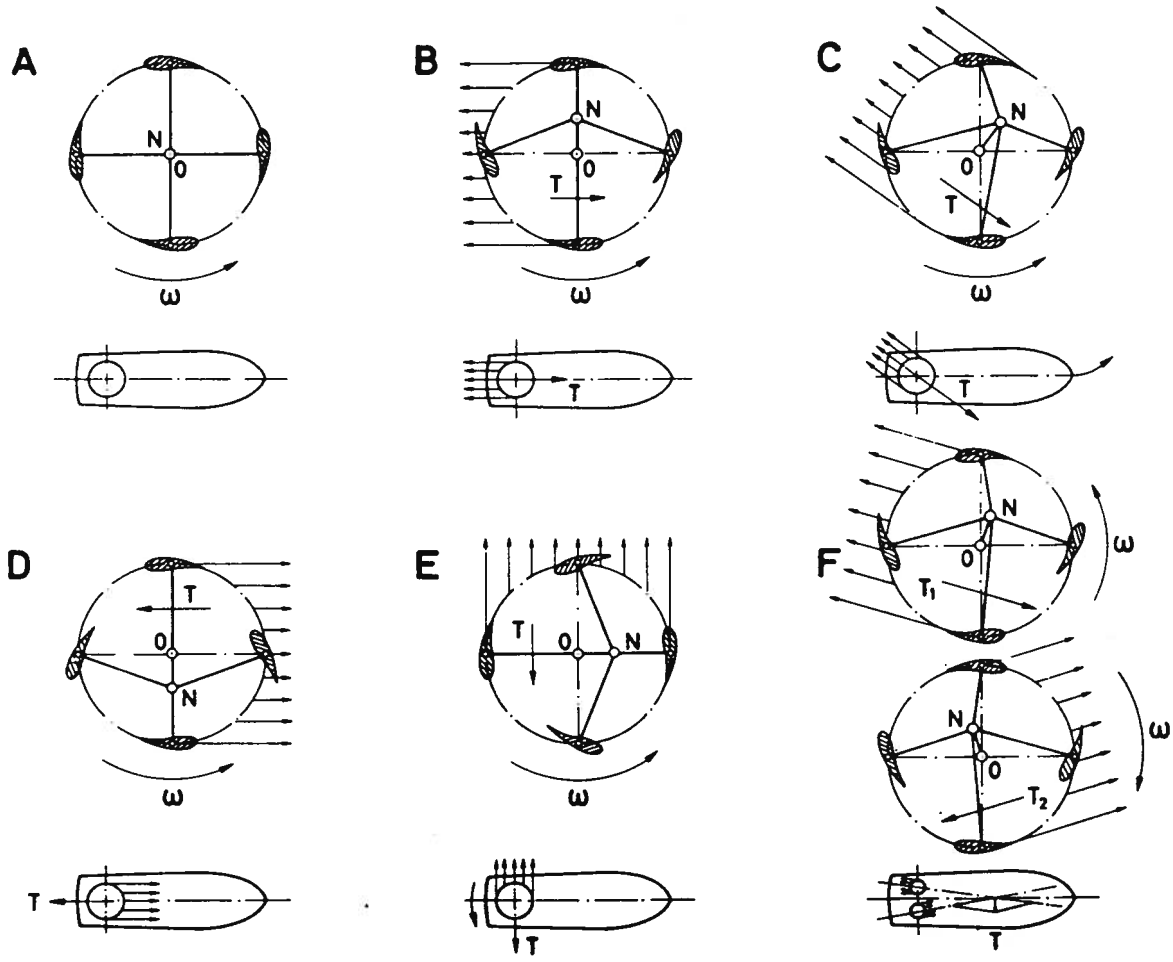

Figure 5.3: Different Maneuvers with Voith-Schneider Propellers

From Harvald (1983, p. 219)

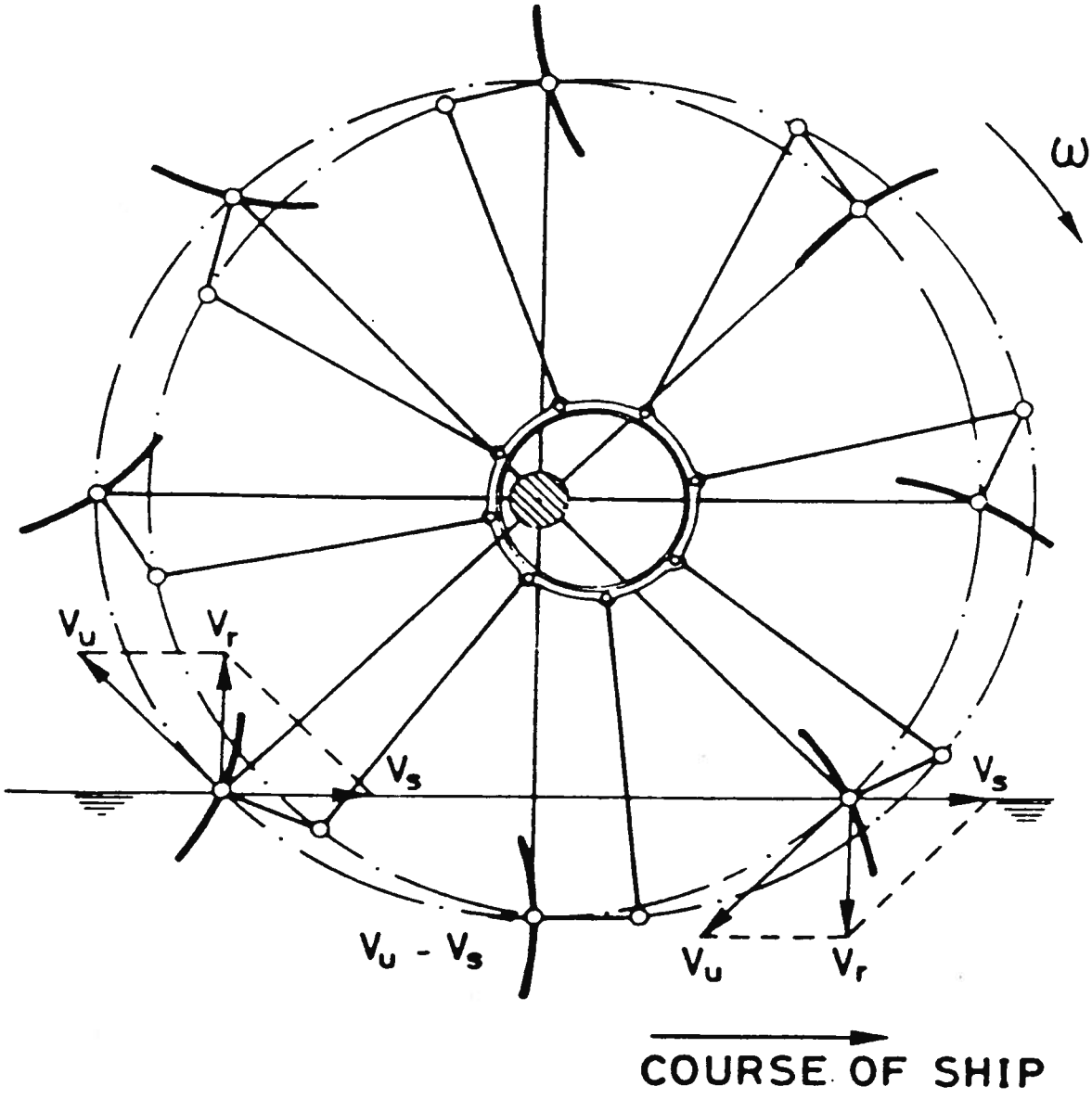

Figure 5.4: A Feathering Paddle Wheel

has been included. This shows the mechanism of a feathering paddle wheel. In this design, the floats (or paddles) are maintained almost vertical to the water surface, thus raising the efficiency by around 10% above that of a fixed-float paddle wheel. One of the main problems associated with the use of paddle wheels is to locate them on the boat so that the proper immersion is achieved.

A ducted propeller is shown in Fig. 5.5. A well designed duct (or nozzle) will enhance the flow into the propeller making it more uniform, thereby increasing the efficiency of the propeller and reducing the possibility of cavitation. Additionally, the pressure distribution over the duct will generate a favorable thrust. This thrust gain exceeds the frictional losses of the duct when the system is highly loaded. Fig. 5.6 shows the main components of a waterjet propulsion system.

Fig. 5.7 is a companion to Fig. 5.1, in that comparisons on the basis of efficiency are made. The performance of a propeller is usually defined by means of the thrust coefficient

$$K_T = T/\rho n^2 D^4 \quad , \tag{5.1}$$

and the torque coefficient

$$K_Q = Q/\rho n^2 D^5 \quad , \tag{5.2}$$

where T is the thrust developed by the propeller, ρ is the water density, n is the rotational speed in the revolutions per unit time (seconds), D is the diameter, and Q is the torque absorbed by the propeller. These two coefficients are a function of the advance coefficient

$$J = V_A/nD \quad , \tag{5.3}$$

where V_A is the speed of advance, which is the velocity of the water in the wake of the ship, where the propeller is located. (Of course, the action of the propeller disturbs this wake velocity.)

From Harvald (1983, p. 217)

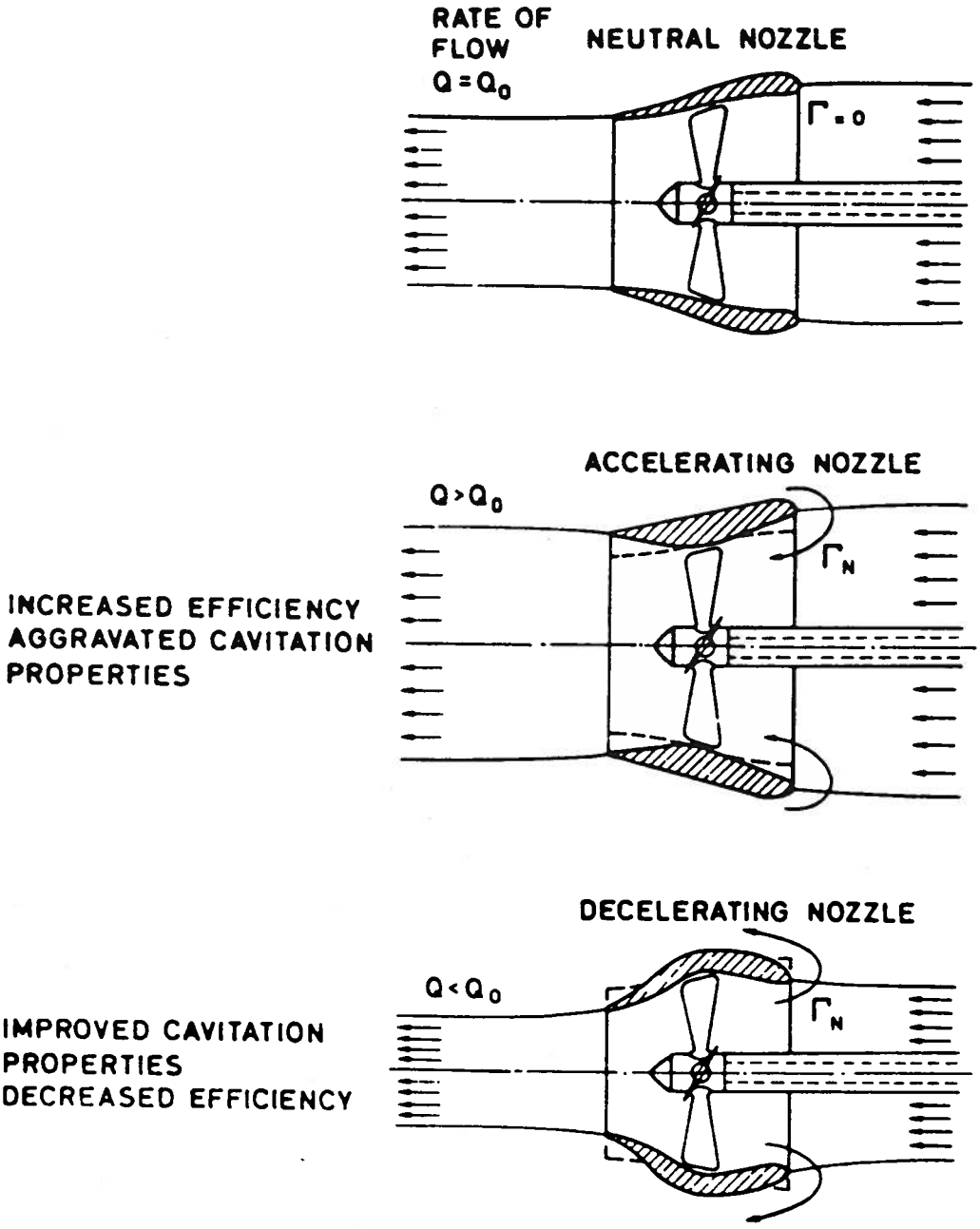

Figure 5.5: A Ducted Propeller

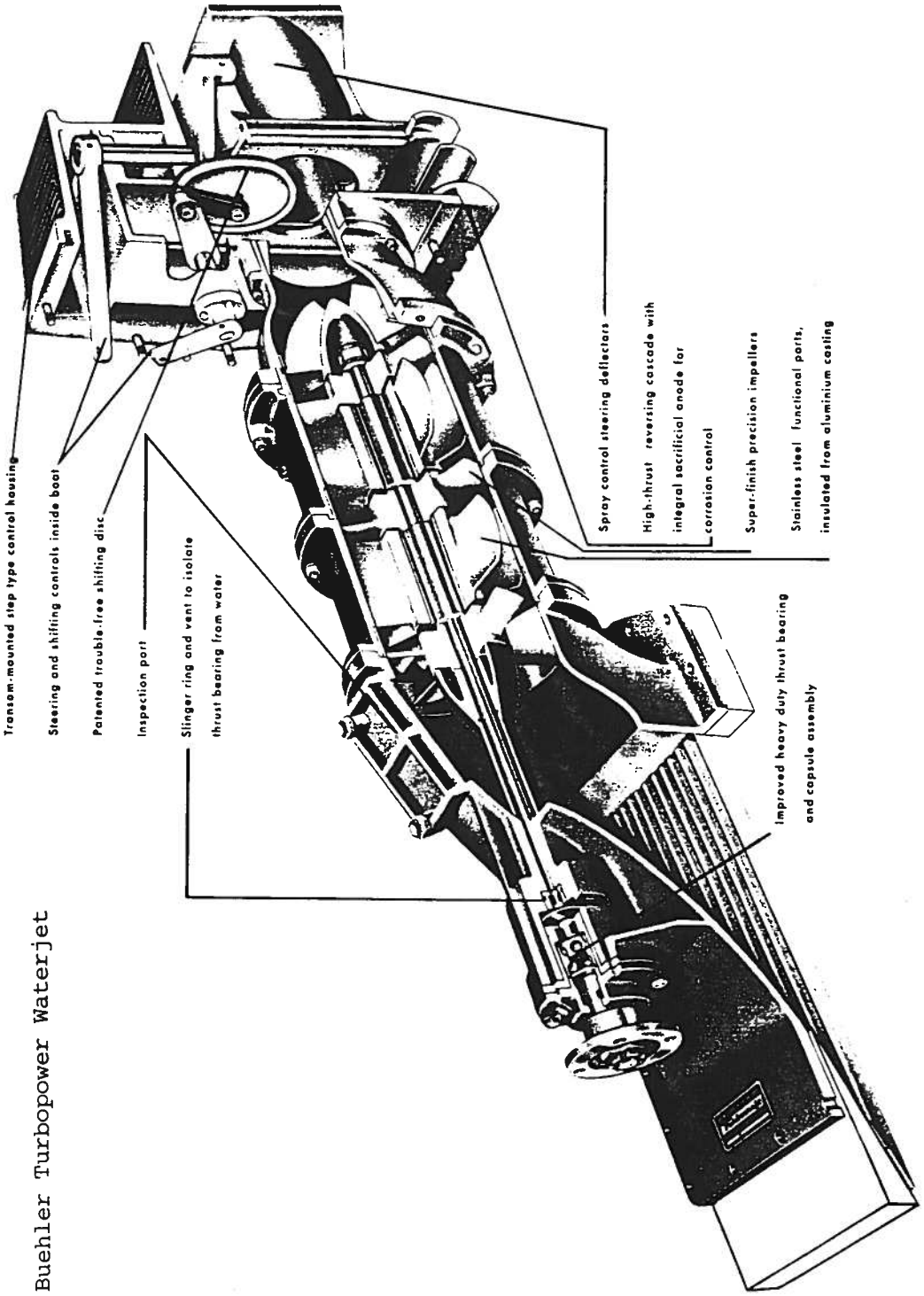

Figure 5.6: Typical Layout of a Waterjet

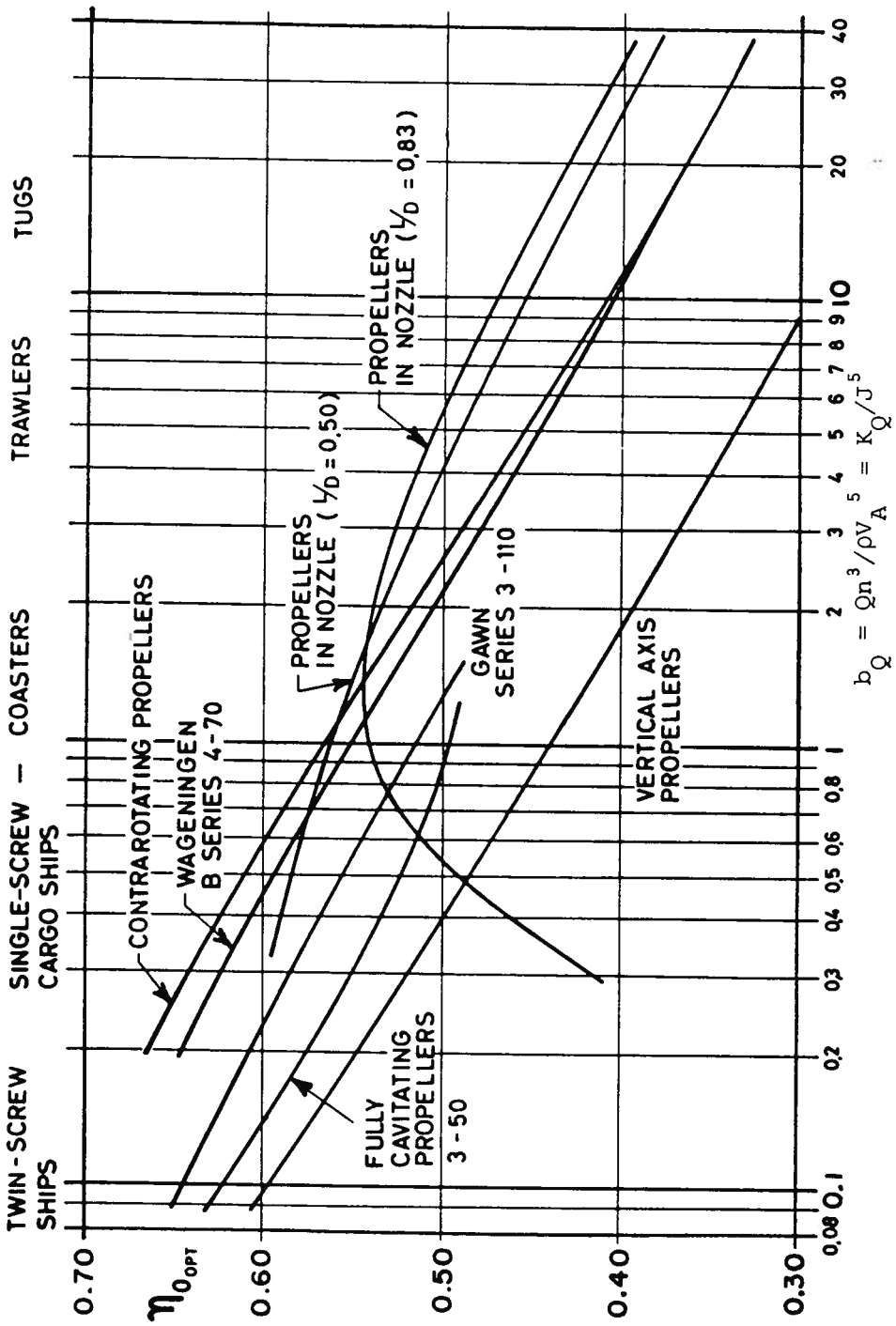

From Harvald (1983, p. 218)

Figure 5.7: Optimum Efficiency for Different Types of Propulsors

The open-water efficiency is defined for the propeller operating in this condition, without reference to any other complicating features. Hence, this efficiency is the ratio of the rate of useful work done, to the power absorbed by the propeller:

$$\eta_0 = TV_A/Q\omega \quad ,$$

where ω is the angular speed of the propeller. Thus, we have

$$\eta_0 = TV_A/Q(2\pi n)$$

$$= \frac{K_T}{K_Q}\frac{J}{2\pi} \quad . \tag{5.4}$$

The abscissa used in Fig. 5.7 is a loading coefficient in which the diameter of the propeller has been eliminated. The diagram shows that the subcavitating propellers (as represented by the Wageningen B-Series Screws) are almost the most efficient in a lightly loaded condition. An interesting development is the use of contrarotating propellers. These are seen to be slightly more efficient as they do not create a rotational wake.

It is also noted that the cavitating propellers (such as the Gawn-Burrill screws) are less efficient, while the vertical-axis propeller possesses the lowest efficiency. The nozzle is seen to improve the performance of a heavily-loaded propeller. However, it is only a hindrance in the lightly-loaded case because of its viscous drag.

When the propeller is installed behind the boat, a number of additional phenomena complicate the situation. We first note that the wake velocity is related to the boat speed V by means of the equation

$$V_A = (1 - w)V \quad , \tag{5.5}$$

where w is the Taylor wake fraction. In fact, the wake fraction varies in the neighborhood of the propeller, so that an average value should be used in (5.5). Fig. 5.8 shows the wake distributions measured on models of different

From Harvald (1983, p. 170)

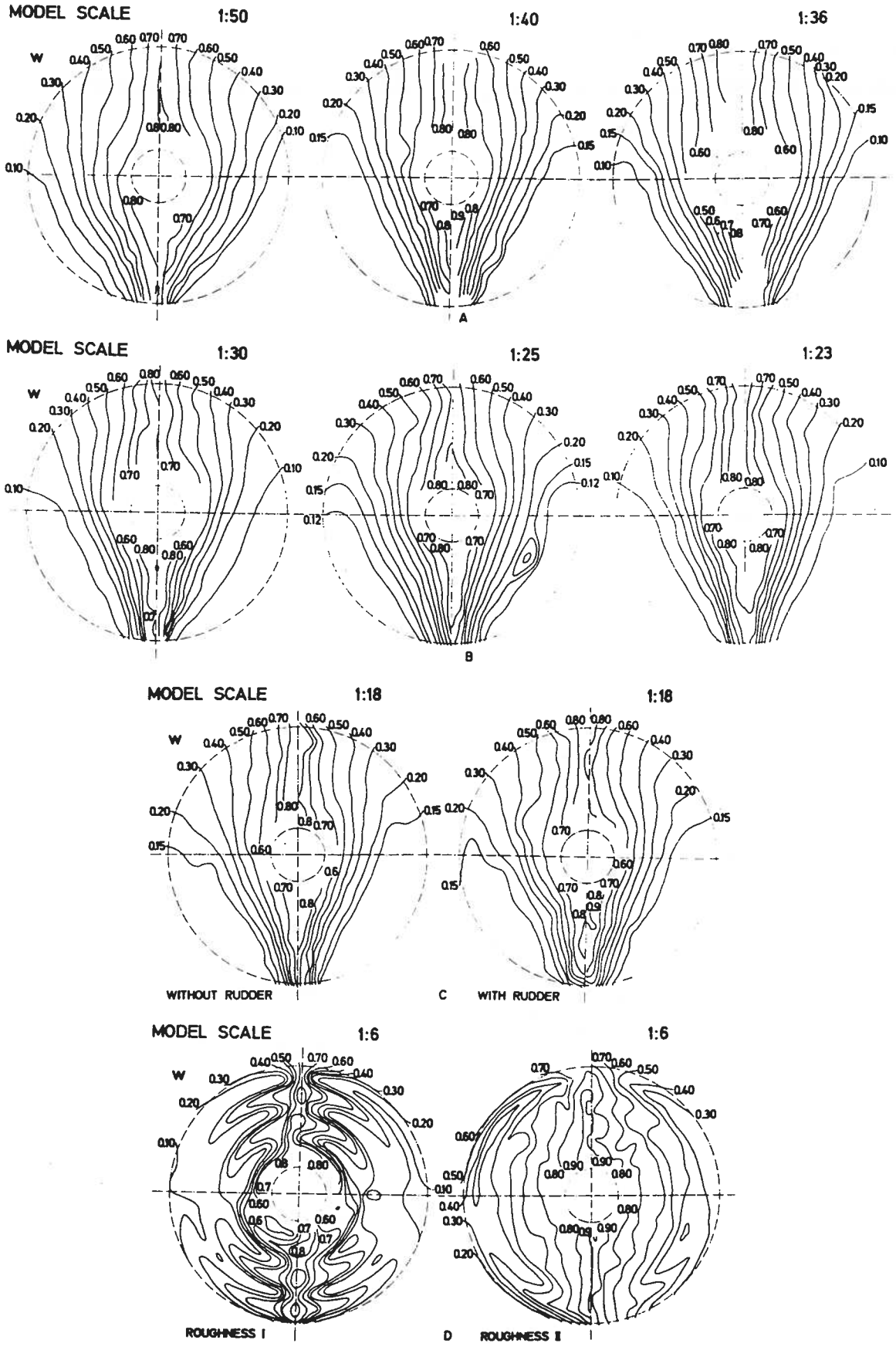

Figure 5.8: The Wake Distribution for Victory Ship Models

scales. In addition, the influences of the rudder and ship-model roughness have been investigated. The wake is a result of three main features of the flow: the first is the lessening of the velocity near the ends of a body (in the stagnation region) and is a potential-flow phenomenon. The second is the influence of the free surface, and would depend on the Froude number. The third is due to the boundary layer on the hull and depends on the Reynolds number. It is the last effect that is studied by changes in model size in this diagram. The smaller models display a stronger wake. In the case of a propeller located under a prismatic planing surface, the wake fraction is relatively small.

The propeller increases the water velocity over the stern of the boat, and this reduces the pressure in that region. As a result, the thrust must be greater than the bare-hull drag R_T. We can therefore write

$$R_T = (1 - t)T \quad , \tag{5.6}$$

where t is the thrust-deduction factor.

The hull efficiency takes into account the two effects defined by (5.5) and (5.6). It is defined as the ratio of the useful rate of work done on the boat to the rate of work done by the propeller on the water. Thus

$$\eta_H = R_T V/TV_A$$
$$= (1 - t)/(1 - w) \quad . \tag{5.7}$$

Another feature of the boat-propeller interaction problem is the non-uniformity of the flow in the wake, which is ignored in (5.5). Thus, the efficiency of the propeller behind the boat is defined as the ratio of the rate of work done by the propeller on the water, to the power absorbed by the propeller (in the boat wake):

$$\eta_B = TV_A/Q_B(2\pi n) \quad , \tag{5.8}$$

where Q_B is the torque required to drive the propeller in the non-uniform

wake. The ratio of the efficiencies in (5.8) and (5.4) is called the relative rotative efficiency, and is simply given by the ratio of the torque behind the ship, to the torque in the open water:

$$\eta_R = \eta_B/\eta_0 = Q/Q_B \quad . \tag{5.9}$$

The quasi-propulsive coefficient includes all the hydrodynamic effects referred to above. They are summarized by (5.4), (5.7), and (5.9). We write

$$\eta_D = \eta_H \eta_0 \eta_R \quad . \tag{5.10}$$

The overall picture can be completed by considering the shaft efficiency η_S , which accounts for the losses in the shafting and gear boxes. That is

$$\eta = \eta_H \, \eta_0 \, \eta_R \, \eta_S \quad . \tag{5.11}$$

5.2. Geometry of the Propeller

Two drawings of a four-bladed propeller are shown in Figs. 5.9 and 5.10. These show typical features of a subcavitating propeller such as the blades, whose sections resemble those of a cambered foil -- with some modifications to reduce cavitation. An important feature of the propeller is its pitch. This is defined as the distance the propeller would advance if it did not slip in the water. The pitch can be computed from the blade pitch angle ϕ shown in Fig. 5.10.

Ideally, one would want the pitch to be constant with respect to the radial distance. This means the pitch angle should decrease with the radius. However, in a wake-adapted propeller, the pitch is decreased somewhat near the hub in proportion to the reduced velocity encountered by that part of the propeller. The pitch distribution is shown in Fig. 5.10, as well as in Fig. 5.11. In the second figure, both a wake-adapted (radially-variable pitch) and an open-water (constant-pitch) geometry are illustrated.

The example propeller possesses rake which is a backward inclination of

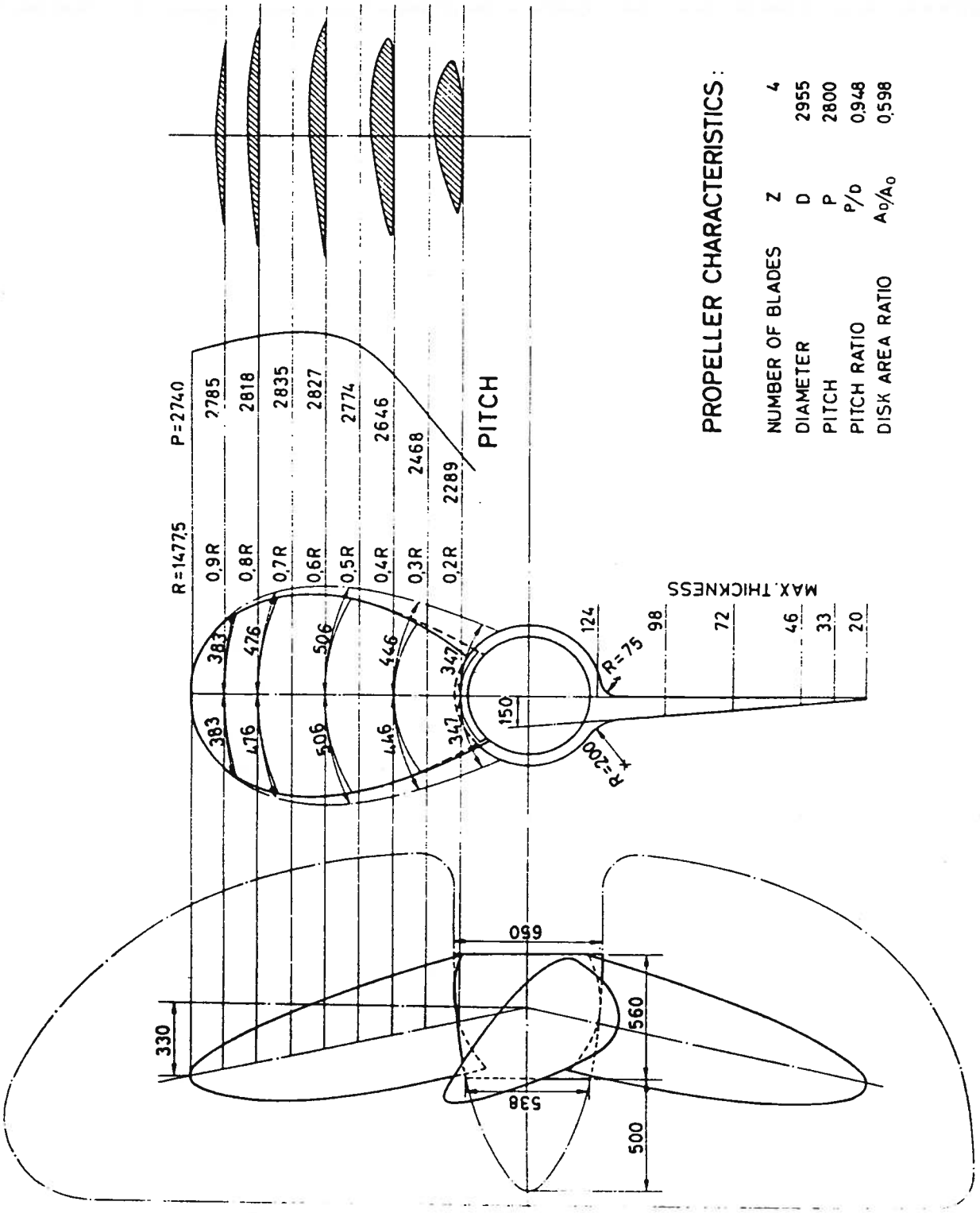

From Harvald (1983, p. 135)

Figure 5.9: A Four-Bladed Propeller

From Harvald (1983, p. 137)

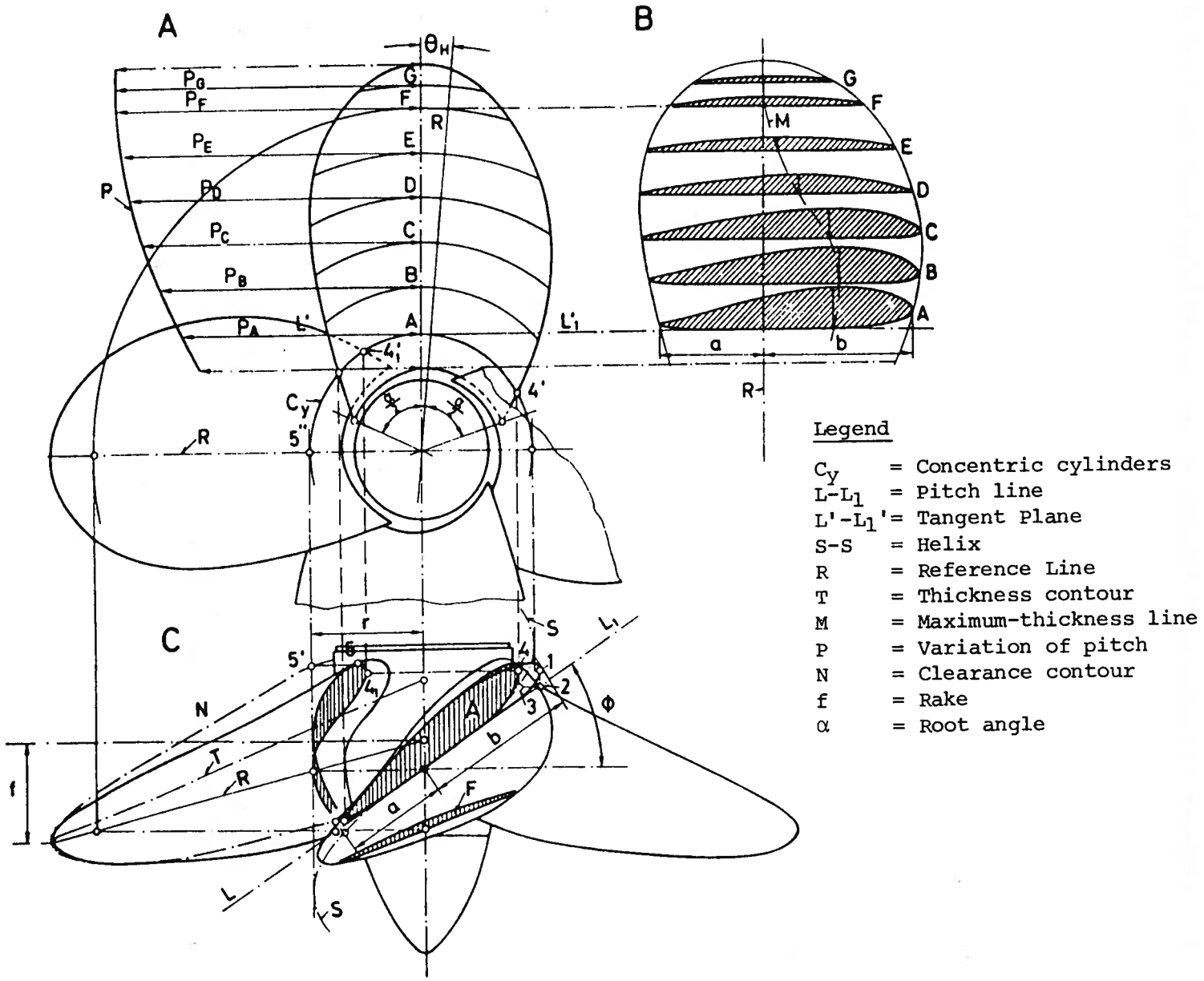

Legend

C_y	= Concentric cylinders
$L-L_1$	= Pitch line
$L'-L_1'$	= Tangent Plane
S-S	= Helix
R	= Reference Line
T	= Thickness contour
M	= Maximum-thickness line
P	= Variation of pitch
N	= Clearance contour
f	= Rake
α	= Root angle

Figure 5.10: Construction of Drawing of Propeller

From Harvald (1983, pp 136 and 138)

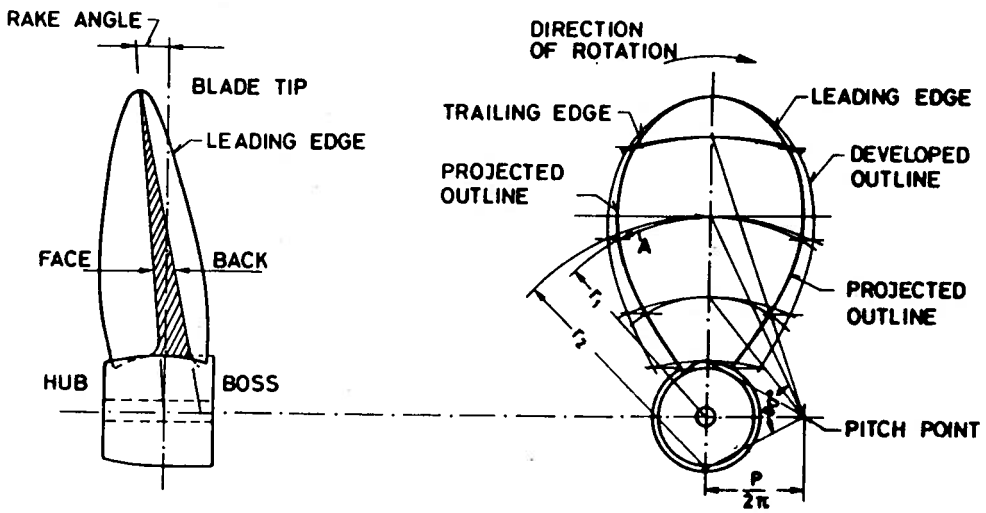

(a) Side View

(b) Axial View

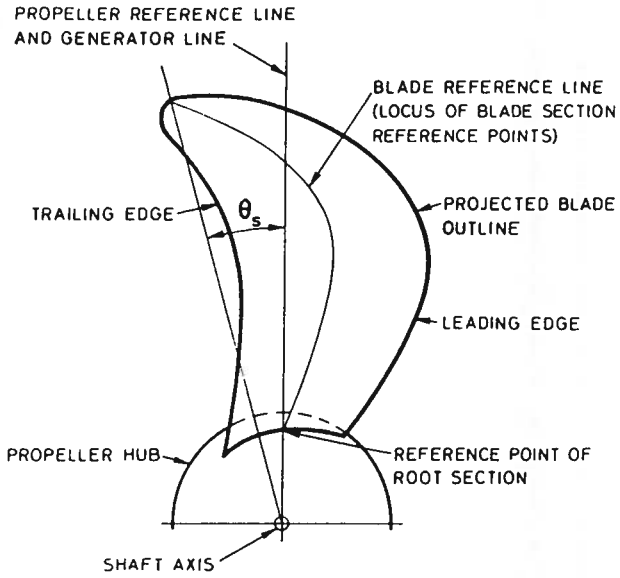

(c) Definition of Lines

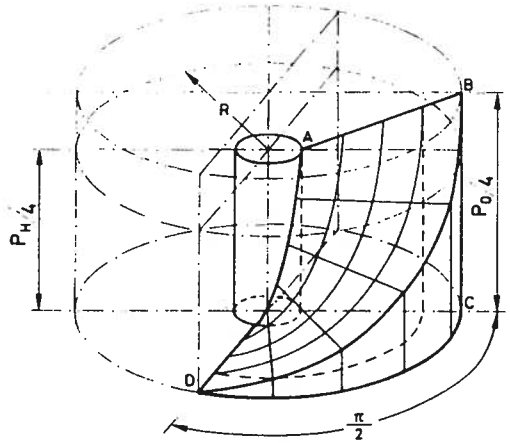

(d) Radially-Variable Pitch

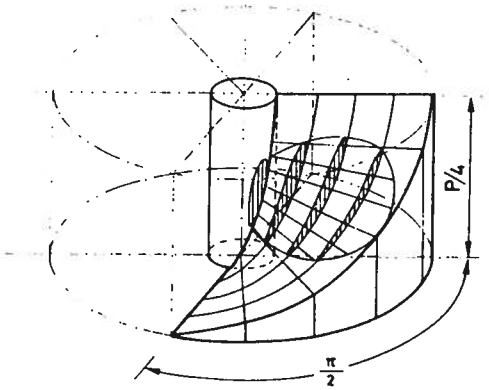

(e) Constant Pitch

Figure 5.11: Geometric Details of a Propeller

the blades as seen in the side view of Fig. 5.11. The use of rake improves the water flow into the propeller when mounted behind the ship. It also increases the clearance between the blades and the hull, which reduces the vibration problem. Many propellers also have some degree of skew, or sweep-back of the blade tips, as seen in the axial view of Fig. 5.11(c). The blade shown in Fig. 5.11(b) does not possess any skew.

We will now consider the main geometric description of a marine propeller. The pitch ratio is defined as the ratio of the pitch to the diameter:

$$r_{pitch} = P/D \quad . \tag{5.12}$$

The disk area is the entire area swept by the propeller:

$$A_0 = \frac{\pi}{4} D^2 \quad . \tag{5.13}$$

The projected area A_P is the area of the blades (excluding the hub), as seen in an axial view. The projected-area ratio is the ratio of this quantity to the disk area:

$$r_P = A_P/A_0 \quad . \tag{5.14}$$

The expanded area A_E is the area obtained by considering the blade sections to lie on cylindrical surfaces. The arc length of these sections can be laid out on straight lines perpendicular to the radial reference line, after having rotated them from the helical surface through the angle ϕ to the propeller plane. The area of the resulting shape is called the expanded area. The expanded-area ratio is the ratio of this quantity to the disk area:

$$r_E = A_E/A_0 \quad . \tag{5.15}$$

Another quantity, which is not used so frequently, is the developed area A_D. This can be obtained by simply developing the blade area. That is, only the rotation through the angle ϕ is carried out. This leads to the developed-area ratio:

$$r_D = A_D/A_0 \quad . \tag{5.16}$$

It is interesting to note that the actual wetted surface of the blades is not considered an important quantity in the description of the propeller. However, both the expanded and the developed areas are good approximations to it.

5.3. Momentum Theory

A simple theory which gives an upper limit to the efficiency of a propeller is based on momentum and energy considerations of the flow. This is illustrated in Fig. 5.12. The flow in the race ahead of the propeller has an axial velocity equal to the speed of advance V_A. Its speed increases to the value V_1 at the disk of the propeller, and finally reaches the value $V_2 = V_A + 2U_A$ some distance downstream in the wake. The propeller race contracts as the flow increases -- in accordance with the principle of conservation of mass.

Fig. 5.12 also shows the variation of the pressure in the race, which can be computed on the basis of the Bernoulli equation, except in the immediate region enclosing the propeller.

Momentum considerations give the thrust on the propeller as the product of the mass flux and the downstream velocity increment:

$$\begin{aligned} T &= \dot{m}(V_2 - V_A) \\ &= \rho A_0 V_1 (V_2 - V_A) \\ &= \rho A_0 V_1 (2U_A) \quad . \end{aligned} \tag{5.17}$$

The thrust is also given by the difference of the pressure just ahead of the propeller p_1^+ and that just behind it p_1^- :

$$T = A_0(p_1^+ - p_1^-) \quad . \tag{5.18}$$

The Bernoulli equation applied between the upstream station and a point just ahead of the propeller disk gives

From Harvald (1983, p. 200)

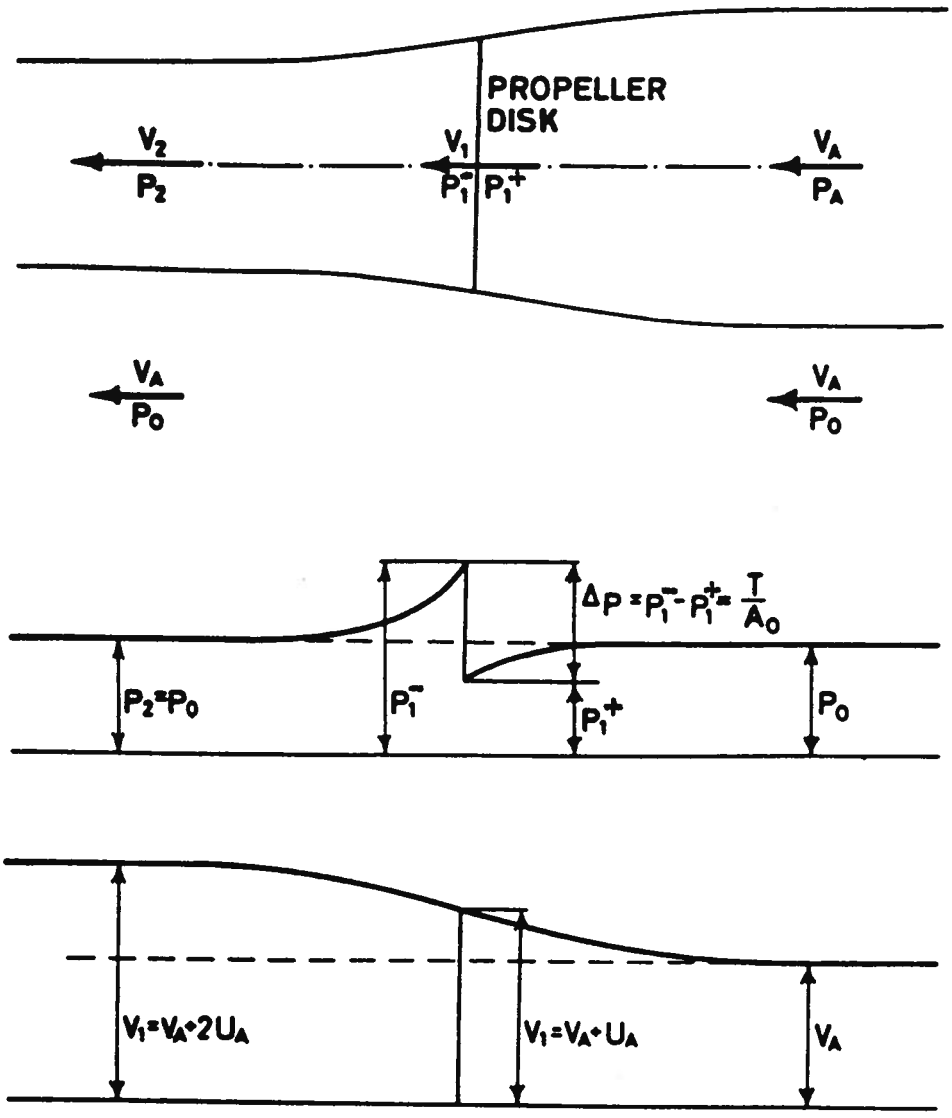

Figure 5.12: Momentum Theory

$$\frac{1}{2}\rho V_A^2 + p_0 = \frac{1}{2}\rho V_1^2 + p_1^+ \quad , \tag{5.19}$$

where p_0 is the upstream static pressure.

We can also apply the Bernoulli equation between a downstream point and a point just behind the propeller:

$$\frac{1}{2}\rho(V_A + 2U_A)^2 + p_0 = \frac{1}{2}\rho V_1^2 + p_1^- \quad . \tag{5.20}$$

Subtraction of (5.19) from (5.20) produces the result

$$2\rho U_A(V_A + U_A) = p_1^- - p_1^+ \quad ,$$

and using (5.18),

$$= T/A_0 \quad , \tag{5.21}$$

and from (5.17),

$$= \rho V_1(2U_A) \quad . \tag{5.22}$$

Thus we obtain the equation

$$V_1 = V_A + U_A \quad . \tag{5.23}$$

This states that half of the downstream axial velocity increment occurs ahead of the propeller.

We can also compute the ideal efficiency as the ratio of the rate of useful work done to the rate of work done by the propeller:

$$\eta_I = TV_A/TV_1$$

$$= V_A/(V_A + U_A) \quad , \tag{5.24}$$

using (5.21). At this point, we introduce the thrust-loading coefficient as follows:

$$C_T = T/\frac{1}{2}\rho V_A^2 A_0 \quad , \tag{5.25}$$

which should be contrasted against the thrust coefficient K_T defined by (5.1). Substitution of (5.21) now gives

$$C_T = 2\rho U_A(V_A + U_A)A_0/\frac{1}{2}\rho V_A^2 A_0$$

$$= 4[(U_A/V_A) + (U_A/V_A)^2] \quad .$$

The meaningful one of the two solutions of this equation is

$$U_A/V_A = (-1 + \sqrt{1 + C_T})/2 \quad . \tag{5.26}$$

Finally, we can substitute (5.26) into (5.24) to give

$$\eta_I = 2/(1 + \sqrt{1 + C_T}) \quad . \tag{5.27}$$

We can see from (5.26) that the velocity increment U_A increases as the thrust loading increases. More importantly, (5.27) shows that the ideal efficiency can be raised by lowering the thrust loading. This implies using the largest possible propeller diameter. In practice, there is actually an optimum propeller diameter because of viscous effects which have been ignored in the present theory. The open-water efficiency η_O (5.4) is also less than the ideal efficiency ((5.24) and (5.27)) because of viscous effects.

A refinement to this momentum theory is to include the induced tangential components of the flow. It is found that the value at the propeller U_T is one-half the downstream increment $2U_T$ -- similar to the situation for the axial velocity increment. Also, the ideal efficiency (5.27) is reduced. The influence of these induced velocities on the inflow to a blade section is shown in Fig. 5.13.

5.4. Subcavitating Propellers

5.4.1. The Propeller Curves

As noted in Sec. 5.3, the geometry of a propeller is defined by the quantities P/D, A_E/A_0, and Z (the last variable being the number of blades). Its performance is given by K_T, K_Q, and η_O, as noted in Sec. 5.1.

From Harvald (1983, p. 201)

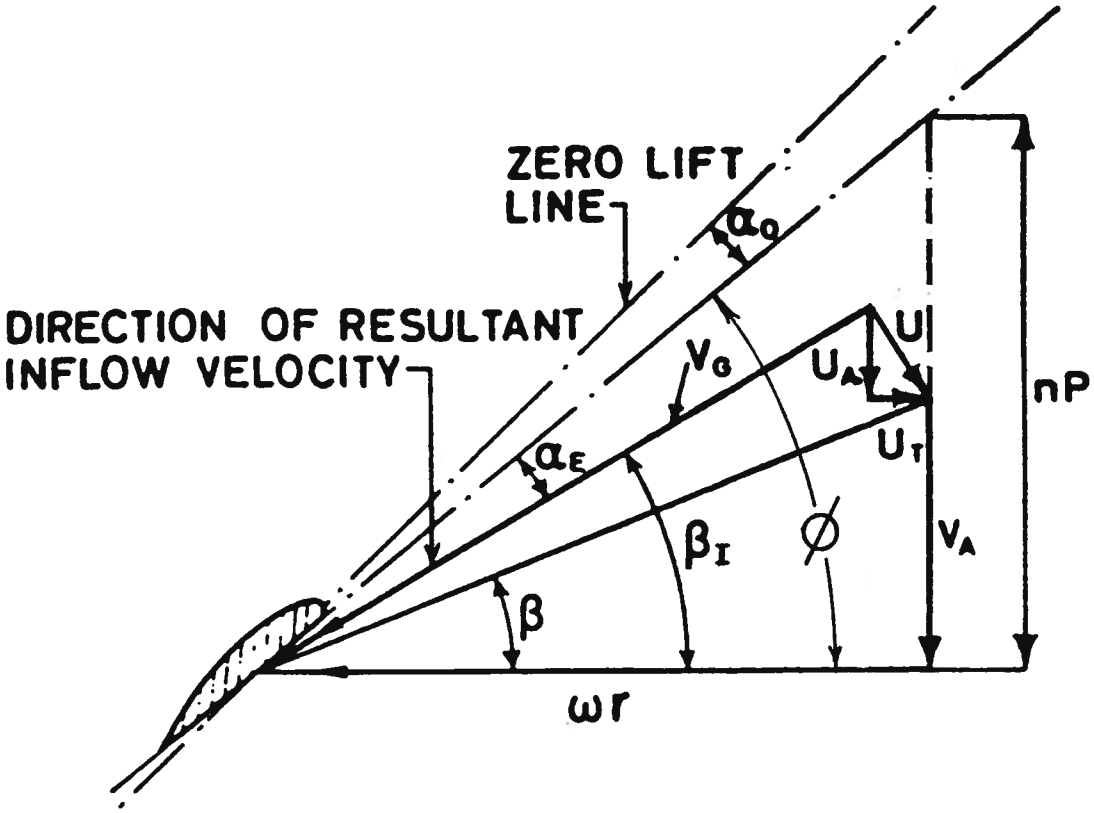

Figure 5.13: Diagram of Velocities at a Propeller Blade

A practical way of obtaining a propeller design for a boat is to select one from a series, which has already been tested. This procedure eliminates much effort as well as any uncertainty in the design analysis. One of the better known propeller series is the Wageningen B-Series screws, which was first described by van Lammeren, Van Manen, and Oosterveld (1969). This series was an outgrowth of the A-Series screws, and included improvements to reduced cavitation problems and to enhance their performance during backing maneuvers. The series covers the following ranges of the abovementioned variables: $0.5 \leq P/D \leq 1.4$, $0.30 \leq A_E/A_0 \leq 1.05$, and $2 \leq Z \leq 7$. The design of these screws is given in Fig. 5.14.

Representing the performance of such a propeller series requires a daunting number of graphs. The process of interpolation between curves and graphs has been simplified by the generation of mathematical representations of their performance, as follows:

$$K_T = \sum_{s,t,u,v} C^{(T)}_{s,t,u,v} J^s (P/D)^t (A_E/A_0)^u Z^v$$

and (5.28)

$$K_Q = \sum_{s,t,u,v} C^{(Q)}_{s,t,u,v} J^s (P/D)^t (A_E/A_0)^u Z^v \quad .$$

In addition, there are polynomials to compute corrections ΔK_T and ΔK_Q if the Reynolds number at the characteristic radius ($r = 0.75\ R$, where R is the propeller radius) is above two million. The Reynolds number is defined here as

$$R_{0.75R} = \rho \sqrt{V_A^2 + (2\pi n \times 0.75\ R)^2}\ c_{0.75R}/\mu \quad , \tag{5.29}$$

where $c_{0.75R}$ is the characteristic blade chord, and μ is the viscosity of the water. These polynomials were given by Bernitsas, Ray, and Kinley (1981).

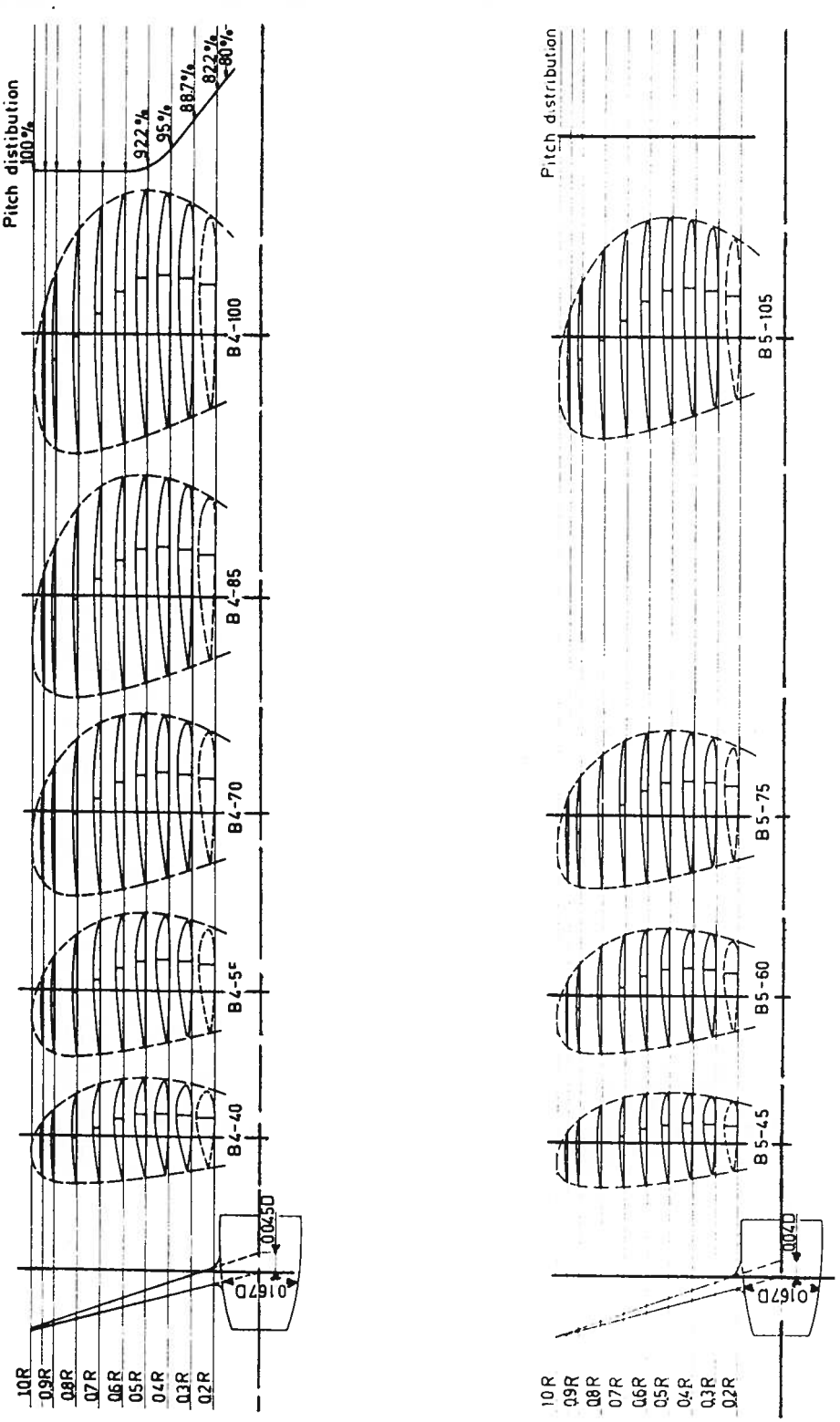

From van Lammeren, van Manen, and Oosterveld (1969, p. 271)

Fig. 5.14: The Geometry of the Wageningen B-Series Screws

A set of typical propeller curves is given in Fig. 5.15. Only K_T and K_Q as functions of J are required in order to state completely the performance of the propeller. However, it is convenient to also plot the efficiency η_O. It can be seen that the thrust is a maximum when the advance coefficient is zero (maximum propeller slip) and it drops to zero when the propeller slip is near zero. The efficiency vanishes at both these extremes, but reaches a maximum value at some intermediate condition.

The condition for no thrust can be estimated from Fig. 5.13. The slip is zero when the relative inflow velocity vector is parallel to the chord of the blade. Hence

$$\tan \phi = \frac{V_{A(T=0)}}{(2\pi n)r} \approx \frac{P}{2\pi r}$$

That is $V_{A(T=0)} \approx nP$.

From (5.3), we have

$$J_{T=0} = V_A/nD$$

$$\approx \frac{nP}{nD}$$

$$= P/D \quad . \tag{5.30}$$

Verification of (5.30) is given by Fig. 5.16 where the propeller curves are plotted for a number of pitch-to-diameter ratios. The equation is only approximately correct because it ignores the effect of camber, amongst other details of the blade profile.

These standard curves are useful for presenting the performance characteristics of propellers, but not for making a selection. The method of selection depends on the data that is available.

From Harvald (1983, p. 141)

K_Q	K_T	η_O	K_T/K_Q	C_T
0,10	0,1	1,00	10	20
0,09	0,9	0,90	9	18
0,08	0,8	0,80	8	16
0,07	0,7	0,70	7	14
0,06	0,6	0,60	6	12
0,05	0,5	0,50	5	10
0,04	0,4	0,40	4	8
0,03	0,3	0,30	3	6
0,02	0,2	0,20	2	4
0,01	0,1	0,10	1	2
0	0	0	0	0

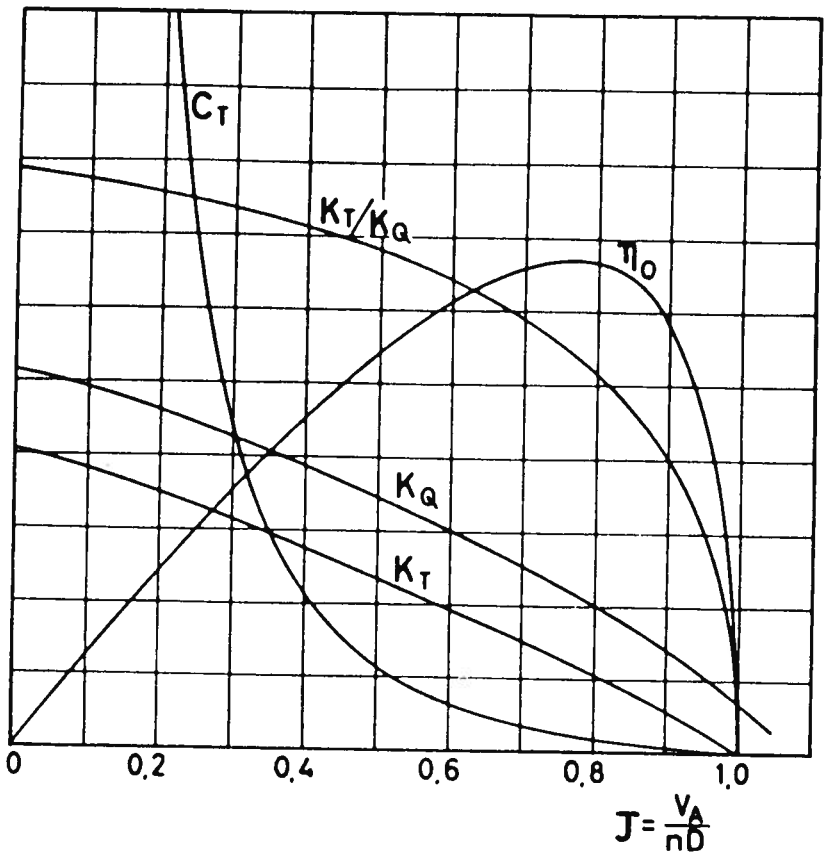

Figure 5.15: Typical Curves for a Propeller

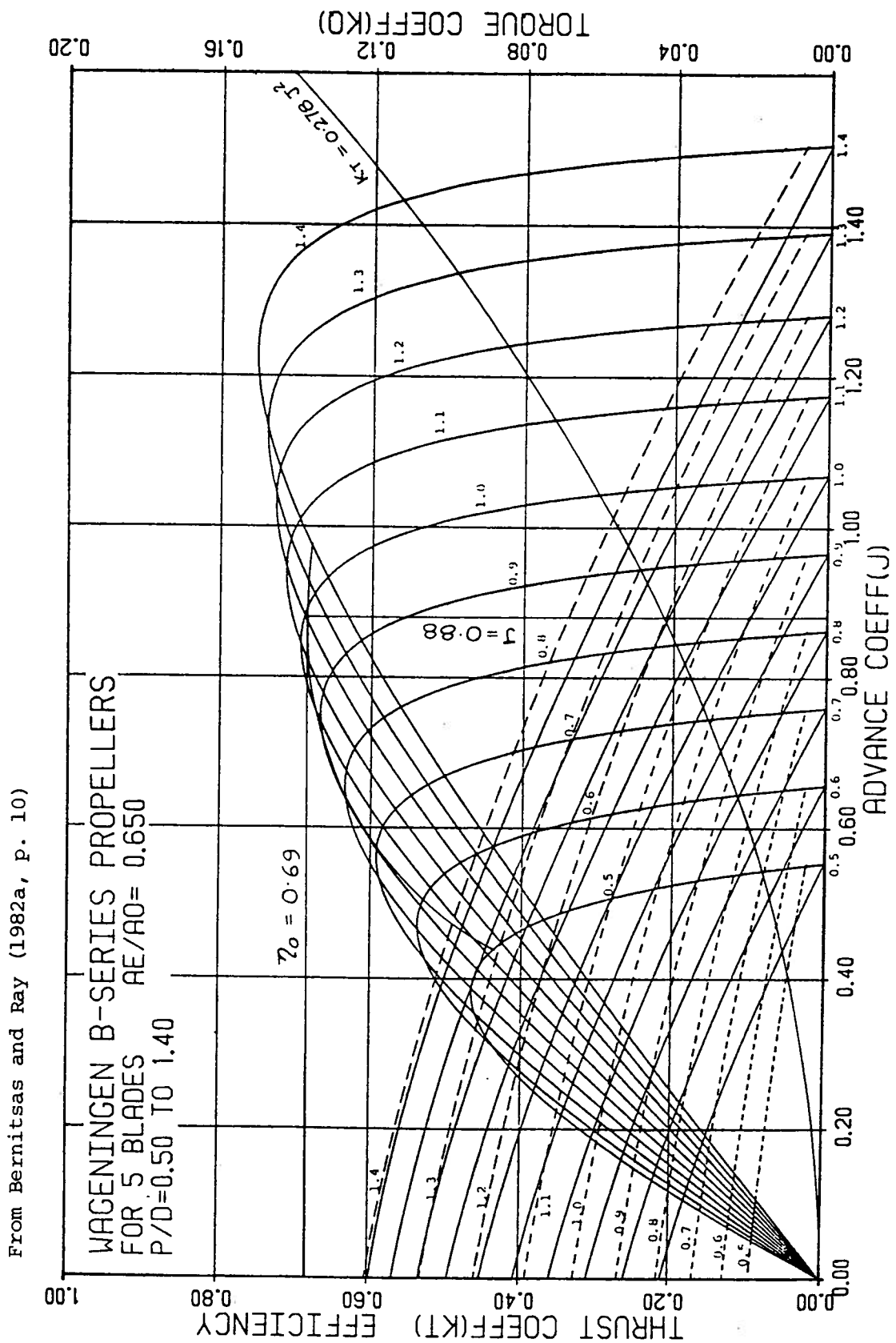

From Bernitsas and Ray (1982a, p. 10)

Figure 5.16: Searching for Optimum Revolutions (Diameter and Thrust Given)

5.4.2. Resistance and Diameter are Known

A common situation is one in which the required thrust and propeller diameter are known. We will assume that the choice of the number of blades has already been made, usually on the basis of minimizing vibration. Furthermore, we will consider the expanded-area ratio to be known. This quantity is chosen with the intention of preventing, or minimizing, the extent of cavitation. The avoidance of cavitation will be discussed in a later section.

Thus the problem reduces to one of finding the optimum propeller speed. We define the coefficient

$$K_T/J^2 = \frac{T/\rho n^2 D^4}{(V_A/nD)^2}$$

$$= \frac{R_T/(1 - t)\rho n^2 D^4}{[V(1 - w)/nD]^2}$$

$$= R_T/\rho D^2 V^2 (1 - t)(1 - w)^2 \quad , \tag{5.31}$$

where (5.1), (5.3), (5.5), and (5.6) have been used. This special loading coefficient was chosen to eliminate the unknown propeller speed.

In the example chosen by Bernitsas and Ray (1982a), $R_T = 275.4$ kN , $\rho = 1025$ kg/m^3 , $D = 5.486$ m , $V = 8.237$ m/s (= 16 kt) , $t = 0.155$, $w = 0.252$, and $\eta_R = 1.018$. This choice of data gives $K_T/J^2 = 0.278$. The variation of K_T with J has been plotted in Fig. 5.16, so that its intersection with the K_T curves of the propeller gives the matching point. The matching point depends on the pitch-to-diameter ratio chosen. A curve of efficiencies has been drawn on the figure, and this givesn a maximum value of $\eta_O = 0.69$ at $J = 0.88$ when $P/D = 1.20$.

This procedure can be automated. Fig. 5.17 shows the optimum values of the parameters η_O , J , and P/D as functions of K_T/J^2 . A large number of graphs such as this, covering a wide range of parameters (Z, A_E/A_O, and

From Bernitsas and Ray (1982a, p. 50)

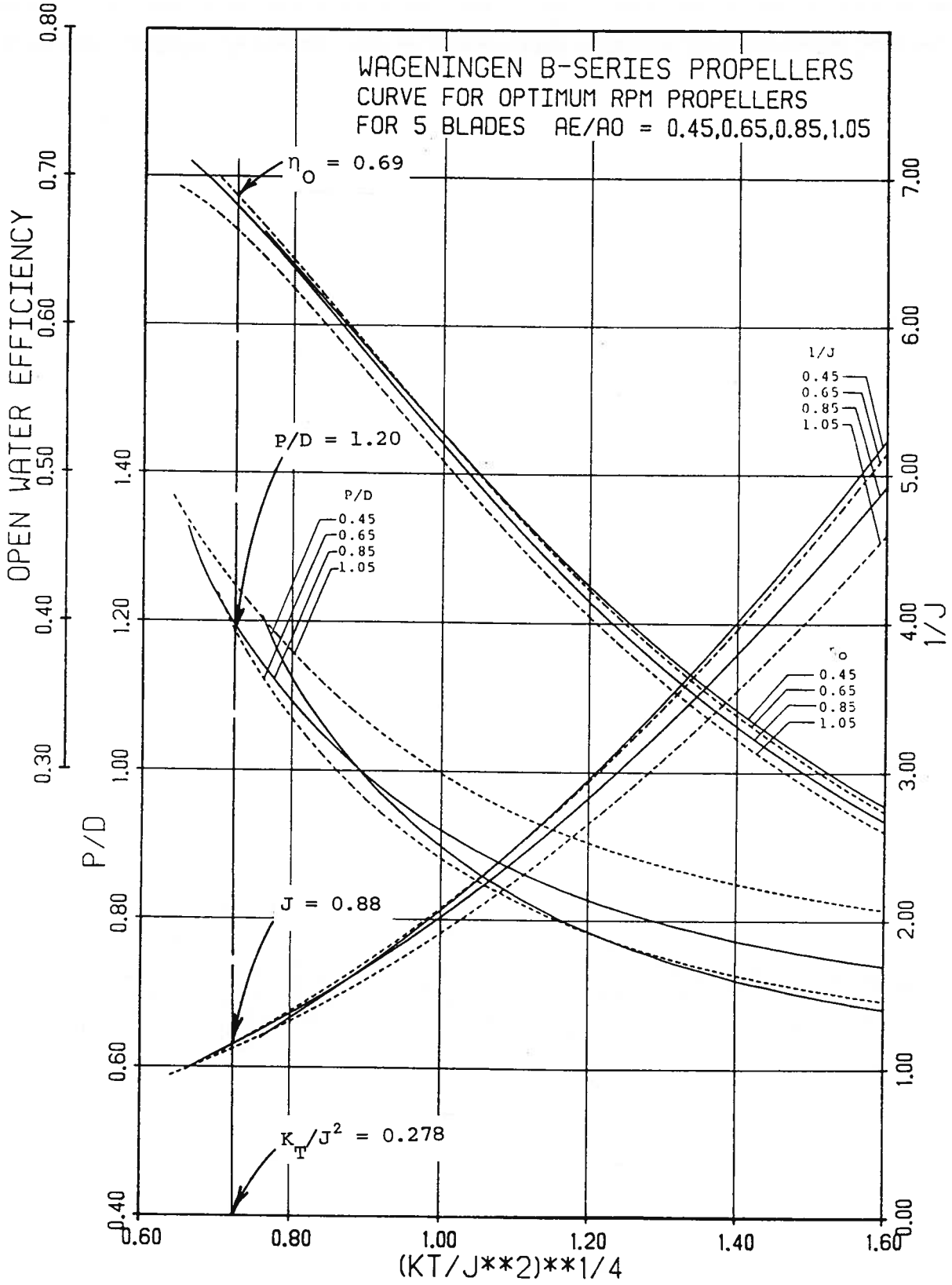

Figure 5.17: Optimum Revolution Propellers (Diameter and Thrust Given)

K_T/J^2) was given by Bernitsas and Ray (1982a).

5.4.3. Delivered Power and Diameter are Known

In this example, we wish to find the optimum revolutions when the propeller diameter and the power absorbed by the propeller P_D are given. The following coefficient is formed:

$$K_Q/J^3 = \frac{Q/\rho n^2 D^5}{(V_A/nD)^3}$$

$$= \frac{P_D \eta_R/2\pi\rho n^3 D^5}{[V(1 - w)/nD]^3}$$

$$= P_D \eta_R/2\pi\rho D^2 V^3 (1 - w)^3 \quad , \tag{5.32}$$

Again, the technique of eliminating the unknown value of n has been used.

The example given by Bernitsas and Ray is the same as in Sec. 5.4.2, except that we are now given $P_D = 2859$ kW instead of the value of R_T. The special coefficient becomes $K_Q/J^3 = 0.0641$. This curve has been plotted in Fig. 5.18. Again the intersections with the K_Q curve from the propeller gives the efficiency for different P/D ratios. The optimum values are found to be $\eta_O = 0.69$ at $J = 0.88$ when $P/D = 1.20$. (The power chosen here is compatible with the first example, and therefore the results are the same.)

As before, a more direct solution is available by means of Fig. 5.19, which gives the optimum solution as a function of K_Q/J^3.

5.4.4. Resistance and Revolutions are Known

In this example, we refer to Bernitsas and Ray (1982b). The appropriate coefficient is

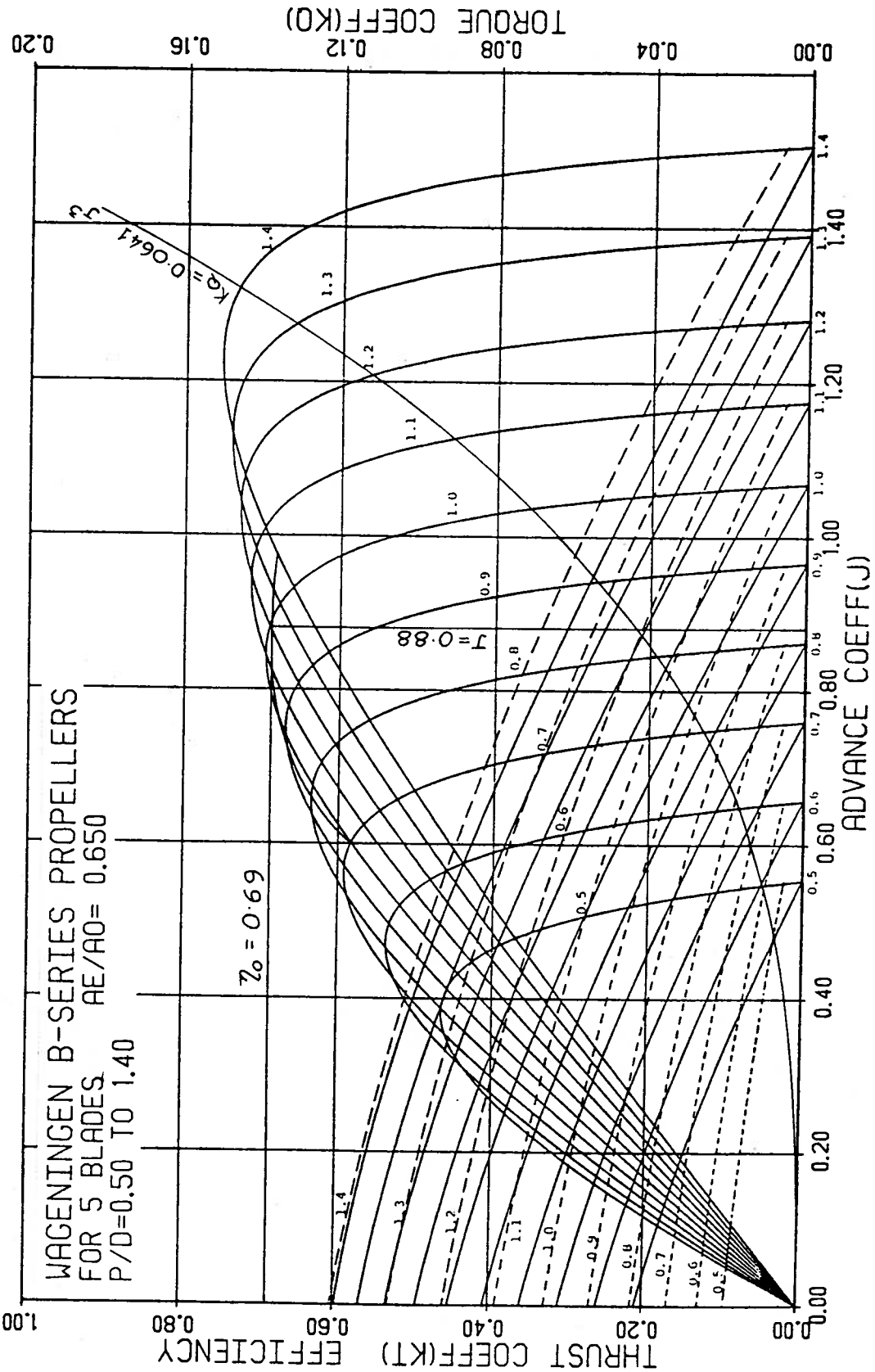

From Bernitsas and Ray (1982a, p. 70)

Figure 5.18: Searching for Optimum Revolutions (Diameter and Delivered Power Given)

From Bernitsas and Ray (1982a, p. 108)

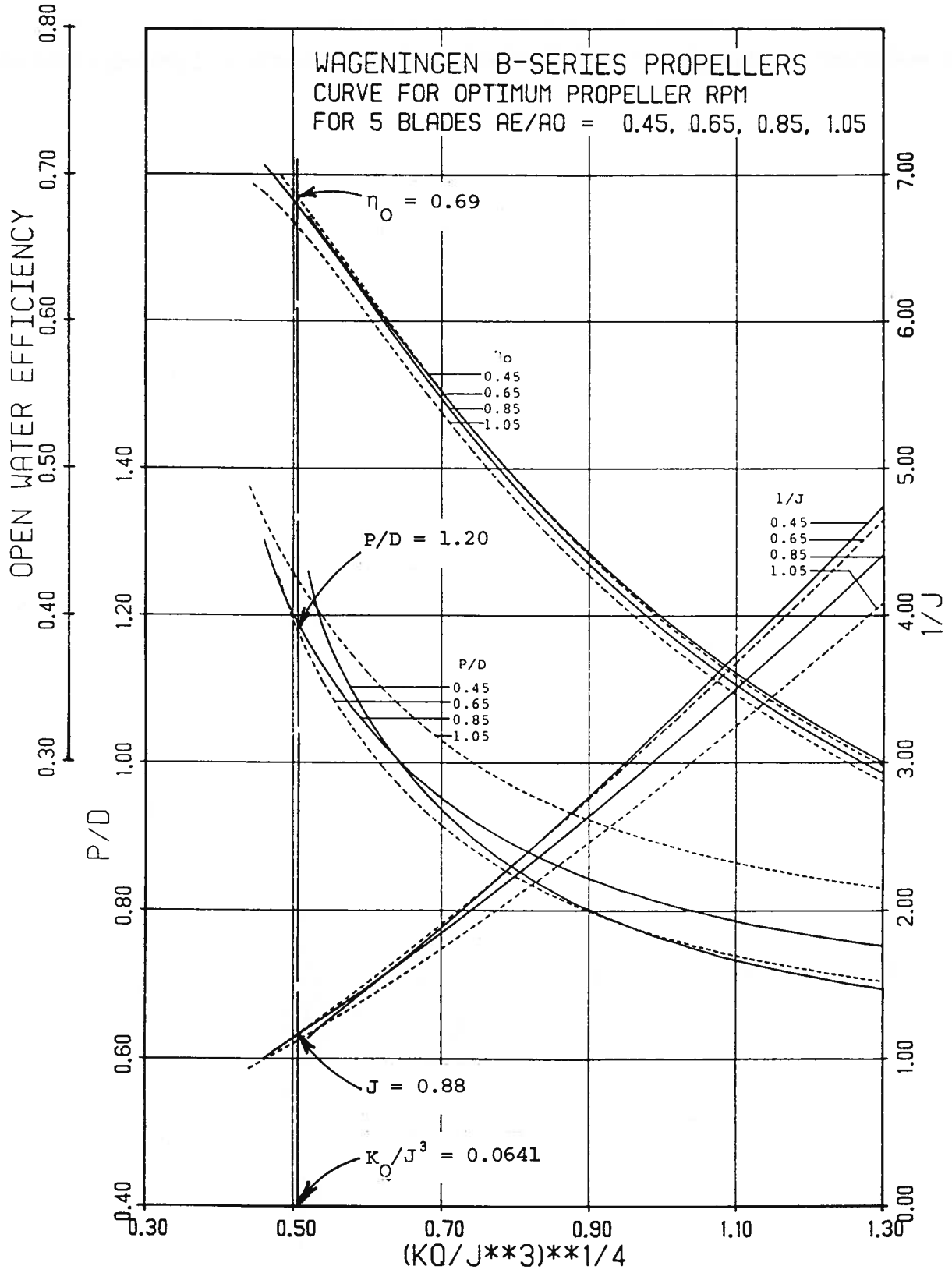

Figure 5.19: Optimum Revolution Propellers (Diameter and Delivered Power Given)

$$K_T/J^4 = \frac{T/\rho n^2 D^4}{(V_A/nD)^4}$$

$$= \frac{R_T/(1 - t)\rho n^2 D^4}{[V(1 - w)/nD]^4}$$

$$= R_T n^2/\rho V^4 (1 - t)(1 - w)^4 \quad . \tag{5.33}$$

Since the diameter D has been eliminated from the coefficient (5.33), this method can be used to optimize the diameter. As an example, we take R_T = 275.4 kN , ρ = 1025 kg/m^3 , n = 1.283 s^{-1} (= 77 rpm) , V = 8.237 m/s (= 16 kt) , t = 0.155 , w = 0.252 , and η_R = 1.018 . The special coefficient is the K_T/J^4 = 0.361 . This function has been plotted in Fig. 5.20. The intersection point with the K_Q curve depends on the value of P/D chosen. The optimum is seen to be given by η_O = 0.70 at J = 0.85 for P/D = 1.10 .

Fig. 5.21 shows how the same results can be obtained in a more expedient manner.

5.4.5. Delivered Power and Revolutions are Known

The appropriate coefficient in this case is

$$K_Q/J^5 = \frac{Q/\rho n^2 D^5}{(V_A/nD)^5}$$

$$= \frac{P_D \eta_R/2\pi\rho n^3 D^5}{[V(1 - w)/nD]^5}$$

$$= P_D \eta_R n^2/2\pi\rho V^5 (1 - w)^5 \quad . \tag{5.34}$$

Again, the unknown diameter does not appear in the coefficient.

Our example is the same as the previous one, except that we take P_D = 2820 kW , in place of stating the revolutions. The coefficient becomes K_Q/J^5 = 0.0822 . Fig. 5.22 shows the curve represented by this function. The intersection with the K_Q curve that gives the highest efficiency yields the

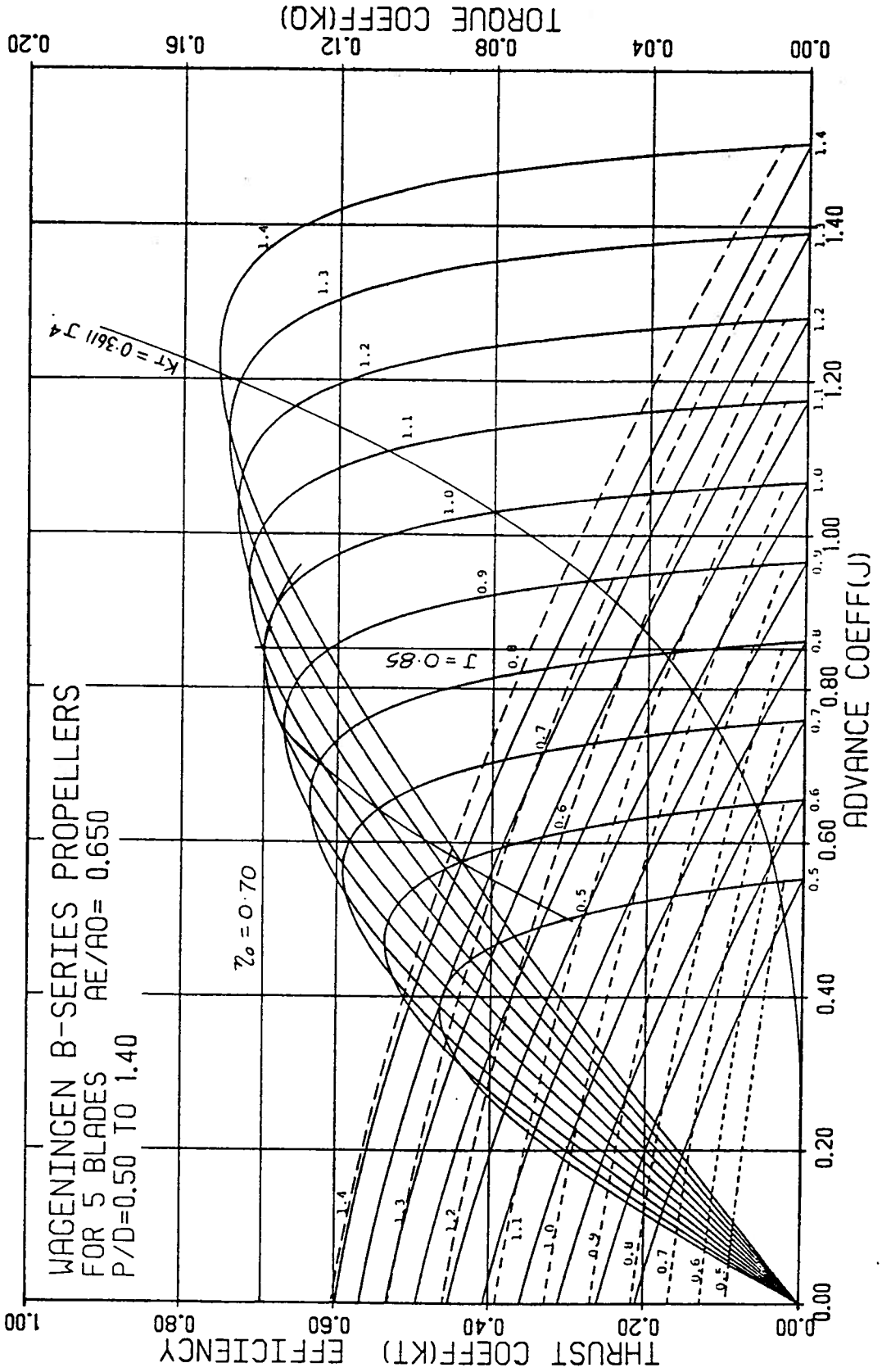

From Bernitsas and Ray (1982b, p. 6)

Figure 5.20: Searching for Optimum Diameter (Revolutions and Thrust Given)

From Bernitsas and Ray (1982b, p. 46)

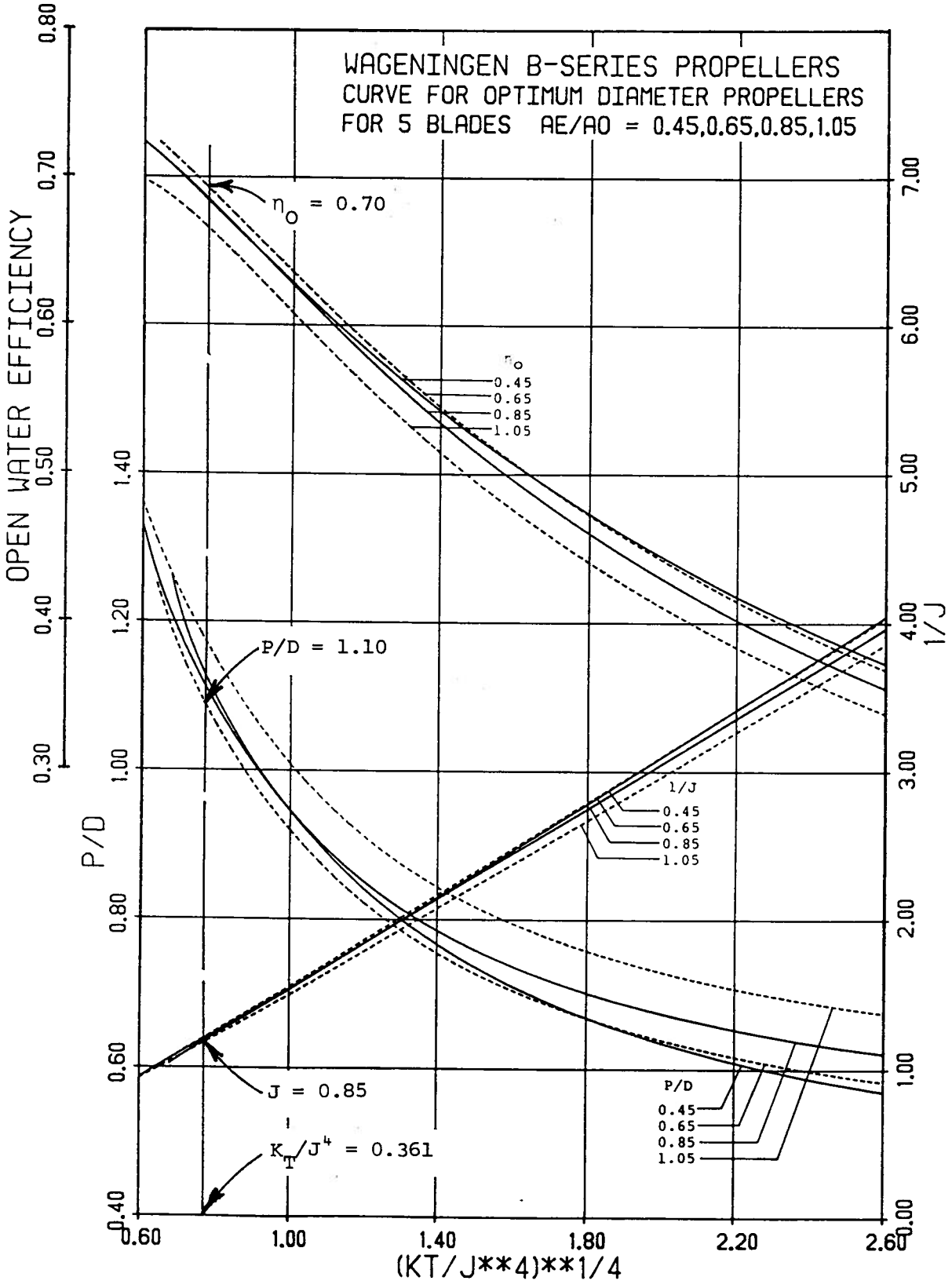

Figure 5.21: Optimum Diameter Propeller (Revolutions and Thrust Given)

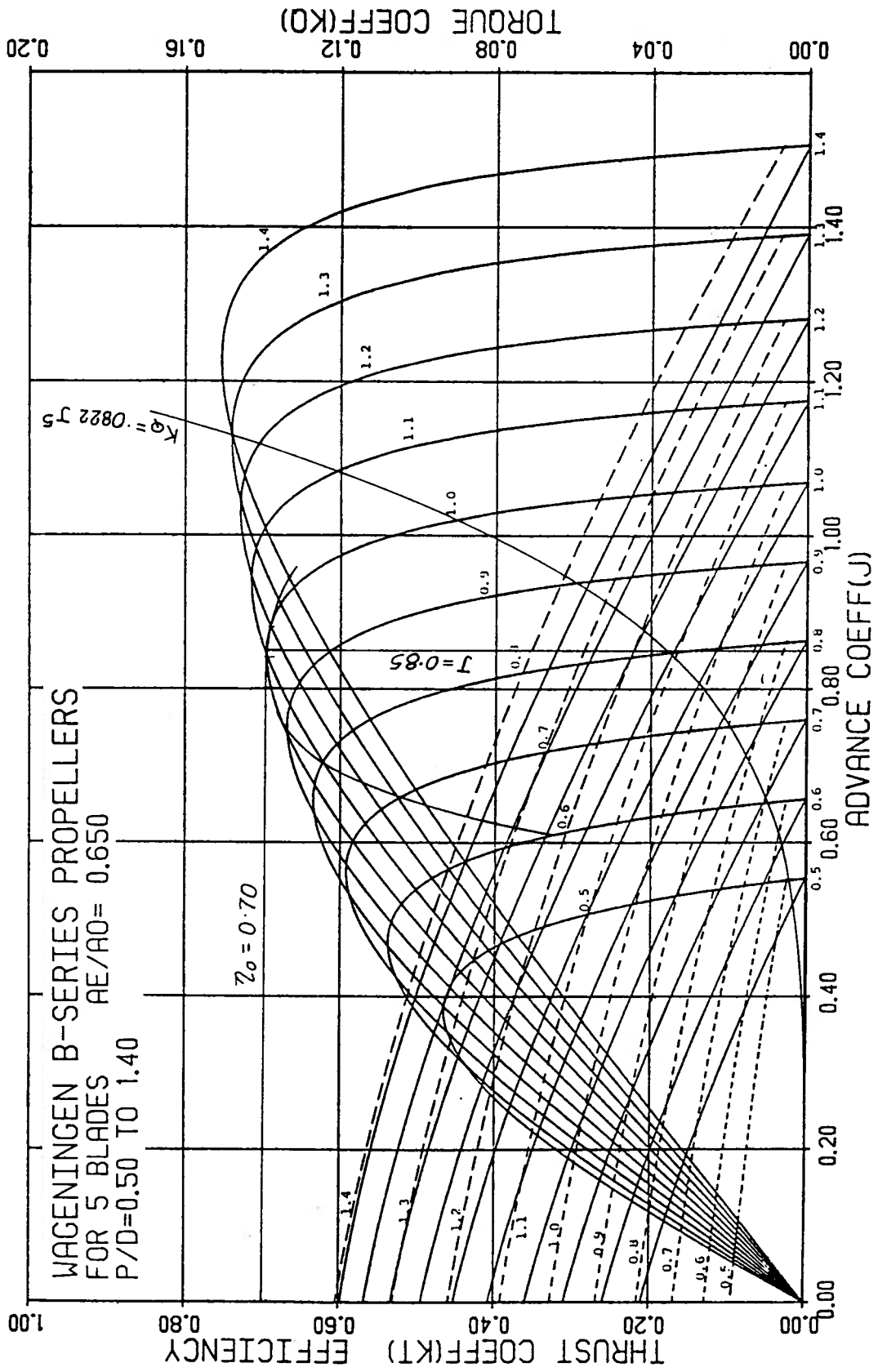

From Bernitsas and Ray (1982b, p. 66)

Figure 5.22: Searching for Optimum Diameter (Revolutions and Delivered Power Given)

results: $\eta_O = 0.70$ at $J = 0.85$ for $P/D = 1.10$.

The optimum case is found more easily when using a graph designed around the special coefficient. That is shown in Fig. 5.23.

5.4.6. Other Methods

Other techniques of presenting propeller data are in use. An example is the B_P-δ diagram, one of which is shown in Fig. 5.24. These two symbols are defined as

$$B_P = nP_D^{1/2}/V_A^{5/2}$$
$$\text{and} \quad \delta = nD/V_A \quad , \tag{5.35}$$

where n is the propeller speed in revolutions per minute, P_D is the delivered horsepower, V_A is the speed of advance in knots, and D is the propeller diameter in feet. These coefficients are dimensional, and cannot be used with a consistent set of units unless a correction factor is used. Additionally, the first coefficient suffers from the fact that it is only correct for fresh water. It must be modified if the propeller is to operate in salt water.

A comparison of (5.35) with the previously defined consistent coefficients ((5.34) and (5.3)) would show that

$$B_P = 33.12\ (K_Q/J^5)^{1/2}$$
$$\text{and} \quad \delta = 101.3/J \quad . \tag{5.36}$$

(A further complication is that P_D in (5.35) is an open-water value, which is a factor η_R larger than the behind-the-ship value used in (5.32) and (5.34)). Therefore, the purpose of a B_P-δ chart is similar to that of the method outlined in Sec. 5.4.5. That is, the delivered power and revolutions are known, and the aim is to find the best diameter. Nevertheless, the presentation in Sec. 5.4.5 seems to be better in that a number of propellers are included on one diagram, so that the options available to the user are

From Bernitsas and Ray (1982b, p. 104)

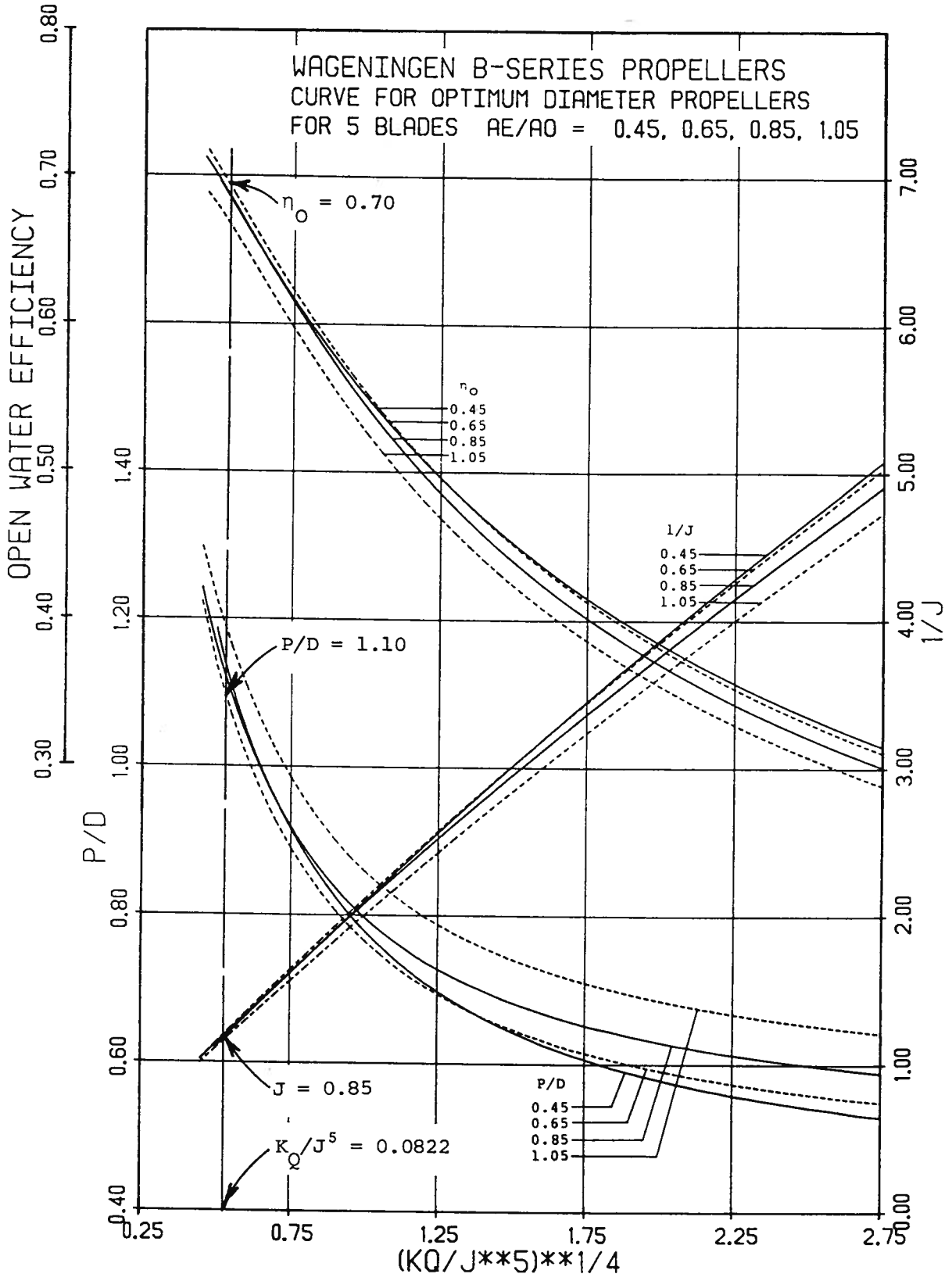

Figure 5.23: Optimum Diameter Propeller (Revolutions and Delivered Power Given)

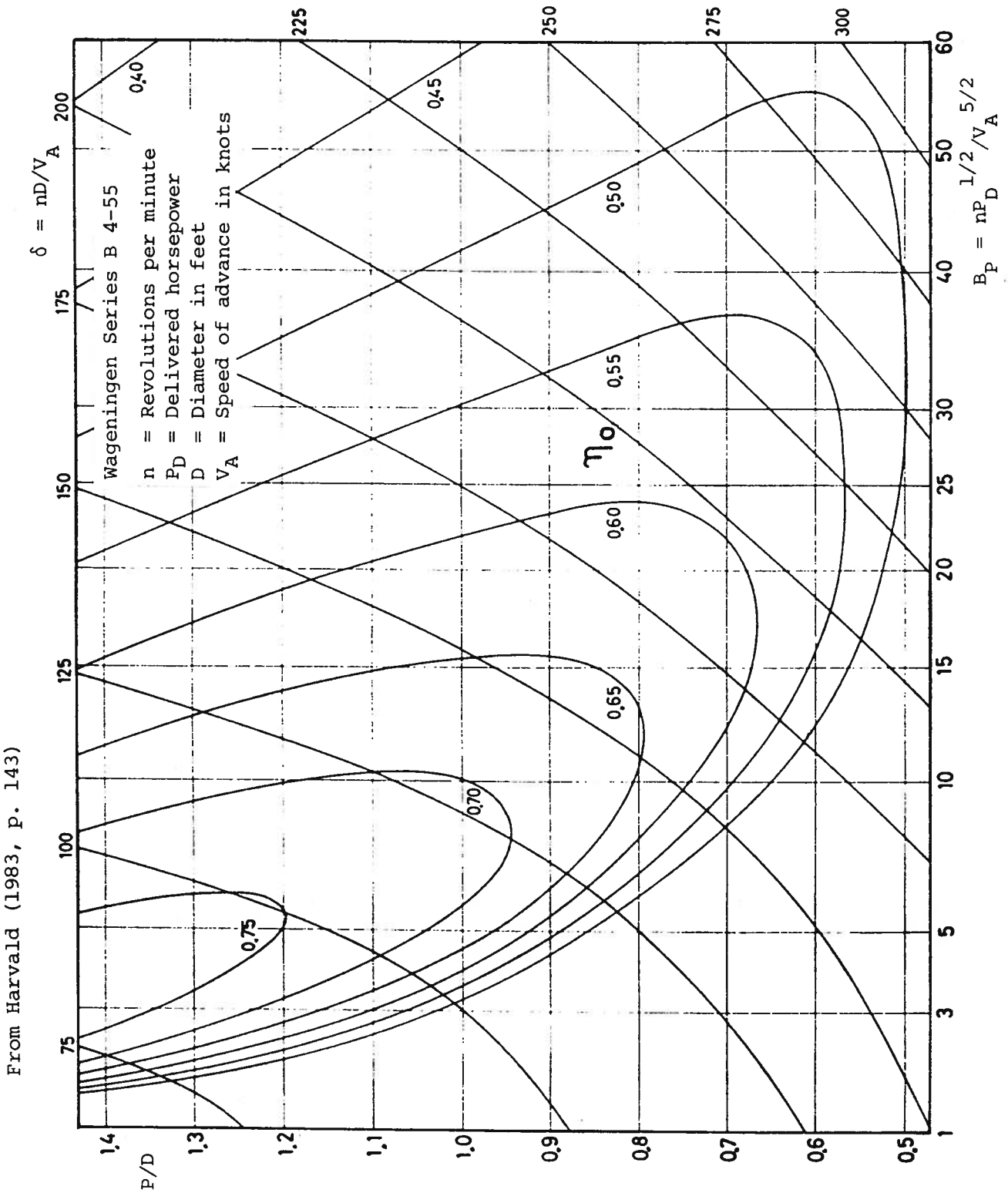

From Harvald (1983, p. 143)

Figure 5.24: Example of a B_P-δ Chart

clearer.

Another inconsistent coefficient which has sometimes been used is

$$B_U = nU^{1/2}/V_A^{5/2} \quad , \tag{5.37}$$

where U is the thrust power (the product of the propeller thrust and the wake speed), but measured in horsepower. It can be shown that

$$B_U = 13.21\ (K_T/J^4)^{1/2} \quad . \tag{5.38}$$

Again, this coefficient must be corrected for use in salt water. Its application would be similar to that described in Sec. 5.4.4.

It is also possible to produce $B_{P'}$-δ and $B_{U'}$-δ diagrams for the cases when the diameter is specified and the optimum revolutions are to be found.

Another approach to the problem of propeller selection is to use an optimizing procedure based on a mathematical representation of the propeller performance (5.28). Markussen (1979) described a method in which both the revolutions and the diameter could be optimized. Unfortunately, there is generally a restriction on the propeller diameter, so that this global optimum does not represent a practical selection.

5.4.7. The Influence of Reynolds Number

Although the model propellers are tested at only one Reynolds number (5.29), the results can be corrected for other cases by estimating the frictional drag on the blades. A sample of such results are shown in Fig. 5.25. The torque coefficient is seen to drop with increasing Reynolds number. This is in accordance with the known behavior, for example, of the friction coefficient for a flat plate. Of course, part of the torque is due to the induced drag on the propeller blades, and is unaffected by the correction to the friction component.

The thrust coefficient is not affected by the Reynolds number. This result is equivalent to the fact that the Reynolds number has negligible influence on the lift of a wing -- at least up to the stall angle.

The results of Fig. 5.25 show that the efficiency of a propeller increases with size. That is, uncorrected model tests are slightly pessimistic.

5.5. Cavitation Inception

If a propeller is overloaded, the pressure on the suction side of the blades (the back) will drop to the vapor pressure and cavitation will occur. An example in which the propeller is just slightly overloaded is given in Fig. 5.26. Here, the propeller is working in a wake where the advance velocity is less near the top. Thus the effective angle of attack (see Fig. 5.13) is greater, which would encourage back cavitation when the blades approach the top. Furthermore, the ambient pressure is less in this region. These two features encourage cavitation near the top position.

As the propeller load is raised (by increasing the slip), the cavitation area will increase too. Excessive cavitation should be avoided if possible because of the loss in efficiency and the blade erosion problem.

The situation which leads to cavitation can be estimated by considering the propeller to be on the point of cavitation at some location (say $r = 0.75R$) on the propeller. The representative cavitation number for the propeller is then

$$\sigma_{0.7R} = (p_a + \rho g d - p_v)/\tfrac{1}{2}\rho V_R^2 \quad , \tag{5.39}$$

where p_a is the atmospheric pressure, g is the acceleration due to gravity, p_v is the vapor pressure, and V_R is the relative velocity at the representative radius. This is given by the formula

From Harvald (1983, p. 150)

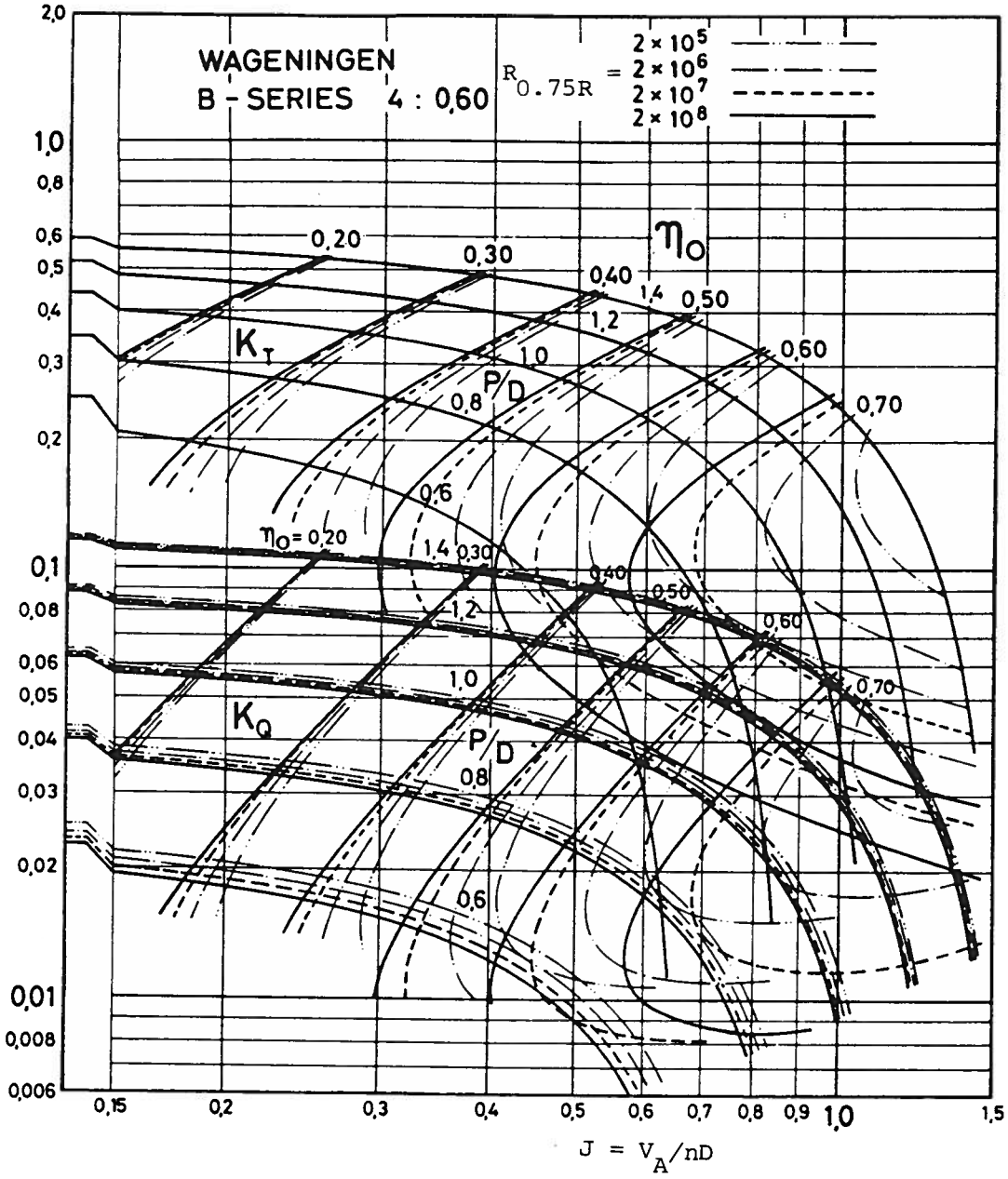

Figure 5.25: The Influence of Reynolds Number on Propeller Characteristics

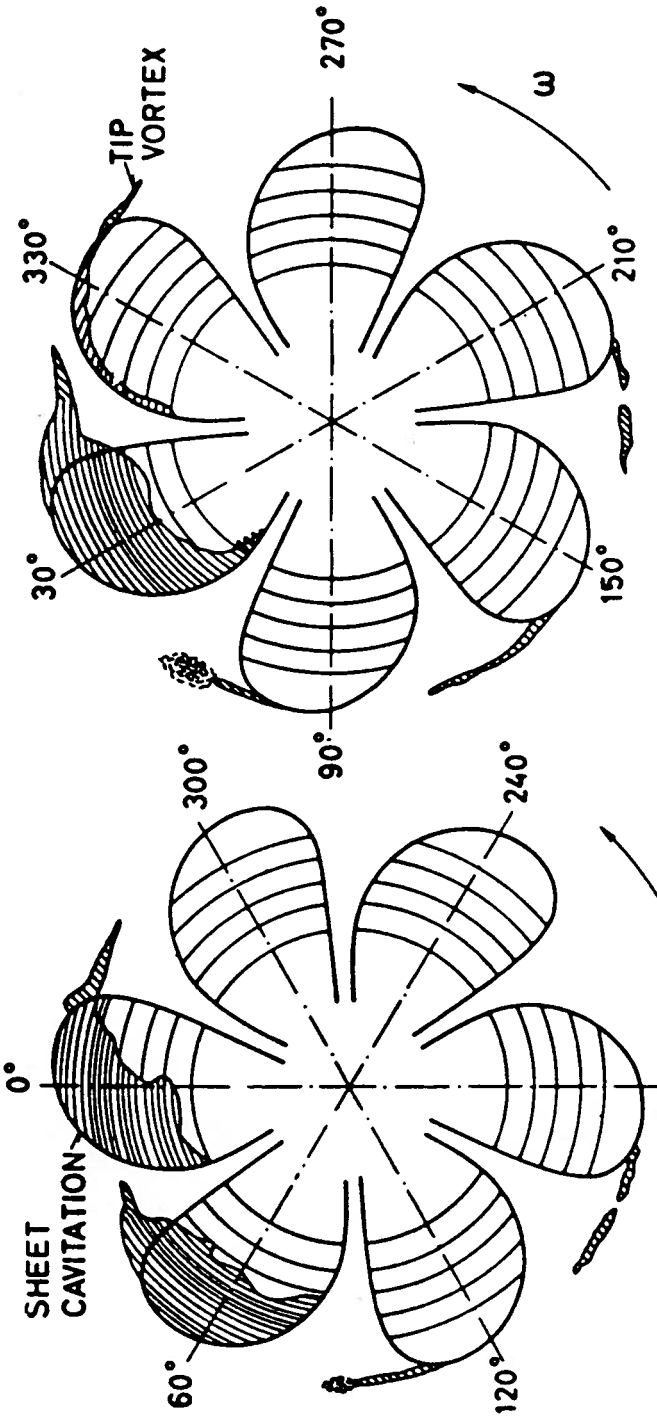

From Harvald (1983, p. 190)

Figure 5.26: Cavitation on a Propeller in a Non-Uniform Wake

$$V_R = [V_A^2 + (2\pi n \times 0.75\ R)^2]^{1/2}$$

$$= V_A[1 + (0.75\ \pi/J)^2]^{1/2} \quad . \tag{5.40}$$

We shall assume that the blade operates at the ideal angle of attack, and that linear theory can be used (the section is thin and the camber and effective angle of attack are small). Thus, we can write for the upper and lower surface of the blade,

$$p = p_a + \rho g d + (C_{p_1} \pm C_{p_2})\frac{1}{2}\rho V_R^2 \quad , \tag{5.41}$$

where C_{p_1} and C_{p_2} are the pressure increments per unit dynamic pressure, due to the thickness and lifting effects, respectively.

We may now combine (5.39) and (5.41) with $p = p_v$. We also use the plus sign in (5.41), corresponding to the upper surface (the back). Thus

$$\sigma_{0.75R} = -(C_{p_1} + C_{p_2}) \quad . \tag{5.42}$$

Progress with this simple theory can now only be made by making some assumptions about the particular propeller being considered. For a thin section, we can write the thickness effect as

$$C_{p_1} = -k(t/c) \quad . \tag{5.43}$$

We now assume that the load is distributed equally between the upper and lower surfaces of the blade, and that it is uniform over the leading fraction a of the section, and then drops linearly to zero at the trailing edge. A foil that generates this type of loading is referred to as a NACA "a" series section. We obtain for the ideal lift coefficient of the section

$$C_{L_i} = -2C_{p_2}\left[a + \frac{1}{2}(1 - a)\right]$$

or

$$C_{p_2} = -C_{L_i}/(1 + a) \quad . \tag{5.44}$$

We can combine (5.42), (5.43), and (5.44) to give

$$\sigma_{0.75R} = k(t/c) + C_{L_i}/(1 + a) \quad . \tag{5.45}$$

Finally, we define the propeller thrust loading coefficient as

$$\tau_c = T/\tfrac{1}{2}\rho V_R^2 A_p \quad , \tag{5.46}$$

where A_p is the projected blade area. It is easy to see that we can replace C_{L_i} in (5.45) by τ_c in (5.46), as the pitch angle β in Fig. 5.13 affects both the useful lift and the projected area in the same way. Thus (5.45) becomes

$$\sigma_{0.75R} = k(t/c) + \tau_c/(1 + a) \quad . \tag{5.47}$$

As a simple case, we can consider a cavitation-perfect propeller. The blades of this propeller would have zero thickness ($t = 0$) and the loading would be uniform ($a = 1$). This gives

$$\sigma_{0.75R} = \tfrac{1}{2}\tau_c \quad \text{for a cavitation-perfect propeller.} \tag{5.48}$$

A more practical propeller is represented by the Wageningen series. The ratio of blade thickness to chord at the representative radius for these propellers was given by van Lammeren and others (1969) as

$$t_{0.75R}/c_{0.75R} = (0.0185 - 0.00125\ Z)/\left(2.073\ \frac{A_E}{A_0}\ \frac{1}{Z}\right) \quad . \tag{5.49}$$

If we choose a four-bladed propeller ($Z = 4$) with an expanded-area ratio of 0.70, we obtain $t_{0.75R}/c_{0.75R} = 0.03721$. We can take the thickness distribution to correspond to a NACA 12 series section (see Abbott and von Doenhoff (1959, p 321)), for which we can put $k = 2.55$ in (5.47). Assuming also that $a = 0.8$, then (5.47) becomes

$$\sigma_{0.75R} = 0.0949 + 0.555\ \tau_c \quad \text{for a typical propeller} \ . \tag{5.50}$$

Fig. 5.27 shows the results of experiments relating the thrust loading coefficient to the characteristic cavitation number. The experimental curves

give the thrust that can be achieved for different levels of cavitation that are tolerated on the propeller. It is interesting to note that (5.50) predicts when cavitation will occur at the $r = 0.75\ R$ section, corresponding to about 25% cavitation. This equation roughly agrees with the experiments. The cavitation-perfect propeller, defined by (5.48) is seen to considerably overpredict the condition for cavitation.

The simple theory in this section can be improved to include nonlinear effects as well as the fact that V_R varies along the length of the blade. An estimate for the projected area is needed for (5.46), when using Fig. 5.27. This was given by Comstock (1967, p. 77) as

$$A_P/A_D = 1.067 - 0.299(P/D) \quad . \tag{5.51}$$

5.6. Supercavitating Propellers

5.6.1. Wageningen B-Series Screws

The Wageningen B-series was described in Sec. 5.4.1, and is illustrated in Fig. 5.14. While these were designed for subcavitating conditions, they can also be used in the supercavitating mode. Of course, a loss in efficiency must then be anticipated. Fig. 5.28 gives the performance of a four-bladed screw with an expanded-area ratio of 0.85, for pitch ratios of 1.2 and 1.4.

It is seen that the performance now depends on the cavitation number defined by

$$\sigma = (p_a + \rho g d - p_v)/\tfrac{1}{2}\rho V_A^2 \quad . \tag{5.52}$$

When σ is sufficiently large, no cavitation occurs, and the previously discussed subcavitating results can be used. The experiments show that when the slip is small (J is large) and the loading K_T is small, then the influence of the cavitation number is less. It is noted that the efficiency, as well as the thrust and the torque are all less when the cavitation is taken

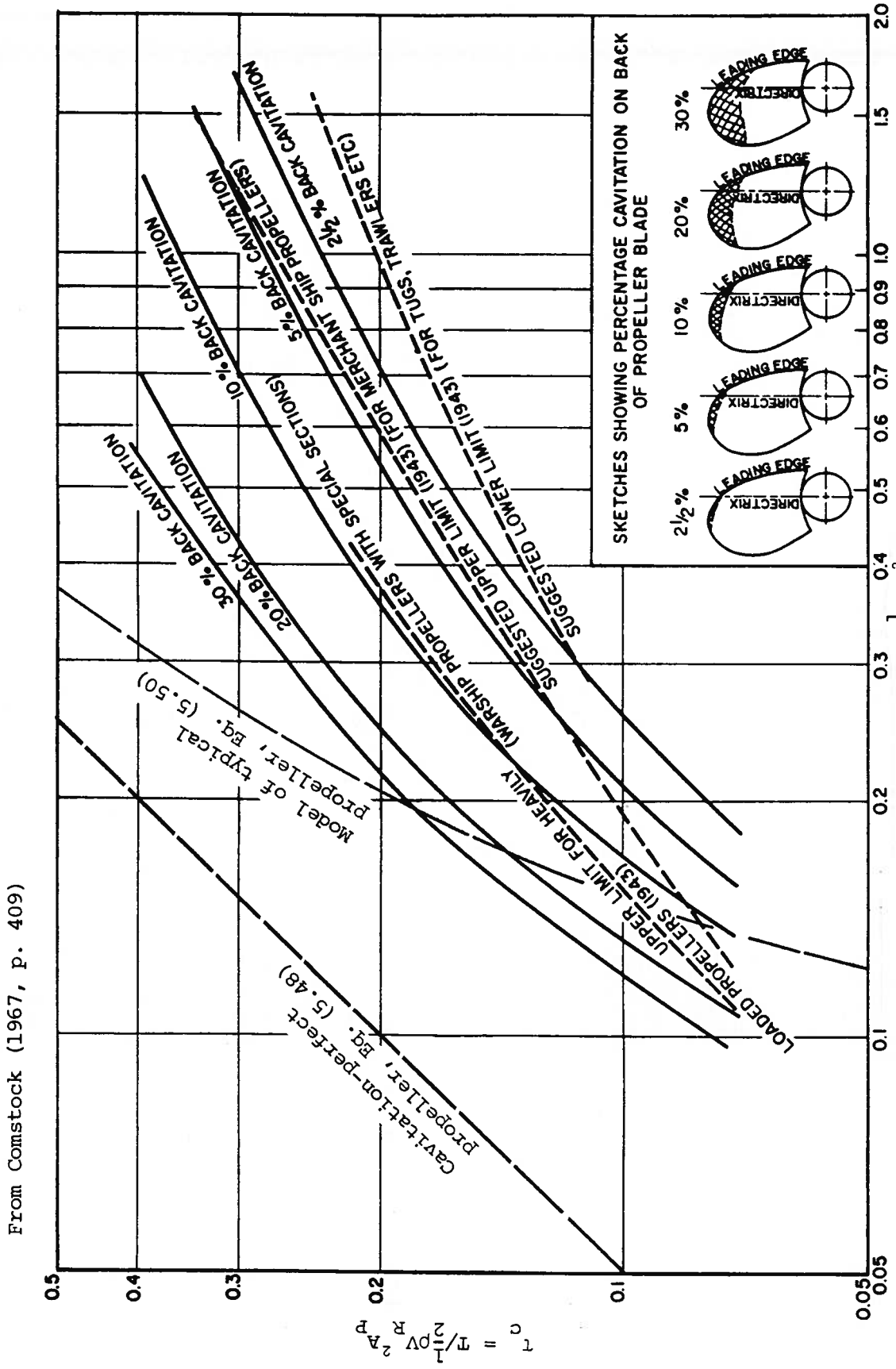

Figure 5.27: Simple Cavitation Diagram

From van Lammeren, van Manen, and Oosterveld (1969, p. 303)

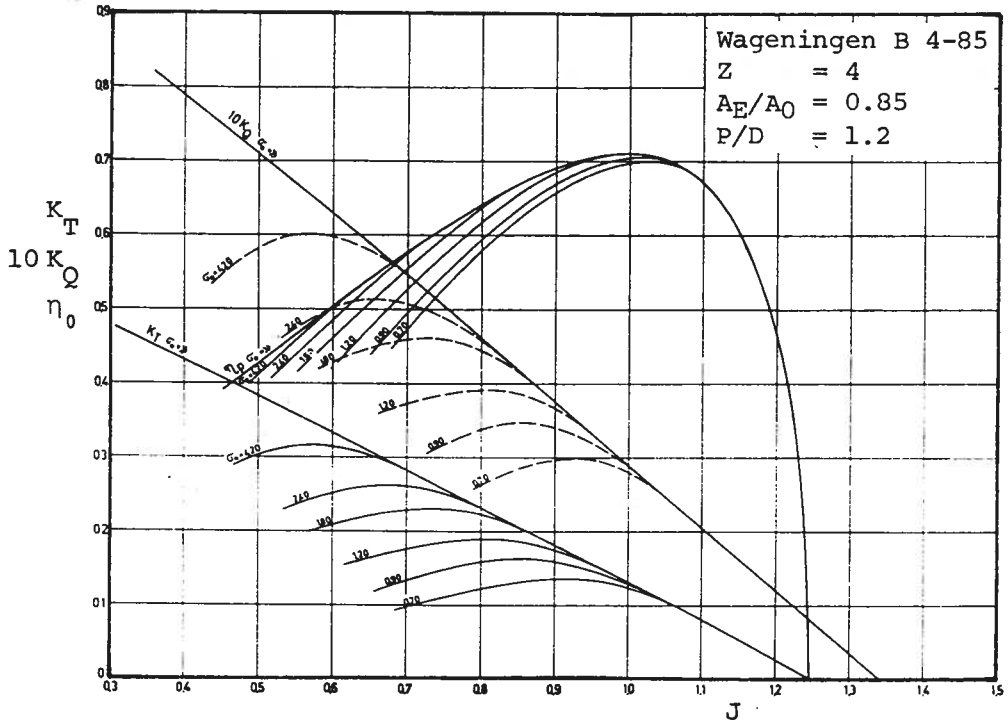

(a) Pitch-Diameter Ratio = 1.2

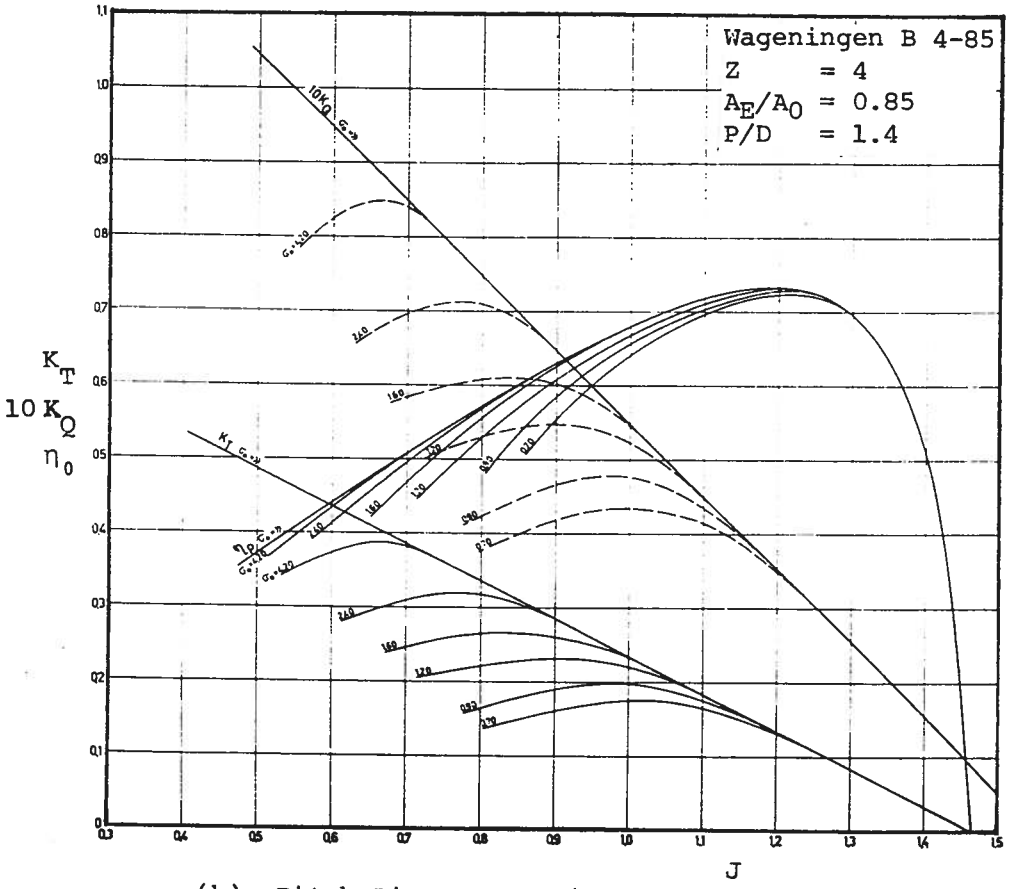

(b) Pitch-Diameter Ratio = 1.4

Figure 5.28: Supercavitating Wageningen Screw (as a Function of J)

into account -- particularly at low values of the advance ratio.

Blount and Fox (1978) replotted these results to a base of K_T/J^2 . An example of their graphs is given in Fig. 5.29. As noted in Sec. 5.4.2, this is a more convenient way of plotting the results when the thrust and diameter are known, as the optimum propeller and revolutions can more easily be chosen then.

5.6.2. Gawn-Burrill Series Screws

The Gawn-Burrill screws were specifically designed to operate in the cavitating mode, unlike the Wageningen screws. The basic geometry of these screws is presented in Fig. 5.30. These propellers have three blades and the blade-area ratio lies between 0.5 and 1.1, while the pitch ratio is between 0.6 and 2.0. The blade face is flat and has a constant pitch (it is not wake adapted). The blade outline is elliptical.

Some results are presented in Fig. 5.31. This particular figure shows how the original experimental results were corrected for the speed effect (because of the tunnel blockage) and for the pressure effect (cavitation number). The overall trend of the behavior is the same as for the Wageningen screws: when the slip is large, the cavitation number is more important, and its influence is to reduce the efficiency, thrust and the torque.

The performance of these screws has also been plotted on a base of K_T/J^2 , by Blount and Fox (1976). An example of these is given in Fig. 5.32.

5.6.3. Newton-Rader Series Screws

The geometry of this series is shown in Fig. 5.33. Like the Gawn-Burrill screws, the Newton-Rader propellers are three-bladed. The pitch ratio was varied from 1.0 to 2.0 and the blade-area ratios from 0.5 to 1.0 in the tests. Fig. 5.33 shows how the leading edges of the blades were modified twice to

From Blount and Fox (1978, p. 155)

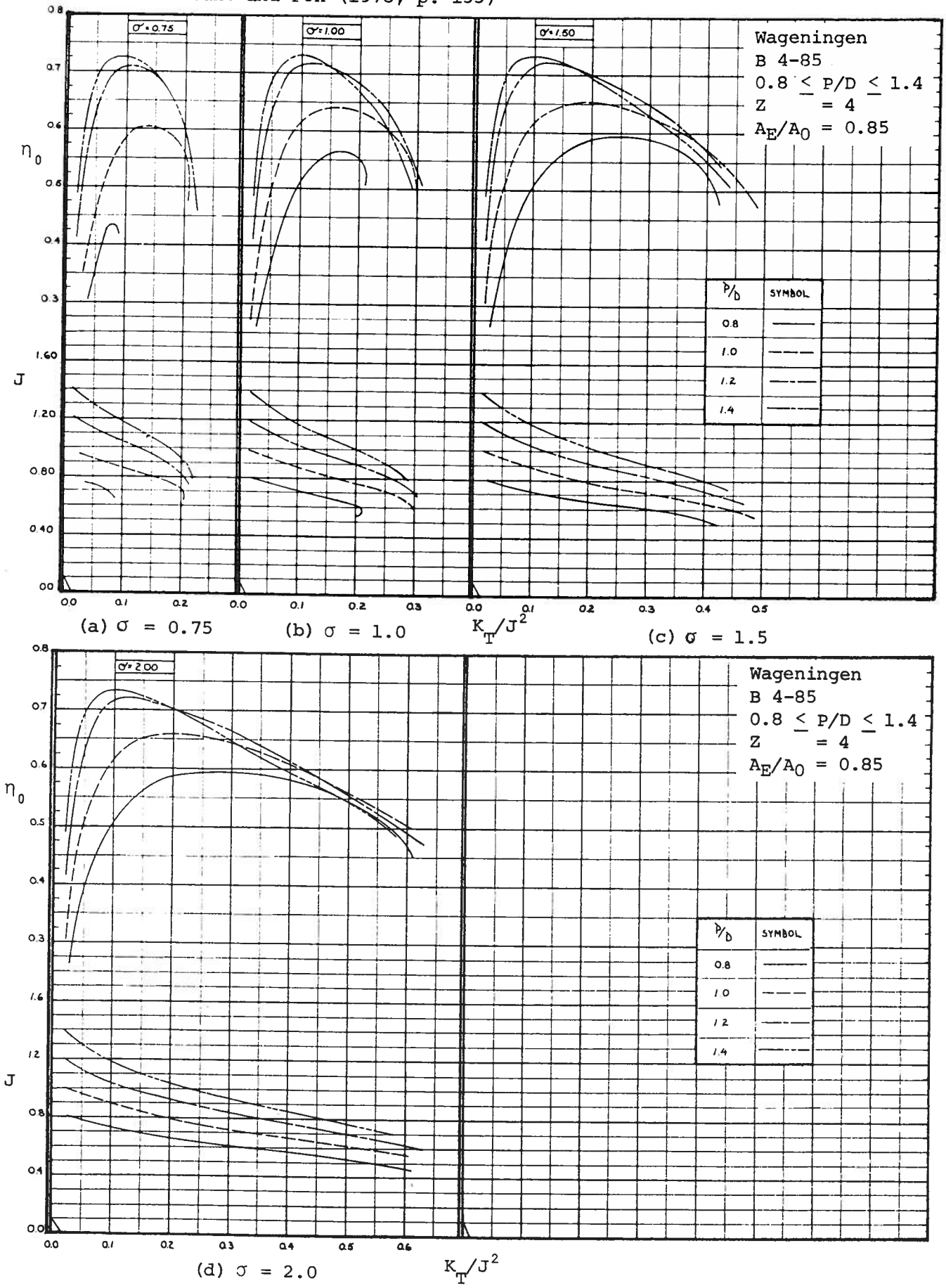

Figure 5.29: Supercavitating Wageningen Screw (as a Function of K_T/J^2)

From Blount and Fox (1978, p. 156)

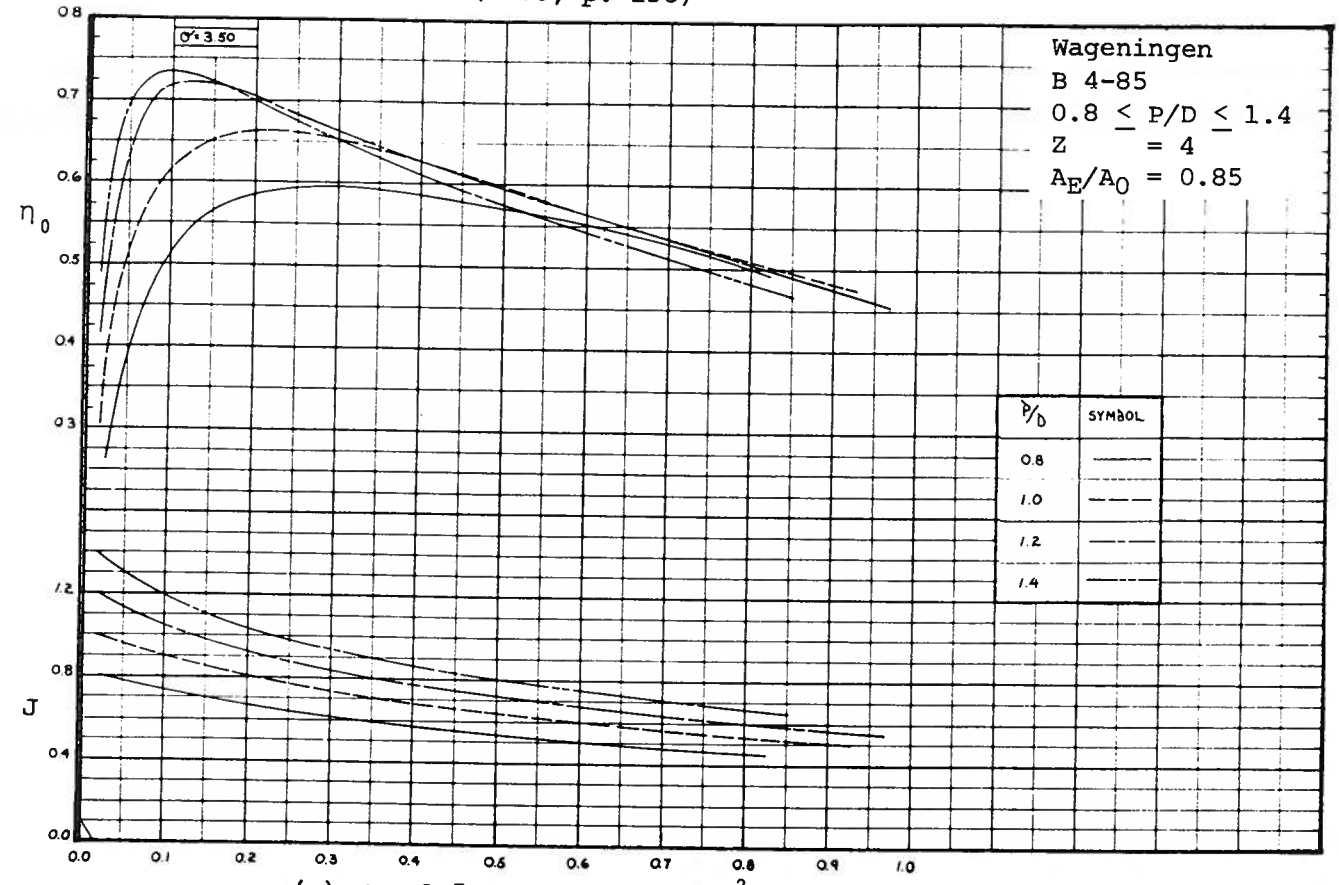

(e) σ = 3.5

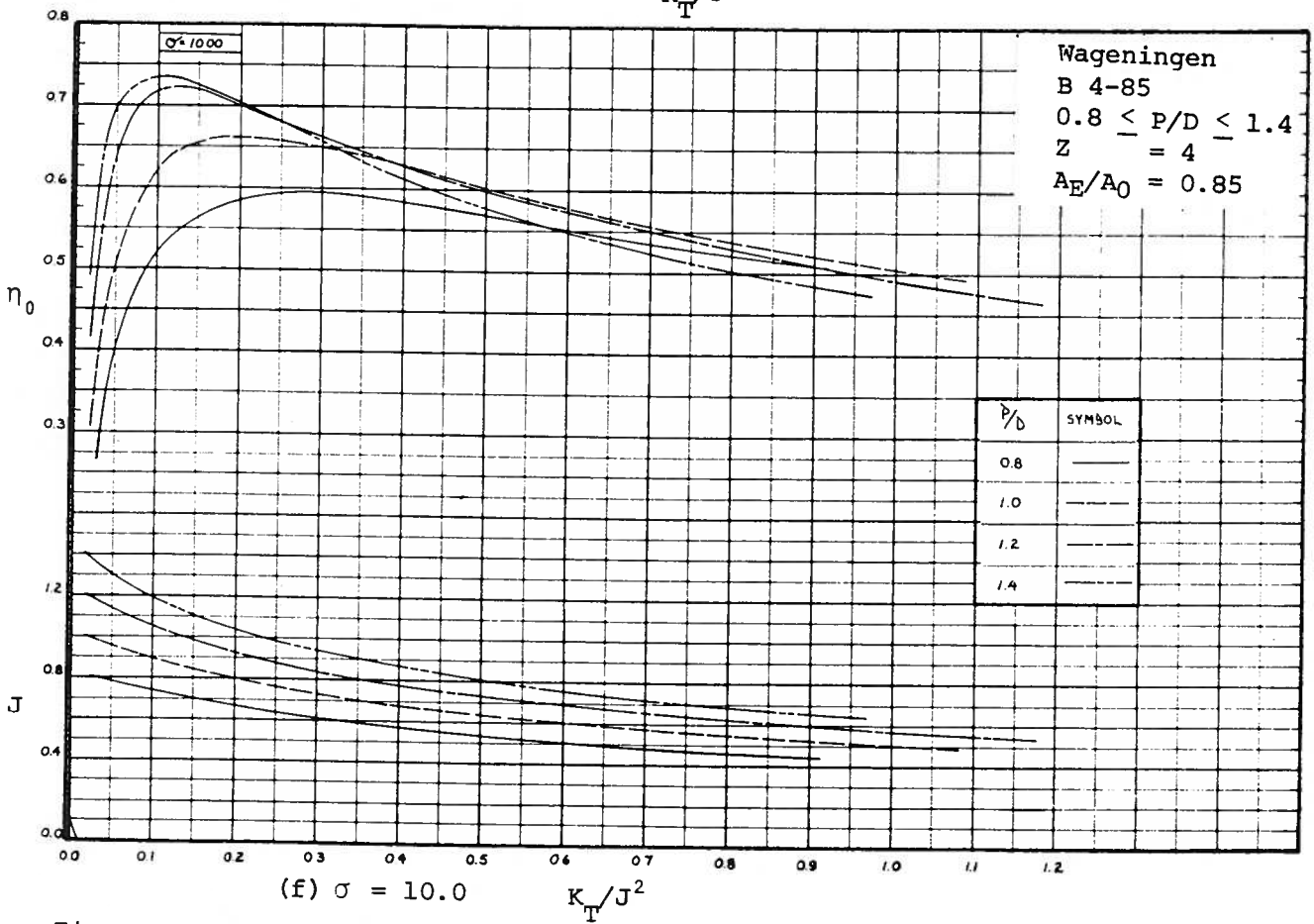

(f) σ = 10.0

Figure 5.29: (Continued)

From Gawn and Burrill (1957, p. 693)

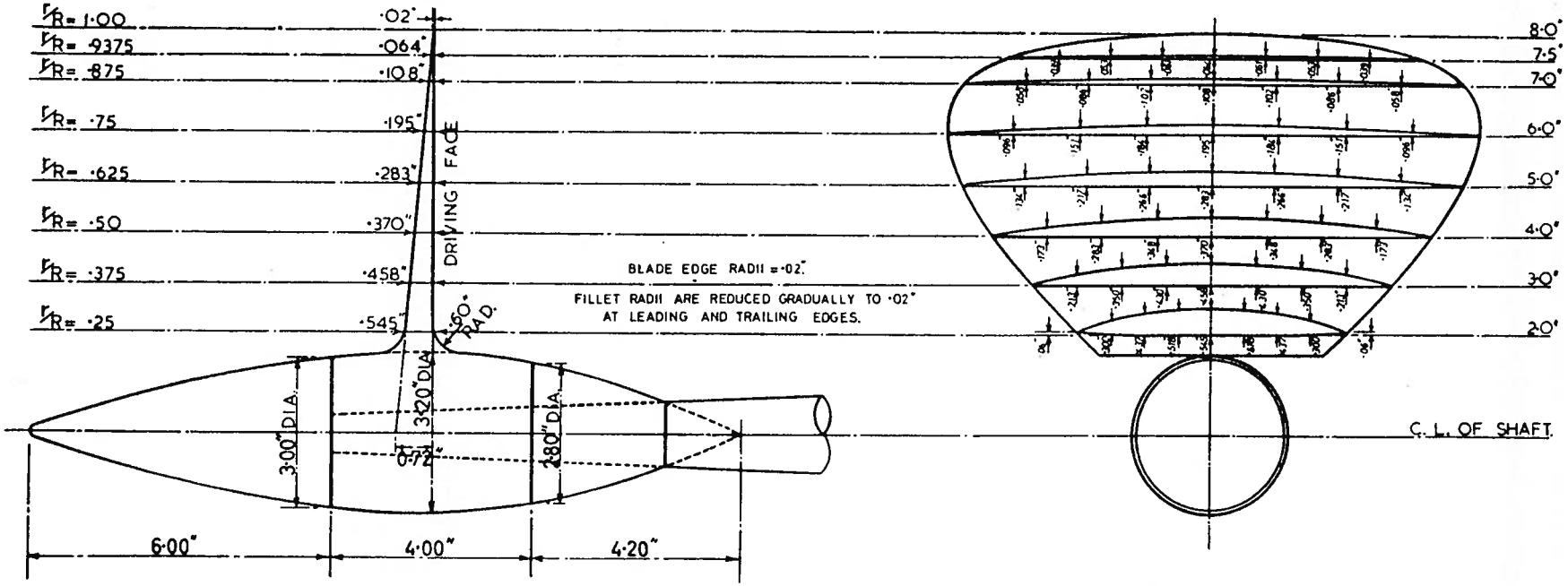

TABLE OF CHORD LENGTHS IN INCHES AND $\omega/\omega_{.50}$

B.A.R.	$\frac{r}{R}$=·25	$\frac{r}{R}$=·375	$\frac{r}{R}$=·50	$\frac{r}{R}$=·625	$\frac{r}{R}$=·75	$\frac{r}{R}$=·875	$\frac{r}{R}$=·9375	EXP. A.R.
0·50	3·35	4·55	5·555	6·33	6·74	6·32	5·25	0·51
0·65	4·38	5·93	7·25	8·26	8·79	8·25	6·86	0·665
0·80	5·38	7·30	8·92	10·18	10·80	10·16	8·42	0·82
0·95	6·56	8·90	10·87	12·38	13·16	12·37	10·28	1·00
1·10	7·73	10·49	12·80	14·60	15·53	14·58	12·11	1·18
$\omega/\omega_{.50}$	·604	·819	1·000	1·140	1·212	1·139	·946	

Parent Screw

D = 16 inches
Z = 3
A_E/A_0 = 0.80
D_{hub}/D = 0.20
Right-handed

Figure 5.30: Geometry of the Gawn-Burrill Series Screws

From Gawn and Burrill (1957, p.713)

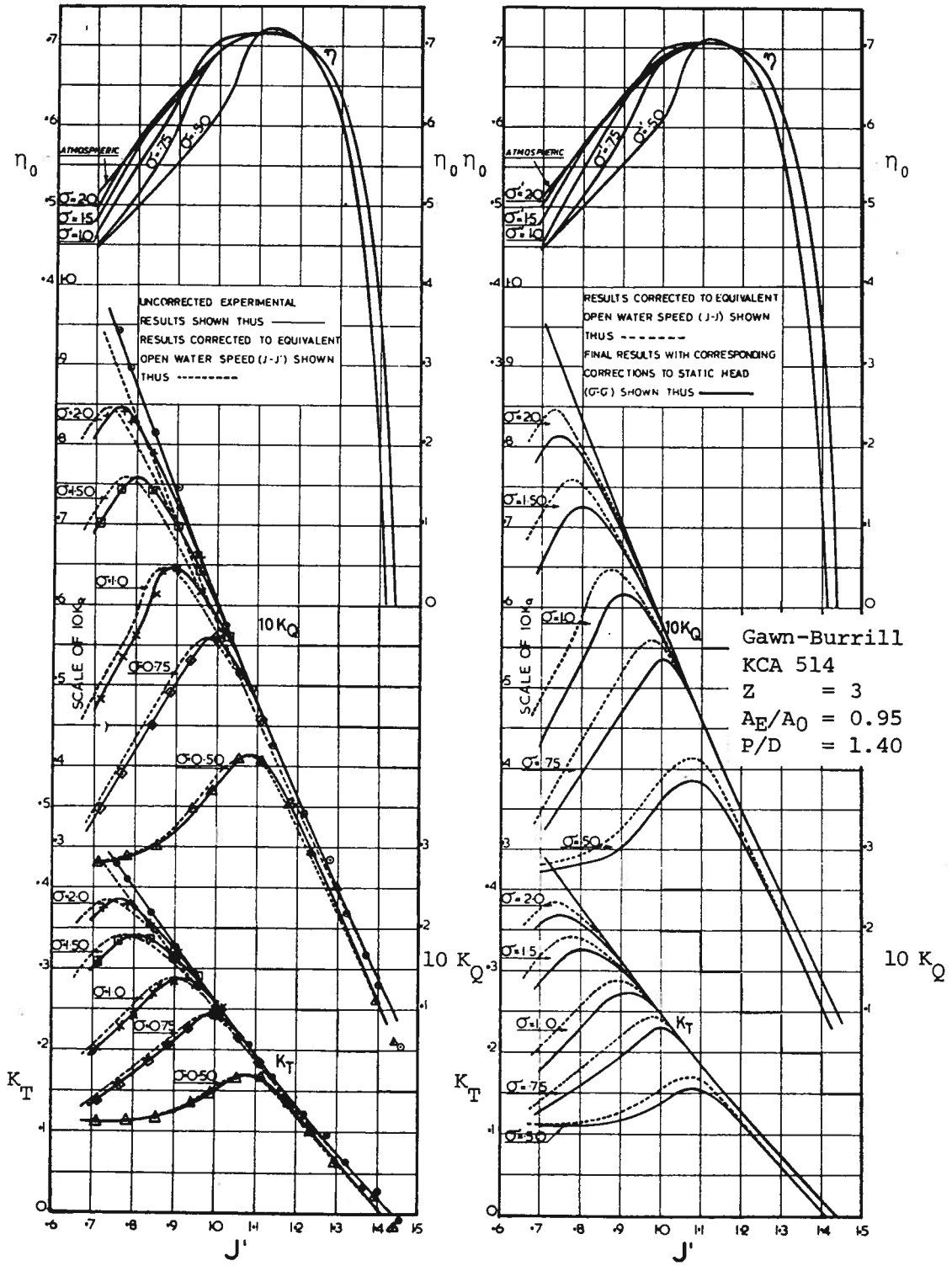

Figure 5.31: Supercavitating Gawn-Burrill Screw (as a Function of J)

From Blount and Fox (1976, p. 37)

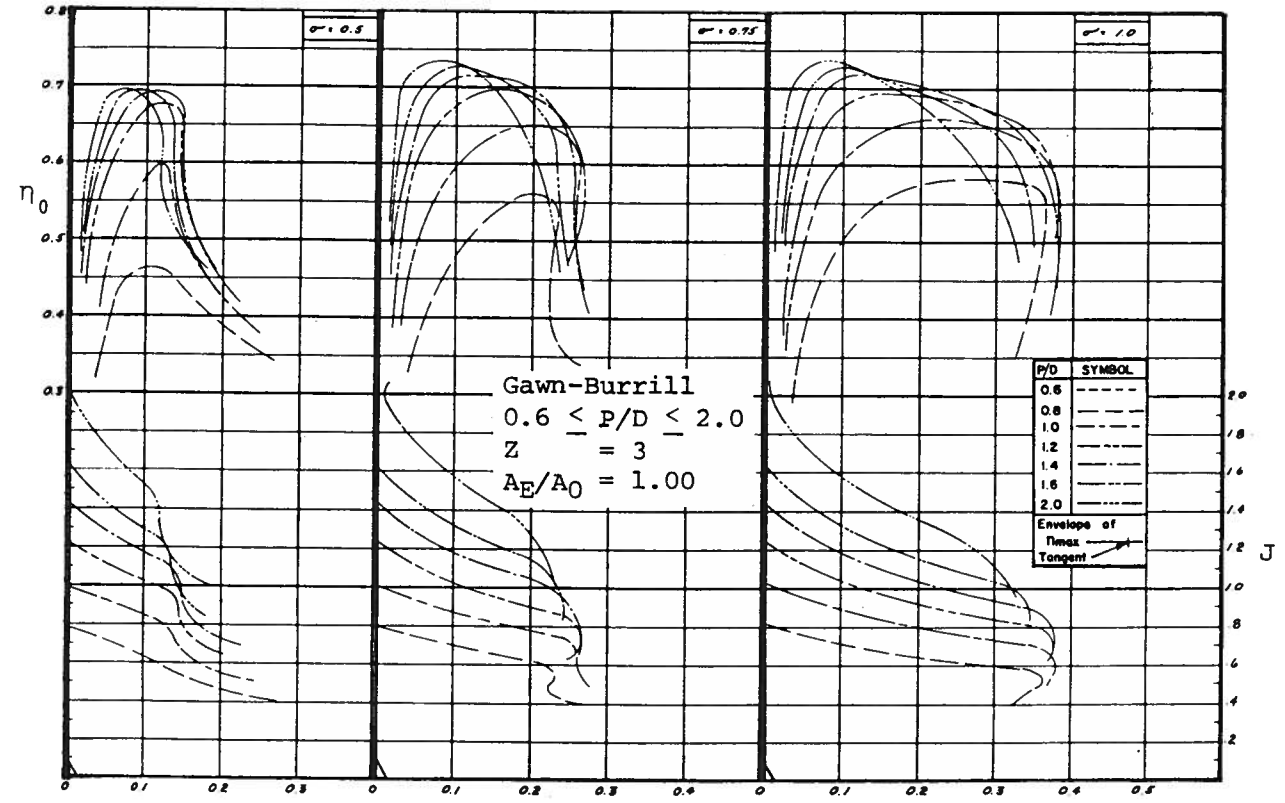

(a) σ = 0.5 (b) σ = 0.75 (c) σ = 1.0

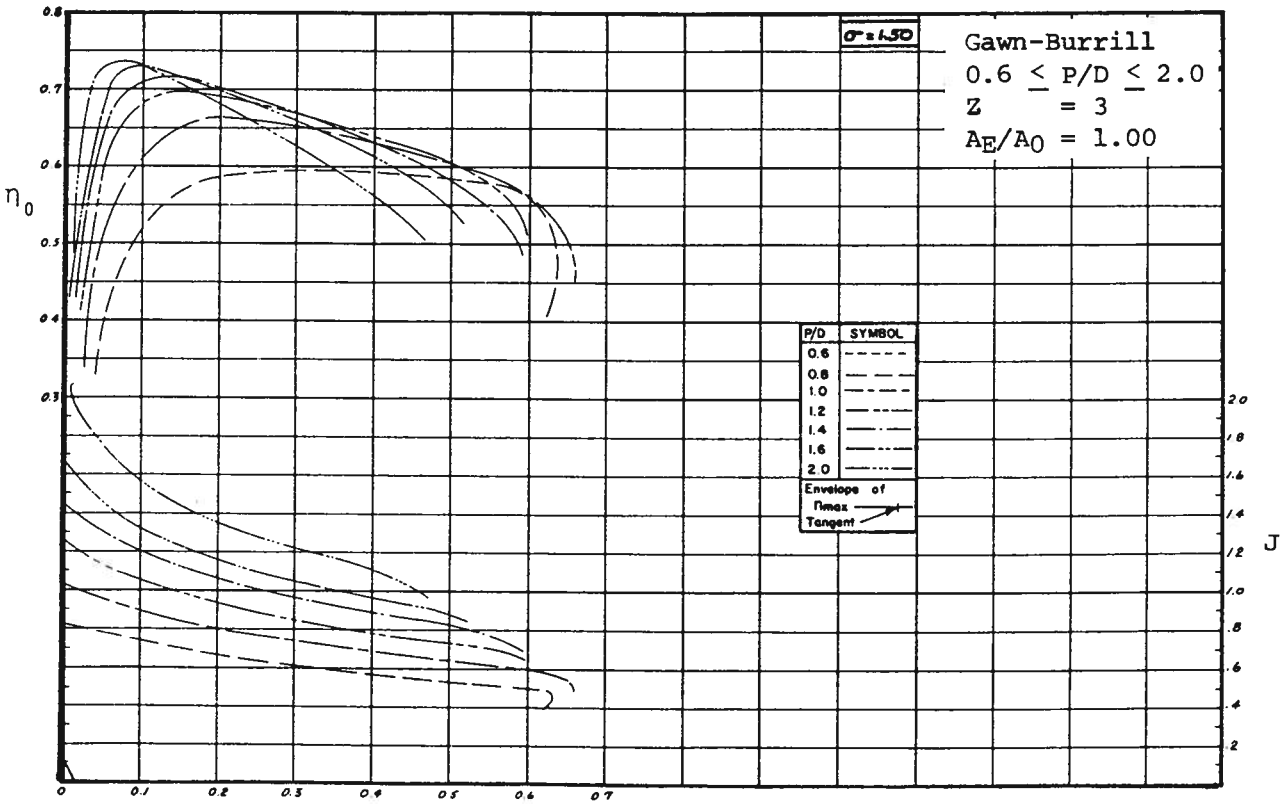

(d) σ = 1.5

Figure 5.32: Supercavitating Gawn-Burrill Screw (as a Function of K_T/J^2)

From Blount and Fox (1976, p. 38)

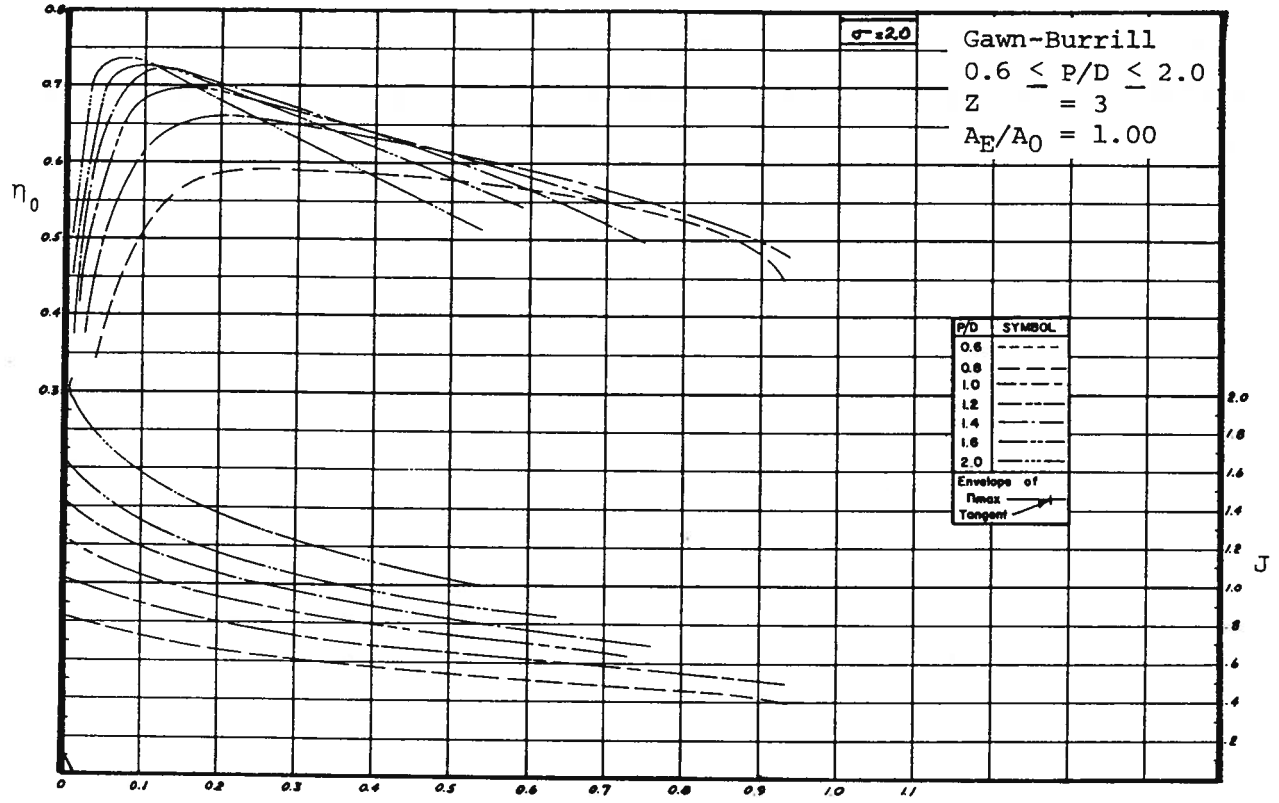

(e) σ = 2.0

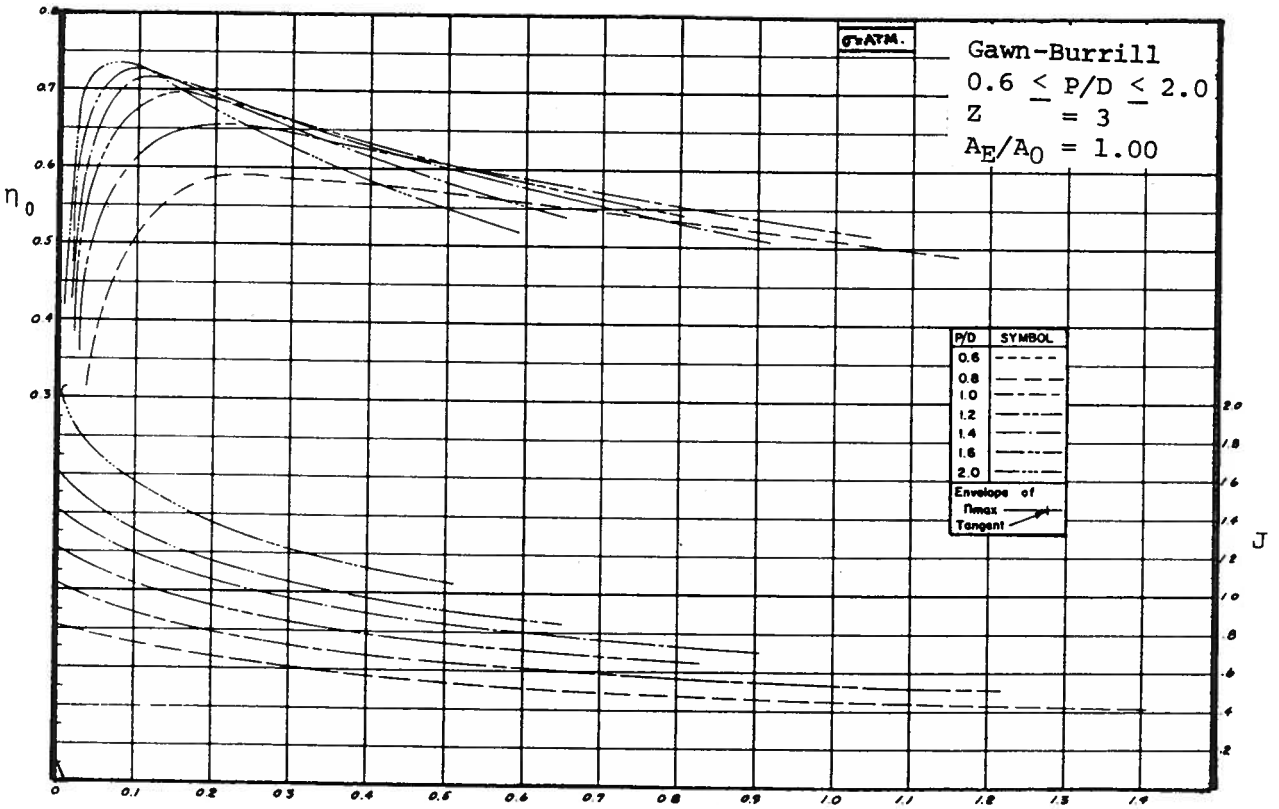

(f) σ = atmospheric

Figure 5.32: (Continued)

From Newton and Rader (1961, pp 94 and 95)

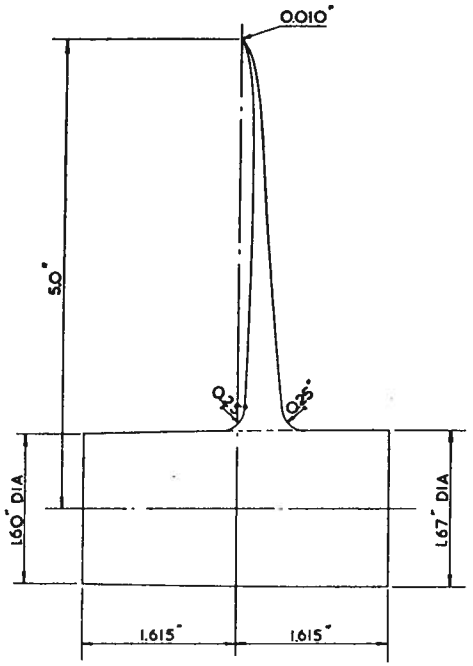

(a) Side View

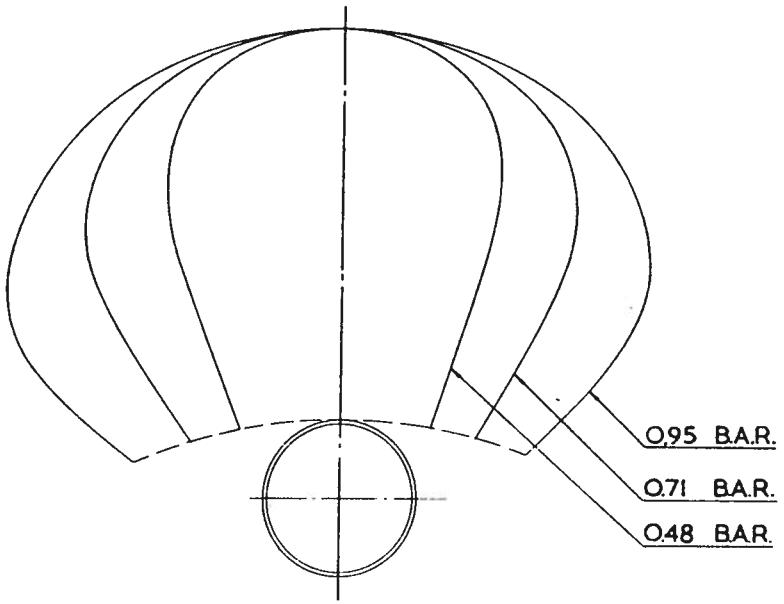

(b) Expanded View of Blades

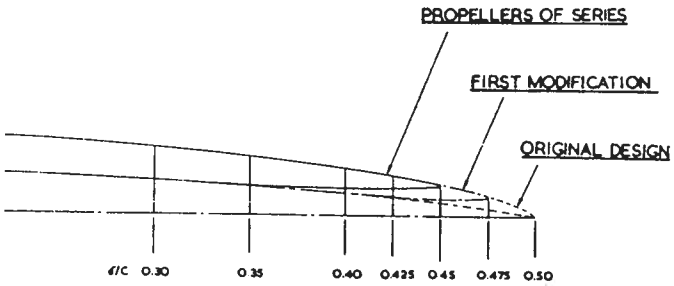

(c) Leading-Edge Detail for Blades

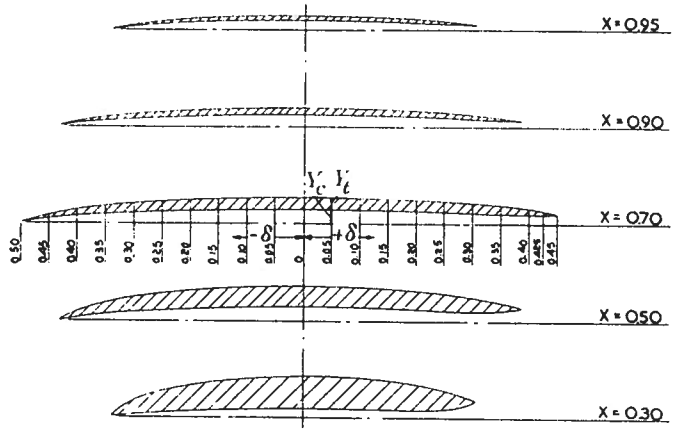

(d) Blade Sections on Model with BAR = 0.71

Figure 5.33: Geometry of the Newton-Rader Series Screws

achieve freedom from face cavitation and to obtain a high efficiency at the design operating conditions.

An example of the performance is shown in Fig. 5.34. The character of the influence of cavitation number is seen to be quite different from that of both the Wageningen and the Gawn-Burrill series. The performance, particularly the efficiency, drops off markedly at high values of the advance ratio, rather than at low values. This feature was noted by Newton and Rader (1961) and was explained by the fact that the blades are more cambered than in the other propeller series.

Finally, Blount and Fox (1978) have also plotted the results of this series using a base of K_T/J^2 . An example is given in Fig. 5.35.

From Newton and Rader (1961, pp 96 and 97)

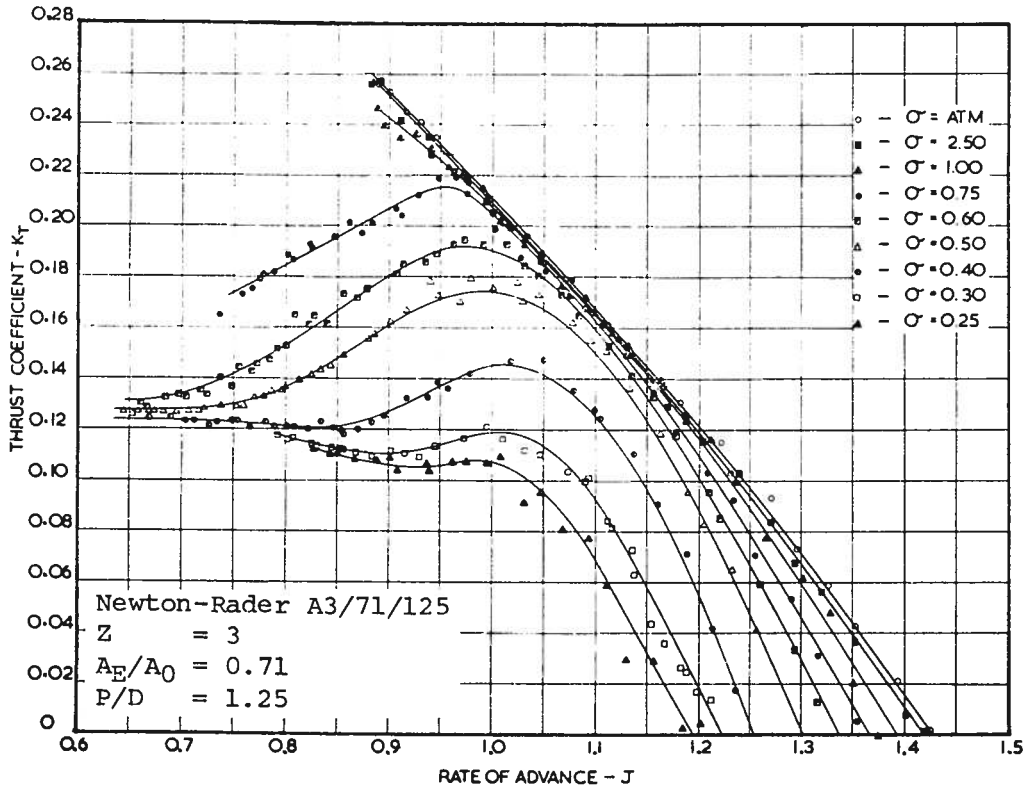

(a) Thrust Coefficient

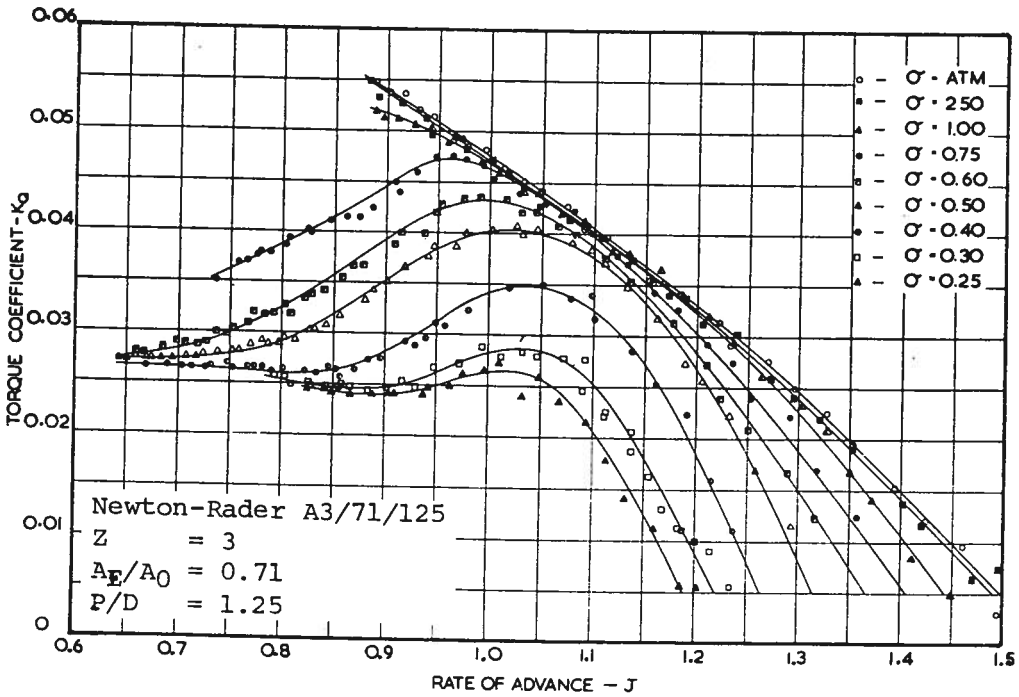

(b) Torque Coefficient

Figure 5.34: Supercavitating Newton-Rader Screw (as a Function of J)

From Newton and Rader (1961, p. 97)

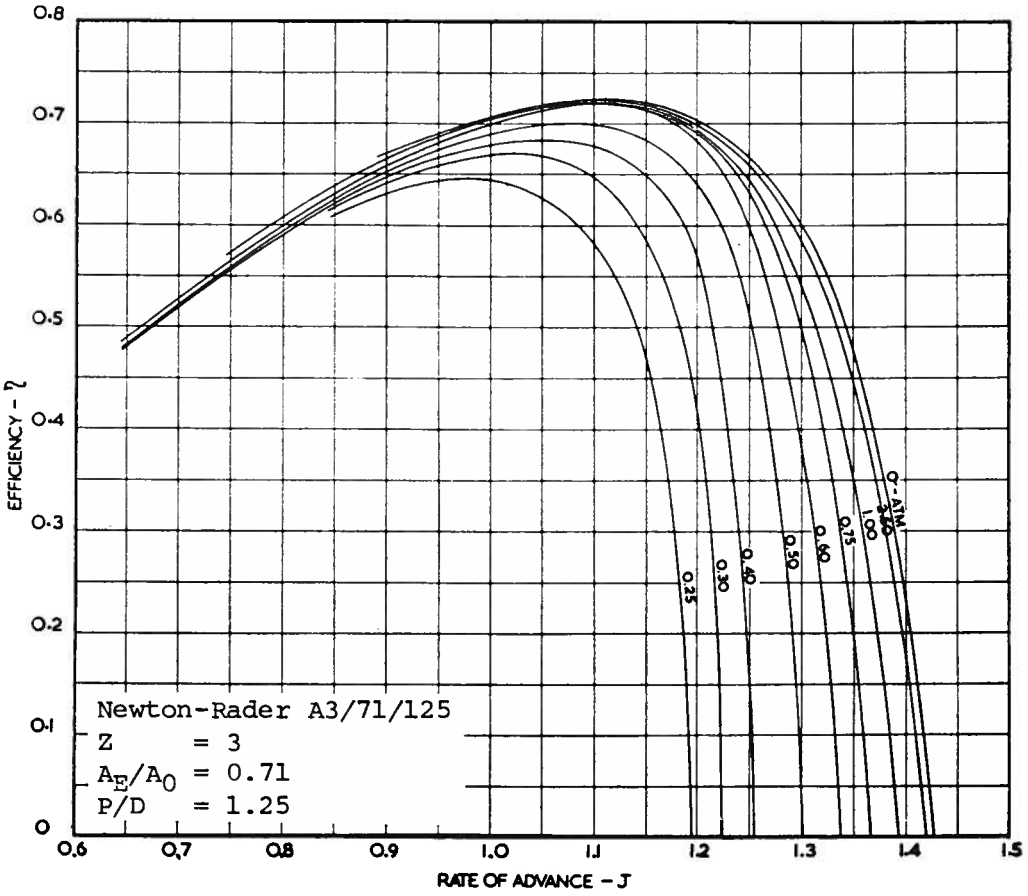

(c) Efficiency

Figure 5.34: (Continued)

From Blount and Fox (1978, p. 165)

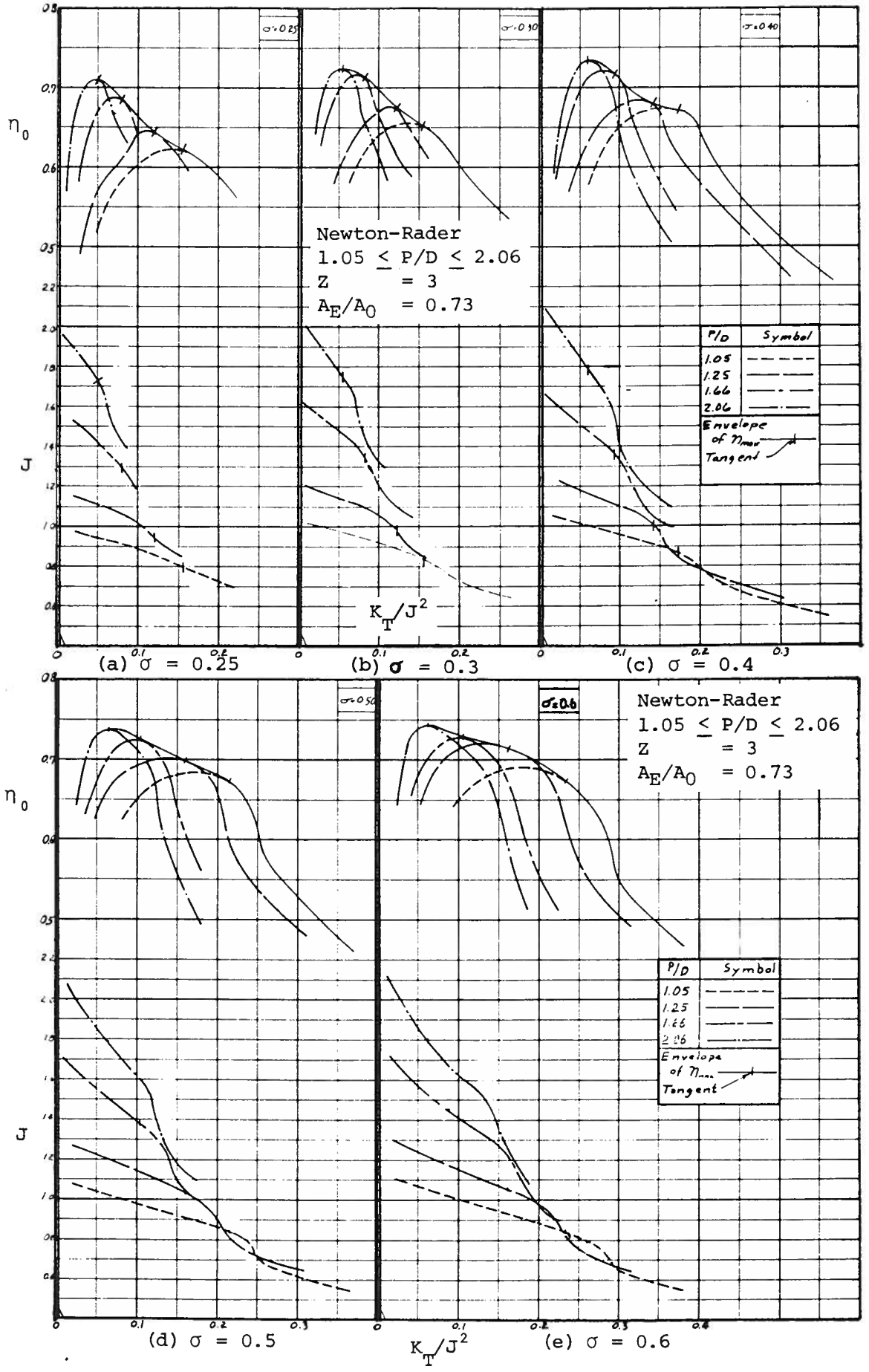

Figure 5.35: Supercavitating Newton-Rader Screw (as a Function of K_T/J^2)

From Blount and Fox (1978, p. 166)

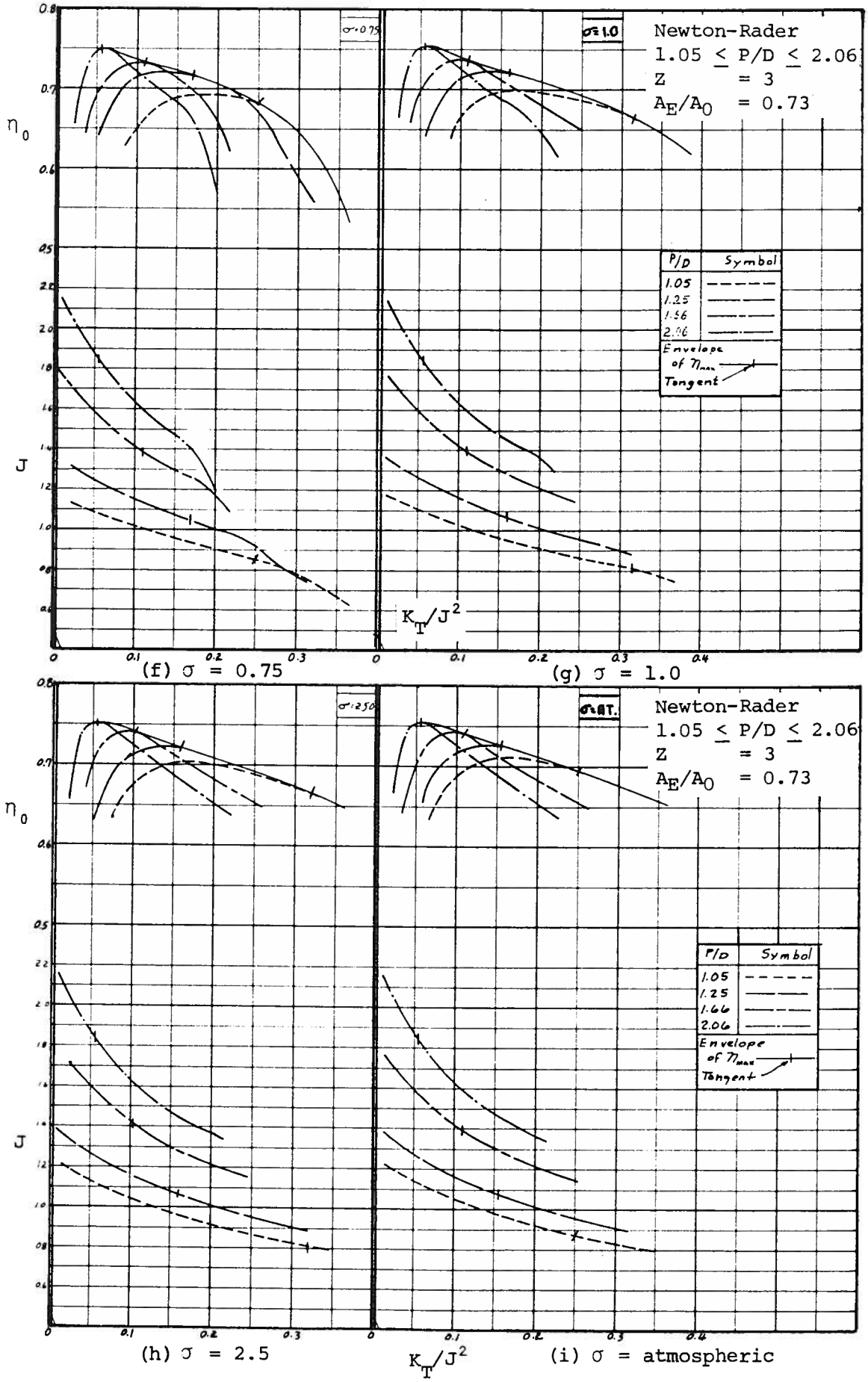

Figure 5.35: (Continued)

6. BIBLIOGRAPHY

Items detailed only by a report number are publications of the Department of Naval Architecture and Marine Engineering. Articles referred to in the text are asterisked.

6.1. References on Air-Cushion Vehicles

1. Barratt, M.J., "The Wave Drag of a Hovercraft," J. Fluid Mechanics, Vol. 22, Part 1, pp 39-47, May 1965.*

2. Doctors, L.J. and Sharma, S.D., "The Wave Resistance of an Air-Cushion Vehicle," Report 099, 180 + xvi pp, December 1970.*

3. Doctors, L.J., "The Hydrodynamic Influence on the Nonlinear Motion of an Air-Cushion Vehicle over Waves," Proceedings Tenth Symposium on Naval Hydrodynamics, Cambridge, Massachusetts, Office of Naval Research, Washington, pp 389-407, discussion: pp 408-420, June 1974.

4. Doctors, L.J., "The Effect of Compressibility of Air on the Nonlinear Motion of an Air-Cushion Vehicle over Waves," Proceedings Eleventh Symposium on Naval Hydrodynamics, London, England, Office of Naval Research, Washington, pp 373-388, March-April 1976.*

5. Elsley, G.H. and Devereux, A.J., Hovercraft Design and Construction, Cornell Maritime Press, Inc., Cambridge, Maryland, 262 pp, 1968.

6. Everest, J.T. and Hogben, N., "Research on Hovercraft over Calm Water," Transactions Royal Institution of Naval Architects, Vol. 109, No. 3, pp 311-326, July 1967.*

7. Hogben, N., Hovering Craft over Water, Advances in Hydroscience, Vol. 4, Academic Press, Inc., New York, pp 1-72, 1966.

8. Lamb, H., Hydrodynamics, Dover Publications, New York, Sixth ed., 738 + xv pp, 1932.*

9. Mair, W.A., "The Physical Principles of Hovercraft," J. Royal Aeronautical Society, Vol. 68, No. 646, pp 683-691, October 1964.

10. Mantle, P.J., "A Technical Summary of Air Cushion Craft Development," David W. Taylor Naval Ship Research and Development Center, Report 4727, 396 + xvi pp, October 1975.*

11. McLeavy, R. (ed.), Jane's Surface Skimmers, Jane's Publishing Company Limited, London, England. Published annually, example: 398 + xx pp, 1982.

12. Stanton-Jones, R., "Hovercraft skirt development - an Engineering and Performance Review," Transactions Royal Institution of Naval Architects, Vol. 110, No. 4, pp 499-524, October 1968.*

13. Trillo, R.L., Marine Hovercraft Technology, Leonard Hill, London, 245 + xiii pp, 1971.

14. Wheeler, R.W., "The Amphibious Hovercraft," Proceedings 1968 Diamond Jubilee International Meeting, Society of Naval Architects and Marine Engineers, 20 pp, June 1968.

6.2. References on Hydrofoil Boats

15. Abbott, I.H. and von Doenhoff, A.E., Theory of Wing Sections, Dover Publications, Inc., New York, 693 + x pp, 1959.*

16. Acosta, A.J., "Hydrofoils and Hydrofoil Craft," Annual Review of Fluid Mechanics, Vol. 5, Annual Reviews, Inc., Palo Alto, California, pp 161-184, 1973.

17. Crewe, P.R., "The Hydrofoil Boat; Its History and Future Prospects," Transactions Institution of Naval Architects, Vol. 100, No. 4, pp 329-362, discussion: 362-373, October 1958.*

18. Doctors, L.J. and Kelly, D.W., "Rank Deficiency in the Surface-Singularity Method for Potential-Flow Problems," Proceedings Eighth Australasian Fluid Mechanics Conference, University of Newcastle, Newcastle, New South Wales, Australia, 5 pp, November 1983.*

19. Doctors, L.J., "The Effects of a Finite Froude Number on a Supercavitating Hydrofoil," 42 + ii pp, to be published in J. Ship Research, October 1984.*

20. Eames, M.C., "HMCS Bras d'Or - An Open Ocean Hydrofoil Ship," Transactions Royal Institution of Naval Architects, Vol. 113, No. 2, pp 111-130, discussion: 130-138, April 1971.*

21. Faber, E., "Hydrofoil Craft and their Marine Engineering Aspects," Transactions Institute of Marine Engineers, Vol. 82, No. 10, pp 365-375, discussion: 375-377, October 1977.

22. Giesing, J.P. and Smith, A.M.O., "Potential Flow about Two-Dimensional Hydrofoils," J. Fluid Mechanics, Vol. 28, Part 1, pp 113-129, April 1967.*

23. Glauert, H., The Elements of Aerofoil and Airscrew Theory, The Macmillan Company, New York, 228 + vi pp, 1944.*

24. Hough, G.R. and Moran, J.P., "Froude Number Effects on Two-Dimensional Hydrofoils," J. Ship Research, Vol. 13, No. 1, pp 53-60, March 1969.*

25. Newman, J.N., Marine Hydrodynamics, The MIT Press, Cambridge, Massachusetts, 402 + xiii pp, 1980.*

26. Parkin, J.H., Bell and Baldwin - Their Development of Aerodromes and Hydrodromes at Baddeck, Nova Scotia, University of Toronto Press, 555 + xvii pp, 1964.*

27. Parsons, M.G., "Informal Notes for NA 420 - Ship Resistance and Propulsion II," Department of Naval Architecture and Marine Engineering, The University of Michigan, 178 + ii pp, 1980.*

28. Schlichting, H., Boundary Layer Theory, McGraw-Hill Book Company, Inc., New York, Fourth ed., 647 + xx pp, 1962.*

29. Tulin, M.P., "Supercavitating Flows - Small Perturbation Theory," J. Ship Research, Vol. 7, No. 3, pp 16-37, January 1964.*

30. Wu, Y.T., "A Theory for Hydrofoils of Finite Span," J. Mathematics and Physics, Vol. 33, No. 3, pp 207-248, October 1954.

31. -----, "SNAME Hydrofoil Symposium," Seattle, Washington, Society of Naval Architects and Marine Engineers, New York, 148 + ii pp, April 1965.

6.3. References on Planing Boats

32. Aferiat, S., "PLANEOPT: Planing boat Optimization Program, Documentation," Report 190, 82 + iv pp, April 1977.

33. Beys, P.M., "Series 63 Round Bottom Boats," Davidson Laboratory, Stevens Institute of Technology, Report 949, 47 + iv pp, April 1963.*

34. Doctors, L.J., "Representation of Planing Surfaces by Finite Pressure Elements," Proceedings Fifth Australasian Conference on Hydraulics and Fluid Mechanics, University of Canterbury, Christchurch, New Zealand, pp 480-488, December 1974.*

35. Doctors, L.J., "Representation of Three-Dimensional Planing Surfaces by Finite Elements," Proceedings First International Conference on Numerical Ship Hydrodynamics, Gaithersburg, Maryland, D.W. Taylor Naval Ship Research and Development Center, and Office of Naval Research, pp 517-537, October 1975.*

36. Du Cane, P., High-Speed Small Craft, David & Charles (Holdings) Limited, Abbot, England, 465 + xiii pp, 1974.*

37. Gray, H.P., Allen, G. and Jones, R.R., "Prediction of Three-Dimensional Pressure Distributions on V-Shaped Prismatic Wedges during Impact or Planing," Naval Ship Research and Development Center, Report 3795, 32 + iv pp, February 1972.

38. Hadler, J.B., "The Prediction of Power Performance on Planing Craft," Transactions Society of Naval Architects and Marine Engineers, Vol. 74, pp 563-610, December 1966.*

39. Hadler, J.B. and Hubble, E.N., "Prediction of the Power Peformance of the Series 62 Planing Hull Forms," Transactions Society of Naval Architects and Marine Engineers, Vol. 79, pp 366-404, December 1971.*

40. Hadler, J.B., Hubble, E.N. and Holling, H.D., "Resistance Characteristics of a Systematic Series of Planing Hull Forms - Series 65," presented to the Chesapeake Section, Society of Naval Architects and Marine Engineers, 53 + iii pp, May 1974.*

41. Holling, H.D. and Hubble, E.N., "Model Resistance Data of Series 65 Hull Forms Applicable to Hydrofoils and Planing Craft," Naval Ship Research and Development Center, Report 4121, 431 + v pp, May 1974.*

42. Hubble, N., "Resistance of Hard-Chine, Stepless Planing Craft with Systematic Variation of Hull Form, Longitudinal Center of Gravity, and Loading," Naval Ship Research and Development Center, Report 4307, 344 + v pp, April 1974.*

43. Millward, A., "Resistance of a Fast, Round Bilge Hull in Shallow Water," J. American Institute of Aeronautics and Astronautics, Vol. 20, No. 8, pp 1092-1096, August 1982.

44. Saunders, H.E., Hydrodynamics in Ship Design, Society of Naval Architects and Marine Engineers, New York, 648 + xxxv pp, 1957.*

45. Savitsky, D. and Neidinger, J.W., "Wetted Area and Center of Pressure of Planing Surfaces at Very Low Speed Coefficients," Experimental Towing Tank, Stevens Institute of Technology, Report 493, 50 + ii pp, July 1954.*

46. Savitsky, D., "Hydrodynamic Design of Planing Hulls," Marine Technology, Vol. 1, No. 1, pp 71-95, October 1964.*

47. Savitsky, D., "On the Seakeeping of Planing Hulls," Marine Technology, Vol. 5, No. 2, pp 164-174, April 1968.*

48. Savitsky, D. and Brown, P.W., "Procedures for Hydrodynamic Evaluation of Planing Hulls in Smooth and Rough Water," Marine Technology, Vol. 13, No. 4, pp 381-400, October 1976.*

49. Sedov, L.I., Two Dimensional Problems in Hydrodynamics and Aerodynamics, Interscience Publishers, J. Wiley and Sons, Inc., New York, 427 + xv pp, 1965.

6.4. References on Propulsion

50. Alison, J.L., "Propellers for High-Performance Craft," Marine Technology, Vol. 15, No. 4, pp 335-380, October 1978.*

51. Bernitsas, M.M., Ray, D., and Kinley, P., "K_T, K_Q and Efficiency Curves for the Wageningen B-Series Propellers," Report 237, 102 + xii pp, May 1981.*

52. Bernitsas, M.M. and Ray, D., "Optimum Revolution B-Series Propellers," Report 244, 130 + xviii pp, August 1982.*

53. Bernitsas, M.M. and Ray, D., "Optimum Diameter B-Series Propellers," Report 245, 127 + xviii pp, August 1982.*

54. Blount, D.L. and Fox, D.L., "Small Craft Power Prediction," Marine Technology, Vol. 13, No. 1, pp 14-45, January 1976.

55. Blount, D.L. and Fox, D.L., "Design Considerations for Propellers in a Cavitating Environment," Marine Technology, Vol. 15, No. 2, pp 144-178, April 1978.*

56. Cohen, S.B., "Class Notes for NA 320 Ship Resistance and Propulsion I," Department of Naval Architecture and Marine Engineering, The University of Michigan, 163 + iii pp, January 1984.

57. Comstock, J.P. (ed.), Principles of Naval Architecture, Society of Naval Architects and Marine Engineers, New York, 827 + xi pp, 1967.*

58. Gawn, R.W.L. and Burrill, L.C., "Effect of Cavitation on the Performance of a Series of 16-Inch Model Propellers," Transactions Institution of Naval Architects, Vol. 99, No. 4, pp 690-728, October 1957.*

59. Harvald, S.A., Resistance and Propulsion of Ships, John Wiley and Sons, New York, 353 + xii pp, 1983.*

60. Kim, H.C., "Hydrodynamic Aspects of Internal Pump-Jet Propulsion," Marine Technology, Vol. 3, No. 1, pp 80-98, January 1966.

61. Levy, J., "The Design of Water-Jet Propulsion Systems for Hydrofoil Craft," Marine Technology, Vol. 2, No. 1, pp 15-25 + 41, January 1965.

62. Markussen, P.A., "On the Optimum Wageningen B-Series Propeller Problem with Cavitation-Limiting Restraint," J. Ship Research, Vol. 23, No. 2, pp 108-114, June 1979.*

63. Michelsen, F.C., Moss, J.L., Koelbel, J., Savitsky, D. and Apollonio, H., "Small Craft Engineering: Resistance, Propulsion and Seakeeping," Report 120, 299 + vii pp, October 1971.

64. Newton, R.N. and Rader, H.P., "Performance Data of Propellers for High-Speed Craft," Transactions Royal Institution of Naval Architects, Vol. 103, No. 2, pp 93-129, April 1961.*

65. Oosterveld, M.W.C. and van Oosanen, P., "Further Computer-Analyzed Data of the Wageningen B-Screw Series," International Shipbuilding Progress, Vol. 22, No. 251, pp 251-262, July 1975.

66. van Lammeren, W.P.A., van Manen, J.D. and Oosterveld, M.W.C., "The Wageningen B-Screw Series," Transactions Society of Naval Architects and Marine Engineers, Vol. 77, pp 269-317, December 1969.*

67. Woodward, J.B., "Small Craft Engineering: Propulsion by the Internal Combustion Engine," Report 122, 241 + vii pp, October 1971.

68. -----, "Proceedings of the Symposium on the Design and Construction of Recreational Power Boats," Vol. 1: 345 + viii pp (Report 214), Vol. 2: 257 + ii pp (Report 215), Vol. 3: 142 + ii pp (Report 216), August 1979.